Material Invariant Properties of Shales: Nanoindentation and Microporoelastic Analysis

by

A. Delafargue

Ingénieur de l'École Polytechnique (2003)

Submitted to the Department of Civil And Environmental Engineering
in partial fulfillment of the requirements for the degree of

Master of Science in Civil And Environmental Engineering

at the

MASSACHUSETTS INSTITUTE OF TECHNOLOGY

September 2004

Signature of Author .....
Department of Civil And Environmental Engineering
23 Aug 2004

Certified by .....
Franz-Josef Ulm
Associate Professor of Civil and Environmental Engineering
Thesis Supervisor

Accepted by .....
Heidi Nepf
Chairman, Department Committee on Graduate Students

Material Invariant Properties of Shales: Nanoindentation and Microporoelastic Analysis

by

A. Delafargue

Submitted to the Department of Civil And Environmental Engineering
on 23 Aug 2004, in partial fulfillment of the
requirements for the degree of
Master of Science in Civil And Environmental Engineering

Abstract

Shales compose the major part of sedimentary rocks and cover most of hydrocarbon bearing reservoirs. Shale materials are probably one of the most complex natural composites, and their mechanical properties are still an enigma that has deceived many decoding attempts from experimental and theoretical sides.

Advanced experimental techniques, such as nanoindentation, and theoretical microporomechanics make it possible today to break such a heterogeneous material down to a scale where physical chemistry meets mechanics, to extract intrinsic material properties that do not change from one material to another, and to upscale the intrinsic material behavior from the submicroscale to the macroscale of engineering application.

This thesis identifies material invariant properties of shales by investigating the elastic properties of shales at multiple scales. We combine new experimental data of shale microstructure and mechanical properties, with nanoindentation analysis and microporomechanics. This leads to the development of a novel multiscale upscaling model for shale poroelasticity.

The proposed model relies on a few quantities that can be easily obtained from mineralogy and porosity data. This model is calibrated and validated, and its domain of application and limitations are discussed. The strong predictive capabilities of the model are particularly important for the Oil and Gas Industry, which can apply our predictive model of shale elasticity for geophysics and exploitation engineering applications.

Thesis Supervisor: Franz-Josef Ulm
Title: Associate Professor of Civil and Environmental Engineering

Contents

List of Tables

List of Figures

Acknowledgements

This research work could not have been done without Franz-Josef Ulm who not only served as my supervisor, but also encouraged and challenged me throughout this intensive year. I also thank him for the financial support which he provided and gratefully acknowledge the support of ChevronTexaco. I thank Russ Ewy and Luca Duranti for their collaboration. I cannot forget the helpful discussions with Georgios Constantinides whose experience and contributions in this project made me learn a lot. I thank him particularly, as well as all the members of the group: Emilio Silva, Nina Paiva, Chris Bobko, Jong-Min Shim and Gabriel de Hauss. Last, a special thanks goes to someone who will recognize herself, for her inspiring visits.

Part I

General Presentation

Chapter 1

Introduction

1.1 Industrial Context

Shales are probably one of the most complicated and intriguing natural materials present widely on earth. It is commonly agreed that shales make up about 75% of sedimentary basins and cover many hydrocarbon-bearing reservoirs (Fig. 1-1) [53], [48]. Clayish sediments are the starting and ending point of hydrocarbon migration: hydrocarbons originate from their organic content and are trapped by their low permeability. Knowing and predicting the mechanical properties of this reservoir entrance door is the key to success in many fields of exploitation, ranging from seismic exploration and log-data interpretation, to well drilling and production [84]. But as a rock, properties of shales are still mysterious and remain a recurrent source of inefficiency in exploration and production processes:

- The accuracy of seismic reservoir imaging is very limited, with a resolution in the range of 10-50m, compared to the thickness of some reservoirs and of impervious shale layers often present within the reservoirs [22]. The predicted reservoir sizes and extraction ratios are therefore not reliable without further investigations. Inherently limited from its range of wave lengths, this method shares with all other acoustic methods the difficulty to know precisely how fast waves are traveling, and to depict the location of characteristic hydrocarbon bearing rocks. Governed by material stiffness properties, wave velocities and reflection properties are particularly influenced by the elastic anisotropy of shale materials.

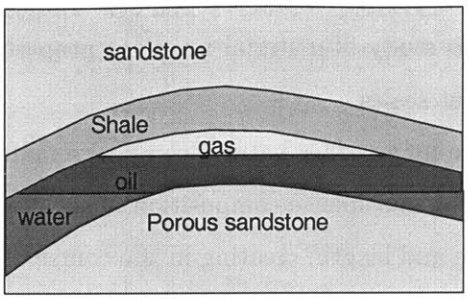

Figure 1-1: Schematic representation of a typical hydrocarbon reservoir

Can one predict these elastic properties without very expensive drilling/sampling/lab testing operations?

- The losses due to wellbore failure cost over $1 billion each year to the Oil and Gas industry [31]. The instability of this complex mixture of minerals is a headache for drilling engineers: shales are material systems that are mostly composed of compacted clay particles whose cohesion is very sensitive to the chemical, thermal, electrical and mechanical environment. How can one best choose drilling fluids in order to avoid such mechanical instabilities?

Two main areas of investigations are correspondingly advanced in the oil industry for studying shale properties: one tries to understand the failure mechanisms, decisive for drilling operations; the other focuses on the elasticity as the source of acoustic wave propagation, which is crucial for seismic exploration. While it seems hard to care about the strength properties of a shale with no information about shale elasticity, the second field of study is rather autonomous. Indeed, acoustic waves generally perturb the material in the form of small reversible displacements, whereas drilling affects shales irreversibly under various chosen mechanical, chemical and thermal conditions.

1.2 Research Motivation and Objective

Is it possible to break down natural porous material systems down to a scale where materials no longer change from one material to another, and upscale ('nanoengineer') the behavior from

the nanoscale to the macroscale of engineering applications? – This is the challenging question we want to address in this study of material invariant properties of shales, through the study of the elasticity at different scales.

Inarguably, shales, like many other natural composite materials are multiphase and multiscale material systems. The multiphase composition of such materials is permanently evolving over various scales of time and length, creating in the course of this process the most heterogeneous classes of materials in existence, with heterogeneities that manifest themselves from the nanoscale to the macroscale.

It is the premise of this study to identify a common poromechanical 'blueprint' of shale materials, in terms of common microstructural features and constitutive mechanical properties.

1.3 Chosen Approach

Recent advances in both experimental and theoretical microporomechanics provides a rational means to quantitatively address multiphase and multiscale material systems. The underlying idea of continuum micro(poro)mechanics is that it is possible to separate a heterogeneous material into phases with on-average constant material properties [79],[100]. A phase, in the sense of continuum micromechanics, is not necessarily a material phase such as a specific mineral as used in physical chemistry, but a material domain that can be identified, at a given scale, with on-average constant material properties, so that a continuum mechanics analysis can be performed, with some confidence and accuracy, at the considered material scale. Such phases are referred to as microhomogeneous phases. When such phases can be identified at different scales in a material, microporomechanics offers tools to relate the materials properties at different scales. This approach has been applied to bones by Hellmich and Ulm [45], who were able to predict the macroscopic properties of all types of bones from known mineral proportions and constitutive properties.

Provided the existence of such microhomogeneous phases, recent progress in instrumented indentation techniques allow the assessment of mechanical properties down to the scale of a few nanometers. The idea is to indent a flat sample surface with a sharp diamond, while measuring load and penetration depth with high accuracy. Then, by an inverse analysis of the load *vs.*

depth curve of each test, one can infer solid mechanical properties of the indented solid in a characteristic region near the indented surface. With regards to shales, this technique has the premise to measure intrinsic mechanical properties at the scale of very small individual solid constituents, here clay minerals. In contrast to other experimental testing methods, nanoindentation is an almost non destructive test and can be performed automatically in series of hundreds consecutive indentation tests on a grid on any smooth material surface. This opens up the possibility of statistical analysis of the results.

The combination of these two advanced experimental and theoretical tools, *ie.* nanoindentation and microporomechanics, has been successfully applied to cementitious materials by Constantinides and Ulm [18], [19], who were able to identify universal solid elastic properties and provide a predictive model for cement paste stiffness from constituent volume fractions only. The new challenge posed *w.r.t.* shales is two fold:

- Shales are anisotropic materials, which renders the analysis difficult, both for the indentation analysis and the homogenization schemes.
- The granular nature of shale materials may not be easy to model in a continuous fashion, requiring some original developments to capture the behavior of the materials at multiple scales.

Three shales provided by ChevronTexaco coming from different origins and depth will serve as an experimental backbone for the identification of general shale material invariant properties. This will be achieved by bringing together mineralogy, microstructure, and indentation properties of the three materials in a multiscale anisotropic elastic upscaling model.

1.4 Thesis Outline

This report is divided in five parts. Following the first part, general presentation of the objectives and methods of our study, the second part sets the base for the interpretation of indentations on shales, by describing the indentation technique (Chapter 2), and proposing an original extension of indentation analysis to transverse isotropic solids (Chapter 3). For the purpose of a microporoelastic analysis of shales, the third parts brings together all available

experimental information on shale microstructure (Chapter 4), and mechanical properties of shales (Chapter 5). The fourth part proposes an original multiscale micromechanical model for shale elasticity (Chapter 6). The model is calibrated and validated (Chapter 7), and its predictive capabilities for engineering practice are discussed (Chapters 8). The last part of this report gives a general conclusion of our study of shale material invariant properties (Chapter 9).

1.5 Research Significance

Finding the code, or blueprint of shales is no doubt a reductionist approach.

The prime challenge of this study is to capture the observed macroscopic variability of shales elastic properties through a handful of easily identifiable varying parameters, and to relate these parameters as much as possible to mineralogy data, that one can extract from drilling fluid composition, depth, pore pressure and other available geological information. Such a reductionist approach requires the use of micromechanical models, which by construction are reductionist.

From a mechanics point of view, the second challenge of this study is to identify and apply appropriate homogenization schemes that are relevant for particulate and colloidal material systems, in which surface forces determine most of the overall mechanical behavior. Nanoindentation, with its unique possibility to measure the properties of matter with an unprecedented resolution, offers a means of validating homogenization schemes.

But most importantly, for the physicist and the chemist, experimental micromechanics reaches a scale at which mechanics meets physics and chemistry. To identify the sources of mechanical behavior, and to relate these sources to chemical composition is a new original way to enhance the understanding about complex materials like clays. This understanding may serve much more than for shales only. Indeed, since clays are used in a large variety of industrial applications, this whole deterministic and reductionist approach could be useful for material optimization purposes.

1.6 Industrial Benefits

Engineering, by its very nature, is based on reductionist models of reality. For the geophysicist or the oil engineer, who often use complex simulators to model a reservoir and optimize its production, the geometry of the reservoir is as important as the knowledge about the properties of each constitutive brick [22]. If a simple tool is available to predict shale elastic properties, the needs and facilities of the Oil industry in this field will quickly verify its utility. Then, if the multiscale morphology is validated mechanically for the elastic properties, this study could be the starting point for modeling even more complex and still open problems: shale anisotropic permeability, strength, viscoelastic behavior, fracturation and so on.

1.7 Notations

In this section we introduce the notations that we will use throughout this report. Some notations and basic relations for elastic transverse isotropy are also given.

1.7.1 Tensor Notations

Throughout this thesis, we use the following notations:

$\underline{z}$ = Vector.

$\boldsymbol{\sigma}$ = Second order tensor.

$\mathbf{E}$ = Uniform second order tensor.

$\mathbf{1}$ = Second order identity tensor.

E_{ij}, σ_{ij} = Second order tensor components. $i, j \in \{1, 3\}$.

$\mathbb{C}$ = forth order tensor.

$\mathbb{I}$ = Forth order identity tensor.

C_{ijkl} = forth order tensor components. $i, j, k, l \in \{1, 3\}$.

'$\cdot$' refers to scalar products, and single tensorial contractions.

':' refers to tensorial double contractions.

For operations on tensors written with the index notation, summation is performed on repeated indices, *ie.* $a_{ij}b_{jk} = c_{ik}$.

1.7.2 Average Operators

The volume average of the field quantity $A(\underline{z})$ defined in a domain Ω of volume V_Ω reads:

$$\overline{A} = \frac{1}{V_\Omega} \int_\Omega A(\underline{z}) d\Omega \tag{1.1}$$

The volume average of $A(\underline{z})$ in a subdomain $\Omega^s \subset \Omega$ will be denoted by:

$$\langle A \rangle_{\Omega^s} = \frac{1}{V_{\Omega^s}} \int_\Omega A(\underline{z}) d\Omega \tag{1.2}$$

Finally, the mean value of a quantity B defined in a statistical sense will be denoted by μ_B:

$$\mu_B = \frac{1}{N} \sum_{i=1}^{N} B \tag{1.3}$$

where N is the number of tests.

1.7.3 Notations and Basic Relations for Transverse Isotropy

A transverse isotropic solid is defined by an axis of material symmetry.

Written in a 6×6 matrix form (see Helnwein [46]), the stiffness tensor of a transverse isotropic solid in a Cartesian system whose direction $x3$ coincides with the solid's axis of symmetry, reads:

$$\mathbb{C} = \begin{bmatrix} C_{11} & C_{12} & C_{13} & & & \\ C_{12} & C_{11} & C_{13} & & (0) & \\ C_{13} & C_{13} & C_{33} & & & \\ & & & 2C_{44} & 0 & 0 \\ & (0) & & 0 & 2C_{44} & 0 \\ & & & 0 & 0 & 2C_{66} = C_{11} - C_{12} \end{bmatrix} \tag{1.4}$$

The five independent stiffness constants are given by:

$$\begin{aligned} C_{11} &= C_{1111}, C_{33} = C_{3333}, C_{12} = C_{1122}, \\ C_{13} &= C_{1133}, C_{44} = C_{2323} = C_{1313}, C_{66} = C_{1212} \end{aligned} \tag{1.5}$$

In this convention [46], all symmetric second order tensors **a** are represented in a 6×1 vector format:

$$\mathbf{a} = \begin{bmatrix} a_{11} & a_{11} & a_{33} & \sqrt{2}a_{23} & \sqrt{2}a_{13} & \sqrt{2}a_{12} \end{bmatrix}^T \tag{1.6}$$

An equivalent set of independent constants describing the elasticity of a transverse isotropic solid can be expressed using two Young's moduli E_{11} and E_{33}, two Poisson's ratios ν_{31} and ν_{12}, and one shear constant G_{12}. These constants are related to the C_{ijkl} values by:

$$E_{11} = C_{11} + \frac{C_{13}^2\left(-C_{11}+C_{12}\right) + C_{12}\left(-C_{33}C_{12}+C_{13}^2\right)}{C_{33}C_{11}-C_{13}^2} \tag{1.7}$$

$$E_{33} = C_{33} - \frac{2C_{13}^2}{C_{11}+C_{12}} \tag{1.8}$$

$$\nu_{31} = \nu_{32} = \frac{C_{13}}{C_{11}+C_{12}} \tag{1.9}$$

$$\nu_{13} = \frac{C_{13}\left(C_{11}-C_{12}\right)}{C_{33}C_{11}-C_{13}^2} \tag{1.10}$$

$$\nu_{12} = \frac{C_{33}C_{12}-C_{13}^2}{C_{33}C_{11}-C_{13}^2} \tag{1.11}$$

$$K = \frac{C_{11}+C_{12}}{2} \tag{1.12}$$

$$G_{13} = G_{23} = 2C_{44} \tag{1.13}$$

$$G_{12} = \frac{C_{11}-C_{12}}{2} \tag{1.14}$$

Note that $\nu_{23} = \nu_{13}, \nu_{21} = \nu_{12}$, but $\nu_{31} \neq \nu_{13}$. In addition the following relationship can be easily shown to hold:

$$\frac{\nu_{31}}{E_{33}} = \frac{\nu_{13}}{E_{11}} \tag{1.15}$$

1.7.4 Notations and Relations for Isotropy

For isotropic solids, bulk and shear moduli k and g, are related to the Young's modulus E, and Poisson's ratio ν, by:

$$k = \frac{E}{3(1-2\nu)} \;\; ; \;\; \mu = \frac{E}{2(1+\nu)} \tag{1.16}$$

Part II

Indentation Technique and Analysis

Chapter 2

Instrumented Indentation

Indentation analysis will play a prominent role in this investigation of material invariant properties of shale materials. For this reason, the objective of this part of the report is to set the base for the analysis of indentations on shales which are complex, heterogeneous and anisotropic materials. Nanoindentation gives a unique opportunity to reduce this complexity by testing material properties at very fine scales. This chapter deals with instrumented indentation technique, and the next one with indentation analysis. In particular, the aim of this chapter is to identify the mechanical properties that are assessed by indentation. We start with a dimensional analysis of the problem to explain how indentation load *vs.* depth curves are analyzed. The potential outcome and limitations of indentation testing on composite materials are discussed. This provides the background for the next chapter, in which we focus on the indentation analysis of transverse isotropic solids.

2.1 Introduction

2.1.1 Historical Background

Indentation tests go a long way back, as early as 1722 (Réaumur, 1722), but really came of age in the early 1900's with the pioneering work of the Swedish engineer Brinell (1901) [8]. By pushing a small sphere of hardened metal or tungsten carbide into a metal alloy, Brinell found empirical relations between the shape of the deformed surface and the strength of the specimens. With the subsequent contributions of Meyer (1908), O'Neill (1944) and Tabor (1951) [81], the

new concept of hardness was introduced. Obtained experimentally from the applied load and the area of the permanent impression, hardness refers to the average pressure in the contact zone below the indenter where high stresses deform the specimen plastically. A simple test was found that provides a good estimate of the yield strength of metals.

More recently, thanks to progress in hardware and software control, depth sensing techniques were introduced that allow a continuous monitoring of the displacement of the indenter into the specimen surface together with the applied load during both loading and unloading periods. The idea of depth sensing techniques and its implementation down to the nanoscale appears to have developed first in the former Soviet Union from the mid 1950ies on throughout the 1970ies. The idea to extract elastic properties from unloading phases was introduced by Bulychev and coworkers in 1975 [82], [10] and received considerable attention world-wide when Doerner and Nix [27] and Oliver and Pharr [67], [64] in the late 1980ies and early 1990ies, also identified this technique for estimating mechanical properties of materials (for a review, see [6]). The key for the determination of material properties is the back analysis of the curve giving the load, P, as a function of the depth of indentation, h, into the indented specimen.

The mechanical analysis of such a problem started in 1881 with the famous study of Heinrich Hertz of the contact between two elastic parabola of revolution [47]. The field of contact mechanics was enriched by Boussinesq (1885) who solved the contact problem between a flat punch and a semi-infinite elastic solid [7]. The elastic solutions were extended to other shapes of indenters by Love (1939) [56], Galin (1946) [39] and Sneddon (1965) [77]. On the other hand, elastoplastic contact problems have not been solved analytically, relying primarily on a combination of dimensional considerations, finite element simulations, and flourishing experimentations aiming at providing helpful approximations. Two very recent reviews by Cheng *et al.* (2004) [16], and Oliver and Pharr (2004) [65] testify of the 'hot' nature of the topic in Material Science and Engineering.

2.1.2 Principle of Indentation Test

In an indentation test, he applied load, P, and the indentation depth, h, between the tip of the indenter and the initial free surface (Fig. 2-1), are measured continuously with time during (at least) a loading phase and a complete unloading one. The load is often held at its maximum

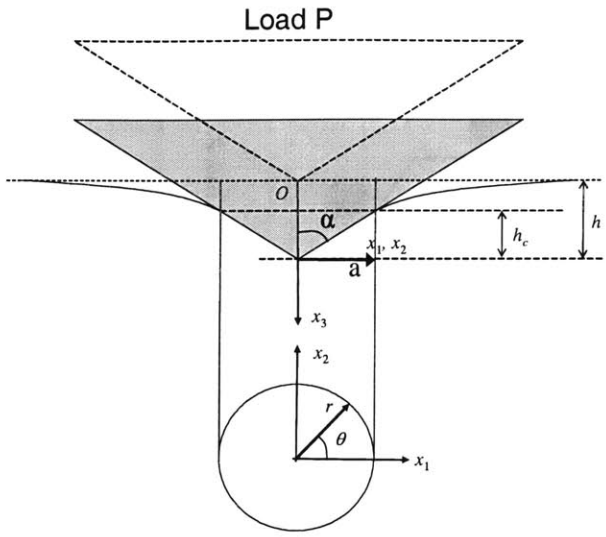

Figure 2-1: Principle of conical indentation.

value, giving rise to a creep period. A typical response is given on Figure 2-2 where $P_{\max}$ and $h_{\max}$ are the maximum measured load and depth, respectively. h_f refers to the depth of the permanent impression, for which the indenter looses contact with the solid.

The following three phases are traditionally interpreted separately (see Fig. 2-2):

1. During the loading phase, the material is deformed plastically and elastically;

2. The unloading phase is generally assumed to be elastic, and gives access to elastic properties;

3. The optional dwelling period can be used to assess time dependent properties such as viscoelastic, viscoplastic and poroelastic properties.

Several combinations of loading, unloading and reloading phases are also possible. In the case of quasistatic indentation, the rates are small enough to avoid any inertia effects. Several techniques of cyclic dynamic loading have been employed as well [57], [38], but these techniques go beyond the scope of this study.

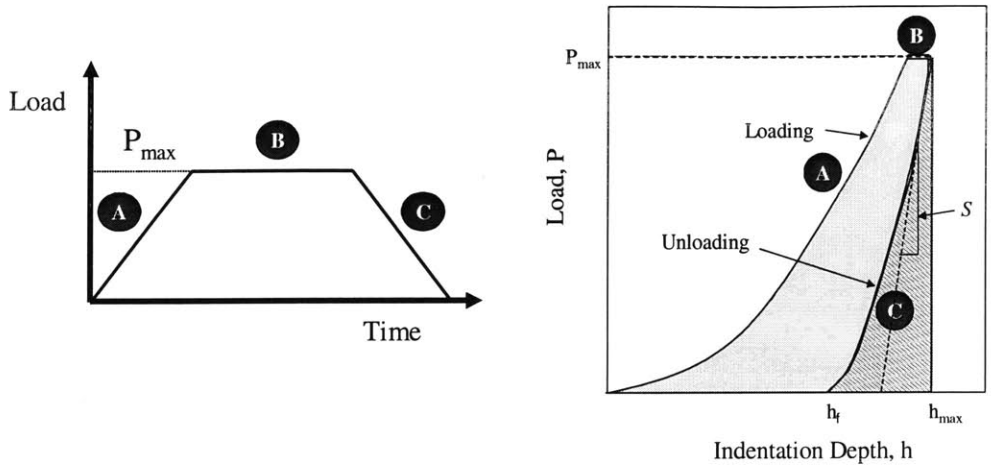

Figure 2-2: Principle of an indentation test: prescribed load history (left), load vs. depth curves (right). It consists in a loading phase (A), a dwelling period (B), and an unloading phase (C). The areas under the $P-h$ curves give the total work provided to the system (plain and striped areas) and the elastic recoverable energy (striped area).

2.1.3 Experimental Set-up

Continuous advances in hardware design, detection methods, and software control over the past ten years make it possible today to measure penetration depths with a resolution in the Angstrom range ($10^{-10}m$), and loads with a resolution in the nanonewton range ($10^{-9}N$) [38]. In order to achieve this accuracy, an indenter, usually a sharp diamond pyramid, is mounted on a mobile column, and is brought in contact with the sample surface on a fixed support (Fig. 2-3). The applied load depends on the intensity of the current applied in a coil attached to the column, interacting with a fixed permanent magnet. Displacements are measured from the change of the capacity of a capacitor composed of fixed and mobile parts. Microindentation machines typically measure loads up to $500\mu N$ and depths up to $50\mu m$.

Most of indentation tests are force-driven experiments, in which the depth is measured as a function of time from a prescribed load rate. Depth controlled tests can be performed with an open loop control, but are more limited in use, because of the sensivity of the feedback control to unexpected material defects.

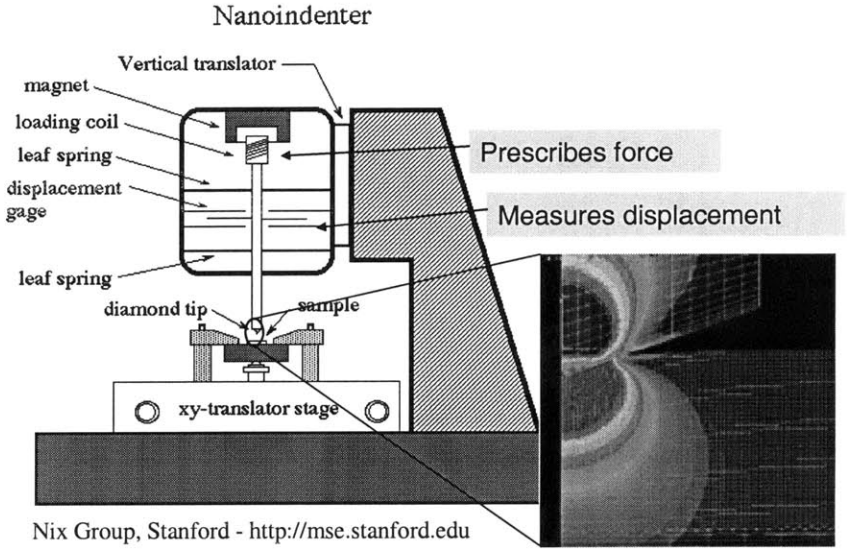

Figure 2-3: Nanoindentation experimental setup, and stress field under the indenter.

2.1.4 Possibilities and Limitations

Nanoindentation is particularly useful for studying the mechanical properties of materials at a scale where no other experimental technique can measure them: thin films, coatings, natural composites, heterogeneous materials, polymers, biological tissues, food products, etc . The present study of shales is a perfect example of a material whose constituents, clay minerals, are too small to be mechanically investigated with traditional mechanical tests.

Initially developed for metals and ceramics, nanoindentation has proved to be a very accurate technique to determine elastic properties [65]. By the way of an example, Figure 2-4 displays the excellent repeatability of the indentation curves for a model material, bulk metallic glass.

Nevertheless, several sorts of limitations can be the source of significant errors. Some experimental limitations related to the measurement capacity can be dealt with by a proper calibration of the machine: Thermal drift, mounting compliance, machine compliance, imperfect indenter geometry. Experimental limitations also include the material sample preparation: one cannot ensure that perfect flat surfaces are indented.

But these sources of errors are less worrying than the lack of knowledge linking measured

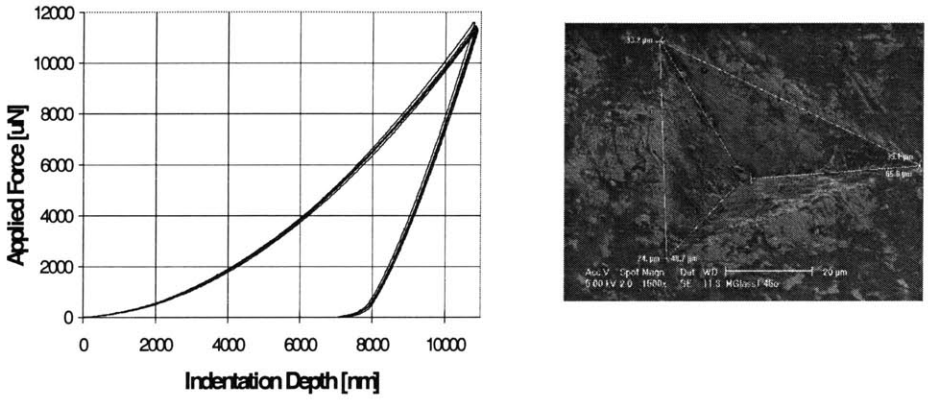

Figure 2-4: Five indentation load *vs.* depth curves and characterization of the final imprint area with SEM imaging for bulk metallic glass (courtesy of G. Constantinides [21]).

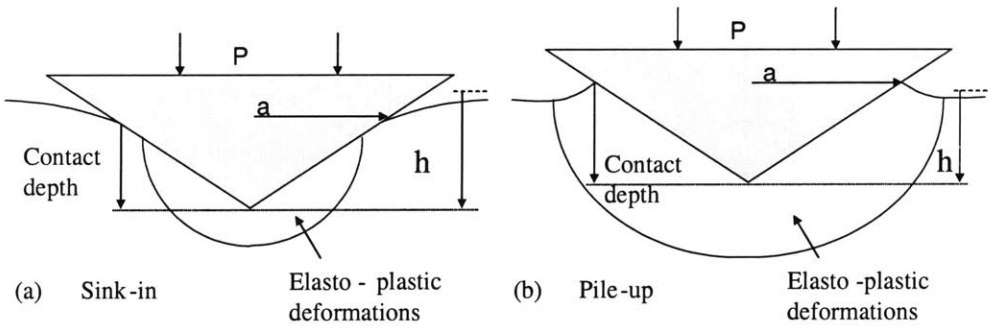

Figure 2-5: Sink-in (a) and Pile-up (b) phenomena. Pile-up occurs if the contact depth is higher than the total depth h. It is the case when the region where plastic deformations occur is larger that the contact area.

quantities to material properties. Analytical solutions for complex elastoplastic contact problems do not exist, and thus limit the indentation analysis. In particular, determining the geometry of plastic deformation that leads to pile-up or sink-in phenomena around the indenter is of critical importance for a correct interpretation of the load *vs.* depth curves. Figure 2-5 shows for a conical indenter how the surface might deform outside the contact area due to (a) sink-in, or (b) pile-up phenomena. As we will see, the area of contact is a critical input for indentation analysis. It can be determined from the load *vs.* depth curves only if the link between the depth of contact h_c and the total depth h is known.

2.2 Dimensional Analysis

The key to the determination of material properties from nanoindentation curves is an inverse analysis of the load *vs.* depth curves. This section aims at showing how this can be achieved when various types of mechanical behavior are considered: elasticity, cohesive frictional plasticity, visco- and poro- elasticity, which may all be relevant for shale materials. Our focus is a dimensional analysis of the involved physical quantities that may affect the indentation response, and which need to be considered in an inverse analysis of this response.

2.2.1 Introduction

Π-theorem

The main principle of dimensional analysis is often referred to as the Π-theorem, or Vaschy-Buckingham theorem, which can be stated as follows (from Barenblatt [1]):

"If a physical law is written as a relationship between some dimensional quantity and several dimensional governing parameters, then:

- it is possible to rewrite this relationship as a relationship between some dimensionless parameters and several dimensionless products of the governing parameters;

- the number of dimensionless products is equal to the total number of the governing parameters minus the number of governing parameters with independent dimensions."

Geometry of the Problem and Measured Quantities

To motivate the forthcoming developments, we consider a three-dimensional, rigid, conical indenter of half-angle α, indenting normally into a half-space $x_3 \geq 0$ (Fig. 2-1). The origin (O) of the Cartesian system is put at the initial contact point between the conical indenter tip and the half-space. A typical indentation test consists of two phases, a loading phase and an unloading phase, during which the force, P, is prescribed at a constant rate $\dot{P}$. The rigid displacement of the indenter is different from the contact depth, h_c, which is the penetration depth relatively to the contact edge (Figs. 2-1 and 2-5). For conical indentation, the contact radius a is linearly related to h_c through

$$a = h_c \tan \alpha \tag{2.1}$$

The main problem in the analysis is that the projected contact surface $A = \pi a^2$, respectively the contact depth h_c, are not known *a priori*, but is a solution of a boundary value problem.

The geometry of the experiment is self-similar: a cone, as well as a semi-infinite solid, is identical to its image through an isotropic contracting transformation. In other words, there is no fixed length scale in the set of governing parameters describing this geometry. In addition to the geometrical parameter α, we need to consider the loading parameters $(\dot{P}, t)$ that describe the boundary conditions of the problem.

With the exception of the projected area of contact, all measured quantities are classically obtained directly from the load *vs.* depth curves: $P_{\max}$, $h_{\max}$ for the loading phase, and $S_{\max} = \frac{dP}{dh}\big|_{h_{\max}}$, h_f for the unloading phase. The area of contact is also extrapolated from $h_{\max}$. Traditionally, the two quantities that are extracted from an indentation test are hardness and indentation stiffness, defined by:

$$H \stackrel{def}{=} \frac{P}{A} \tag{2.2}$$

$$M \stackrel{def}{=} \frac{S}{\sqrt{A}} \frac{\sqrt{\pi}}{2} \tag{2.3}$$

Two alternative quantities that can be determined from the indentation curves are the total

work provided to the system , and the elastic recoverable energy (Fig. 2-2):

$$W_t = \int_{h=0}^{h_{\max}} P_{loading}(h)dh \; ; \; W_e = \int_{h=h_f}^{h_{\max}} P_{unloading}(h)dh \tag{2.4}$$

H/M, W_e/W_t or $h_f/h_{\max}$ quantify the relative influence of elasticity and strength properties in an indentation test. The measure quantities H, M (respectively W_e, W_t) are not material properties, but rather snapshots of them.

2.2.2 Isotropic Cohesive Frictional Materials

The second set of parameters that need to be considered in the dimensional analysis are the governing material parameters.

Many natural composites including shales are porous and cohesive frictional materials defined by the Young's modulus E, the Poisson's ratio ν, the cohesion c and the friction angle φ. The full set of governing parameters is given by $(E, \nu, c, \varphi, \alpha, \dot{P}, t)$. Since the considered behavior is not time dependent, t can be removed from the loading parameters. Then $\dot{P}$ needs to be replaced by $P_{\max}$ or equivalently $h_{\max}$[1]:

$$(E, \nu, c, \varphi, \alpha, h_{\max}) \tag{2.5}$$

The measured quantities are

$$(P_{\max}, S_{\max}, A_{\max}, h_f, W_t, W_e) \tag{2.6}$$

The exponent matrix of the dimension function of all involved parameters in (2.5) and (2.6) reads

	$[P_{\max}]$	$[S_{\max}]$	$[A_{\max}]$	$[h_f]$	$[W_t]$	$[W_e]$	$[E]$	$[\nu]$	$[c]$	$[\varphi]$	$[\alpha]$	$[h_{\max}]$
M	1	1	0	0	1	1	1	0	1	0	0	0
L	−1	0	2	1	2	2	−1	0	−1	0	0	1
T	−2	−2	0	0	−2	−2	−2	0	−2	0	0	0

(2.7)

[1] $P_{\max}$ and $h_{\max}$ both determine the boundary conditions. It is convenient to consider $P_{\max}$ as an observed quantity, and $h_{\max}$ as a governing parameter.

where M, L and T refer to mass, length and time dimensions respectively. From the Π-theorem, it follows

$$\left[\frac{A_{\max}}{h_{\max}^2}, \frac{P_{\max}}{Eh_{\max}^2}, \frac{S_{\max}}{Eh_{\max}}, \frac{h_f}{h_{\max}}, \frac{W_t}{Eh_{\max}^3}, \frac{W_e}{Eh_{\max}^3}\right] = \Pi_p^{E,h_{\max}}\left(\frac{c}{E}, \varphi, \nu, \alpha\right) \tag{2.8}$$

where $\Pi_p^{E,h_{\max}}$ is a dimensionless function related to the dimensionless parameter p on the left hand side of (2.8). The two scaling parameters with independent dimensions are E and $h_{\max}$ ((2.7) is a matrix of rank two). $\Pi_p^{E,h_{\max}}$ and thus all dimensionless measurements p in (2.8) are independent of the indentation depth h. As a consequence, the ratio between total and contact depths is also constant during the loading phase. Indeed, from the indenter geometry, the ratio $(h_c/h)^2$ is proportional to $A_{\max}/h_{\max}^2$:

$$\frac{h_c}{h} = \frac{a}{\tan\alpha h} = \frac{1}{\sqrt{\pi}\tan\alpha}\frac{\sqrt{A}}{h} \tag{2.9}$$

If one replaces $h_{\max}$ by the area $A_{\max}$ as a governing parameter in the dimensional analysis, one obtains:

$$h_{\max} = \sqrt{A_{\max}}\Pi_{h_{\max}}\left(\frac{c}{E}, \varphi, \nu, \alpha\right) \tag{2.10}$$

$$H = \frac{P_{\max}}{A_{\max}} = E\,\Pi_H\left(\frac{c}{E}, \varphi, \nu, \alpha\right) \tag{2.11}$$

$$M = \frac{\sqrt{\pi}S_{\max}}{2\sqrt{A_{\max}}} = E\,\Pi_M\left(\frac{c}{E}, \varphi, \nu, \alpha\right) \tag{2.12}$$

$$h_f = \sqrt{A_{\max}}\Pi_{h_f}\left(\frac{c}{E}, \varphi, \nu, \alpha\right) \tag{2.13}$$

$$W_t = EA_{\max}^{3/2}\Pi_{W_t}\left(\frac{c}{E}, \varphi, \nu, \alpha\right) \tag{2.14}$$

$$W_e = EA_{\max}^{3/2}\Pi_{W_e}\left(\frac{c}{E}, \varphi, \nu, \alpha\right) \tag{2.15}$$

Thus, for given half-angle and material properties, the average pressure H below the indenter is independent of the indentation load or depth. (2.11) yields the classical definition of hardness H, which can be determined at any point along the $P - h$ curve for which the contact area is known:

$$H = \frac{P_1}{A_1} = \frac{P_2}{A_2} = \ldots = \frac{P_{\max}}{A_{\max}} \tag{2.16}$$

Similarly, the dimensionless relation (2.12) shows that for a given set of parameters $(c, E, \varphi, \nu, \alpha)$, M is independent of $h_{\max}$. But in contrast to H, M is evaluated only once from (2.3) at the beginning of the unloading phase. In fact, the load and the slope defined during the unloading phase depend on two lengths: the maximum depth $h_{\max}$ and the current depth $h < h_{\max}$, which make the dimensional analysis more complex.

The next and most important step consists in relating the hardness H, and the indentation modulus M to material strength and elasticity. Cheng *et al.* [14], [12], performed some finite element simulations of conical indentation into a Von Mises material, and studied the influence of all dimensionless governing parameters *w.r.t.* the determination of hardness and indentation stiffness. Some results are reported on Figure 2-6:

Hardness H

Hardness is a very complicated function of the relative influence of strength and elasticity (and also friction at the contact interface). Thus, the determination of material properties from a given load *vs.* depth loading curve is not guaranteed: One parameter $C = P/h^2$ characterizing the curve can be obtained from different sets of (E, c, φ) for a given cone angle (for Von Mises materials with strain hardening, see [16]). It seems from finite element simulations [15] with Von Mises type criteria of yield strength Y, that hardness does not depend on E when E/Y is very high as shown on Fig. 2-6(b) (rigid-plastic behavior). In this case, an appropriate approach is to use yield design theory [40]. By contrast, elasticity is predominant in the deformation for small E/c solids, and the effect of strength becomes negligible. The ratios $(1 - h_f)/h$ and W_e/W_t tend to 0 in the first case, and are equal to 1 in the perfect elastic case.

Indentation Stiffness M

In order to relate M to material elastic properties, a simple analytical formula (shown in Chapter 5) has been found for a pure isotropic elastic indentation:

$$M = \frac{E}{1 - \nu^2} + \frac{E_i}{1 - \nu_i^2} \tag{2.17}$$

where E_i and ν_i are the Young's modulus and Poisson's ratio of a non rigid indenter. Relation (2.17) shows that M is a function of the material elastic constants only (for rigid indenters). M is independent of geometry of a conical indenter, through the cone angle α ([39], [43], [56], [77]). (2.17) even holds for any convex axi-symmetric indenter shape [64].

Another useful analytical relation valid in perfect elasticity, shown later on, states that for conical indentation, the ratio h_c/h is independent of the material properties and of the cone angle:

$$\frac{h_c}{h} = \frac{2}{\pi} \tag{2.18}$$

Referring to Figure 2-5, relation (2.18) means that perfect elasticity always produces sink-in. In this case, hardness and indentation modulus are linearly related. Using the relations (2.9) and (2.18) for the integration of (2.3) *w.r.t.* h, yields:

$$H = \frac{M}{2\tan\alpha} \tag{2.19}$$

Bulychev, Alekhin, Shoshorov and coworkers [10] have shown that eq. (2.17) also holds for isotropic elastoplastic indentation tests. The combination of equations (2.3) and (2.17) yields the so-called BASh formula:

$$S_{\max} = \frac{2}{\sqrt{\pi}} M \sqrt{A_{\max}} = \frac{2}{\sqrt{\pi}} \frac{E}{1-\nu^2} \sqrt{A_{\max}} \tag{2.20}$$

where the indenter is supposed rigid.

Many arguments are in favor of the application of the BASh formula (2.20) to the beginning of the unloading phase: first, the dimensional analysis (2.12) shows that the self similarity is kept at the beginning of the unloading. Second, the unloading phase involves generally no reverse plasticity phenomena [65], [16], and is completely elastic. Furthermore, finite element simulations have shown (Fig. 2-6(c) from [14], [16]) that the indentation modulus does not depend on the yield strength of the solid, other parameters kept equal. In fact, whatever stress profile the plastic deformation creates under the indenter, one can find an indenter shape that would lead to an approaching stress profile on an elastic half-space, for which the BASh formula (2.20) holds. Therefore, the determination of the indentation stiffness depends on strength

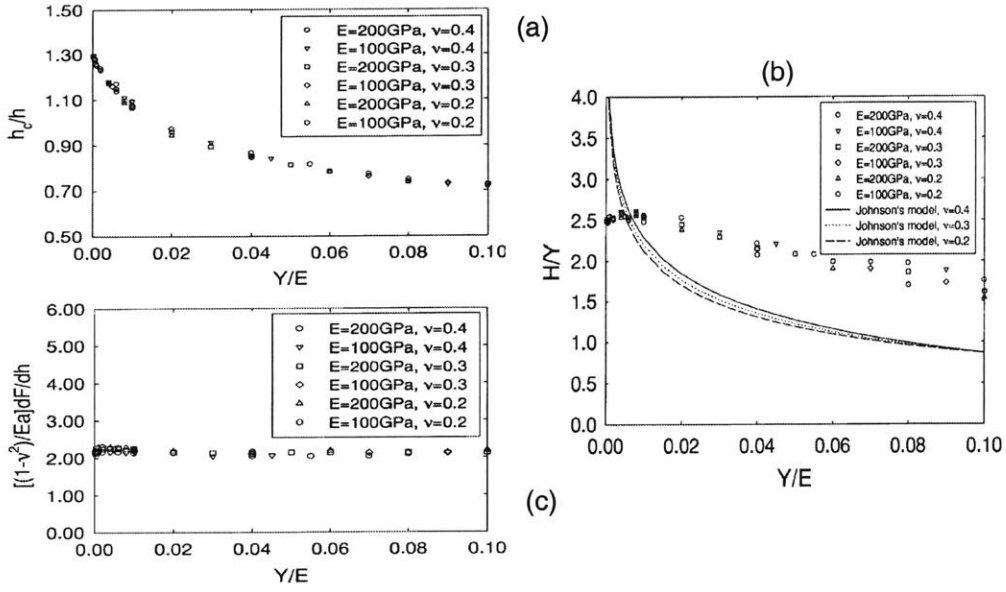

Figure 2-6: Results of finite element simulations from Cheng et al. (2000) [15] of frictionless conical indentation ($\alpha = 68°$) on an elastic/Von Mises half-space. The ratios h_c/h (a), M/E (b), H/Y (c) are calculated for various Poisson's ratios and Young's moduli. Y stands here for the uniaxial yield strength of the material.

properties (Y, c, φ) mostly through the size of the area of contact. For rigid axi-symmetric indenters, M coincides in the isotropic case with the plane stress modulus $E/(1-\nu^2)$. That is why M is also called the indentation modulus (or reduced modulus) as it refers to the elastic properties of the indented solid.

2.2.3 Visco- and Poro- Elastic Solids

When the time dependent behavior of the solid needs to be considered, the governing parameters must include the loading history; for instance $(\dot{P}, t)$, $(\dot{P}, P)$, $(\dot{P}, h)$, $(\dot{h}, h)$ or equivalently (t, h) in the case of a constant indentation loading rate. In the following we consider separately the cases of linear isotropic viscoelasticity and poroelasticity.

Linear viscoelasticity

The simplest models in linear viscoelasticity are based on a set of elastic moduli that refer to instantaneous and delayed elastic properties, in addition to at least one viscosity parameter η homogeneous to a time per unit compliance in constitutive laws of the form $\sigma = \eta\dot{\varepsilon}$. A representative example of the set of governing parameters in a constant loading rate indentation is given by:

$$(E_0, \nu_0, \eta, E_\infty, \nu_\infty, \alpha, t, h) \tag{2.21}$$

The application of the Π-theorem shows that the ratio h_c/h is still independent of h, but depends now on time t:

$$\frac{h_c}{h} = \Pi_{h_c}\left(\frac{E_0}{E_\infty}, \nu_0, \frac{\eta}{E_\infty t}, \nu_\infty, \alpha\right) \tag{2.22}$$

In the case of a prescribed instantaneous step displacement in the form of a Heaviside function, *ie.*

$$h(t) = \begin{cases} 0, t < 0 \\ h_0, t > 0 \end{cases} \tag{2.23}$$

relation (2.22) becomes, for $t > 0$:

$$\frac{h_c}{h_0} = \Pi'_{h_c}\left(\frac{E_0}{E_\infty}, \nu_0, \frac{\eta}{E_\infty t}, \nu_\infty, \alpha\right) \tag{2.24}$$

Since the instantaneous and delayed responses are fully elastic, the ratio h_c/h_0 should be equal to $2/\pi$ as in perfect elasticity at least for $t = 0$ and $t = \infty$. With some minor assumptions, one can consider that this ratio holds for all times. Since the Heaviside function contains no time scale, we can rewrite the governing parameters by introducing a time dependent elastic constant $M(t) = E(t)/(1 - \nu(t)^2)$ that intervenes in the incremental load *vs.* depth relation adapted from the static case (from relations (2.11) and (2.19)):

$$dP \propto M(t)d(h^2) \tag{2.25}$$

The relevance of (2.25) is discussed in [16] and seems to apply for transformations where the area of contact increases or decreases monotonously. In this case, time appears through the elastic properties only. Hence, $(M(t), \alpha)$ is the new set of governing parameters in (2.21), and (2.24) simplifies to:

$$\frac{h_c}{h_0} = \Pi''_{h_c}(\alpha) \equiv \frac{2}{\pi} \tag{2.26}$$

Relation (2.26) means that the displacement field is self-similar: it does not depend on the indentation depth.

Similarly, the scaling relation $P \propto h^2$ is not conserved in general:

$$\frac{P}{E_\infty h^2} = \Pi_P\left(\frac{E_0}{E_\infty}, \nu_0, \frac{\eta}{E_\infty t}, \nu_\infty, \alpha\right) \tag{2.27}$$

even for the simplified set of governing parameters $(M(t), h_0, \alpha)$, for which:

$$\frac{P}{M(t)h_0^2} = \Pi'_P(\alpha) \tag{2.28}$$

According to [16], analytical solutions have been proposed to describe viscoelastic contact problems. Different methods have been proposed for a flat punch [12], spherical [13] or conical [73], [16] indenters. A new full analytical solution for conical indentation is proposed in Appendix B for deviatoric creep modeled with a standard viscoelastic model and a Maxwell model.

Linear poroelasticity

We consider next an isotropic poroelastic material, composed of a solid and porosity ϕ, saturated by a fluid phase. The fluid can transmit hydrostatic pressure from the outside, and induce a deformation of the solid skeleton. Depending on the loading rate and the permeability of the material, the fluid can be trapped in the pores or completely mobile with uniform pressure. We refer to the first extreme case as undrained deformation, and to the second case as drained deformation.

The initial pore pressure p is assumed to be in equilibrium with the external fluid pressure p_0. Three constitutive laws are necessary: the two poroelastic state equations and the mass conservation law (see *e.g.* Coussy [23])

$$\sigma_{ij} = \frac{2g}{1-\nu}\varepsilon_{kk} + 2g\varepsilon_{ij} - bp\delta_{ij} \tag{2.29}$$

$$m - m_0 = \frac{p - p_0}{M} + b\varepsilon_{kk} \tag{2.30}$$

$$\frac{\partial m}{\partial t} = c_\kappa \nabla^2 m \tag{2.31}$$

where g is the shear modulus, ν the drained Poisson's ratio, b the isotropic Biot coefficient, M the Biot modulus, and $m - m_0$ gives the fluid mass content. Finally c_κ is the diffusivity coefficient:

$$c_\kappa = \kappa M \frac{(1-\nu_u)(1-2\nu)}{(1-\nu)(1-2\nu_u)} \tag{2.32}$$

where ν_u is the undrained Poisson's ratio, and κ is the permeability. The set of governing parameters reads here

$$(g, \nu, \nu_u, M, b, \alpha, h, t, \kappa) \text{ or } (g, \nu, \nu_u, M, b, \alpha, h, t, c_\kappa) \tag{2.33}$$

Analogously to (2.7), the dimension function of all relevant parameters is given by

	$[P_{\max}]$	$[S_{\max}]$	$[A_{\max}]$	$[h_f]$	$[g]$	$[\nu]$	$[\nu_u]$	$[M]$	$[b]$	$[\alpha]$	$[\kappa]$	$[c_\kappa]$	$[h]$	$[t]$
M	1	1	0	0	1	0	0	1	0	0	-1	0	0	0
L	-1	0	2	1	-1	0	0	-1	0	0	3	2	1	0
T	-2	-2	0	0	-2	0	0	-2	0	0	1	-1	0	1

(2.34)

The main difficulty comes here from the two length scales in the problem. The first one is the indentation depth h as encountered before; the second, h_d, defines the distance over which the pore pressure diffuses, and scales with the square root of time as typical diffusion problems (see Fig. 2-7):

$$h_d = \sqrt{c_\kappa t} \tag{2.35}$$

In order to keep self-similarity in the analysis, one needs to consider the particular load case of a constant load rate $\dot{P}$, and therefore the loading parameters (P, t) or $(P, \dot{P})$. Dimensional analysis yields:

$$\frac{h}{\sqrt{P/g}} = \Pi\left(\nu, \nu_u, \frac{M}{g}, b, \alpha, \frac{\dot{P}}{c_\kappa g}\right) \tag{2.36}$$

where P, g, c where chosen as independent scaling parameters. Remarkably, this ratio does neither depend on the load nor on the time; in other words, the relation $P \propto h^2$ holds during loading. The characteristic diffusion length (2.35) reads now:

$$h_d = h\sqrt{\frac{c_\kappa g}{\dot{P}}} \tag{2.37}$$

Finally, a relation similar to (2.36) is obtained for $h_c/\sqrt{P/g}$, so that h_c/h and h_d/h do no more depend on time, load or depth. However, in this case no analytical solution gives h_c/h as a function of $\dot{P}$, except for two extreme cases $\frac{\dot{P}}{c_\kappa g} \longrightarrow 0$ and $\frac{\dot{P}}{c_\kappa g} \longrightarrow \infty$. In the first case (Fig. 2-7a), the diffusion is much faster than the indentation: the response is drained, fully elastic and equivalent to the one of an empty skeleton (g, ν). In the second case (Fig. 2-7b), the characteristic diffusion length is much smaller than the indentation depth at any time: the response is undrained (g, ν_u). Both situations have perfect elastic solutions and $h_c/h \equiv 2/\pi$. In between these extreme cases we deal with self-similar indentation of a drained consolidated

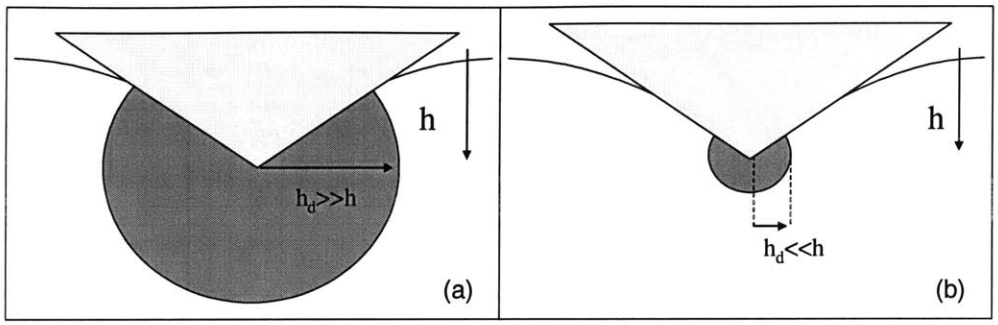

Figure 2-7: Schematic representation of the indentation on a poroelastic half-space. The diffusion length h_d is proportional to the depth h for a constant loading rate $\dot{P}$. For small values of $\dot{P}$, $h_d >> h$ (left), and the indentation is performed in drained conditions. For high values of $\dot{P}$, $h_d << h$ (right), and the indentation is performed under undrained conditions. Pore pressure is uniform in the central zone.

zone, surrounded by a stiffer undrained region so that $h_c/h > 2/\pi$.

In practice, comparing the load rate to estimates of $c_\kappa g$ allows one to estimate whether one operates under drained or undrained conditions. Further analysis would open up the possibility to measure the permeability from indentation experiments, by looking at the characteristic times of relaxation, or other relevant quantities like hardness measurements for various loading rates. These advanced poroelastic consolidation studies go beyond the focus of this investigation.

2.2.4 General Indenter Geometries

From the performed dimensional analysis, it is readily understood that a single set of hardness and indentation stiffness will not be sufficient to determine a full set of material properties such as (E, ν, c, φ). In order to achieve a better inverse analysis of material invariant properties, several authors (Chollacoup *et al.* [17], Ganneau [40]) suggested indentation analysis with various indenter geometries. In practice, three sided pyramidal (Berkovich and cube-corner), four sided pyramidal (Vickers), or spherical indenters are used (see Fig. 2-8). In order to understand the underlying scaling relations with more complex geometries than the conical one, and thus to understand why a conical indenter is well suited to model pyramidal ones, one needs to go further into the dimensional analysis of the problem. An essential feature of indentation analysis is the self-similarity of Hertz-type contact problems. The conditions under

which frictionless Hertz type contact problems possess classical self-similarity were stated by Borodich (1988 according to [5]); and include:

1. The shape of the indenter is described by a homogeneous function whose degree is greater or equal to unity. Using a Cartesian coordinate system $Ox_1x_2x_3$ whose origin O is at the indenter tip and x_3 is the orientation of the indentation (Fig. 2-1), the shape of the indenter (height) is defined by:

$$f(\lambda x_1, \lambda x_2) = \lambda^d f(x_1, x_2) \tag{2.38}$$

for arbitrary positive λ. Here d is the degree of the homogenous function f; in particular $d = 1$ for a cone and $d = 2$ for the parabolic shape considered by Hertz. Such axi-symmetric indenters can be described by monomial functions of the form (first introduced by Galin, 1946 [39] according to [6]):

$$f = f(x_1 = r\cos\theta, x_2 = r\sin\theta) = Br^d \tag{2.39}$$

where B is the shape function of the indenter at unit radius, and d is the degree of the homogeneous function. For a conical indenter ($d = 1$), having a semi-vertical angle α; $B = \cot\alpha$. For a spherical indenter of radius R, $d = 2$ and $B = 1/(2R)$. The previous expression was recently extended to indenters of non-axi-symmetric shape, such as pyramidal indenters that are frequently employed in depth-sensing indentation tests [5]:

$$f = B(\theta)\, r^d \tag{2.40}$$

where $B(\theta)$ describes the height of the indenter at a point $(\theta, r = 1)$. For a three-sided pyramid, $d = 1$, and making use of the triple symmetry:

$$B(\theta) = \cot\alpha_0 \sin(\pi/6 + \theta) \tag{2.41}$$

where α_0 is the angle in vertical cross-sections (see Fig. 2-8). For a Berkovich indenter, having a face angle of 115.13°, $\alpha_0 = 65.3°$; and for a cube corner indenter of 90° face

angle, $\alpha_0 = 35.26°$.

2. The operator of constitutive relations F for the indented material is a homogeneous functions of degree κ with respect to the components of the strain tensor:

$$F(\lambda\varepsilon) = \lambda^{\kappa} F(\varepsilon) \tag{2.42}$$

Evidently, a linear elastic law satisfies this relation since $\kappa = 1$; as does any nonlinear secant elastic formulation of the form $\boldsymbol{\sigma} = \mathbb{C}(\varepsilon) : \varepsilon$ for which the secant elastic stiffness tensor satisfies:

$$\mathbb{C}(\lambda\varepsilon) = \lambda^{\kappa-1}\mathbb{C}(\varepsilon) \tag{2.43}$$

Provided these conditions, the whole load-displacement curve in a depth-sensing test is scaled by [5]:

$$\frac{P}{P_1} = \left(\frac{h}{h_1}\right)^{\frac{2+\kappa(d-1)}{d}} ; \frac{h}{h_1} = \left(\frac{A}{A_1}\right)^{d/2} \tag{2.44}$$

where A is the projected contact area, which appears to be not affected by the constitutive relation. In return, the hardness is scaled with the indentation depth by:

$$\frac{H}{H_1} = \left(\frac{h}{h_1}\right)^{\frac{\kappa(d-1)}{d}} \tag{2.45}$$

We verify that the load-displacement relation is scaled by $P \propto h^2$ for conical and ideal (sharp) pyramidal indentation, for which $d = 1$, irrespective of the constitutive relation (2.42). As a consequence, the hardness is a constant over the loading process, as defined by (2.2). On the other hand, the constitutive relation power κ significantly affects the load-displacement relation for spherical or parabolic indenter geometries, for which $d = 2$, and must be known in advance in order to analyze the load-displacement curve. For instance, for an elastic behavior, $P \propto h$ (which corresponds to $d \to \infty$) is indicative of flat indentation, and is described by Boussinesq's solution [7]; $P \propto h^{1.5}$ is indicative of linear elastic spherical or paraboloids of revolution.

Finally, given the same $d = 1$ degree of the homogeneous shape function of three-sided pyramidal (Berkovich, corner cube) and conical indentation, it is common practice to consider, instead of the original three-dimensional pyramidal shape (see Fig. 2-8), an equivalent cone of

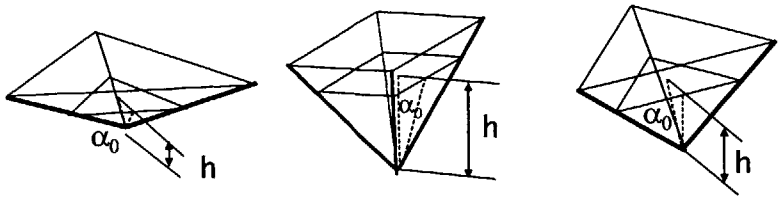

Figure 2-8: Various pyramidal indenters used for indentation experiments: Berkovich (left), Vickers (middle) and Cube corner (right). α_0 is the angle between the axis of the pyramid and the center of its faces.

revolution in sharp indentation analysis, such that the projected contact area with respect to indentation depth of the cone is the same as that for the real indenter, i.e. from (2.44):

$$A(h) = C_0 h^2 = \pi (h \tan \alpha_{eq})^2 \Longrightarrow \tan \alpha_{eq} = \sqrt{\frac{C_0}{\pi}} \tag{2.46}$$

where C_0 is a constant characterizing the specific pyramidal indenter, and α_{eq} is the equivalent half-apex cone angle. Using (2.46), the flat Berkovich indenter ($\alpha_0 = 65.3°$), for which $C_0 = 24.56$, can be assimilated to an equivalent cone of semi-apex angle $\alpha_{eq}^B = 70.32°$; and a Corner Cube Corner indenter ($\alpha_0 = 35.26°; C_0 = 2.598$) to one with $\alpha_{eq}^{CC} = 42.28°$.

2.2.5 Determination of the Area of Contact

The key to a successful determination of the elastic and strength properties from indentation tests relies on the determination of the correct projected contact area. This is not an easy task. Traditionally, the contact area has been determined by direct measurement of the size of the residual hardness impression after a complete unloading as shown on Figs. 2-4 and 2-9. For practical reasons, however, some means other than direct observation of the hardness impressions is needed to measure contact areas, since imaging very small indentations is both time-consuming and difficult. Making use of the dimensionless nature of the BASh formula (2.20), the contact surface can be scaled, for a given material, from two unloading slopes:

$$\frac{A}{A_1} = \left(\frac{S}{S_1}\right)^2 ; \frac{h_c(\alpha)}{h_c(\alpha_1)} = \frac{\tan \alpha_1}{\tan \alpha} \times \frac{S}{S_1} \tag{2.47}$$

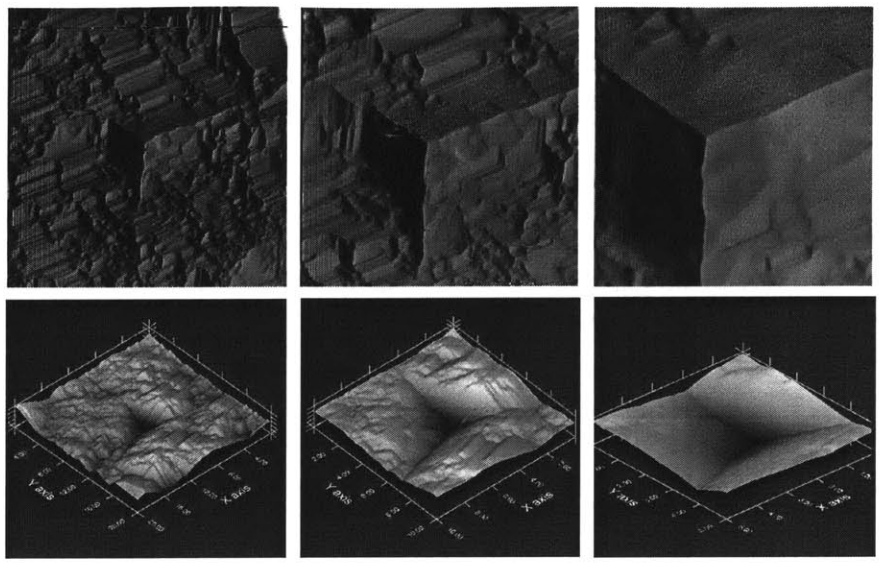

Figure 2-9: Gradient Images (Top) and AFM Images (Bottom) of residual impressions after microindentation in a shale material (from [86]).

For instance, if the contact area for a specific indentation depth or indentation geometry (half-apex angle α) is measured, it is possible to either determine the contact area or contact depth for another indentation depth for the same indenter (same α), or scale the contact area from one indenter geometry to another. In the latter case, use of (2.47) allows one to determine the hardness ratio from:

$$\frac{H}{H_1} = \frac{P}{P_1}\left(\frac{S}{S_1}\right)^{-2} \tag{2.48}$$

In particular, from definitions (2.2) and (2.3), we obtain:

$$\frac{H}{M^2} = \frac{P_{\max}}{S_{\max}^2}\frac{4}{\pi} \tag{2.49}$$

Thus, the experimental ratio H/M^2 does not depend on $A_{\max}$ for a given material.

An original method for conical indentation that circumvents the necessity to measure the contact area, was suggested by Oliver and Pharr [64], by applying relation (2.18) to the pure

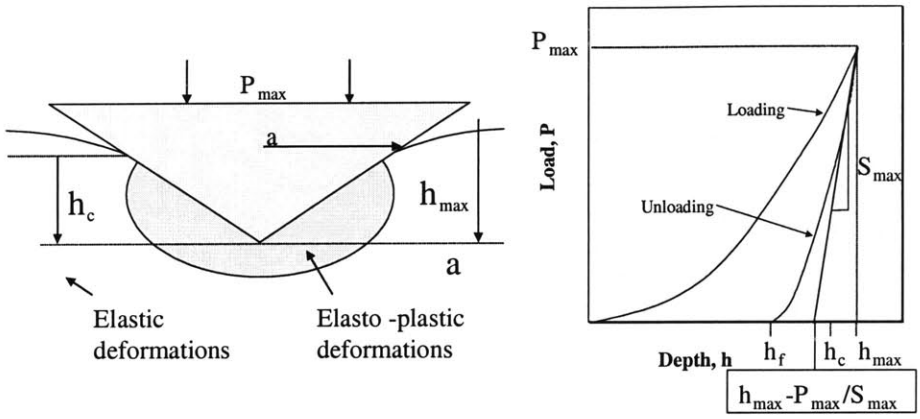

Figure 2-10: Determination of the area of contact with the Oliver and Pharr method [64]. h_c is related to $h_{\max}$ and $P_{\max}/S_{\max}$.

elastic recovery during unloading (see Fig. 2-10):

$$h_c - h_f = \frac{2}{\pi}\left(h_{\max} - h_f\right) \tag{2.50}$$

where h_f is the residual indentation depth. $h_{\max}$ is experimentally measured, but h_f is very sensitive to non ideal surface preparations. By considering that the elastic unloading is scaled, for conical indentation, by a power-two function,

$$P = c\left(h - h_f\right)^2;\ h - h_f = 2\frac{P}{S} \tag{2.51}$$

the final depth is no longer needed. Indeed, a combination of (2.50) and (2.51) yields:

$$h_c = h_{\max} - \epsilon\frac{P_{\max}}{S_{\max}} \tag{2.52}$$

where $\epsilon = 2\left(1 - 2/\pi\right) = 0.73$. Relation (2.52) is also valid for other indenter shapes: $\epsilon = 1$ for a flat punch, and $\epsilon = 0.75$ for a parabola of revolution.

The main problem of the Oliver and Pharr method is that is assumes the shape of the deformed solid outside the area of contact to be elastic (Fig. 2-10, left). This is not true when plastic deformations occur around the indenter to form pile-ups (Fig. 2-5). Indeed, (2.52)

cannot predict $h_c/h > 1$ which may be the source of important errors of modulus determination. The second concern about this method is that the unloading phase is not self similar, and should not have a parabolic shape (relation (2.51)). In fact, most of the unloading curves obey to a power relation of the form:

$$P = b(h - h_f)^m \tag{2.53}$$

Pharr [69] obtained values for m comprised between 1.2 and 1.6 for various indentation tests. He then compared this experimental scaling relation with the closed form solution obtained for parabolic indenters, $P \propto h^{3/2}$ [78]. As a consequence, he proposed to choose $\epsilon = 0.75$ in (2.52) instead of 0.73. In fact, dimensional analysis of (2.53) at the beginning of the unloading, shows that m and b in (2.53) are not independent of the maximum depth $h_{\max}$. b and m cannot be considered as material properties (see discussion in [16]). Thus, an advanced understanding and interpretation of indentation unloading curves needs a more consistent analysis. An original model is presented in Appendix A of this thesis that tries to circumvent these obstacles.

2.3 Indentation on Composite Materials

Is it possible to apply the classical indentation analysis to heterogeneous materials like shales, and if – how?

The indentation analysis presented above is based on two assumptions: the homogeneity of the solid, and the infinite half-space boundary conditions. The objective of this section is to show how the solutions of continuum indentation can be applied to multiscale, multiphase composites, such as shales.

2.3.1 Continuum analysis

Continuum mechanics is based on the existence of a material representative elementary volume (r.e.v.) of characteristic size $\mathcal{L}$ that obeys to the scale separability conditions:

$$d \ll \mathcal{L} \ll L \tag{2.54}$$

where L is the characteristic size of the considered problem and loading; and d is the characteristic size of the (largest) heterogeneity contained in the r.e.v..

In order to know whether classical indentation analysis is applicable to heterogeneous solids, it is convenient to consider two problems at separate scales: the indentation of a microhomogeneous composite, and the indentation of a homogeneous heterogeneity.

2.3.2 Indentation of a Microhomogeneous Material

For a homogeneous solid, the tested material properties and stress-strain relation remain the same for any depth of indentation. The only characteristic length is the indentation depth h or equivalently the indentation contact radius a. For heterogeneous solids, strictly speaking, (2.54) with $L \sim h$ will not be satisfied all along the loading phase, since h increases continuously from 0 and cannot be always smaller than any heterogeneity size d. But we can assume that the final properties $P_{\max}$ and $h_{\max}$ do not depend much on the nature of the first indented heterogeneities, as long as $h_{\max}$ is much greater than d (see Fig. 2-11). This assumption, $L \sim h_{\max}$, is not valid for perfect elasticity, because the stress singularity at the tip of a sharp indenter induces a characteristic loading length scale $L = 0$. Since the materials can obviously not bear such singularities, plastic deformations are likely to create a smooth pressure profile under the indenter, so that the minimum characteristic length scale of the loading L becomes proportional to $h_{\max}$ (see Appendix C). In addition, indenters tips are always blunt. Thus, the continuum analysis can be employed with confidence using the maximum indentation parameters $h_{\max}, P_{\max}, S_{\max}$. The unloading phase does not lead to the same difficulty, since it already contains the length scale $h_{\max}$ referring to the size of the permanent impression.

In summary, provided that (2.54) is satisfied in the form,

$$d \ll \mathcal{L} \ll h_{\max} \tag{2.55}$$

an indentation test operated to a penetration depth $h_{\max}$ gives access to the material properties that are characteristic of a material system at a length scale of $\mathcal{L}$.

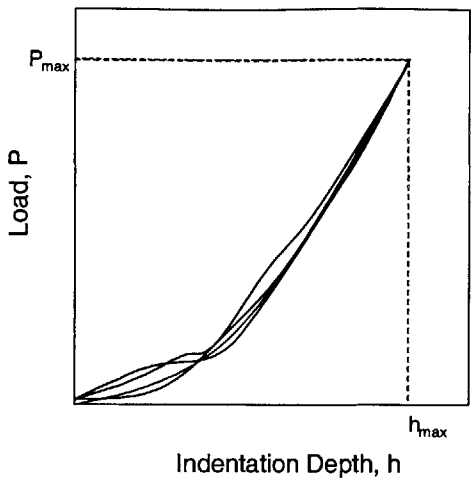

Figure 2-11: Expected indentation curves on a composite. The heterogeneity of the material affects the beginning of the loading curve only ($h_{\max} \sim d$).

2.3.3 Indentation in a Heterogeneity

When indenting to a depth much smaller than the size of the heterogeneities, one must ensure that the boundary conditions are the same as in the conventional indentation analysis, otherwise the extracted properties are not representative of the indented heterogeneity. The three conditions to satisfy are: the half-space is infinite, perfectly flat and supported far from the indent.

The first condition implies $h << d$, the characteristic size of the (largest) heterogeneities. The second gives the same condition if the surface roughness has a period on the order of d. The third one is somewhat tricky and reads:

$$\underline{u}(\underline{z}) = \underline{0}, \ \ |\underline{z}| \rightarrow \infty \tag{2.56}$$

where $\underline{u}(\underline{z})$ stands for the displacement of the half-space at the location denoted by the position vector $\underline{z}$. If one considers the indentation on a stiff inclusion lying in a very soft matrix, even for $h << d$, the whole inclusion can move and thus interfere with the stiffness measurements. In particular, the stiffness of the inclusion is underpredicted, and the load *vs.* depth curve is no longer parabolic. This situation needs some refined analysis.

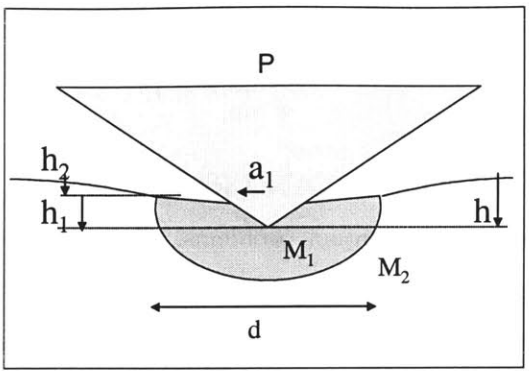

Figure 2-12: Indentation in an inclusion. As long as $a_1 \ll d$, the total indentation depth h is composed of two parts relating to the indenter displacement relative to the inclusion (h_1), and the inclusion displacement relative to the matrix (h_2).

Fig. 2-12 shows an example for which $h << d$, with a spherical inclusion indented at its center. The load P is transmitted through two elements in series. The first contact problem is associated with an indentation depth h_1, the second with a vertical displacement h_2 of the inclusion. We approximate the second element as a flat punch of radius $d/2$ (Sneddon [78]) so that:

$$P = \frac{2}{\pi} M_1 h_1^2 \tan\alpha = M_2 h_2 d \tag{2.57}$$

where M_1 and M_2 are the stiffness of the inclusion and of the matrix respectively. These indentation moduli are captured by (2.3), but are rather mechanical properties in the sense of (2.17). Unlike the second element, the first contact problem is non linear, since the compliance depends on the applied load. For small loads, the matrix compliance can be neglected in the system. In order to ensure the displacement boundary conditions (2.56) at the scale of the inclusion, h_2 needs to be negligible:

$$\frac{h_2}{h_1} << 1 \tag{2.58}$$

ie. from (2.57)

$$\frac{h_1}{d} \frac{M_1}{M_2} \frac{2}{\pi} \tan\alpha << 1 \tag{2.59}$$

If a_1 is the contact radius for the indentation, (2.57) will be verified provided that

$$\frac{a_1}{d}\frac{M_1}{M_2} << 1 \tag{2.60}$$

Condition (2.60) is particularly important for stiff inclusions in a soft porous matrix, but is also helpful for grain-to-grain contact problems. Consider an indentation performed on a grain sitting on other grains with identical properties. If the compliance of the grain to grain contact depends on the applied load, (2.60) can possibly never be verified. In turn, if the elastic properties of the porous structure are known in a linear framework, (2.60) can be checked by replacing M_2 by the indentation modulus of the porous system. If the geometry of the heterogeneity is not spherical, but elongated in one direction, either horizontally like a thin film or vertically like a needle, (2.60) is a sufficient condition, if d is the smallest characteristic size. It may however not be a necessary condition.

Advanced Analysis[2]

If (2.58) is verified but not (2.59), one can go a step further and analyze the indentation load P *vs.* h curve using:

$$h = h_1 + h_2 \tag{2.61}$$

curve as a means for analysis the properties of both inclusion and matrix. (2.57) and (2.61) give:

$$h = \sqrt{\frac{\pi}{2\tan\alpha}\frac{P}{M_1}} + \frac{P}{M_2 d} \tag{2.62}$$

and

$$P = M_2 dh + \frac{\pi M_2^2 d^2}{4M_1\tan\alpha}\left(1 - \sqrt{1 + \frac{M_1}{\pi M_2 d}8\tan\alpha h}\right) \tag{2.63}$$

$$S = \frac{dP}{dh} = M_2 d\left[1 - \left(1 + \frac{M_1}{\pi M_2 d}8\tan\alpha h\right)^{-1/2}\right] \tag{2.64}$$

[2]**In the thesis, the sections named "Advanced Analysis" refer to original derivations that have not been explicitly used in our study, but that could be useful in other cases.**

The area of the indentation imprint is equal to

$$A = \pi \left(\frac{2}{\pi} h_1 \tan \alpha \right)^2 \tag{2.65}$$

where h_1 is given from (2.57) and (2.61) by:

$$h_1 = \frac{\pi M_2 d}{4 M_1 \tan \alpha} \left(\sqrt{1 + \frac{M_1}{\pi M_2 d} 8 \tan \alpha h} - 1 \right) \tag{2.66}$$

In this case it is not possible to define an overall indentation stiffness in the sense of the BASh formula (2.20): $S/\sqrt{A}$, derived from relations (2.64), (2.65) and (2.66) is no more independent of h.

The analysis presented here is restricted to perfect elasticity, but can be extended to elasto-plastic contact problems. Indeed, as long as there is no plasticity involved at the interface between the inclusion and the matrix, relation (2.62) can be used to analyze the unloading slope from:

$$S^{-1} = \frac{dh}{dP} = \frac{dh_1}{dP} + \frac{dh_2}{dP} = \frac{\sqrt{\pi}}{2 M_1 \sqrt{A_1}} + \frac{1}{M_2 d} \tag{2.67}$$

The relation between A_1 and h_1 has yet to be determined. If one knows for instance M_2 and d, it is possible to correct $h_{\max}$ and $S_{\max}$ from the translation of the inclusion $h_2 = P/(M_2 d)$. This gives $h_{1\max} = h_{\max} - h_{2\max}$ and $S_{1\max} = (S_{\max}^{-1} - S_{2\max}^{-1})^{-1}$. Then, by using the Oliver and Pharr method (see Section 2.2.5) for the determination of the area of contact we obtain

$$h_{1c} = h_{1\max} - \epsilon \frac{P_{\max}}{S_{1\max}} \; ; \; A_1 = \pi (h_{1c} \tan \alpha)^2 \tag{2.68}$$

Finally, M_1 can be determined with relations (2.67) and (2.68), from $P_{\max}, S_{\max}, h_{\max}$.

In summary, indentation on heterogeneities in multiphase composites requires a careful analysis of the indentation curves. Conditions (2.60) may strongly limit the indentation depth on stiff inclusions or particles supported by a softer matrix. We keep this in mind for the indentation analysis of shale materials.

Apart from these concerns, the conventional indentation analysis can be employed with confidence for the interpretation of individual tests.

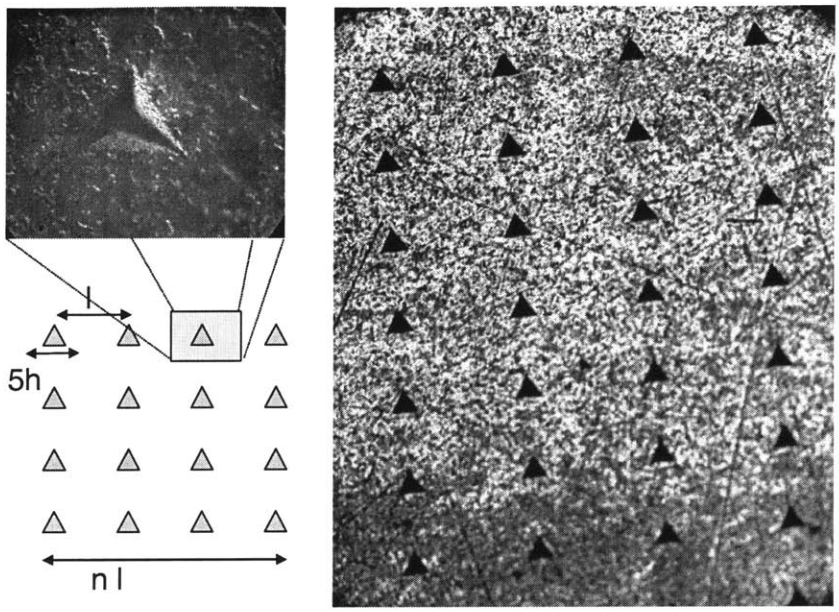

Figure 2-13: Principle of grid-indentation technique (bottom left). Optical microscope images of indentation grid: (right) example of microindentation grid; (top left) residual impression after unloading (magnification x100); (from [20]).

2.3.4 Grid Indentation Technique

Indentation on natural composites are performed on a surface that is composed of several materials. Fig. 2-13 shows how an automatized series of indentation tests is performed on a material surface. The grid step size is chosen to be sufficiently large such that interactions between adjacent indents are avoided. If a sufficient number of tests is performed to small indentation depths so that condition (2.59) is valid for all tests, and if the size of the indentation grid is greater than the size of the r.e.v. of the composite, then we can analyze the tests both individually and statistically.

These conditions are summarized as follows:

$$h \ll d \tag{2.69}$$

$$N \gg 1 \tag{2.70}$$

$$l\sqrt{N} \gg \mathcal{L} \tag{2.71}$$

$$h \ll l \tag{2.72}$$

where h is the indentation depth, d is the characteristic size of the phases, l is the distance between to indentation spots (grid step size), and $\mathcal{L}$ is the size of the r.e.v. of the composite. Fig. 2-14 shows the expected frequency distributions histogram of the indentation moduli at very small depths, under such conditions with a two-phase composite. The bimodal distribution reflects the properties of the two phases a, b through the peak values $M_{\text{exp}}^{I,a}$ and $M_{\text{exp}}^{I,b}$. In turn, greater indentation depths give access to homogenized material properties of the composite (Fig. 2-14, right).

One can go a step further and interpret the area under the peaks as phase volume fractions (Constantinides *et al.* [18]). This advanced analysis is valid under the restriction that the indented phases are isotropic, and that the volume fractions are conserved near the material surface.

Finally, a mapping of mechanical properties in form of contour plots allows one to identify (if any) characteristic morphologies within the resolution defined by the grid step size. A supplementary condition

$$l < d \tag{2.73}$$

allows one to ensure that the spatial distribution of constituents is reflected properly.

Combining these three levels of statistical analysis provides us with phase properties but also volume fractions and morphological features. These are all input parameters for a micro-mechanics approach.

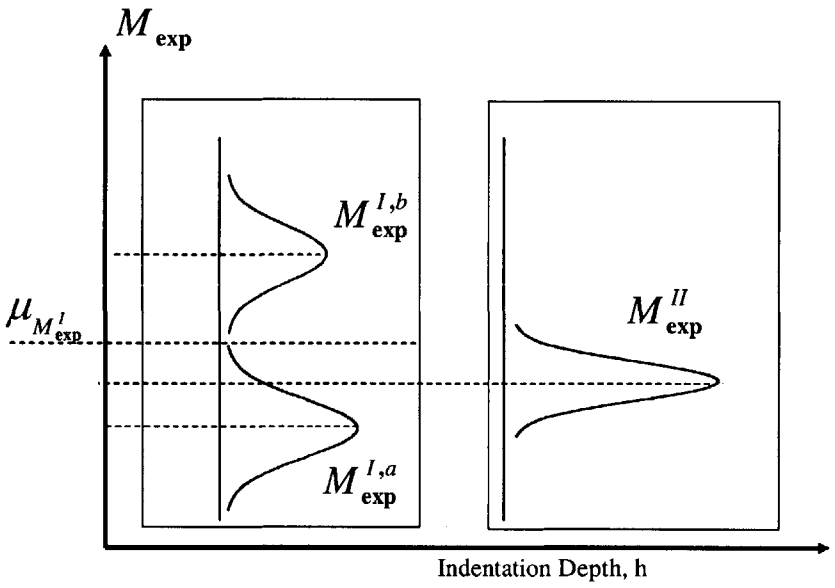

Figure 2-14: Principle of statistical indentation analysis of natural composites: small indentation depths (denoted by I) give access to properties of individual phases; large indentation depths (denoted by II) yield a homogenized response of the material (from [20]).

2.4 Conclusion

The dimensional analysis of the indentation technique reveals that the loading and unloading load *vs.* depth curves of conical indentation provide self-similar quantities: hardness is related to intrinsic properties in perfect elastic and plastic cases [40], and the indentation modulus is a function of the indented material elastic properties [64]. This analysis can be extended to the case of pyramidal indenters once the relation between the area of contact and the contact depth (2.46) is known. Once the contact depth is known, with (2.52) for instance, the determination of the indentation modulus is accurate.

Provided certain conditions, the same analysis can be performed, with confidence and accuracy, on natural composites. This forms the basis for our indentation campaign on shale materials, for which we will employ the presented grid indentation technique as an experimental basis for a statistical analysis of indentation stiffness results.

These indentation stiffness values need to be translated into stiffness values C_{ijkl} of shale materials at different scales. Given the anisotropy of shale materials, Eq. (2.17) linking M to (E, ν), does not apply to our materials. The next chapter will focus on the establishment of this link through an advanced contact mechanics analysis.

Chapter 3

Indentation Analysis of Transverse Isotropic Solids

The indentation modulus M extracted from an indentation test is not a material property of the indented material, but rather a snapshot of the elasticity of the indented material. This chapter is devoted to establishing the link between M and the stiffness tensor of a transversely isotropic material (which are shales). The chapter starts with a review of indentation contact problem and solution methods, and develops a new, simple and explicit expression for the $M - C_{ijkl}$ relation, when the indented surface is a plane of material symmetry. The expression is validated for some model materials.

3.0.1 Frictionless Indentation of Isotropic Solid

In this section, we recall two ways of obtaining the BASh formula (2.20) for frictionless conical indentation of isotropic solids. These solutions introduce the methods that will be used for the more general case of anisotropy. The only available analytical solutions deal with perfect elastic solids (see review in [5]), but can be applied to the beginning of the unloading phase [64] (see Section 2.2.5).

3.0.2 Problem Statement

With "On the contact of elastic solids" in 1881 [47], Heinrich Hertz pioneered a new field of study, known as contact mechanics. Hertz found the elastic field resulting from the contact between two smooth parabolic elastic solids for small interpenetration depth. Ever since, great deal of effort has been devoted to more and more complex elastic contact problems, with indenters of various shapes [7], [39], [56], [77].

The main focus of contact mechanics is the determination of size and exact shape of the contact area. Unlike classical mechanical problems, the contact zone is unknown so that areas where displacements (in the contact region), and those where forces (free surface) are prescribed, are not known *a priori*. This makes the analysis intrinsically *non linear*, since the surface boundary conditions have to be written under conditions of a point $\underline{z}$ that is either situated in the contact zone or in the stress free surface. The contact problem between a rigid axi-symmetric indenter and an infinite half-space is described by the following set of equations, written with the polar coordinates (ρ, θ, z) [78]:

$$
\begin{aligned}
div\ \boldsymbol{\sigma} &= 0 && \text{(3.1a)}\\
\boldsymbol{\sigma} &= F(\boldsymbol{\epsilon}) && \text{(3.1b)}\\
\boldsymbol{\epsilon} &= \frac{1}{2}(\boldsymbol{\nabla}\underline{u} + \boldsymbol{\nabla}^t\underline{u}) && \text{(3.1c)}\\
P &= -\int_{\rho=0}^{a}\int_{\theta=0}^{2\pi} \boldsymbol{\sigma}_{zz}(\rho,\theta,0)\rho d\rho d\theta && \text{(3.1d)}\\
u(\rho,\theta,0) &= h - f(\rho)\ ,\ \boldsymbol{\sigma}_{zz}(\rho,\theta,0) < 0\ \rho < a && \text{(3.1e)}\\
\sigma_{zk}(\rho,\theta,0) &= 0\ ,\ \rho \geq a, k \in \{1,3\} && \text{(3.1f)}\\
u(\rho,\theta,z) &\rightarrow 0\ ,\ \rho, z \rightarrow \infty && \text{(3.1g)}
\end{aligned}
$$

where P is the total load applied, in direction z as shown on Figure 3-1, $f(\rho)$ defines the axi-symmetric shape of the indenter, and a is the contact radius. (3.1a) is the static equilibrium condition, (3.1b) gives the stress strain relation through a function F, (3.1c) derives strain from displacements, and the remaining relations are the boundary conditions for the total load (3.1d), the displacement in the contact region (3.1e), the stress outside of the contact region (3.1f), and the displacements far from the indent (3.1g).

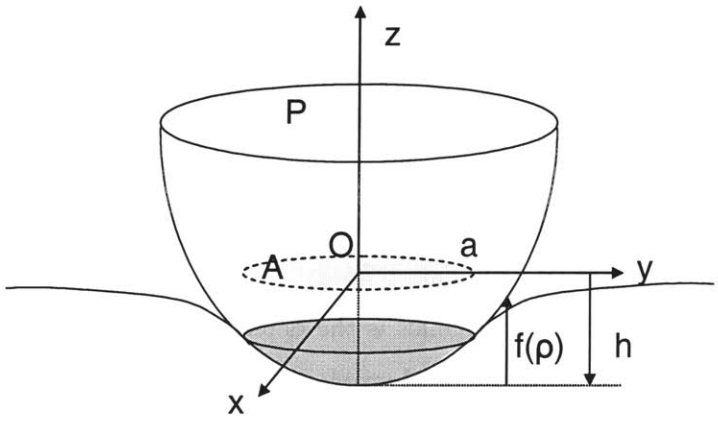

Figure 3-1: Contact between a rigid axi-symmetric indenter of shape $f(\rho)$ and an infinite half-space. The total applied load is P, the indentation depth is h and the projected area of contact is A.

There are two ways to solve such a set of equations, in the framework of infinitesimal strains and displacements[1]. One solution is to transform the equations using the geometry of the problem, by applying integral transforms (Sneddon [77]), and/or defining potential functions (Fabrikant [35], [36]). Another interesting and popular approach was developed in the last decades. The idea is to construct the solution using the principle of superposition in linear elasticity, from the individual displacement solutions to a point indentation problem. These elementary solutions are called Green's functions.

3.0.3 Sneddon Solution

The method developed by Sneddon [77],[78][2] consists in performing on all problem equations two dimensional Fourier transforms in the directions of the surface coordinates x and y. In the case of axi-symmetry, this integral transform is called a Hankel transform on the polar coordinates ρ and θ. The polar coordinates ρ and θ are transformed into a variable ξ of dimension L^{-1}.

[1] The assumption of small strains was not a matter of concern in Hertz original contact problem formulation, in which displacements were assumed to be small compared to the radii of the contacting parabolae. To the best of our knowledge, no finite element simulation reported unexpected discrepancy with the infinitesimal theory, for sharp indenters that lead to not even small elastic strains.

[2] The solution for a frictionless axisymmetric indentation has apparently been found earlier by Galin [39] (See discussion in [5]).

The area of contact is circular by symmetry and its projected radius a is kept as an unknown. It turns out that the equations written with a new set of non-physical coordinate can be solved analytically in the transformed space. Finally, the integral transforms are performed backwards to come back to the initial problem. Following this procedure, the expressions for h and P for an isotropic half-space read:

$$h = a\int_{\rho=0}^{a} \frac{f'(\rho)d\rho}{\sqrt{a^2-\rho^2}} \tag{3.2}$$

$$P = 2\frac{E}{1-\nu^2}\int_{\rho=0}^{a} \frac{\rho^2 f'(\rho)d\rho}{\sqrt{a^2-\rho^2}} \tag{3.3}$$

where f is any smooth convex function, and f' stands for its derivative *w.r.t.* ρ. This result implicitly relies on an assumption about the contact area, through a. By inverting (3.2) or (3.3), the contact radius a can be expressed as a function of the prescribed depth h or load P. The displacements in the half-space are given by:

$$u_\rho(\rho,z) = -\frac{1}{2(1-\nu)}\int_0^\infty (1-2\nu-\xi z)A(\xi)e^{-\xi z}J_1(\rho\xi)d\xi \tag{3.4}$$

$$u_z(\rho,z) = \frac{1}{2(1-\nu)}\int_0^\infty (2-2\nu+\xi z)A(\xi)e^{-\xi z}J_0(\rho\xi)d\xi \tag{3.5}$$

where $A(\xi)$ depends on the shape of the indenter and J_0 and J_1 are Bessel functions of the first kind.

It is interesting to write here the solutions (3.2) and (3.3) for an axi-symmetric indentation with a cone of semi apex angle α, for which:

$$f(\rho) = \frac{\rho}{\tan\alpha} \tag{3.6}$$

In this case

$$A(\xi) = \frac{1}{\tan\alpha}\frac{1-\cos(a\xi)}{\xi^2} \tag{3.7}$$

and

$$u_z(\rho > a, 0) = \frac{1}{\tan\alpha}\left[a\sin^{-1}\left(\frac{a}{\rho}\right) + \sqrt{\rho^2 - a^2} - \rho\right] \tag{3.8}$$

$$\sigma_{zz}(\rho < a, 0) = \frac{1}{2\tan\alpha}\frac{E}{1-\nu^2}\cosh^{-1}\left(\frac{a}{\rho}\right) \tag{3.9}$$

Eq. (3.9) shows a stress singularity for $\rho = 0$ right below the tip of an infinitely sharp cone. This is not the case for smooth indenters, but it appears in the case of a flat punch for $\sigma_{\rho z}(\rho = a, 0)$. Relations (3.2) and (3.3) give the explicit values of the depth and load as a function of the contact radius:

$$h = \frac{\pi}{2}\frac{a}{\tan\alpha} \tag{3.10}$$

$$P = \frac{\pi}{2}\frac{E}{1-\nu^2}\frac{a^2}{\tan\alpha} \tag{3.11}$$

Eliminating a from (3.10) and (3.11) gives the load *vs.* depth relation:

$$P = \frac{2}{\pi}\frac{E}{1-\nu^2}h^2\tan\alpha \tag{3.12}$$

As expected from the dimensional analysis (see Section 2.2), P is scaled by h^2, which provides an interesting insight into the non linearity of the contact problem: for each increment of load, the area of contact increases, as well as the depth of indentation does. Similarly, a and h are linearly related, and one can define the contact depth as the distance measured on the z axis between the indenter tip and the contact edge. From (3.10) we obtain relation (2.18) which we had postulated in the Section 2.2.2:

$$h_c = \frac{a}{\tan\alpha} = \frac{2}{\pi}h \tag{3.13}$$

Furthermore, if one rewrites P and h in (3.10) and (3.11) as a function of the projected area of

contact $A = \pi a^2$, then one obtains

$$h = \frac{\sqrt{\pi}}{2}\frac{\sqrt{A}}{\tan\alpha} \tag{3.14}$$

$$P = \frac{1}{2}\frac{E}{1-\nu^2}\frac{A}{\tan\alpha} \tag{3.15}$$

Finally, deriving (3.15) *w.r.t.* depth, the shape of the indenter defined by α disappears, and we obtain the BASh formula (2.20):

$$S = \frac{dP}{dh} = \frac{2}{\sqrt{\pi}}\frac{E}{1-\nu^2}\sqrt{A} \tag{3.16}$$

3.0.4 Green's Functions Method

The Hankel transform method can also be used to derive the Green's function, *ie.* solutions for a point indentation. The Green's function method then consists in using the principle of superposition and integrating the contributions of all point indentations over the contact area. Compared to the Hankel transform method described above, the strength of a Green's functions approach is two fold:

1. Once the fundamental solution for a point indentation is known, it can be easily applied to various situations without having to reconsider the set of governing equations;

2. The approach can be used to obtain estimates of stress and displacement fields if the problem has no analytical solution. In this case, one needs to assume a stress field in the area of contact, as well as the shape and size of the projected contact surface. The accuracy of the chosen field is checked by comparing the resulting displacements in the contact region with the actual indenter shape. An eventual mismatch can help to quantify the accuracy of the stress field assumption.

To illustrate the procedure, we consider the conical indentation into a linear elastic isotropic half-space. The Green's surface function reads [89]:

$$\eta = \frac{\mathcal{H}}{\rho} \tag{3.17}$$

where $\mathcal{H}$ is a constant depending on the elastic properties of the solid. In the case of isotropy, it reads:

$$\mathcal{H} = \frac{1-\nu^2}{\pi E} \tag{3.18}$$

The contact area is a circle of radius a, and the pressure distribution is assumed of the form (3.9):

$$p(\rho) = p_0 \cosh^{-1}\left(\frac{a}{\rho}\right) \tag{3.19}$$

where $p_0 = P/\left(\pi a^2\right)$ is the average pressure *w.r.t.* the projected contact area. The displacement in any point $Q(\rho_1, \theta)$ situated on the projected contact surface is given by:

$$u_1(\rho_1, \theta) = \int\int_S p(\rho)\ \eta(|\rho_1 - \rho|)\ \rho d\rho d\theta \tag{3.20}$$

The indentation depth h is equal to the displacement u_1 at the cone tip. Evaluating (3.20) for $r = 0$ gives:

$$h = u_1(\rho_1 = 0) = 2\pi\mathcal{H}p_0 \int_0^a \cosh^{-1}(a/\rho)\, d\rho = \pi\mathcal{H}\frac{P}{a} \tag{3.21}$$

The vertical displacements at the contact edges are found using a change of variables $(\rho, \theta) \rightarrow (r, \gamma)$ as defined on Fig. 3-2:

$$h - h_c = u_1(\rho_1 = a) = \mathcal{H}p_0 \int_{-\pi/2}^{\pi/2} \int_{r=0}^{2a\cos\gamma} \cosh^{-1}(a/\rho)\, dr d\gamma \tag{3.22}$$

where $\rho^2 = (a - r\cos\gamma)^2 + (r\sin\gamma)^2$. After integration with respect to r, (3.22) yields

$$h - h_c = \mathcal{H}p_0 a\pi \int_{\gamma=-\pi/2}^{\pi/2} (1 - |\sin\gamma|) d\gamma = \mathcal{H}\frac{P}{a}(\pi - 2) \tag{3.23}$$

Finally, combining (3.21) and (3.23), the ratio h_c/h already given by (2.18) and (3.13) is obtained:

$$h_c = \frac{2}{\pi} h \tag{3.24}$$

So far, the assumed stress field (3.19) has not been proved to agree with the displacement boundary conditions under the cone. To do so, one needs to calculate the displacement $u_1(\rho_1)$ and show that it is indeed linear in ρ_1 so that it matches the actual conical indenter shape:

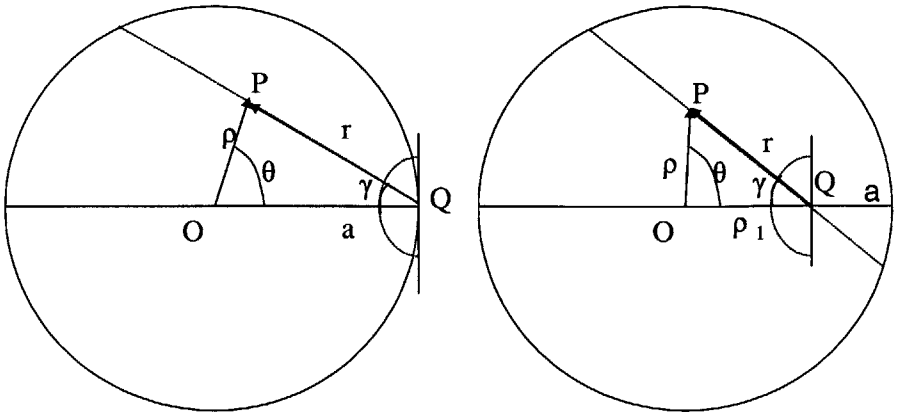

Figure 3-2: Coordinate systems (ρ, θ) and (r, γ) on the edge (left); and inside the projected contact area (right).

$$u_1(0 < \rho_1 < a) = \mathcal{H} p_0 \int_{\gamma=-\pi/2}^{\pi/2} \int_{r=r_-}^{r=r_+} \cosh^{-1}(a/\rho)\, dr d\gamma \tag{3.25}$$

where r_+ and r_- are obtained from the change of variables into the coordinates (r, γ), $r_- = \rho_1 \cos\gamma - \sqrt{a - (r\sin\gamma)^2}$, $r_+ = \rho_1 \cos\gamma + \sqrt{a - (r\sin\gamma)^2}$ (Fig. 3-2), and $\rho^2 = (r - \rho_1\cos\gamma)^2 + (\rho_1 \sin\gamma)^2$. After rearrangement, integration *w.r.t.* r yields:

$$u_1(0 < \rho_1 < a) = \mathcal{H} p_0 a\pi \int_{\gamma=-\pi/2}^{\pi/2} (1 - \frac{\rho_1}{a}\,|\sin\gamma|) d\gamma = \mathcal{H}\frac{P}{a}\left(\pi - 2\frac{\rho_1}{a}\right) \tag{3.26}$$

Eq. (3.26) proves that the displacement field is linear in ρ_1, which confirms that the assumed pressure field (3.19) is the exact one.

After rearrangement the BASh formula (2.20) is recovered:

$$P = \frac{2}{\pi}\frac{h^2 \tan\alpha}{\pi\mathcal{H}};\; S = \frac{2}{\sqrt{\pi}}\sqrt{A}\frac{1}{\pi\mathcal{H}} \tag{3.27}$$

By definition of the indentation modulus (2.3), we obtain:

$$M = \frac{1}{\pi\mathcal{H}} \tag{3.28}$$

and in the isotropic case, using (3.18):

$$M = \frac{E}{1-\nu^2} \tag{3.29}$$

The simple example of a conical indentation in an isotropic half-space shows that the key to the establishment of the link between the indentation modulus M and the elastic constants of the indented half-space is the Green's surface function expression (3.17). The only drawback of this flexible approach is that it needs an *a priori* assumption of the stress field .

3.1 Indentation Modulus of a Transverse Isotropic Solid

As we will see, shales are transverse isotropic solids. The analysis of indentations in terms of elastic constants requires a formula similar to (3.29) for transverse isotropic materials.

It is readily understood that the link between the indentation modulus and the elastic constants of a general anisotropic material is far more complicated than in the isotropic case. Closed form solutions, such as (3.29) are only available for some particular cases, such as the Elliot-Hanson solution [32], [42] for conical indentation of a transversely isotropic half-space in the axis of symmetry, using harmonic potentials [36]. Much of the recent contributions to the analysis of the Hertzian contact for anisotropic solids can be traced back to the work of Willis, 1966, [95], who reduced the problem to the evaluation of contour integrals for parabolic indenters. Green's functions methods were first used in this context by Vlassak and Nix, 1994, [90]. They simplified the solution using the surface Green's functions determined by Barnett and Lothe, 1975, [2], and provided implicit solution schemes for other indenter shapes. To our knowledge, the most refined solution schemes for general anisotropic materials are those proposed by Swadener and Pharr (2001) for conical and parabolic indenters [80] and by Vlassak *et al.* (2003) for conical and spherical indenters [91]. Both solution schemes involve computational demanding operations even in their approximated versions. Ovaert [66] and more recently Shi *et al.* [76] investigated the particular cases of transverse isotropy and orthotropy and proposed an implicit solution method for ellipsoidal indenters. This section describes an original solution for orthotropic materials indented in the axes of symmetry. Some new easy implementable explicit expressions are developed, based on some approximations of the Green's function [25].

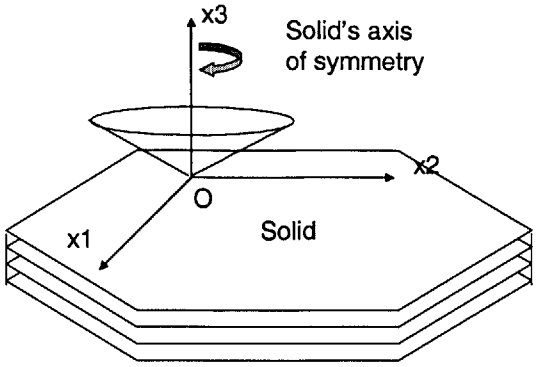

Figure 3-3: Indentation in the solid's axis of symmetry

First, the explicit expression for the indentation modulus of transversely isotropic materials indented in the axis of symmetry, is given, based on the Elliot-Hanson solution. This solution also motivates the extension to indentation normal to the axis of symmetry, based on a sinusoidal approximation of the surface Green's function. Instead of keeping the first two terms of the Fourier transform as suggested by Vlassak *et al.* [91], the Green's function is interpolated from some extreme values that are known in closed form. This method does not require the entire expression of the function and thus leads to explicit expressions of the indentation modulus. Finally the approach is extended to orthotropic materials, and the approximations are compared for model materials with the results obtained by Swadener and Pharr [80] and Vlassak *et al.* [91].

3.1.1 Indentation In The Axis of Symmetry

Let direction $x3$ be normal to the planes of isotropy; directions $x1$ and $x2$ be parallel to the planes of isotropy so that the resulting coordinate system S is a right-hand Cartesian one, with the first indented point as origin O.

For transversely isotropic materials, the problem of elastic conical indentation in direction $x3$, *ie.* when the plane of isotropy is parallel to the half space surface, has been solved analytically [32], [42]. The problem is axi-symmetric, the projected area of contact in the plane

$(x1, x2)$ is circular (Fig. 3-3). The Elliot-Hanson solution reads, similarly to (3.27):

$$P = \frac{2}{\pi^2 \mathcal{H}} h^2 \tan(\alpha) \tag{3.30}$$

$\mathcal{H}$ is the constant in the Green's function already introduced by (3.17), *ie.* the surface displacement induced by a concentrated unit load:

$$\eta(\rho) = \frac{\mathcal{H}}{\rho} \tag{3.31}$$

$\mathcal{H}$ depends on the material stiffness constants through:

$$\mathcal{H} = \frac{1}{2\,\pi} \sqrt{\frac{C_{11}}{C_{31}^2 - C_{13}^2} \left(\frac{1}{C_{44}} + \frac{2}{C_{31} + C_{13}} \right)} \tag{3.32}$$

where we use the reduced notations (see Section 1.7):

$$\begin{aligned} C_{11} &= C_{1111} \\ C_{13} &= C_{1133} = C_{3311} \\ C_{44} &= C_{2323} = C_{1313} \\ C_{31} &= \sqrt{C_{11}\, C_{33}} > C_{13};\ \text{with } C_{33} = C_{3333} \end{aligned} \tag{3.33}$$

It is interesting to note that the solution does only depend on four of the five elastic constants of a transversely isotropic material $(C_{11}, C_{33}, C_{44}, C_{13})$. The fifth independent constant $C_{12} = C_{1122} = C_{1111} - 2\,C_{1212}$ does not appear in the expression of $\mathcal{H}$. We will see that this observation is restricted to the perfect axi-symmetric case.

In general, the Green's function (3.31) depends on both polar coordinates (ρ, θ) defined on the indented surface and centered at the load point; but for the perfect material axi-symmetric case it does not depend on θ.

Finally, since the ratio h_c/h as defined by (3.24) is also valid in this axi-symmetric problem [42], deriving (3.30) *w.r.t.* h yields the following explicit expression (similar to (3.28)) of the indentation modulus M_3 in the axis of symmetry (direction $x3$):

$$M_3 = \frac{1}{\pi\, \mathcal{H}} \tag{3.34}$$

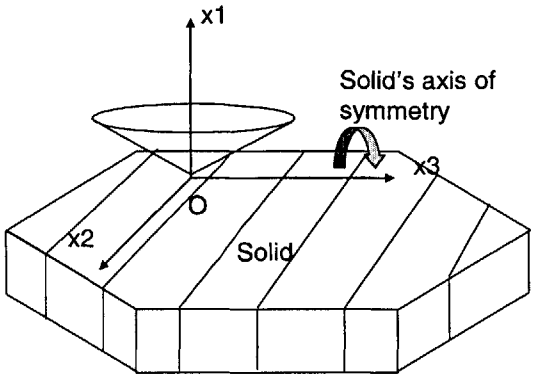

Figure 3-4: Indentation orthogonal to the solid's axis of symmetry

Last, using (3.32), we obtain:

$$M_3 = 2\sqrt{\frac{C_{31}^2 - C_{13}^2}{C_{11}}\left(\frac{1}{C_{44}} + \frac{2}{C_{31}+C_{13}}\right)^{-1}} \tag{3.35}$$

3.1.2 Normal to the Axis of Symmetry

When the half-space's surface is orthogonal to the material's planes of isotropy, the area of contact is not circular, and the problem is no longer axi-symmetric (Fig. 3-4).

The load *vs.* displacement relation in such a contact problem can be found in two steps:

1. Finding the displacement field corresponding to a concentrated load; that is the Green's function [89]:

$$\eta(\underline{z}) = \frac{1}{8\,\pi^2\,|\underline{z}|}\left[\alpha_k\; B_{km}^{-1}\left(\frac{\underline{z}}{|\underline{z}|}\right)\;\alpha_m\right] = \eta(\rho,\theta) = \frac{\mathcal{H}(\theta)}{\rho} \tag{3.36}$$

where $\underline{z}$ is the position vector of Q relative to the load point P; (ρ,θ) are polar coordinates of Q ($\theta = 0$ along direction $x2$); $\alpha_1, \alpha_2, \alpha_3$ are the cosines of the direction normal to the indented surface; $\mathbf{B}$ is a symmetric second order tensor defined by [2]:

$$\mathbf{B}(\underline{t}) = \frac{1}{8.\pi^2}\int_0^{2\pi}(\mathbf{mm} - \mathbf{mn}\cdot\mathbf{nn}^{-1}\cdot\mathbf{nm})d\phi \tag{3.37}$$

where $\mathbf{ab}$ is a second order tensor defined by $ab_{jk} = a_i\; C_{ijkl}\; b_l$ (with the summation of

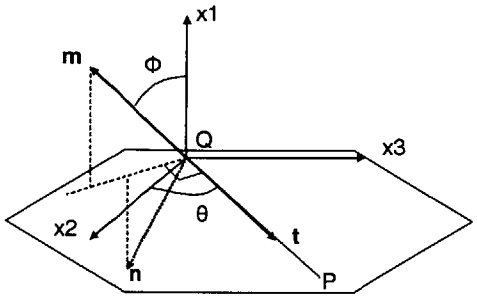

Figure 3-5: (m,n,t) coordinate system.

repeated indices); $\underline{t}$ is the normalized form of $\underline{z}$; $(\underline{m}, \underline{n}, \underline{t})$ forms a right hand Cartesian system, and ϕ is the angle between vector $\underline{m}$ and direction $x1$ (Fig. 3-5). And finally, $\eta(\rho, \theta)$ is the surface Green's function, homogenous in ρ^{-1}.

2. Integrating the Green's function to find the displacement field resulting from an assumed pressure distribution under the indenter ([95], [80]), and verifying that the result matches with the boundary conditions.[3]

In our particular case of transverse isotropy, the indentation axis ($x1$) belongs to two planes of symmetry (Fig. 3-4): $(x1, x3)$ is orthogonal to the planes of isotropy, and $(x1, x2)$ is parallel to them. In this case, an evaluation of (3.36) for $(\alpha_1, \alpha_2, \alpha_3) = (1, 0, 0)$ yields the exact values of the Green's function η in the $x2-$direction ($\theta = 0$), and in the $x3-$direction ($\theta = \pi/2$):

$$\mathcal{H}(\theta = 0) = \frac{1}{2\,\pi} \sqrt{\frac{C_{33}}{C_{31}^2 - C_{13}^2} \left(\frac{1}{C_{44}} + \frac{2}{C_{31} + C_{13}} \right)} = \mathcal{H}_2 \tag{3.38}$$

$$\mathcal{H}\left(\theta = \frac{\pi}{2}\right) = \frac{1}{\pi} \frac{C_{11}}{C_{11}^2 - C_{12}^2} = \mathcal{H}_3 \tag{3.39}$$

In the isotropic case, (3.36) simplifies into (3.18). It is interesting to note, from a comparison of (3.32) and (3.38), that $\mathcal{H}_2 = \sqrt{C_{33}/C_{11}}\,\mathcal{H}$ where $\mathcal{H}$ is defined by (3.32); while $\mathcal{H}_3$ turns out to be the Green's function constant for an isotropic material with stiffness constants C_{11} and

[3] An original alternative to the assumption of a pressure distribution was proposed by Vlassak et al. [91], using Barber's theorem (1975).

C_{12}.

Furthermore, since the Green's function is even and π-periodic by symmetry, $\mathcal{H}_2$ and $\mathcal{H}_3$ are extreme values of $\mathcal{H}(\theta)$. Therefore, it seems appropriate to consider a first order approximation $\tilde{\mathcal{H}}(\theta)$ that interpolates the Green's function $\eta(\rho,\theta) \approx \tilde{\mathcal{H}}(\theta)/\rho$ so that $\tilde{\mathcal{H}}(\theta = 0) = \mathcal{H}_2$ and $\tilde{\mathcal{H}}(\theta = \frac{\pi}{2}) = \mathcal{H}_3$:

$$\tilde{\mathcal{H}}(\theta) = \mathcal{H}_0 + \mathcal{H}_{c1}\cos(2\,\theta) \tag{3.40}$$

where

$$\mathcal{H}_0 = \frac{\mathcal{H}_2 + \mathcal{H}_3}{2} \text{ and } \mathcal{H}_{c1} = \frac{\mathcal{H}_2 - \mathcal{H}_3}{2} \tag{3.41}$$

The proposition of interpolating the Green's function between two extreme values is restricted to the geometrical configuration of indentation in the principal material axes. A more general first order approximation is obtained by performing a Fourier transform of $\mathcal{H}(\theta)$, and keeping only the first terms of the sinusoidal decomposition (see [91] Appendix A). This approximation gives a slightly different sine function whose coefficients must be evaluated numerically; whereas $\mathcal{H}_0, \mathcal{H}_{c1}$ in our solution procedure are found analytically from (3.38), (3.39) and (3.41). In return, since the first order approximation from Fourier transform was found to be very accurate for many materials, it should also be the case with our explicit evaluation of the Green's function.

It is generally assumed that the projected contact area is elliptical for conical indentation of general anisotropic materials [91], [80][4]. By symmetry, the axes of the elliptical contact area must coincide with $x2$ and $x3$. If a_2 and a_3 are the ellipse dimensions in the respective directions $x2$ and $x3$, then the ellipse eccentricity is $e = \sqrt{1 - \left(\frac{a_2}{a_3}\right)^2}$ if $a_2 < a_3$, and $e = \sqrt{1 - \left(\frac{a_3}{a_2}\right)^2}$ otherwise. We assume that the pressure field $p(y_2, y_3)$ at point P of coordinates (y_2, y_3) has the form proposed by Swadener and Pharr [80]:

$$p(y_2, y_3) = p_0\ \cosh^{-1}\left(\frac{y_2^2}{a_2^2} + \frac{y_3^2}{a_3^2}\right)^{-1/2} \tag{3.42}$$

The displacement in any point $Q(z_2, z_3)$ situated on the projected contact surface is:

[4] It is worth mentioning that a unique contact depth h_c can not be defined for such a projected contact area. However the relation (3.14) between the projected contact area and the total depth remains valid [80].

$$u_1(z_2, z_3) = \int\int_S p(y_2, y_3)\ \eta(z_2 - y_2, z_3 - y_3)\ dy_2 dy_3 \tag{3.43}$$

The indentation depth h is equal to the displacement $u_1(0,0)$ at the cone tip. It can be expressed in (3.43) as a function of the load $P = \pi a_2 a_3 p_0$ and identified with (2.3) and (3.14), so that M_1 is given by ([80], [91]):

$$M_1 = \frac{1}{\alpha(e, \Theta)\ (1-e)^{1/4}} \tag{3.44}$$

where:

$$\alpha(e, \Theta) = \int_0^{\pi} \frac{\eta(\theta + \Theta)}{\sqrt{1 - e^2 \cos^2(\theta)}} d\theta \tag{3.45}$$

Θ is the angle between the major axis of the contact ellipse and the direction $x2$ or $\theta = 0$. By symmetry, it follows $\Theta = 0$ if $\mathcal{H}_2 < \mathcal{H}_3$, and $\Theta = \pi/2$ otherwise.

The solution of (3.44) and (3.45) requires as input the eccentricity. For our proposed Green's function approximation (3.40), integration of (3.43) with (3.42) yields the displacement field u_1, that is subjected to the condition of axi-symmetry imposed by the contact of the rigid indenter. Following faithfully the method described by Swadener and Pharr [80] and Vlassak *et al.* ([91] Appendix A), we obtain an explicit expression of the eccentricity:

$$e = \sqrt{\frac{2\ |\mathcal{H}_{c1}|}{\mathcal{H}_0 + |\mathcal{H}_{c1}|}} = \left\{ \sqrt{1 - \frac{\mathcal{H}_2}{\mathcal{H}_3}},\ \text{if } \mathcal{H}_2 < \mathcal{H}_3\ ,\ \sqrt{1 - \frac{\mathcal{H}_3}{\mathcal{H}_2}},\ \text{else} \right\} \tag{3.46}$$

or equivalently,

$$\frac{a_2}{a_3} = \sqrt{\frac{\mathcal{H}_3}{\mathcal{H}_2}} \tag{3.47}$$

Finally, substituting the eccentricity (3.46) in (3.44) and (3.45), we obtain:

$$M_1 = \frac{1}{2\ E(e)\ \mathcal{H}_2^{3/4}\ \mathcal{H}_3^{1/4}} \tag{3.48}$$

where $E(e)$ is the complete elliptic integral of the second kind. It is useful to rewrite (3.48) in

the form:

$$M_1 = \Psi(e)\frac{1}{\pi\sqrt{\mathcal{H}_2\,\mathcal{H}_3}};\ \text{where}\ \Psi(e) = \pi\frac{(1-e^2)^{1/4}}{2\,E(e)} \tag{3.49}$$

We note that $0.99 \leq \Psi(e) \leq 1$ if $e \leq 0.6$, which corresponds to an ellipse axis ratio smaller than 1.25. Hence, using $\Psi(e) \approx 1$ in (3.49) simplifies the expression of the indentation modulus normal to the axis of symmetry:

$$M_1 \approx \frac{1}{\pi\sqrt{\mathcal{H}_2\,\mathcal{H}_3}} = \sqrt{M_{12}\,M_{13}} \tag{3.50}$$

where:

- M_{13} appears as the indentation modulus obtained by indentation in an isotropic solid, for which the elastic properties in direction $x3$ coincide with the elastic properties in direction $x1$ and $x2$:

$$M_{13} = \frac{1}{\pi\mathcal{H}_3} = \frac{C_{11}^2 - C_{12}^2}{C_{11}} \tag{3.51}$$

- M_{12} would be the indentation modulus in direction $x1$, if the elastic properties in direction $x2$ had been set equal to the properties in direction $x3$:

$$M_{12} = \frac{1}{\pi\mathcal{H}_2} = \sqrt{\frac{C_{11}}{C_{33}}}M_3 \tag{3.52}$$

Expressions (3.35) and (3.50) of M_1 and M_3 provide a snapshot of the elastic properties in two different directions of a transversely isotropic material.

3.1.3 Advanced Analysis: Indentation Modulus of Orthotropic Media

The method described above can be extended to orthotropic materials, which are defined by three orthogonal planes of material symmetry.

If we consider the same Cartesian coordinates system, such that the orthotropic solid's three planes of symmetry are along $(x1, x2)$, $(x1, x3)$ and $(x2, x3)$, the indentation moduli in the directions $x1, x2$ and $x3$ can be approximated. For example, in the case of indentation in direction $x1$ of surface $(x2, x3)$, there are two perpendicular planes of symmetry, $(x1, x2)$ and $(x1, x3)$.

For an orthotropic solid, we consider the nine independent stiffness constants of the material:

$$\begin{array}{lll} C_{11} = C_{1111} \text{ or } C_{21} = \sqrt{C_{1111}\, C_{2222}} & C_{12} = C_{1122} = C_{2211} & C_{44} = C_{2323} \\ C_{33} = C_{3333} \text{ or } C_{31} = \sqrt{C_{1111}\, C_{3333}} \; ; & C_{13} = C_{1133} = C_{3311} \; ; & C_{55} = C_{1313} \\ C_{22} = C_{2222} \text{ or } C_{32} = \sqrt{C_{2222}\, C_{3333}} & C_{23} = C_{2233} = C_{3322} & C_{66} = C_{1212} \end{array} \tag{3.53}$$

Along similar lines of arguments developed before, we obtain:

$$\begin{aligned} M_1 &\approx \sqrt{M_{12}\, M_{13}} \\ M_2 &\approx \sqrt{M_{21}\, M_{23}} \\ M_3 &\approx \sqrt{M_{31}\, M_{32}} \end{aligned} \tag{3.54}$$

where:

$$M_{21} = 2\sqrt{\frac{C_{21}^2 - C_{12}^2}{C_{11}} \left(\frac{1}{C_{66}} + \frac{2}{C_{21} + C_{12}}\right)^{-1}}$$

$$M_{31} = 2\sqrt{\frac{C_{31}^2 - C_{13}^2}{C_{11}} \left(\frac{1}{C_{55}} + \frac{2}{C_{31} + C_{13}}\right)^{-1}} \tag{3.55}$$

$$M_{32} = 2\sqrt{\frac{C_{32}^2 - C_{23}^2}{C_{22}} \left(\frac{1}{C_{44}} + \frac{2}{C_{32} + C_{23}}\right)^{-1}}$$

and

$$\begin{aligned} M_{12} &= M_{21}\sqrt{\frac{C_{11}}{C_{22}}} \\ M_{13} &= M_{31}\sqrt{\frac{C_{11}}{C_{33}}} \\ M_{23} &= M_{32}\sqrt{\frac{C_{22}}{C_{33}}} \end{aligned} \tag{3.56}$$

3.2 Validation of the Method

The presented approximations were tested on several transversely isotropic and orthotropic model materials. The results were compared with the 'exact' values obtained by the implicit methods of Swadener and Pharr [80], and Vlassak *et al.* (2003 [91]). By way of example, we consider an hexagonal crystal of zinc that can be modeled as transversely isotropic. Using the elastic coefficients, $C_{1111} = C_{2222} = 164$, $C_{3333} = 62.93$, $C_{2323} = C_{1313} = 39$, $C_{1122} = 36$, $C_{2233} = C_{1133} = 52$ (GPa), our approximated indentation modulus in the direction parallel to the hexagonal planes is $M_{1x} = 132.2$ GPa, which is very close to the one evaluated using Vlassak *et al.*'s solution: $M(x1) = 133.4$GPa. For this particular case, Fig. 3-6 represents the 'exact' surface Green's function computed from [91], and two first order approximations: the Fourier transform approximation suggested by Vlassak *et al.* (2003 [91]), and our Green's function interpolation approximation (3.40). Both approximations are close to the target function. By construction, our explicit approximation is exact for $\theta = 0$ and $\theta = \pi/2$.

By way of example of an orthotropic material, we determine the indentation modulus for the human tibial cortical bones tested by Swadener and Pharr [68], using the constants $C_{1111} = 19.5$, $C_{2222} = 20.1$, $C_{3333} = 30.9$, $C_{2323} = 5.72$, $C_{1313} = 5.17$, $C_{1212} = 4.05$, $C_{2233} = C_{1133} = 12.5$, $C_{12} = 11.4$ (GPa). Our approximation (3.54) yields:

$$M_1 = 14.0659 \text{ GPa}, M_2 = 14.6090 \text{ GPa}, M_3 = 19.6784 \text{ GPa} \tag{3.57}$$

which cannot be distinguished from the values given by Swadener and Pharr [68]: $M(x1) = 14$ GPa, $M(x2) = 14.6$ GPa, $M(x3) = 19.7$ GPa.

The high accuracy of the relative simple closed form expressions seems to be due to a combination of two facts: (1) a first order approximation of the Green's function appears to be highly relevant for many materials; and (2) the eccentricities encountered with many materials are rather small. On the other hand, the proposed solutions only apply to the three principal material directions. The full back-analysis from indentation tests of the five (respectively nine) independent elastic constants for transversally isotropic (respectively orthotropic) materials will require three (respectively six) further solutions in inclined directions. However, the solutions in the principal material directions have the premise to display the highest contrast in indentation

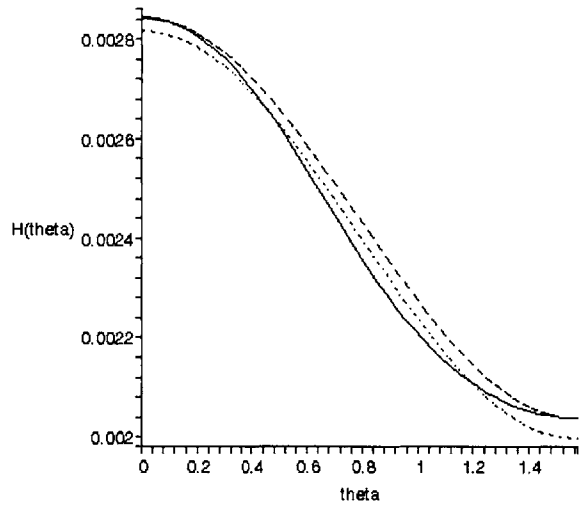

Figure 3-6: Green's function of zinc's surface (x2,x3) in 1/GPa (solid line). Our first order approximation (dashed). The equivalent one from a Fourier transform (dotted). Theta varies from 0 to 90 degrees.

stiffness.

3.3 Conclusion

The interpretation of indentation tests on transverse isotropic materials is accurate and can now be applied to shales. Indenting shales in the two directions 1 and 3 will provide two snapshots M_{ib} and M_{nb} of the five stiffness coefficients $C_{11}, C_{33}, C_{12}, C_{13}, C_{44}$ using (3.35) and (3.50). These snapshots are obtained at different scales as long as the conditions (2.69) to (2.72) and (2.55) are verified. But we can already see that M_{ib} and M_{nb} cannot give a full picture of the five elastic constants of transversely isotropic materials. We will need some additional information to reduce the number of model parameters to match the number of experimentally accessible indentation values. This motivates the development of a micromechanics approach, as detailed in what follows.

Part III

Experimental Poromechanics of Shale Materials

Chapter 4

Multiscale Microstructure of Shale Materials

The third part of this report is devoted to the experimental base of our study. The present chapter focuses on the microstructure of shale materials. The next chapter will present all the available experimental measures of shale elasticity.

Inarguably, shale materials are highly heterogeneous materials, with heterogeneities that manifest themselves from the nanoscale to the macroscale. This chapter reviews the different scales of shale material heterogeneities, by breaking this highly heterogeneous material system up into different scales defined by characteristic sizes of heterogeneities.

In addition to shale composition that can be obtained separately from X-Ray diffraction measurements, we look for all the information that is available on an image of the material at different magnifications: particle sizes, orientations and spatial distributions. The result of this procedure is a multiscale think-model of the microstructure of shale materials, which will form much of the backbone of our poromechanics analysis.

Our investigation will focus on three shales provided by ChevronTexaco of different origins and depths. We seek to identify what these materials have in common (and what not), in order to construct a general multiscale model of shales.

4.1 Origin of Shales

It is hard to find an unanimous definition of shales. The main feature of shale rocks is that they are mainly composed of sedimented clay particles, and that they present a layered structure, sometimes visible when shales naturally slit along privileged directions [3]. This anisotropic fracture behavior is a good way to distinguish shales from non-compacted other types of clayish sediments.

Clay sediments have different origins, but most of them are inherited from an original weathered rock, then transported and deposited as a sediment [3]. Some are transformed version of a transported clay, or depending on the chemistry of the environment, can even be formed in the sedimentary rock formation.

4.2 Clay Crystals

4.2.1 Definition and Classification

Clays are defined as the finest part of soils with grain sizes smaller than $4\mu m$. Here we refer to phyllosilicate particles with a characteristic flat shape of diameter $\sim 1\mu m$ (Fig. 4-1), which can either be a pure crystal or a face to face association of several crystal leaving very small spaces (20 Å) in between [26]. At a smaller level the crystals contain two main base elements: A silica atom with a surrounding tetrahedra of 4 oxygen atoms (Fig. 4-2), and an aluminum atom with a surrounding octahedra of 8 oxygen atoms. As shown on Figure 4-2, theses elements are clustered in sheets with a characteristic hexagonal symmetry of Al and Si atoms. These sheets are sandwiched in specific combinations to form crystal layers (Figs. 4-2 and 4-3).

Clay minerals are classified in two main families (see Fig. 4-3) :

- 1:1 clays are formed by one Al sheet and one Si sheet. This structure is mainly representative of kaolinite;
- 2:1 clays are formed by one Al sheet and two Si sheet. This structure is mainly representative of illite and smectite clays.

The internal planar structure is at the origin of the sheet-like shape of clay minerals (Fig. 4-1). The type of a clay mineral also depends on the nature and number of ions present in the

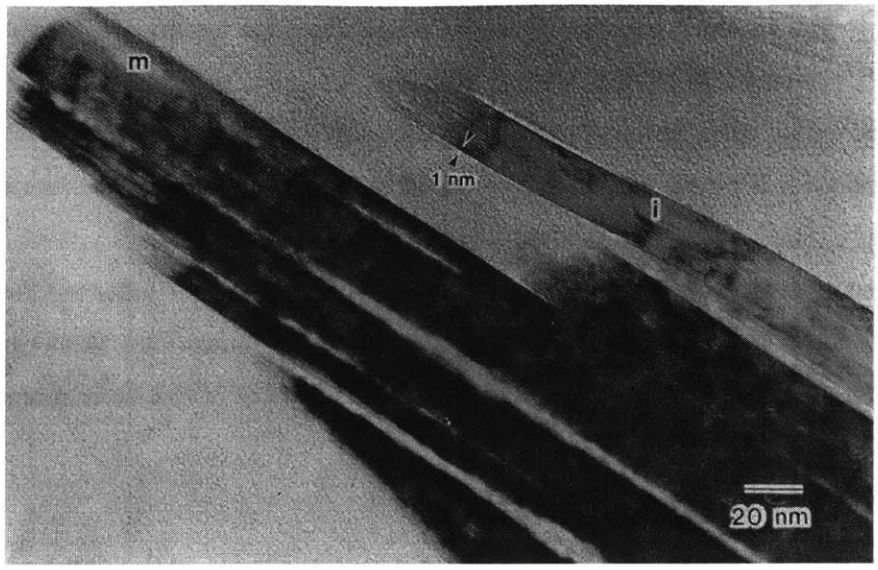

Figure 4-1: TEM image of two clay particles: mica (m) and illite (i). The layered structure is visible with a period of 1nm (in [3], pp 545-560).

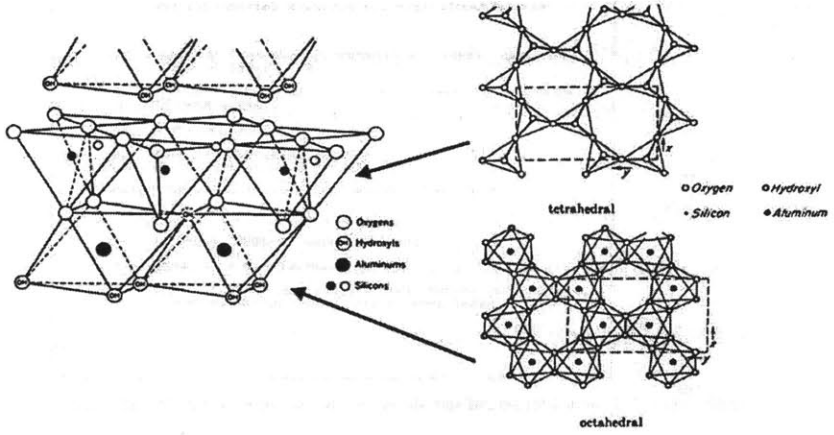

Figure 4-2: Formation of the phyllosilicate structure from tetrahedral and octahedral elements (from [94]).

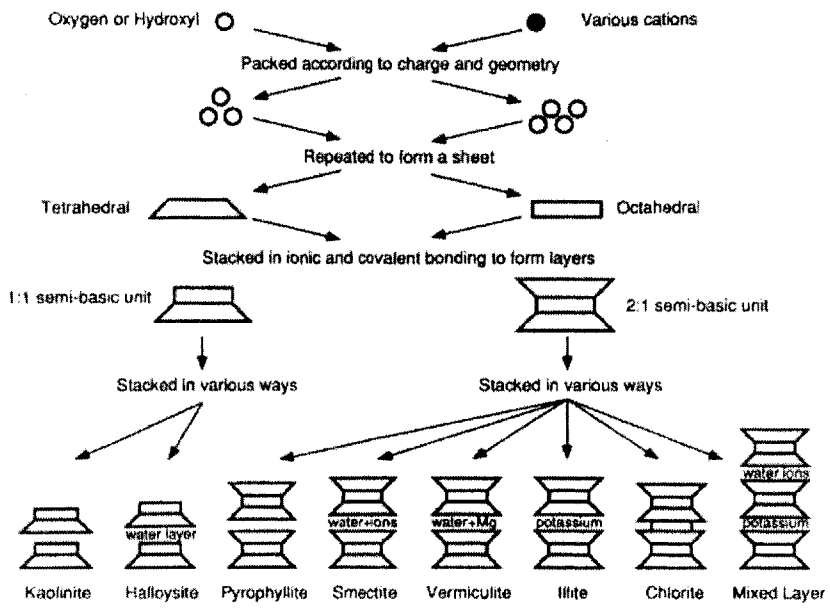

Figure 4-3: Synthesis pattern of clay minerals, from Mitchell (1993, 2nd edition) [60].

space between two identical crystal layers. In some clays, this interlayer space is sufficient to contain several water molecules bound together with hydrated cations. This is the origin for the swelling of Montmorillonite (smectite). For a non-swelling clay like illite, the interlayer space is occupied by a non hydrated cation, and the specific surface area is small, on the order of $50 - 120m^2/g$ compared to $840m^2/g$ for smectite [60]. Some crystals mix two different types of layers, as illite-smectite clays. The ordering can be periodic, or random. Figure 4-3 summarizes the various types of clay minerals one can encounter in sediments.

4.2.2 Clay Mineralogy of Shales

The proportion of clay minerals and silt inclusion in a shale results from complex superposition of influencing parameters. Each sediment field has its own characteristics, depending on the mode of deposition, the geological history, the thermo-chemical conditions, the depth, etc. It is difficult to draw some general observations, but some trends appear as a function of the depth and compaction: for high depths (2,000-3,000m), smectite starts to transform into illite

		density	Shale 1	Shale 2	Shale 3
Inclusions	Total	-	16.6	24.3	28.3
	Quartz	2.65	13	17	20
	KFedspar	2.57	2	3	1
	Plagioclase	2.69	1	2	2
	Calcite	2.71	0	1	0
	Mg-Calcite	2.71	0	0	0
	Dolomite	2.9	0	0	0
	Pyrite	5	0	2	0.4
	Siderite	3.74	1	1	0
	Ankerite	3	0	0	0
	Hematite	2.9	0	0	4
Porosity (PMI) ϕ		-	26	13.3	7.45
Clay	Total	-	57.5	62.9	64.6
	Kaolinite	2.67	27	19	9
	Illite	2.7	19	27	37
	Smectite	2.7	10	16	19
	Other (Chl.)	2.7	2	1	0
Clay Porosity ϕ_c			31.2	17.5	10.3(*9.8)
Natural RH			N.A.	N.A.	N.A.

Table 4.1: Mineralogy (volume percent) of the investigated shale materials, and mineral densities.(*) The porosity is calculated in the porous clay+hematite phase.

(diagenesis), via some intermixed layers of both [60].

Table 4.1 gives the composition of the three shales investigated in this study[1]. The mineral composition (in mass percent) was provided by ChevronTexaco from X-Ray diffraction measurements (XRD), and is given in Appendix D. This technique consists in analyzing some X-ray diffraction patterns characteristic of specific crystal layers and interlayer thicknesses (see Fig. 4-3), which allows one to distinguish inclusions from clay minerals by type. The results or XRD are mass fractions, which we transform into volume fractions using:

$$f_i = (1-\phi)\,\frac{m_i/d_i}{\sum_{k=1}^{p} m_k/d_k} \tag{4.1}$$

where ϕ, the porosity, was obtained from Mercury Porosimetry (PMI); m_i are the mass fractions of the shale constituents; and d_i are the corresponding mineral densities. The values given in Table 4.1 are volume fractions obtained from (4.1). For shale 2 two sets of mineralogy with

[1]In Table 4.1 and in this report, N.A.(*non available*) refers to ChevronTexaco proprietary data.

quite different mass fractions were provided to us. The values in Table 4.1 are the average of these two data sets.

It will be useful to have the expression of the porosity in a reference volume consisting of the porous clay phase only. In this case, if $f_{inc} = \sum_{k=1}^{p_{inc}} f_k$ denotes the volume fraction of all solid phases that intervene at a scale higher than the one of clay minerals, the porosity ϕ_c in the clay phase reads:

$$\phi_c = \frac{\phi}{1 - f_{inc}} \tag{4.2}$$

4.2.3 Oxides

Oxides and hydroxides of iron, aluminum, silicon and iron are often present with the clay minerals, in form of gels or precipitates that coat or cement clay particles, or as crystalline units of Gibbsite, boehmite, hematite, and magnetite [60]. In one of the investigated shales (#3), a 5% volume content of hematite was found; and SEM pictures show regularly distributed precipitates of matter of a size of 5-10nm, which may be attributed to hematite; most probably hematite coating clay flakes. This will be discussed later on, with the results of indentation experiments on shale 3. The clay porosity of shale 3 in Table 4.1 was determined by taking a reference volume containing pores, clay minerals and hematite.

4.3 Shale Morphology

Physicochemical processes, bioorganic mechanisms, and burial diagenesis (see Table 4.2) determine the microfabric of shales [3]. The microfabric of a shale results from the interaction of processes involving different energies, which lead to fairly random particle orientation distributions, or on the contrary to very aligned states, depending on the scale of observation.

4.3.1 Level 'I': Porous Clay Composite:

SEM and ESEM images (Figures 4-4 to 4-6) of the three shales considered in this study show that shales, at a length scale of some microns, are porous clay composites. At this scale, the composite comes in a large variety of forms and shapes, ranging from highly ordered sheet bundles to wavy flake structures and highly pressed and crushed structures of clay sheets. The

Fundamental process Mechanism	Fabric Signature (predominant)*	Scale length and time
Physicochemical		
Electrochemical	E-F	$< 4\mu m$, μsec to $m$sec (atomic and molecular)
Thermomechanical	F-F (some E-F)	molecular up to$\sim 0.2mm$, $m$sec to min
Interface dynamics	F-F and E-F	μm to $\sim 0.5mm$, sec
Bioorganic		
Biomechanical	E-F	$\sim 0.5mm$ to $> 2mm$, sec to min
Biophysical	E-E and F-F	μm to mm, sec to min
Biochemical	Nonunique (unknown)	μm to mm, hr to yr
Burial diagenesis		
Mass gravity	F-F localized swirl	cm to km, >yr
Diagenesis-cementation	Nonunique (unknown)	molecular, >yr

(*) E-F, edge to face; E-E, edge to edge; F-F, face to face.

Table 4.2: Various mechanisms influencing the microstructure of shale during its formation (from Bennett et al. [3]).

characteristic dimension of the clay particles visible in these pictures in on the order of 500-1000nm, and 20-50nm thick, which confirms the aspect ratio of roughly $1/25-1/20$, as generally reported in the clay literature [60], [3], [88]. However, the microphotographs in figures 4-4 to 4-6 also display a high degree of disorder of the clay sheet orientation, and this both normal to the bedding direction (labeled 'x_3') and in bedding direction (labeled 'x_1' or 'x_2'). At the considered scale of the porous clay composite, it is quite frequent that clay packages are found to strongly divert from the deposition orientation.

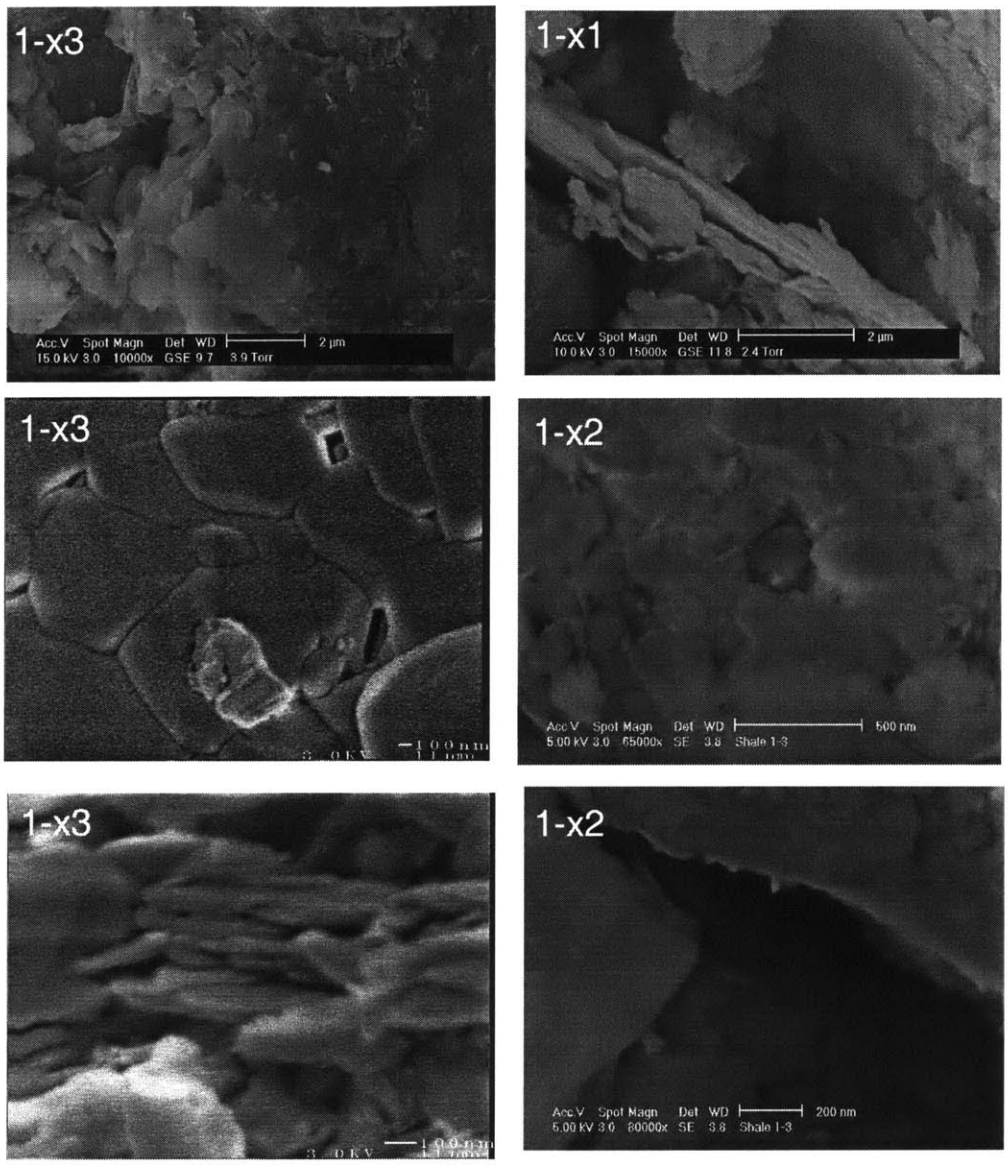

Figure 4-4: Shale#1 (level I): SEM and ESEM micrographs. 'x_i' designates the surface orientation: 'x_3'=view normal to the bedding direction; 'x_1' and 'x_2'=view in bedding direction.

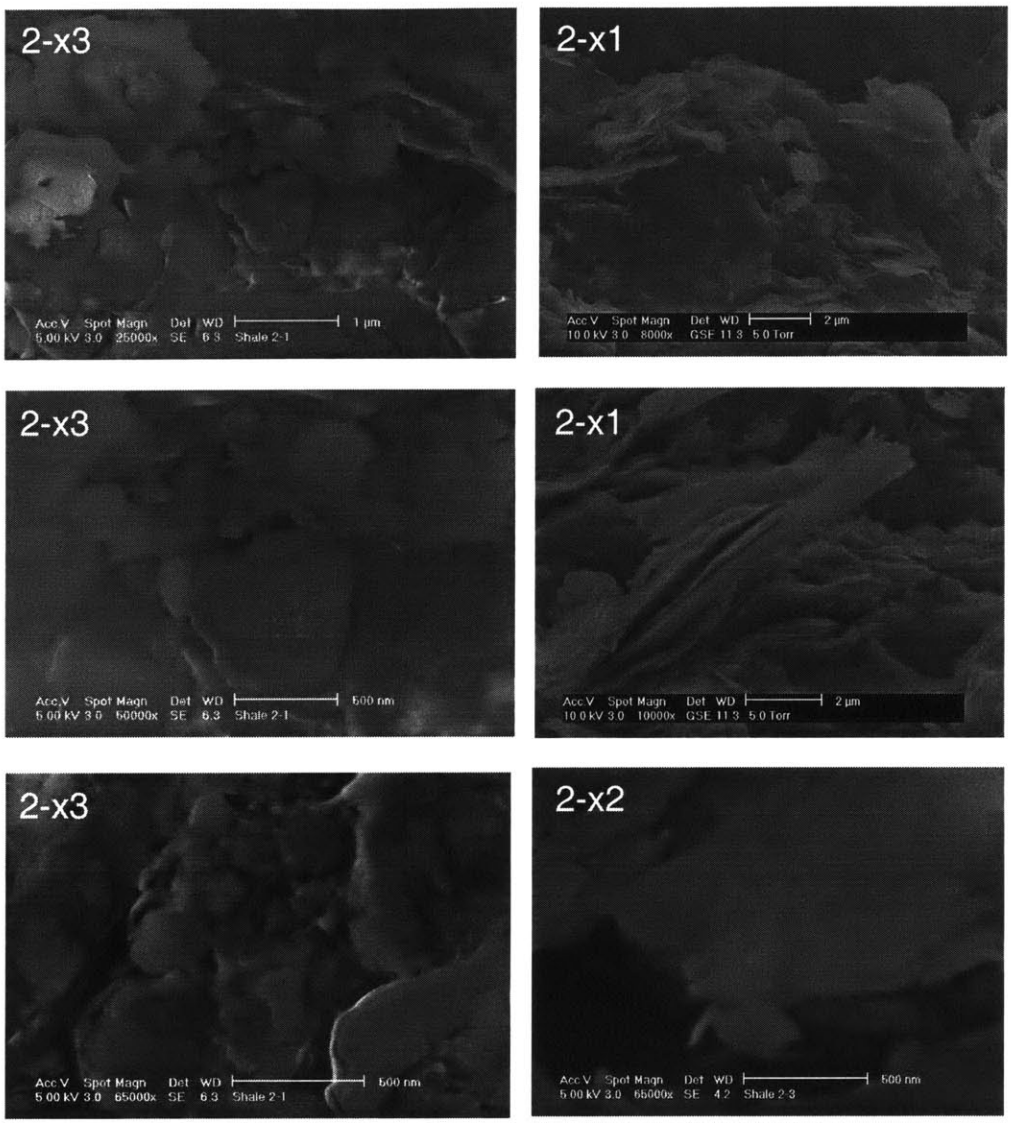

Figure 4-5: Shale#2 (level I): SEM and ESEM micrographs. 'x_i' designates the surface orientation: 'x_3'=view normal to the bedding direction; 'x_1' and 'x_2'=view in bedding direction.

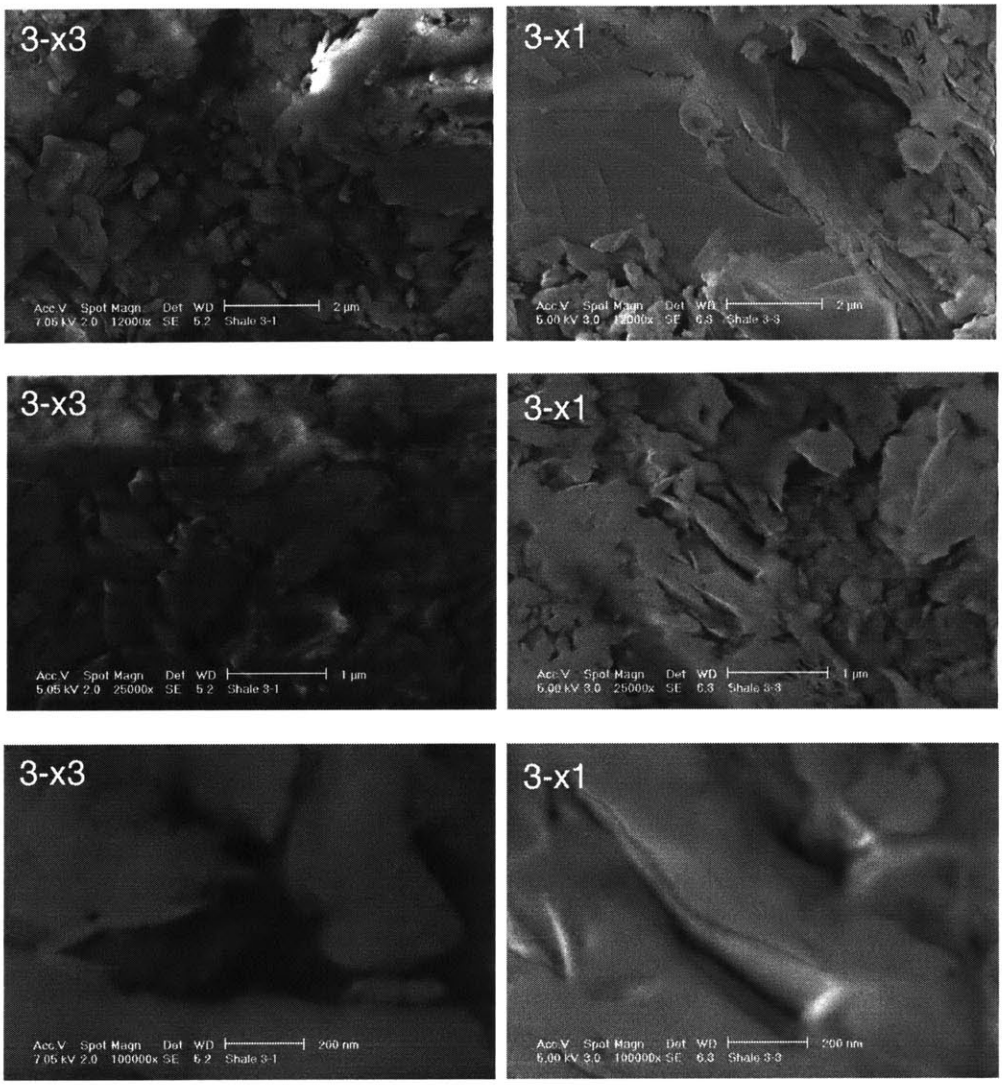

Figure 4-6: Shale#3 (level I): SEM and ESEM micrographs. 'x_i' designates the surface orientation: 'x_3'=view normal to the bedding direction; 'x_1' and 'x_2'=view in bedding direction.

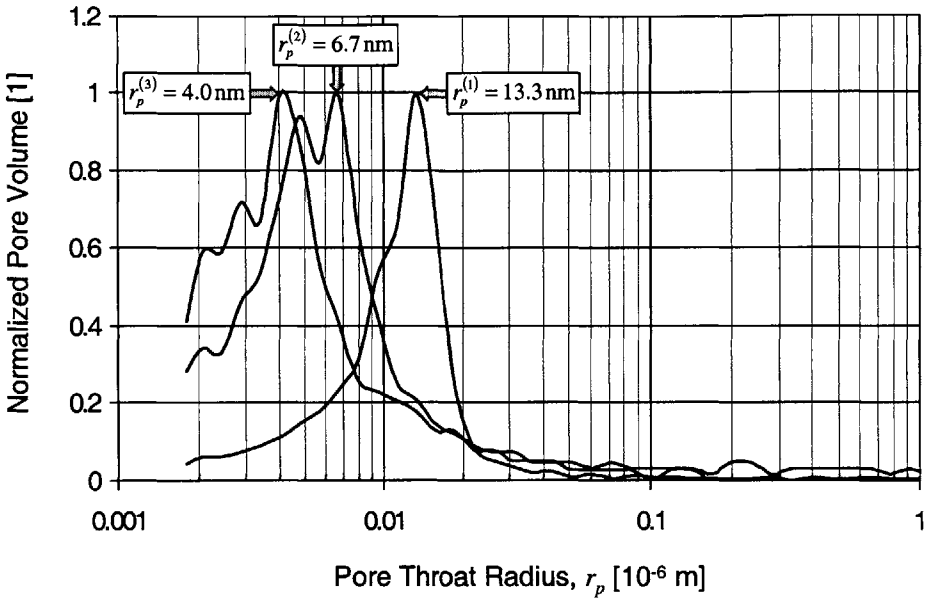

Figure 4-7: Pore throat radius distribution obtained by poro mercury intrusion (PMI) of the three investigated shale materials (from ChevronTexaco).

The space in between the clay sheets forms almost the totality of the porosity of shales, as poromercury intrusion studies show (Fig. 4-7), displaying a very low characteristic pore access radius[1] of some nanometers; thus situating the porosity of shales at a scale below the porous clay composite. This justifies considering shales at a length scale of $500 - 5,000\,\text{nm}$ as porous composites.

We refer to this scale as Level 'I': it is the smallest scale that is currently accessible to mechanical testing, *ie.* nanoindentation. At this scale, it is most likely that the local fabric signature of the materials is determined by the type of contacts between particles.

[1]The poromercury intrusion model is based on a pore cylinder model, and it is generally admitted that PMI allows invasion of (cylindrical) pores of pore radius 3.6×10^{-9} m to 60×10^{-6} m. Given the sheet shape of the clay particles, it is most unlikely that the pores in shales are cylindrical, as the porosity is the space in between the sheets, so that the pore geometry should be similar to the sheet geometry.

4.3.2 Level 'II': Layered Textured Matrix.

The porous clay composite from level I forms a layered textured matrix that is representative of shales at a scale of tens of micrometers. This microfabric signature of shale materials, which is most likely a consequence of the deposition history, is clearly visible in SEM images of 100 to 1000 times magnification, as shown in Figure 4-8 for the three shale materials. Some trend-lines have been superimposed on the microphotographs to highlight the layered texture at the considered scale, as well as the perturbation of the layered structure through the presence of silt inclusions of micrometer size. The smaller the magnification the more regular and homogeneous the visible layered structure, which suggests that the shale fabric becomes more and more dominant at larger than at smaller scales. That what changes from Level I to Level II is the texture. This texture may arise from a privileged orientation of clay particles in the directions of the bedding planes. But it can also result simply from a particular spatial distribution of clay particles having similar orientations. Indeed, Figure 4-8 shows horizontal continuity of horizontal clay particles (the separations lines), but no vertical continuity of vertically oriented flakes. Referring to the origin of shales (Table 4.2), these deposition lines become visible at the scale where gravitational forces, during deposition and compaction periods, start to dominate over short range physico- and bio- chemical driving forces. We refer to this scale of visible texture as Level 'II'.

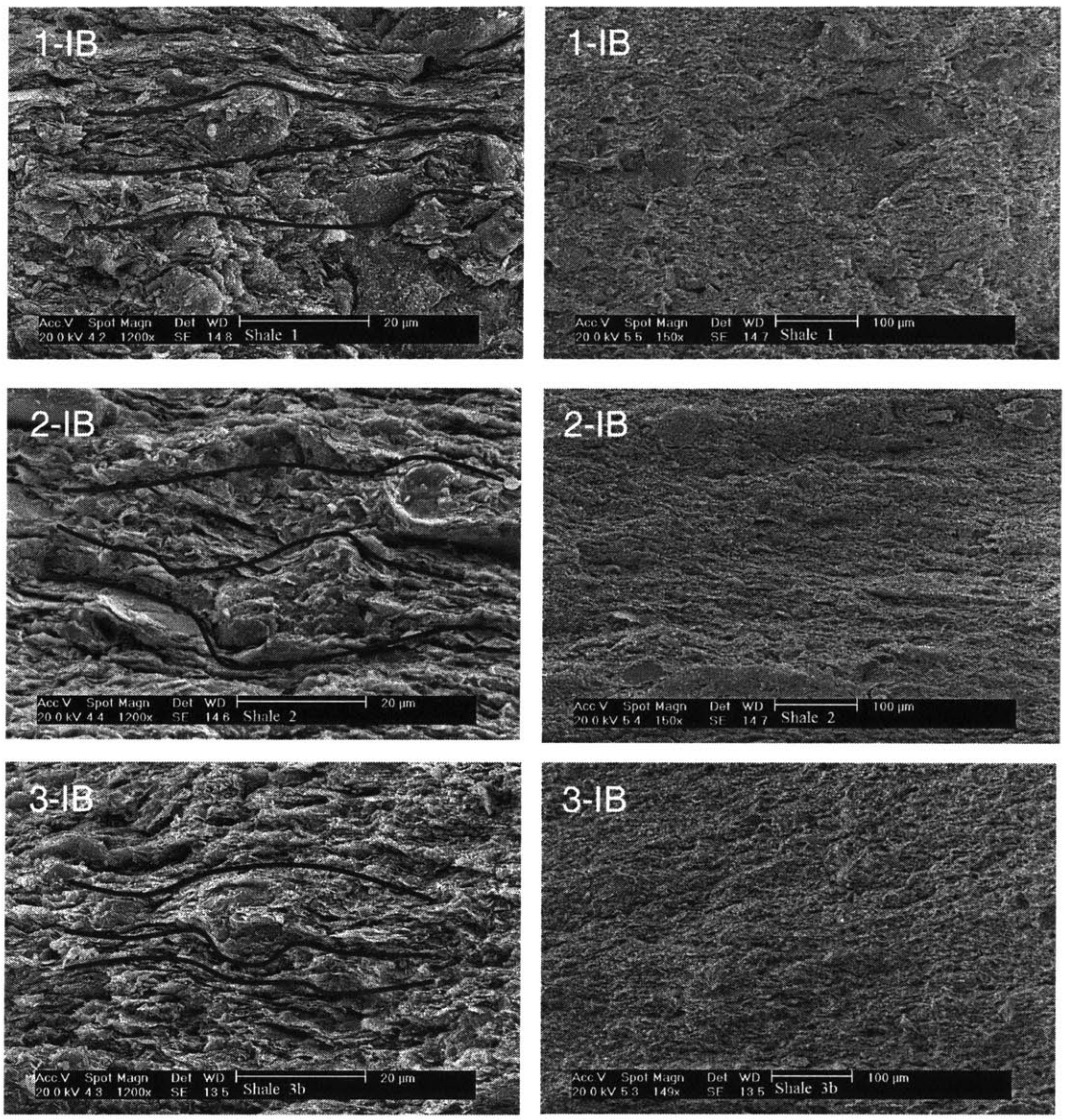

Figure 4-8: SEM Images of shales at level II (from Chevron Texaco).

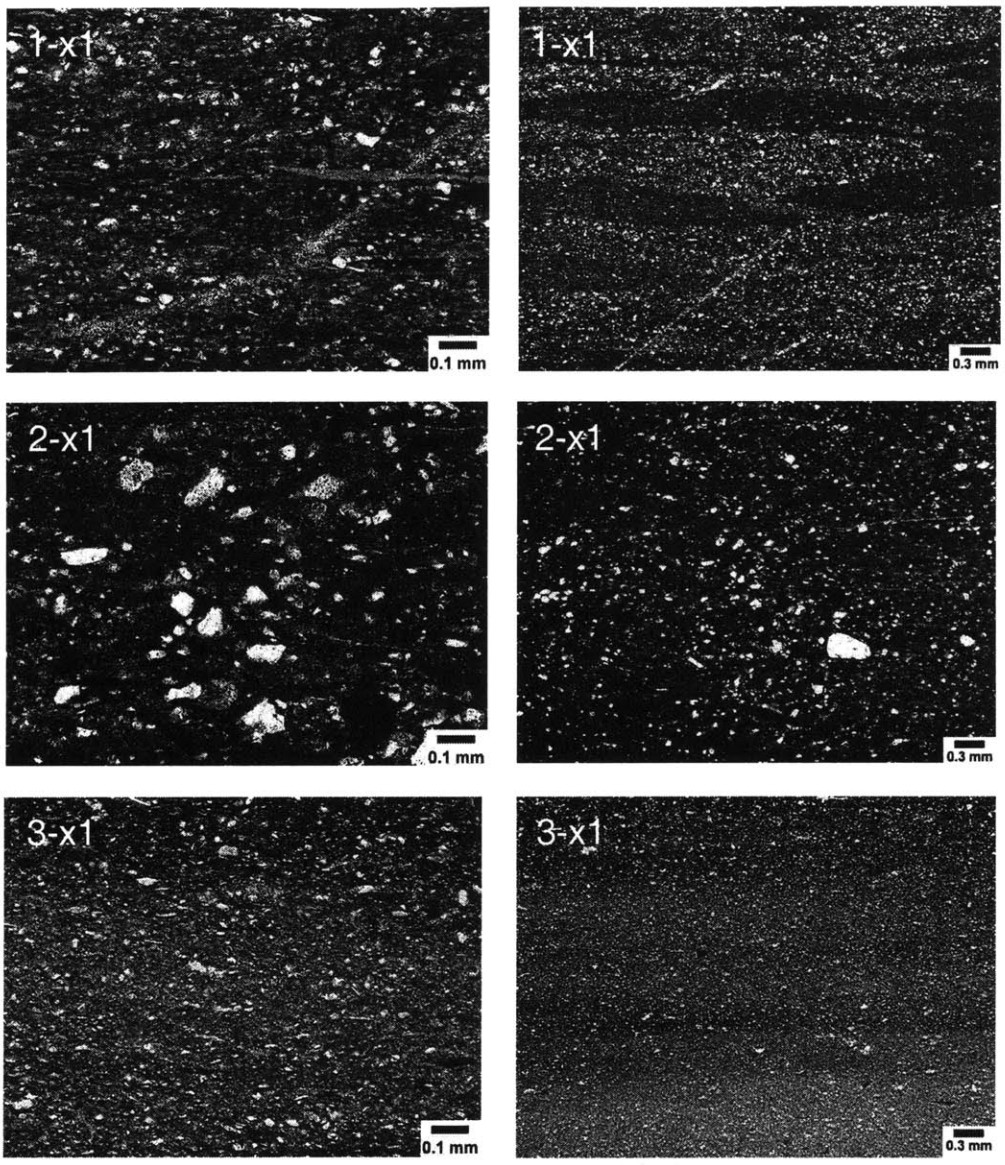

Figure 4-9: Level III: Plane polarized light thin-section photomicrographs, of 100X (left) and 25X (right) magnification, for the three shale materials (from ChevronTexaco).

4.3.3 Level 'III': Shale

The textured clay composite of level II together with quartz inclusions forms a macroscopic composite material, that becomes visible at the sub-millimeter to millimeter scale. Figure 4-9 displays a number of plane polarized light thin-section photomicrographs, of 100X and 25X magnification, for the three shale materials considered in this study. The mineralogy of the three investigated shales in Table 4.1 reports inclusion volume fractions situated in the range of 15-30%.

The images highlight the composite nature of shale materials composed of a clay matrix with an in-general abundant population of poorly sorted detrital grains (mainly quartz inclusions) of angular to subangular shape, that are either concentrated into laminations located between thinner, clay rich (or quartz starved), lens shaped lams (shale 1), or homogeneously distributed throughout (shale 2 and 3). This scale is the macroscopic scale of material description. At this scale, one may consider the presence of cracks representative of the natural state of the rock, or depending on the problem considered: sampling, hydraulic fracturing, faulting.

4.4 Conclusion: Four-level Think-Model of the Microstructure of Shale Materials.

The information provided by mineralogy, porosity measurements and advanced microscopy is summarized in Figure 4-10 in form of a four-level think-model of the multiscale structure of shale materials. This microstructural model forms much of the backbone of our experimental and theoretical microporomechanics investigation below. Level '0' is the scale of the clay minerals. Level 'I' is the lowest scale currently accessible to mechanical testing, *ie.* nanoindentation. Level 'II' can also be accessed by microindentation, while Level 'III' is classically tested mechanically with acoustic methods. The experimental values available at different scales are reviewed next.

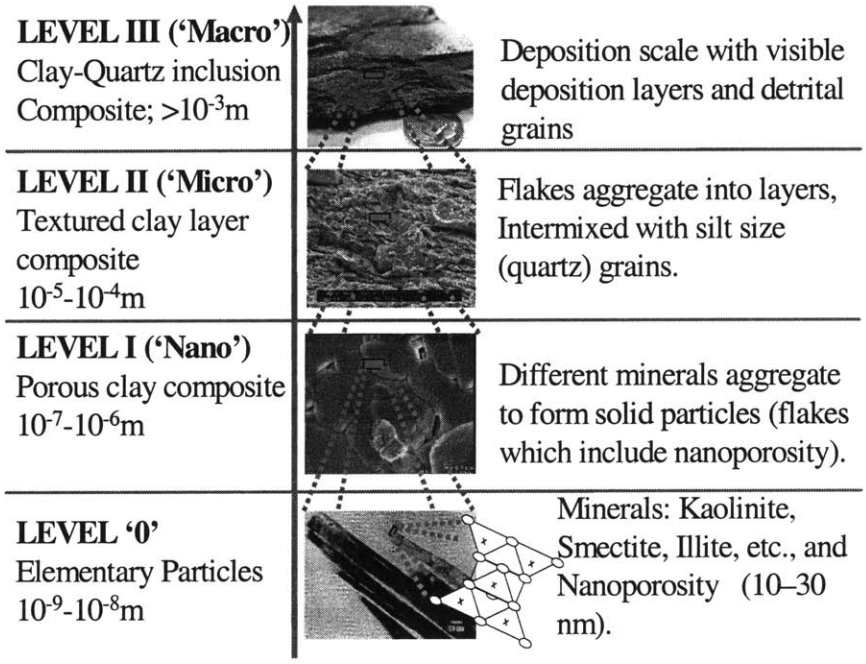

Figure 4-10: Four-level multiscale think-model of the microstructure of shale materials.

Chapter 5

Multiscale Elastic Properties of Shales

Elastic properties of shales are still an enigma that has deceived many decoding attempts from both experimental and theoretical sides. The aim of this chapter is to bring all the available information about shale elastic properties together, from the scale of the clay minerals (Level '0'), to the the macroscopic scale (Level 'III'). This includes a review of the literature, and acoustic and indentation tests performed on the three shales investigated in our study. The acoustic measurements were provided by ChevronTexaco. The indentation tests were performed by G. Constantinides at M.I.T. as a part of this research project on shale mechanical properties[1]. The ensemble of these experimental results will give a comprehensive mechanical picture of shale elasticity on the basis of the shale microstructure described in the previous chapter, which will serve for our micromechanical modeling of shales.

5.1 Introduction

Two characteristics of shale elasticity have been analyzed independently: the overall stiffness of clay-sand mixtures, and the anisotropy of shales.

Empirical relations between stiffness and porosity have been established experimentally for

[1]The indentation tests were carried out in M.I.T.'s nanolab, directed by A. Schwartzman and supervised by K. Van Vliet.

shales, and tested on artificially compacted porous sand-clay mixtures [58]. The influence of sand content has also been investigated [72]. But the proposed relations are pure empirical and fitting functions and lack a very important physical information: the stiffness of pure clay minerals.

Shale anisotropy has been the focus of the geoacoustics community for some time; and it is now well recognized that shales behave as transverse isotropic materials (Jones and Wang, 1981, [53]), such that the plane of isotropy coincides with the bedding directions. A lot of research efforts have been devoted to relating seismic velocities to shale anisotropic elastic properties [83], [84], and to the origins of such behavior [48], [49], [74], [75].

Among the potential sources of anisotropy at the macroscale, the layered structure of clay minerals at Level '0' seems to be a good candidate. In addition, the effect of microstructure through the flat shape of clay flakes and their privileged orientation parallel to the bedding planes has to be taken into account. Finally, some authors suggest that the orientation distribution of parallel compacted clay particles is the main cause of observed anisotropy variability [74], [52], assuming universal anisotropic properties of porous clays.

The focus of our study is the relative effects of porosity, pure clay minerals stiffness, texture and spatial distributions, on the elastic properties of shales at multiple scales.

5.2 Forces at Stake

The particularity of clays is their very high specific surface, from 15 to 800 m^2/g. This is the reason why clays are considered to be colloid systems, in which surface forces have a critical influence on the properties and the state (suspension or solid) of the material. In compacted clay rocks, there is no continuity of ionic-covalent forces, from clay particle to clay particle [60], [41]. In addition to mechanical, non-cohesive, low energy contacts, the equilibrium of clay systems is determined by complex interactions of repulsive and attractive surface forces. Adding water to a rock composed of easy hydrated smectite clays can turn it into a low viscosity colloidal suspension. These surface forces belong to several categories [41], repulsive electrical double layer, hydration forces and attractive Van der Waals and capillary forces:

1. Electrical double layer repulsion forces are a combination of two opposing interactions: an

osmotic pressure between charged crystal plates separated by a cationic solution, and an electrostatic attraction. Knowing the chemical potential associated with this interaction allows one to estimate the swelling pressure that develops in clays.

2. Hydration forces are related to the hydration of the crystal layers and interlayer cations. The adsorbed water by hydrogen or ionic bonds leads to a short range repulsion, that could also be the source of additional cohesion for very close charged surfaces.

3. Van der Waals attraction results from dipolar interactions, mainly mutually induced (London) dipolar interactions.

4. Finally, capillary forces can play a critical role in partially saturated materials. The negative pressure induced by surface tensions at the fluid-gas interface lead to a strong attraction, particularly visible through drying shrinkage phenomena.

As a consequence, for a given morphology, the elastic behavior of a solid porous clay composite in its natural state may depend on the contributions of four types of deformations involving different levels of forces, energies and stiffness:

- Intrinsic deformation of anisotropic clay crystals (ionic covalent bonds), including the interlayer weakening interactions (all forces above) [41],
- Bending of clay particles, which involves the same forces,
- Mechanical deformation at the contact between clay flakes, which also involves the same forces,
- Influence of electrical, hydration, Van der Waals and capillary forces between distinct clay particles, whose corresponding compliance is hard to define.

Hydration forces may induce a very low shear modulus, since adsorbed water molecules do not completely loose their mobility.

5.3 Level '0': Stiffness of Pure Clay Minerals

Unlike many other minerals, clay stiffness values are extremely rare in handbooks [59]. To our knowledge, the only direct measurements of the anisotropic elasticity of clay minerals are

reported for large muscovite crystals [59], possessing transversely isotropy: $C_{11} = 178$ GPa, $C_{33} = 55$ GPa, $C_{44} = 12$ GPa, $C_{12} = 42$ GPa, $C_{13} = 15$ GPa, or equivalently expressed in terms of indentation stiffness (3.50) and (3.35),

$$M^0_{1,\text{exp}} = 118 \text{ GPa}; \; M^0_{3,\text{exp}} = 46 \text{ GPa}; \; \frac{M^0_{1,\text{exp}}}{M^0_{3,\text{exp}}} = 2.6 \tag{5.1}$$

The main difficulty of measuring the mineral elasticity stems from the fact that clay particles are too small to be tested in pure solid form. Several attempts to overcome this difficulty have been reported (Table 5.1):

- The stiffness of compacted clay samples has been measured and extrapolated to a zero porosity assuming that this extrapolation technique yields a 'pure clay' stiffness value ([58], [48], [87]). There is quite some difference in stiffness values obtained with this technique, which makes it difficult to state with certainty whether such extrapolation techniques give access to intrinsic stiffness values or not. In particular, depending on the degree of saturation of the sample and other parameters influencing surface forces, the interactions between clay particles might exhibit different compliances which may in turn modify the extrapolated stiffness value. In order to have relevant experimental measures of clay minerals stiffness, Prasad *et al.* [71] have recently made some dynamic measurement of clays using Atomic Force Acoustic Microscopy (AFAM). They reported a very low Young's modulus for dickite of 6.2 GPa.

- Ultrasonic velocities of composite mixture of individual clay particles (powder) diluted, at various concentrations, in an epoxy matrix have been measured [92]. Using a backward homogenization derivation, the Young's modulus for randomly distributed clay particles was found to be on the order of $50-60$ GPa for kaolinite, $65-80$ GPa for illite, $40-50$ GPa for montmorillonite, and greater than 100 GPa for Chlorite. These results appear to be very consistent with theoretical estimates of single crystal elastic properties by Katahara (1996) for kaolinite, illite and chlorite, based on data of Alexandrov and Ryzhova (1961; cited from [92]).

- Very recently, Steered Molecular Dynamics simulations of pyrophyllite clay provide an

order of magnitude of the interlayer stiffness of 130 GPa, while the clay layers are almost rigid [54], with a stiffness value of 547 GPa in the direction perpendicular to crystal planes for a simple structure of two crystal layers with an interlayer space.

The scarcity of experimental values for solid clay stiffness and the large range of reported values highlight the difficulty to assess the intrinsic elasticity of single clay crystals. This has been recognized as one current major weakness of existing micromechanical models of shales [50]. Nanoindentation tests on a kaolin powder were recently performed by G. Constantinides at M.I.T.. The powder was composed of 97% kaolinite (EPK Kaolin, Feldspar Corporation, Atlanta Georgia). Using indentation depths of $70-90$ nm, that is an order of length magnitude smaller than the grain size, indentation stiffness values of

$$\text{EPK Kaolin: } M_{\text{exp}}^{0} = 40.3 \pm 8.8 \text{ GPa} \tag{5.2}$$

were obtained. Fig. 5-1 displays an Atomic Force Microscopy image of the indented kaolin powder grain, together with five force–indentation depth curves, from the unloading branch of which, the indentation stiffness was determined. The order of magnitude of the indentation stiffness of kaolin powder is found to be situated in between the values reported in [58] and [92], respectively. Finally, an interesting observations is that the $P-h$ indentation curves display almost no irreversible deformation ($h_f \simeq 0$), suggesting that the pure mineral rather behaves viscoelastic than elastoplastic. The unexpected almost linear shape of the loading curve could be explained from this time dependent behavior (see Appendix B for quantitative explanations).

5.4 Indentation Campaign

Indentations on single flakes cannot be performed experimentally on natural shales: the surface roughness and condition (2.60) impose smaller ranges of depth than the technique permits. That is why the indentation tests presented below start at Levels 'I' and 'II' of shales.

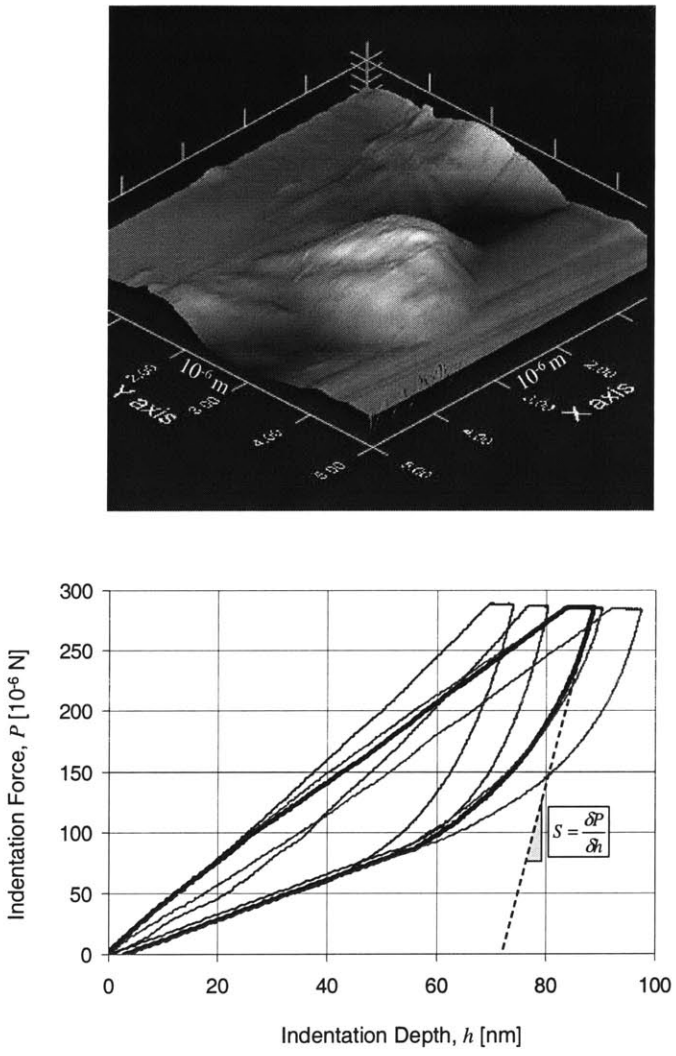

Figure 5-1: Nanoindentation on kaolin powder: (top) AFM image; (bottom) load-displacement curves (from [86]).

Clay Mineral	Sample	Experim. Techn.	Stiffness [GPa]		Source
Muscovite	nat. crystal		$C_{11} = 178, C_{33} = 55,$ $C_{12} = 42, C_{13} = 15, C_{44} = 12,$		[59]
Kaolinite	clay mixture	acoustic (MicroMech)	$E = 27.6, \nu = 0.3$		[58],[48]
Dicktite	clay mixture	AFAM	$E = 6.2$		[71]
Kaolinite Smectite Montmorillonite	clay-mixture suspensions	acoustic (Extrapol.)	$E = 9.8 - 15.4, \nu \approx 0.25$		[87]
Kaolinite	powder	acoustic	$E = 52 - 57, \nu = 0.3$		[92]
Illite	in epoxy	(MicroMech)	$E = 67, \nu = 0.32$		[92]
Smectite/Illite			$E = 47, \nu = 0.29$		[92]
Montmorillonite			$E = 40.7 - 49.6, \nu = 0.3$		[92]
Chlorite			$E = 74.8 - 194.7, \nu = 0.3$		[92]
Pyrophyllite	-	Mol. Dyn.	sheet axis	547	[54]
		$\Sigma/(\Delta L/L)$	interlayer	130	[54]

Table 5.1: Reported elastic stiffness values of clay minerals.

5.4.1 Sample Preparation

The three shale materials, labeled 1 to 3 in this study, are from different locations and different depths. The three materials were analyzed in terms of their mineral composition, porosity and density (see table 4.1).

Cylindrical shale specimens cored in three perpendicular directions of shale cuttings were delivered in sealed jars with decane, and stored in desiccators at their natural relative humidity (see Tab. 4.1) until testing. For the indentation testing, the cylinder specimens were cut into slices of approximate thickness 5-10mm. The surfaces were ground and polished with silicon carbide papers and diamond particles to obtain very flat and smooth surface finish. This was achieved in 6 stages of decreasing fineness with the last one being in the range of 250nm. Special attention was paid to keep the surfaces flat and parallel on both sides, since this could influence the angle of indentation and thus the result of the measurements. After polishing, the samples were placed in an ultrasonic bath to remove the dust and diamond particles left on the surface or in the pore structure, and then replaced in the desiccator until testing. The roughness of the surface was checked for some samples analyzing AFM images (Fig. 5-2) using Triboview®, and was found to be on average on the order of 90nm.

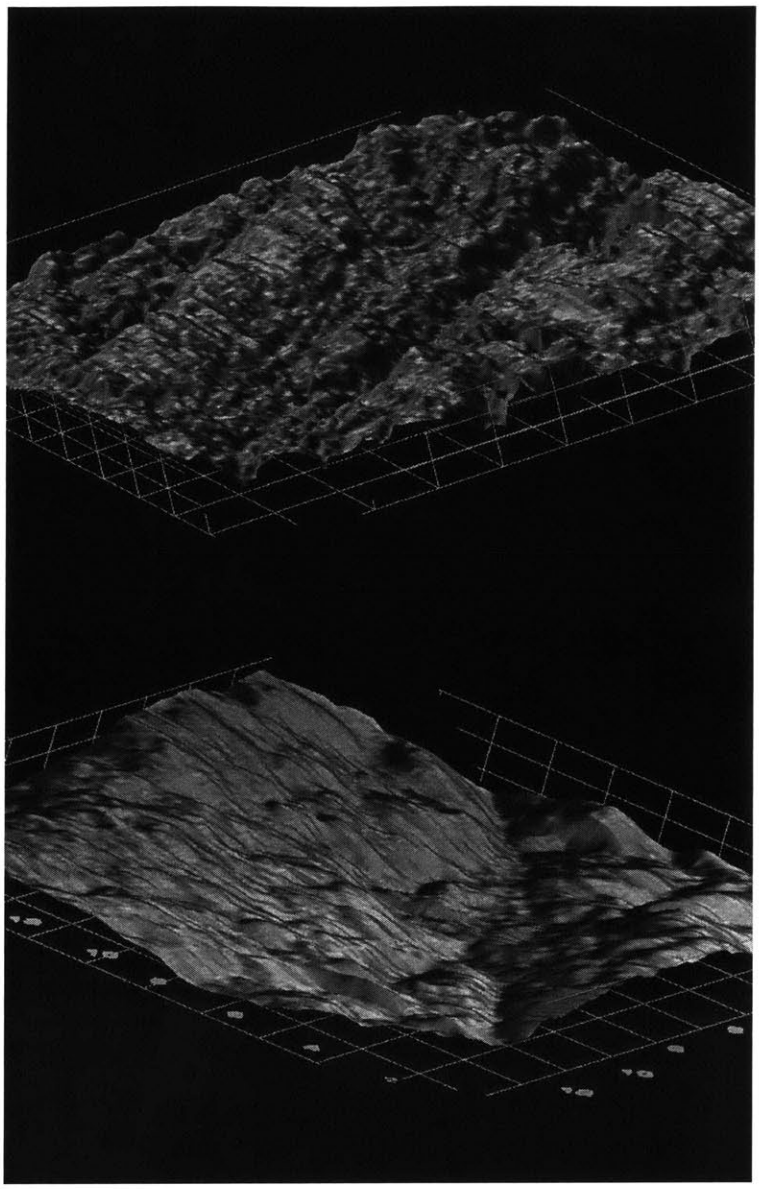

Figure 5-2: AFM-images of polished shale surface, employed for roughness measurements. Horizontal grid size is $10^{-6}m$.

Shale #	Scale (Level)	Name #–N/M–dir	No. (acc(*))	P_{max} [μN]		h_{max} [nm]	
				μ	σ	μ	σ
1	Nano (I)	1-N-x3	100(85)	262	21	230	61
		1-N-x1	100(70)	256	18	275	109
	Micro (II)	1-M-x3	100(53)	12,348	111	2,183	618
		1-M-x1	100(54)	12,363	98	2,252	533
		1-M-x2	100(94)	12,332	96	2,310	593
2	Nano (I)	2-N-x3(1)	100(76)	257	17	270	100
		2-N-x3(2)	100(65)	251	18	302	107
		2-N-x1	100(80)	265	12	219	70
	Micro (II)	2-M-x3	100(76)	12,305	70	1,947	396
		2-M-x1	100(97)	12,206	31	1,414	194
3	Nano (I)	3-N-x3	100(69)	251	18	306	107
		3-N-x1	100(60)	260	12	254	73
	Micro (II)	3-M-x3	100(92)	12,255	80	1,634	452
		3-M-x1	100(64)	12,268	107	1,735	607

Table 5.2: Summary of experimental indentation program on three shale materials, together with mean values (mu) and standard deviation (sigma) of the maximum applied force and maximum rigid indenter displacement. The series of tests are labeled shale-scale-indentation direction. (*) 'acc' stands for number of accepted data considered in the analysis of the results.

5.4.2 Summary of Experimental Results

Table 5.2 provides a breakdown of the indentation tests carried out on the three shale materials, together with the maximum force applied in the force driven nanoindentation and microindentation tests, and the average maximum indentation depth. The shale materials are labeled 1, 2 and 3, 'N' and 'M' stand respectively for *n*anoindentation and *m*icroindentation tests, and 'x_i(i=1,2,3)' stands for the indentation axis. We refer to the indentation tests operated to average indentation depth of 200-300nm as *nano*indentation. This indentation depth was chosen to assess the material properties of an r.e.v. of roughly $1\mu m$, and to restrict the effects of the surface roughness (on the order of 90 nm) in the analysis of the results. For the analysis of the results, therefore, indentation depths smaller than 100nm (which correspond often to the indentation on a quartz grain) and greater than 500nm (which corresponds often to the indentation into spaces affected by surface roughness) are rejected. In return, by microindentation we refer to indentation tests operated to on-average depths of 1,500-2,500 nm so that the material properties extracted from microindentation are characteristic of an r.e.v. size of 7-10μm. For the analysis of the microindentation results, indentation depths smaller than $1\mu m$

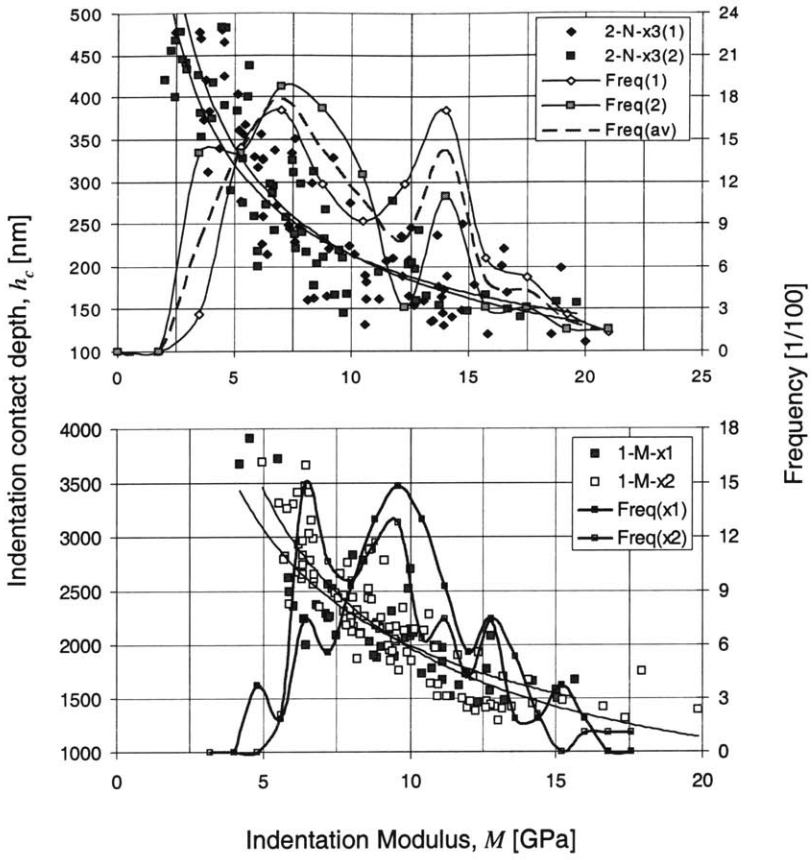

Figure 5-3: Proof of repeatability and statistical representativity of nanoindentation tests (Top) and microindentation tests (Bottom): indentation contact depth scaling and indentation stiffness frequency plots.

and greater than $5\mu m$ are rejected. In fact, very small depths are most probably obtained with the indentation of stiff quartz inclusions, for which the continuum indentation analysis may not be reliable (see Section 2.3.3).

The repeatability of the test procedure, and thus the statistical representativity of the results, was checked by several series of 100 indentation tests carried out on different specimen surfaces of the shale sample. The highly heterogeneous nature of shale materials calls for statistical analysis. The top chart in Figure 5-3 displays the indentation modulus-contact indentation depth scaling relations and the frequency distribution (histogram) of the indentation modulus for two series of nanoindentation tests on shale 2 in the direction x_3 normal to bedding. Not

only do the scaling relations of the indentation depth *vs.* the indentation modulus almost coincide (which can be seen from the fitted power function), but also the frequency with which a specific indentation modulus is encountered in the two series of tests on different surfaces is very similar. The bottom chart in Figure 5-3 displays similar results for two series of microindentation tests that were carried out in the two bedding directions, x_1 and x_2. The good agreement of the scaling relation and of the histograms do not only underscore the repeatability of the test procedure, but provide clear evidence that shales at the microscale r.e.v. (size 7-10μm) are transversely isotropic materials.

5.5 Indentations at the Nano-Scale, Level 'I'.

Prasad *et al.* [71] used atomic force acoustic microscopy (AFAM) to determine the Young's modulus of a thin layer of dickite to be on the order of 6.2 GPa. The authors concluded from this and a subsequent study [87], in which $P-$ and $S-$ wave velocity measurements on cold-pressed clay aggregates of different porosity/grain density were extrapolated to zero porosity values, that the actual stiffness of clay crystals was on the order of $10-15$ GPa, which is much smaller than typical values reported previously. Given the inarguably small size of the porosity in shale materials (Fig. 4-7), consequence of the natural compaction, and our confirmation of the clay crystal stiffness by nanoindentation (*ie.* Eq. (5.2) and Fig. 5-1), it appears very likely that the reported values by Prasad *et al.* [71] are those of the porous clay composite rather than the ones of the clay crystals themselves! (see Section 2.3.3). Clear evidence is provided by our nanoindentation results of shale materials.

5.5.1 Results

Table 5.3 reports the nanoindentation results on three types of shale materials of different mineralogy and porosities. Each series of tests consist of a hundred force driven indentation tests performed on a grid of $50\,\mu$m grid step size. The maximum indentation depth in the nanoindentation tests is on the order of $150-400\,$nm, and the derived properties, therefore, should be representative of a bulk material size on the order of $1,000\,$nm. This is the scale of the porous clay composite at level I, that includes the inter-grain clay porosity (see Section 4.3.1).

Shale #	Scale (Level)	Name #–N/M–dir	No. (Acc)	M [GPa]		H [nm]	
				μ	σ	μ	σ
1	Nano (I)	1-N-x3	85	9.5	3.1	0.30	0.16
	$\phi^I = 0.31$	1-N-x1	70	10.1	5.4	0.26	0.20
2	Nano (I)	2-N-x3(1)	76	9.7	4.3	0.23	0.16
	$\phi^I = 0.18$	2-N-x3(2)	65	8.0	4.3	0.18	0.13
		2-N-x1	85	14.2	5.5	0.31	0.19
3	Nano (I)	3-N-x3	69	10.2	5.1	0.18	0.14
	$\phi^I = 0.10$	3-N-x1	60	11.8	3.9	0.21	0.11

Table 5.3: Summary of nanoindentation results (Level I): mean values (mu) and standard deviations (sigma) of nanoindentation modulus M(I) and nanohardness H(I) (phi(I) stands for the clay porosity at level I).

We remark that the order of magnitude of the average nanoindentation stiffness is indeed on the same order of magnitude as the values reported by Vanorio *et al.* [87]:

$$M^I_{\text{exp}} = 8 - 14 \text{ GPa} \tag{5.3}$$

Moreover, the anisotropy varies between shales. Measured as the ratio between the average indentation moduli, we find that the anisotropy of the three materials at level I is roughly half the value of the clay minerals:

$$\frac{M^I_{1,\text{exp}}}{M^I_{3,\text{exp}}} = 1.06 - 1.46 - 1.16 \tag{5.4}$$

5.5.2 Preliminary Analysis

The three types of data-display on which we focus our analysis are (see Section 2.3.4):

1. The indentation modulus *vs.* indentation depth data, which provide information on how the indentation moduli are scaled by the indentation depth in the force-driven indentation tests. Indeed, what is sensed in a force driven indentation test on natural composites (like shales), is the highly heterogeneous nature of such materials, which translates into a stiffness scaling relation as a result of the BASh equation (2.20) on the projected contact area, as shown in Figure 5-4 for the three shale materials. Figure 5-4 also displays fitted normal distributions to all test series, and show that shale 1 is almost isotropic –in a

statistical sense–, while shale 2 and 3 are somewhat anisotropic. While the mean value of the indentation stiffness shows some anisotropy feature, the indentation depth does not depend on the direction for a given indentation modulus. This indicates that the same material is present –on-average– in different indentation directions. What changes most significantly from one shale material to the other is the mean indentation modulus in bedding while the mean indentation modulus normal to bedding varies little from one shale material to the other.

2. The frequency plot (histogram) of the indentation modulus that provides information of the distribution of stiffness within the microstructure. It corresponds to the probability with which a specific stiffness is encountered in the microstructure. Figure 5-5 shows that there is some difference in frequency distribution of the stiffness values obtained by grid indentation on different material planes. Since the same distribution in different indentation directions is a condition for isotropy (see Section 2.3.4), we recognize that it is the frequency distribution which is at the origin of the observed anisotropy of shale materials at the nanoscale.

3. The indentation moduli maps obtained by assigning each indentation result to a point on the grid that corresponds to the center of the indent. The discrete data points are linearly interpolated in between grid points to obtain continuous fields of mechanical properties, with a resolution defined by the grid-size. In our study, a constant grid step size of $50\mu m$ is applied, which satisfies condition (2.72). The results are displayed on the x-y plane in form of contour plots that capture ranges of mechanical properties. The mapping of the indentation moduli in Figure 5-6 displays the highly heterogeneous distribution of the nanoindentation moduli within the microstructure. The data is unfiltered and thus include also the one that were rejected for scaling and distribution analysis. The maps are almost free of any spatial continuity of properties at the considered scale, so that the nanoindentation tests can be seen as truly representative of a randomly distributed population of different phases present within the porous clay matrix (conditions (2.70) and (2.71)). However, the resolution of the contour plots given by the grid step size of $50\mu m$, is too large for the observation of any particular morphology whose length scale is

on the order of the indentation depth. Condition (2.73) is not satisfied.

Bringing these three observations together provides evidence for the origin of the anisotropy at level I: Given the identical stiffness scaling relations in both directions, the same mechanical materials defined by a set $(M^I_{\mathbf{exp}}, h_{\max})$ are seen in both directions, but with different probabilities. From a microstructural point of view, indenters sense packs of oriented crystals whose soft and stiff directions do not coincide necessarily with the indentation axes and can be felt identically in one or the other direction. The measure of anisotropy (5.4) at Level 'I' thus reflects some overall privileged orientation of parallel, packed clay flakes in the bedding directions. Moreover, porosity (resp. $\phi^I = 0.31, 0.18, 0.10$ for shales 1, 2, 3 defined by (4.2)) and anisotropy seem not to be directly correlated.

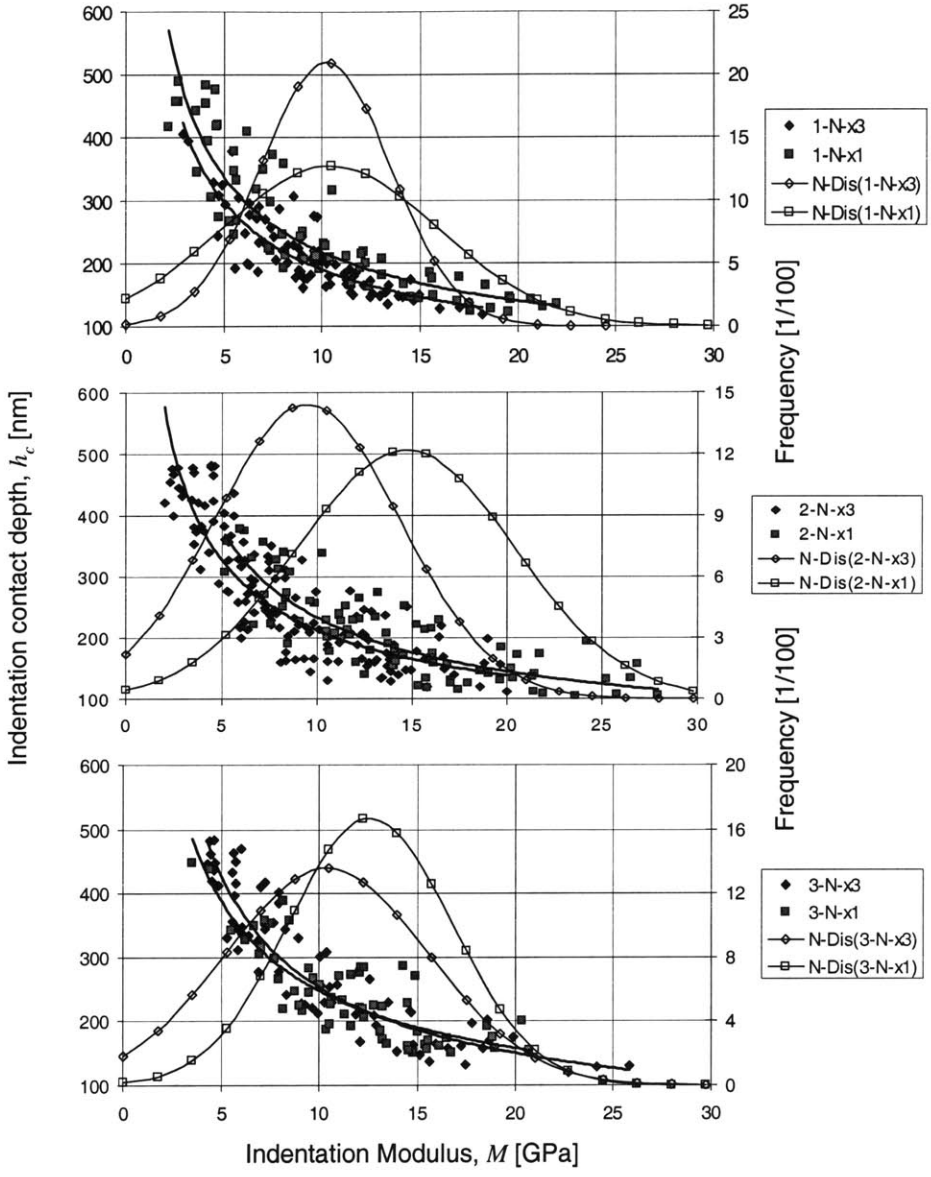

Figure 5-4: Nanoindentation stiffness scaling relation.

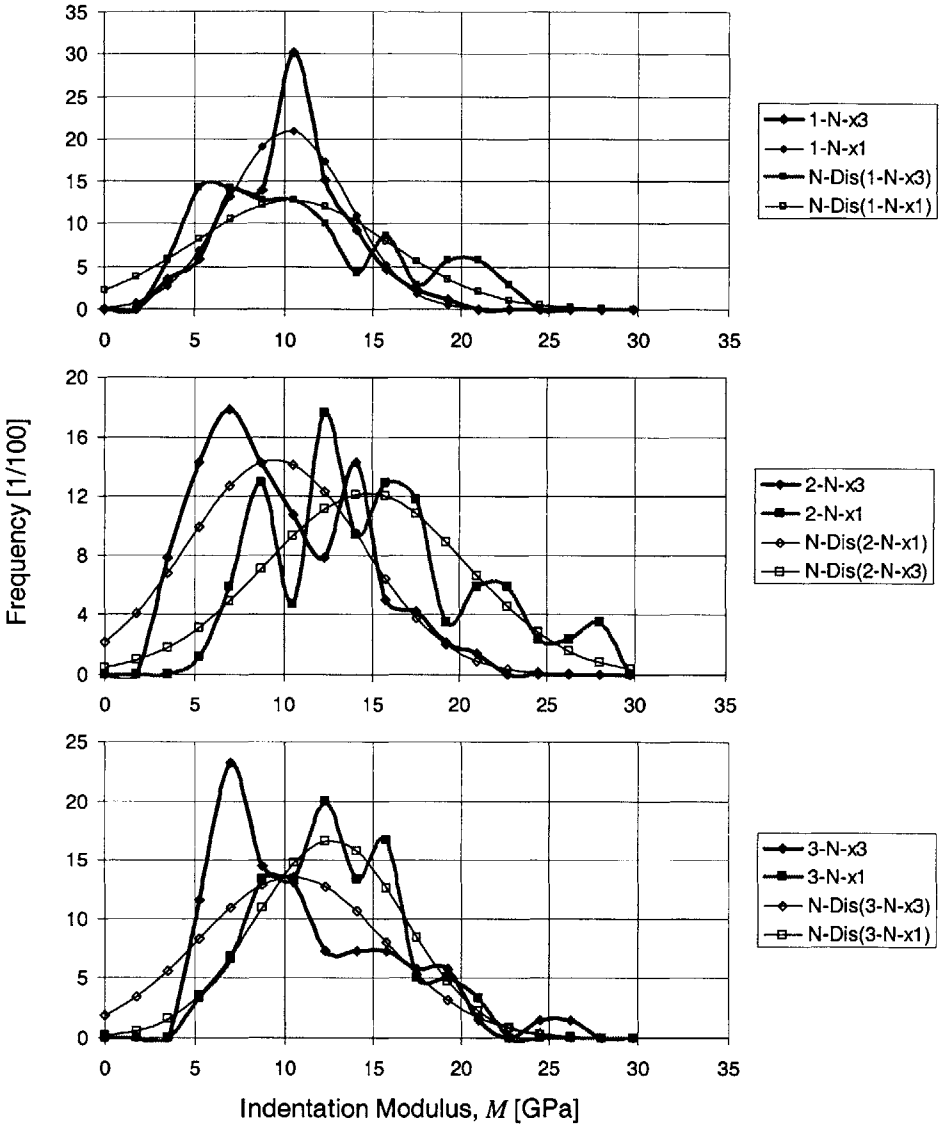

Figure 5-5: Nanoindentation stiffness frequency distribution.

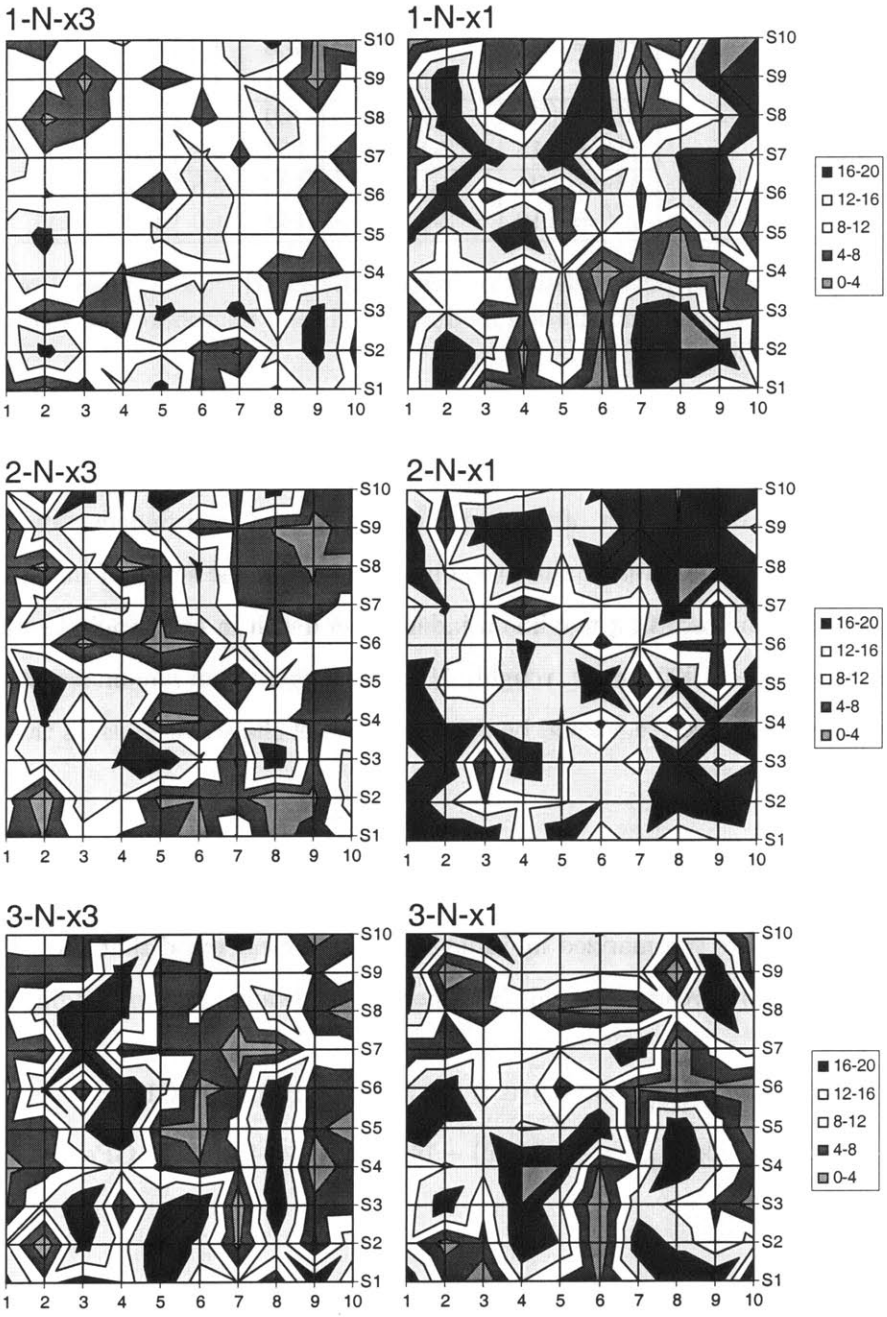

Figure 5-6: Nanoindentation stiffness maps.

Shale #	Scale (Level)	Name #–N/M–dir	M [GPa] μ	σ	H [nm] μ	σ
1	Micro (II)	1-M-x3	6.9	2.5	0.30	0.16
	$\phi^{II} = 0.31$	1-M-x1	9.5	2.7	0.26	0.20
		1-M-x2	9.4	3.0	0.23	0.16
2	Micro (II)	2-M-x3	8.0	1.9	0.18	0.13
	$\phi^{II} = 0.18$	2-M-x1	15.0	2.8	0.31	0.19
3	Micro (II)	3-M-x3	10.1	2.5	0.18	0.14
	$\phi^{II} = 0.10$	3-M-x1	14.9	4.0	0.21	0.11

Table 5.4: Summary of microindentation results (Level II): mean values (mu) and standard deviations (sigma) of microindentation modulus M(II) and microhardness H(II) (phi(II) stands for the porosity at level II).

5.6 Indentations at the Micro-scale, Level 'II'.

A clear indication of the effect of texture is obtained from *micro*indentation. The maximum force is roughly 50 times greater than the one employed in the series of *nano*indentation tests (see Table 5.2). The resulting maximum indentation depth in the nanoindentation tests is on the order of $1,000 - 5,000\,\text{nm}$, *ie.* roughly 10 times greater than nanoindentation depths. The derived properties, therefore, should be representative of shale materials on the order of tens of micrometer.

5.6.1 Results

The results which are summarized in Table 5.4, show a clear trend that the stiffness decreases as a function of the porosity, and this both normal to bedding and in bedding direction:

$$M^{II}_{3,\text{exp}} = 6.9\,(6.4) - 8.0\,(8.0) - 10.1\,(9.9)\ \text{GPa} \tag{5.5a}$$

$$M^{II}_{1,\text{exp}} = 9.5\,(9.6) - 14.2\,(15.3) - 14.9\,(16.2)\ \text{GPa} \tag{5.5b}$$

5.6.2 Preliminary Analysis

In contrast to the nanoindentation results, there is a clear separation of the microindentation stiffness scaling relation (Figure 5-7) between normal-to-bedding and in-bedding direction. Indeed, for the same indentation modulus value, the corresponding depth and hardness in two

different directions are not the same: the indented materials are different. This result is indicative that the material volume that is sensed (with microindentation depths of 1,000 to 5,000 nm) is anisotropic and that its weak and stiff axes coincide with the indentation direction. The frequency plots in Fig. 5-8 confirm this observation, and display a dominating one-peak distribution of the stiffness present in the microstructure, with a clear distinction in between normal to bedding and in bedding directions. The peak values (which are given in parenthesis in Eq (5.5a) and (5.5b) are characteristic of the porous clay matrix at level II. They display a strong anisotropic ratio:

$$\frac{M^{II}_{1,\text{exp}}}{M^{II}_{3,\text{exp}}} = 1.5 - 1.9 - 1.6 \tag{5.6}$$

A comparison of (5.4) and (5.6) shows the added anisotropy due to the layered structure visible on Fig. 4-8, which strongly exceeds the anisotropy present at smaller scales. This anisotropy is also visible in the indentation moduli maps in Fig. 5-9 that show, except for some inclusions, strong spatial continuity of properties at the considered scale defined by the grid step size of $50\mu m$.

5.7 Shale Acoustics at the Macro-scale, Level 'III'

At the macroscopic scale, shales are composed of a fluid-saturated porous clay matrix with silt inclusions. This scale has been extensively investigated in the shale acoustics and exploration geophysics community, by means of compressional and shear wave velocity measurements [9], [49], [53], [72], [83]. It is interesting to compare the elastic properties of shales at the macroscopic scale with the indentation results and the reported values of clay mineral stiffness.

5.7.1 Shale Acoustic Anisotropy

Shale anisotropy is an issue for the interpretation of ultrasonic velocities and amplitude *vs.* offset (AVO) seismic measurements. Probably because of the difficulties encountered in deep sediment extractions, only a few experimental results of shale elastic anisotropy have been reported in the literature [49], [83], [93]. Laboratory tests generally measure ultrasonic velocities of compressive and shear waves in respectively 3 and 2 different directions. The typical wave length employed in laboratory ultrasonic pulse velocity (UPV) studies operated at frequencies

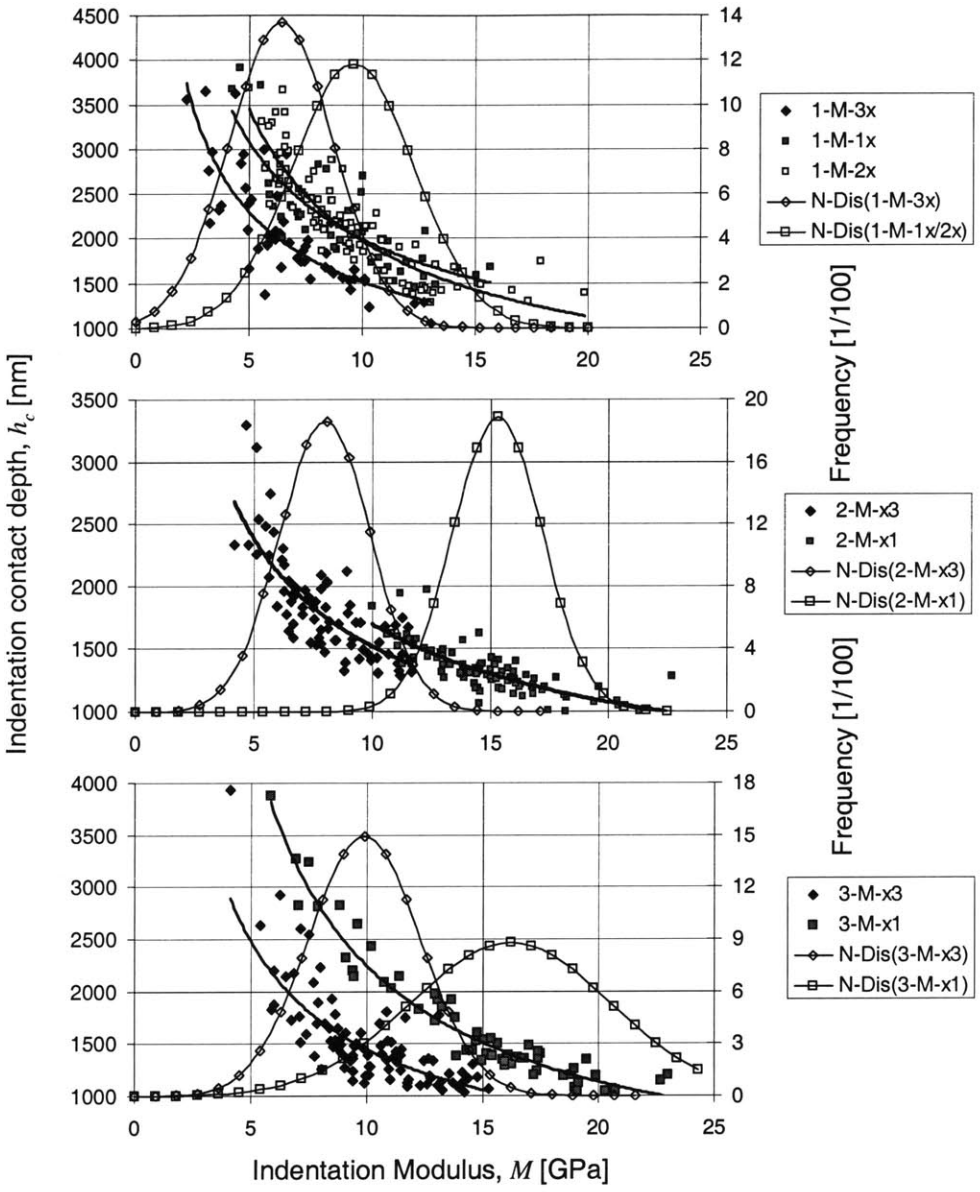

Figure 5-7: Microindentation scaling relation.

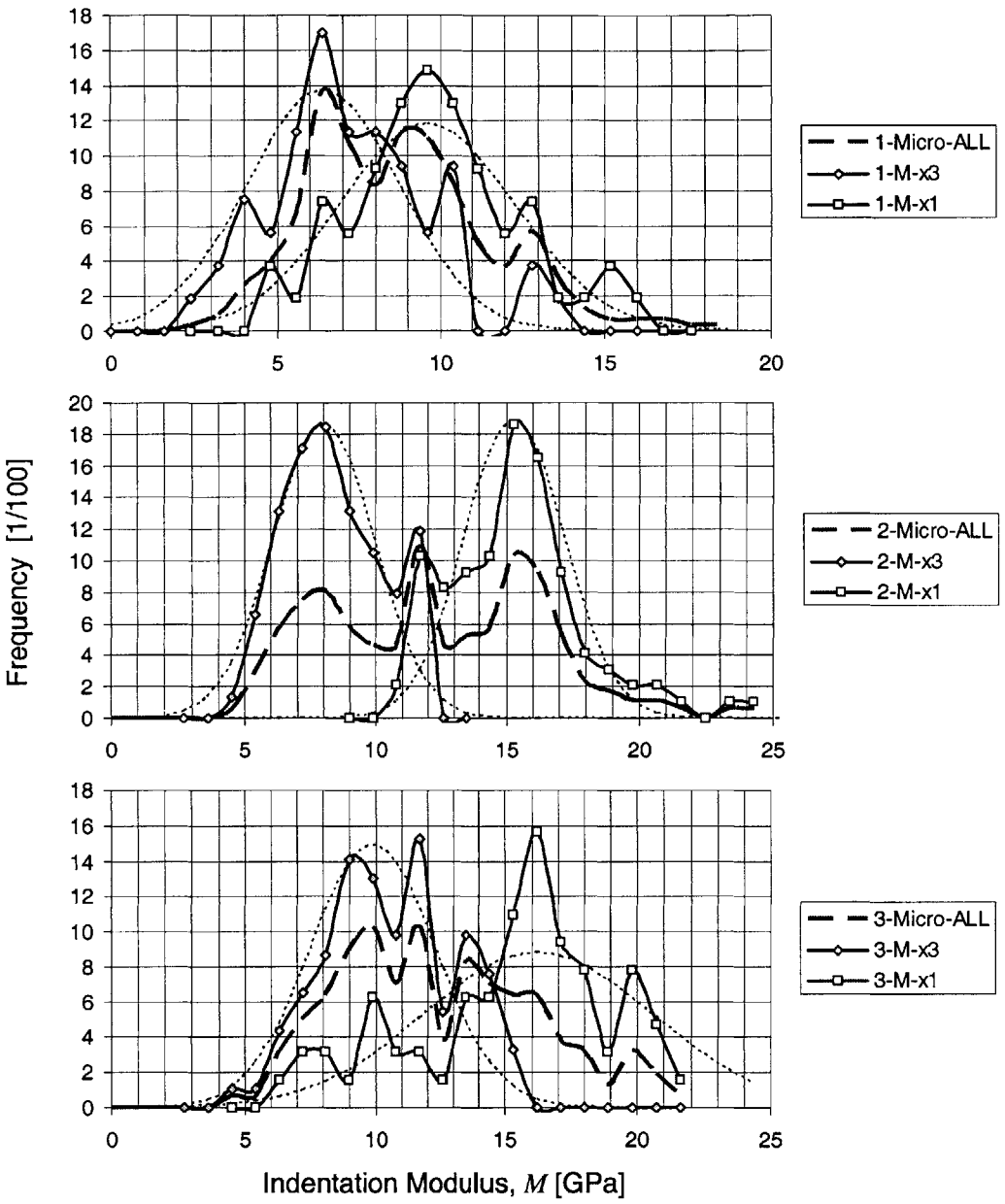

Figure 5-8: Microindentation frequency plot.

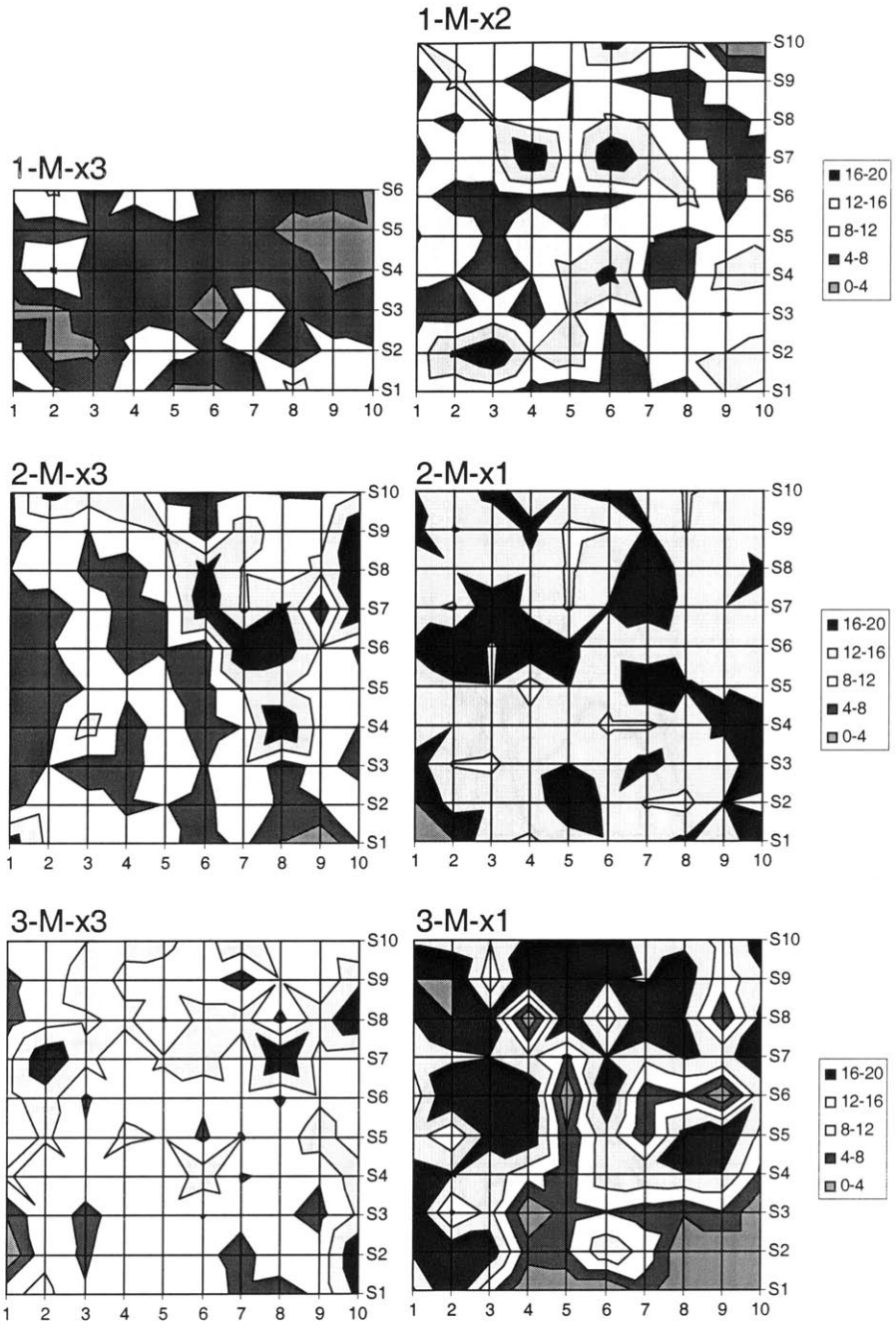

Figure 5-9: Microindentation moduli maps (Grid size=50μm), showing some clear trends towards continuity of material phases at level II.

in the MHz range, is in the millimeter range, which captures well the composite stiffness of the macroscopic clay-quartz inclusion composite [97], [24]. This is also the case for seismic waves. Finally, the frequency applied in UPV tests is by far sufficiently high to ensure that the fluids do not leave the pores [23]. This condition was checked using the values of permeability of the three shales provided by ChevronTexaco. For transverse isotropic solids (Feodorov, 1968 [37]), the expression of the wave velocities as a function of the macroscopic undrained stiffness coefficients read:

$$\begin{aligned} C_{11} &= \rho_m v_1^2 \\ C_{33} &= \rho_m v_3^2 \\ C_{66} &= \rho_m v_{12}^2 \\ C_{44} &= \rho_m v_{13}^2 \end{aligned} \tag{5.7}$$

where ρ_m stands for the density of the fluid saturated shale at the macroscopic scale. v_1 and v_3 are the longitudinal wave velocities in directions $x1$ and $x3$ respectively, and v_{12} and v_{13} are the transverse wave velocities in the direction $x1$, with particle motion in the directions $x2$ and $x3$, respectively. The problem is to assess the last stiffness coefficient C_{13} (C_{12} is given by $C_{12} = C_{11} - 2C_{66}$, see Section 1.7). This can be done by sending a longitudinal wave oriented at 45° with direction $x1$. But in this case the inversion method to access C_{13} is very complex and not accurate [49].

Wang [93] recently proposed a simple standardized experimental procedure. Wang also reported values of velocities and porosity for many shales, but did not examine the influence of inclusion volume fractions. Thomsen (1986) [83] introduced several parameters to give a measure of anisotropy that are commonly used in the geophysics community:

$$\varepsilon = \frac{C_{11} - C_{33}}{2C_{33}} \tag{5.8}$$

$$\gamma = \frac{C_{66} - C_{44}}{2C_{44}} \tag{5.9}$$

$$\delta = \frac{1}{2C_{33}^2}\left[2(C_{13} + 2C_{44})^2 - (C_{33} - C_{44})(C_{11} + C_{33} - 2C_{44})\right] \tag{5.10}$$

ε and γ are measures of the anisotropy respectively for longitudinal and transverse waves, while

Sh. #	Scale (Level)	Name #–N/M–dir	C_{11} [GPa]	C_{12} [GPa]	C_{13} [GPa]	C_{33} [GPa]	C_{44} [GPa]	M [GPa]
1	(III)	1-UPV-x3	20	N.A.	N.A.	13	N.A.	10.9
		1-UPV-x1						14.7
2	(III)	2-UPV-x3	34	N.A.	N.A.	20	N.A.	13.8
		2-UPV-x1						22.9
3	(III)	3-UPV-x3	46	N.A.	N.A.	30	N.A.	21.0
		3-UPV-x1						31.7

Table 5.5: Summary of UPV-measurements. The tests were carried out under different confining pressures, but little influence of the confining pressure on the stiffness values was found. (phi(III) stands for the porosity at level III, that is the porosity of the shale cuttings).

the more complex δ-parameter influences the shape of the reflected waves. The indentation measurements cannot give access directly to these three anisotropic coefficients, because the 5 stiffness coefficients cannot be identified individually from only two stiffness values $M^{III}_{1,\text{exp}}, M^{III}_{3,\text{exp}}$.

5.7.2 Results

Table 5.5 provides some of the C_{ijkl} values (C_{11} and C_{33}) and the equivalent indentation moduli derived from UPV measurements of the three shale materials. It should be noted that UPV-measurements carried out on saturated shale materials are undrained stiffness values, which may explain some hydraulic stiffening effects, in addition to stiffening induced by the presence of mainly quartz inclusions. For pure purpose of comparison, we calculate the anisotropy ratio:

$$\frac{M^{III}_{1,\text{exp}}}{M^{III}_{3,\text{exp}}} = 1.4 - 1.7 - 1.5 \tag{5.11}$$

These values correlate very well with the microindentation anisotropies (5.6). This means that the shale anisotropy that is sensed at level 'II' is representative of the overall macroscopic shale anisotropy. The fact that the anisotropy of the macroscopic composite is slightly smaller than the one of the textured clay composite (level II; (5.6)) is not surprising: mixing (more-or-less) isotropic inclusions into an anisotropic material system reduces the anisotropy.

The second key information from Table 5.5 comes from the overall stiffness values. Stiffness from the UPV measurement is much higher than the indentation moduli at Level 'II' for shales 1, 2 and especially for 3. This can be explained by the effect of inclusions, and hydraulic

stiffening effects. But we need a model that predicts this difference quantitatively.

5.8 Conclusions

The results of nanoindentations provide strong evidence that shales at level 'I' are composed of one single elementary brick of clay flakes and pores, that is encountered in various orientations in both normal to bedding and in bedding directions. Since the weak and stiff directions change with each test regardless of the indentation direction, the resulting average anisotropy calculated in (5.4) has no direct mechanical signification.

The same 'basic building blocks' are felt in Level 'II' indentations, but already within their microstructure: the weak and stiff axes in each indented region are now governed by the spatial distribution of the bricks, aligned with bedding and indentation directions. The measure of anisotropy defined in (5.6) corresponds to a real mechanical domain. The morphology of shales that appears at level 'II' seems to have a mechanical trace: the anisotropy increases, while the overall stiffness is on the same order as is Level 'I' indentations.

With this complete experimental base, and the tools of indentation analysis developed in the previous part, we are now able to build a multiscale micromechanical model of shales.

Part IV

Microporomechanics Shale Materials

Chapter 6

Multiscale Microporoelastic Model

The forth part of this report is devoted to the development of an original micromechanical model for shales. The motivation for a micromechanical model of shales naturally arises from the fact that the stiffness estimated at the micron scale has no reason to be the same as the macroscopic one.

The main objective of the model development is to analyze the experimental elastic properties of shales presented in Chapter 5 by means of a microporomechanics approach, capable of providing all stiffness coefficients of shales at different scales. In other words, the sought model has to be completely determined from a few indentation moduli, while sufficiently representative of reality. This chapter is devoted to the construction of the model, the next chapter details the model calibration for the three shales investigated in this study, and the model validation, by comparing the predicted stiffness of these three shales at the macro scale with experimental results. Finally, the third chapter of this part examines the predictive capabilities of the model for other shales and refines the model for engineering practice.

6.1 Sources of Anisotropy Representation

As an experimental base, we have six experimental indentation stiffness values for each shale material: $M^I_{1,\text{exp}}, M^I_{3,\text{exp}}, M^{II}_{1,\text{exp}}, M^{II}_{3,\text{exp}}, M^{III}_{1,\text{exp}}, M^{III}_{3,\text{exp}}$ (see Tables (5.3) and (5.4)). Using (3.35) and (3.50), each of these indentation stiffness values provide a snapshot of the elasticity of the stiffness values $C^J_{1111}, C^J_{3333}, C^J_{1122}, C^J_{1133}, C^J_{2323}$ (or $C^J_{11}, C^J_{33}, C^J_{12}, C^J_{13}, C^J_{44}$) at each considered

scale $J = I, II, III$. Since there is *a priori* no reason that the five elasticity constants at different scales should coincide, there is a total of 6 knowns for a total of 15 unknowns. This imbalance highlights the necessity for a micromechanics approach, requiring at each scale three further information to complete the stiffness characterization, which cannot rely on an empirical choice only. The first task of the model construction, therefore, consists in translating the four-level multiscale microstructure of shales (Fig. 4-10) into equations by means of the tools of continuum microporomechanics. This micromechanics model aims at answering the following questions:

6.1.1 Level '0': Clay Minerals

What is the impact of the intrinsic anisotropy of clay minerals on the anisotropy of the elementary building blocks ?

The load bearing phase of shales is essentially a colloidal system of clay particles, in which repulsive forces are in equilibrium with cohesive bonds. Since the stiffness values of clay minerals (Table 5.1) are (at least) one order of magnitude greater than the nanoindentation stiffness values (Table 5.3), it is most likely that the elastic deformation in the porous clay phase originate from the deformation of the pore space. In this case, it is not the mineral elasticity itself, but rather the contact regions in between minerals, *ie.* the inter-mineral porosity, that governs the elasticity. In fact, deformation in the crystalline structure vis-à-vis deformation at the interface between clay particles involves much higher forces, energies and stiffness (see Section 5.2). The simplest continuous representation of such a discrete material system comes to replace a discrete assembly of grains by a continuous solid phase intermixed with some porosity (Fig. 6-1, top). This assumption (and it is one!) provides a convenient way to localize the total elastic deformation in a conceptual continuous pure clay phase, whereas it physically occurs both in very stiff clay flakes and in the contact regions between them.

The two possible sources of anisotropy are then the anisotropy of the solid phase and the pore morphology. Given the trend that clay minerals appear in packages, forming the surrounding solid of the porosity (see Section 4.3.1), it is convenient to attribute the entire anisotropy at the scale of the elementary building block of shale materials, to the pore morphology by assuming the pure clay phase isotropic. This reduces the number of unknowns to three: two

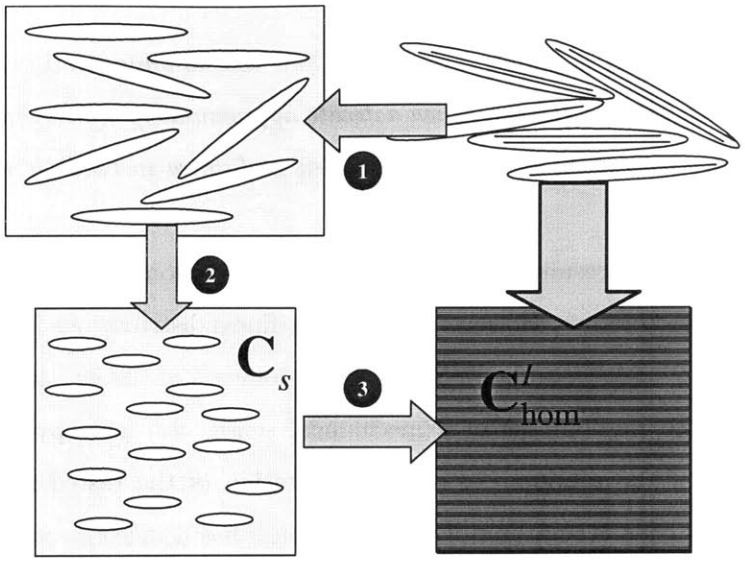

Figure 6-1: Level '0' model assumptions: Three steps to model the shale elementary building block: (1) replace a discrete system by a continuous system composed of an isotropic matrix and inter-particle porosity; (2) simplify the porosity morphology; (3) resulting (micro)homogeneous continuum.

elastic constants and the pore aspect ratio. More specifically, the shape of clay particles can be approximated by flat ellipsoids. We will assume that the pores have the same morphology, an oblate spheroid of varying aspect ratio $\rho = h/D$, where h is the thickness and D the diameter of the pore (Figure 6-1, bottom left). A similar representation of the elementary building block has been employed by Hornby *et al.* (1994) [48], who chose a unique value for the pore aspect ratio, 1/20, equivalent to the one of clay particles. The pore aspect ratio depends more generally on other parameters as well, like pore pressure and depth [50]. Moreover, if we consider that the pores are the sole source of the shale anisotropy at level '0' defined by a unique value of ρ, one should expect a significant decrease in macroscopic anisotropy with decreasing porosity, other parameters being equal. The pore aspect ratio ρ, therefore, is one key variable to capture the anisotropy of different shale materials.

6.1.2 Level 'I': Shale Building Block

If the shale building block is clearly anisotropic, how did nanoindentation operated to nanoindentation depths of 100 and 400 nm which activate approximately a bulk comparable to the shale building block, give very close average values when performed in bedding or normal to bedding planes?

The nanoindentation results show a fair amount of randomness of the distribution of the stiffness in the microstructure. However, since the stiffness distributions in different indentation directions do not coincide (see Figure 5-4), the randomness of the extracted properties should not be attributed to randomness in a mechanical sense, *ie.* isotropy. Instead, it appears as a consequence of the randomness of the orientation of the tested shale building blocks. For instance, if the pore orientation of building blocks has a uniform orientation distribution, then the statistical average of individual stiffness values would be the same for in-bedding and normal-to-bedding indentations, although the stiffness distribution in each indentation direction contains a large range of values (Fig. 6-2). The highest (resp. lowest) expected stiffness is obtained when the pore normal direction is perpendicular (resp. parallel) to the axis of indentation. Any difference in between the two averages can be explained by a non-uniform orientation distribution function (ODF) of pores, flakes or shale building blocks. This non-uniform orientation distribution is a third model parameter capturing the disorder of shale materials at level I.

6.1.3 Level 'II': Porous Textured Matrix

How does the pore morphology from the building block translates into the pronounced anisotropy of the layered shale structure?

The microindentation results display a (more-or-less) clear one-peak distribution, so that values obtained at this scale can be associated with averages in a mechanical homogenization sense, averaging stiffness values of shale building blocks over a large volume. At this scale, the anisotropy increases for all shales which suggests that an additional morphological feature appears. Porosity, pore shape and orientation distribution functions are already determining the anisotropy at scales below. The only possible reason for additional anisotropy is a particular spatial distribution of shale building blocks. From SEM pictures at that scale (Fig. 4-8),

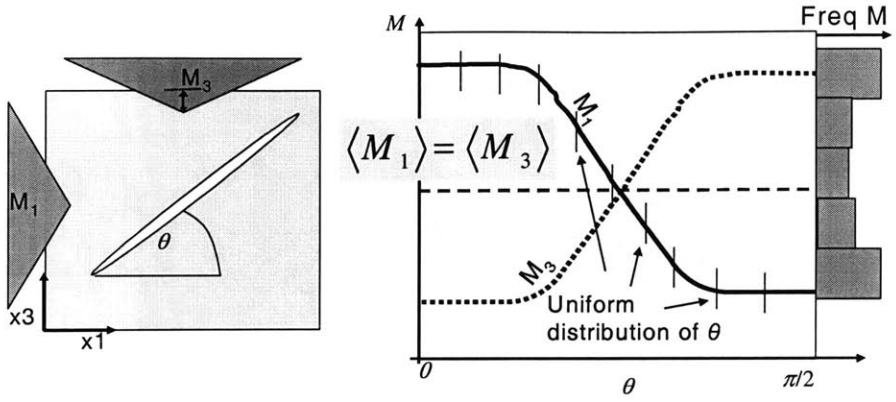

Figure 6-2: Level 'I' model assumptions: Nanoindentation on an elementary shale building block: The indentation stiffness depends on the orientation of the pores, within each building block. In the case of a uniform distribution of the pore orientation, the average indentation modulus obtained by grid indentation does not depend on the surface orientation. The stiffness frequency exhibits a two-peak distribution.

the orientation of the flakes is locally variable, but some wavy separation lines in the bedding directions indicate a clear privileged direction. This structure can be translated in a schematic laminate of shale building blocks oriented in the bedding directions, where each layer corresponds to one particular orientation of building blocks, as Figure 6-3 shows. Similar to a brick wall composed of bricks and joints, such a representation suggests that horizontal pores (joints) are connected whereas vertical ones are interrupted, so that the pronounced anisotropy of shales at larger scales appears as a consequence of the connectivity of pores, with lower stiffness values in the direction normal to bedding (axis $x3$) than in-bedding (axis $x1$ and $x2$).

The suggested microporomechanics representation of shale materials is no-doubt reductionist, reducing the complexity of shales to an isotropic pure clay phase, an oriented pore space and an orientation distribution function. The model has a total of four model parameters, if we exclude the two volume fractions, porosity and inclusion, which are generally known from independent measurements (see Table 4.1). The porosity at level I and II is the same and equal to the clay porosity : $\phi^I = \phi^{II} = \phi_c$ (relation (4.2)). In return, the porosity at level III is related to the former by:

$$\phi_0^{III} = (1 - f_i)\phi_0^{II} \tag{6.1}$$

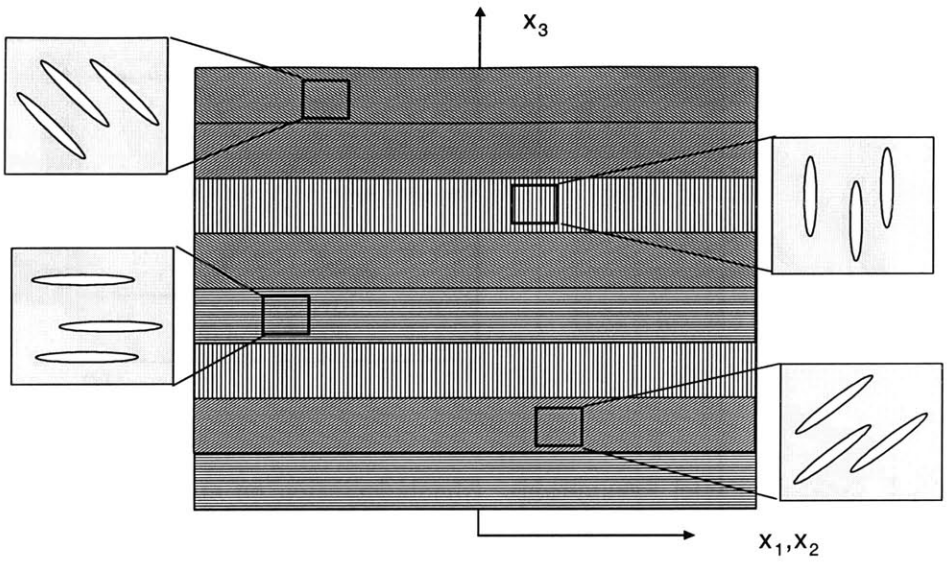

Figure 6-3: Level 'II' model assumption: Schematic porous laminate. Each layer is defined by a unique orientation of pores. The resulting laminate is aligned along the shale bedding planes.

where $f_i = f_{inc}$.

6.1.4 Summary of Model Assumptions

Figure 6-4 summarizes the model microstructure of shales that will serve as a base for the forthcoming upscaling relations. Level 'II' refers in our model to the textured clay porous matrix. In fact, inclusions appear roughly at the same scale (see Fig. 4-8). This contradiction is not an issue here, since the microindentation tests were filtered to exclude from the analysis the indentations on inclusions (see Section 5.4.2). Given this reduced number of model input parameters, we use the four indentation stiffness values $M^I_{1,\text{exp}}, M^I_{3,\text{exp}}, M^{II}_{1,\text{exp}}, M^{II}_{3,\text{exp}}$ as a first data set for a calibration of the model. Using the calibrated model parameters, we then predict the macroscopic stiffness, and compare these predictions with the stiffness values from a second independent data set obtained by UPV-measurements.

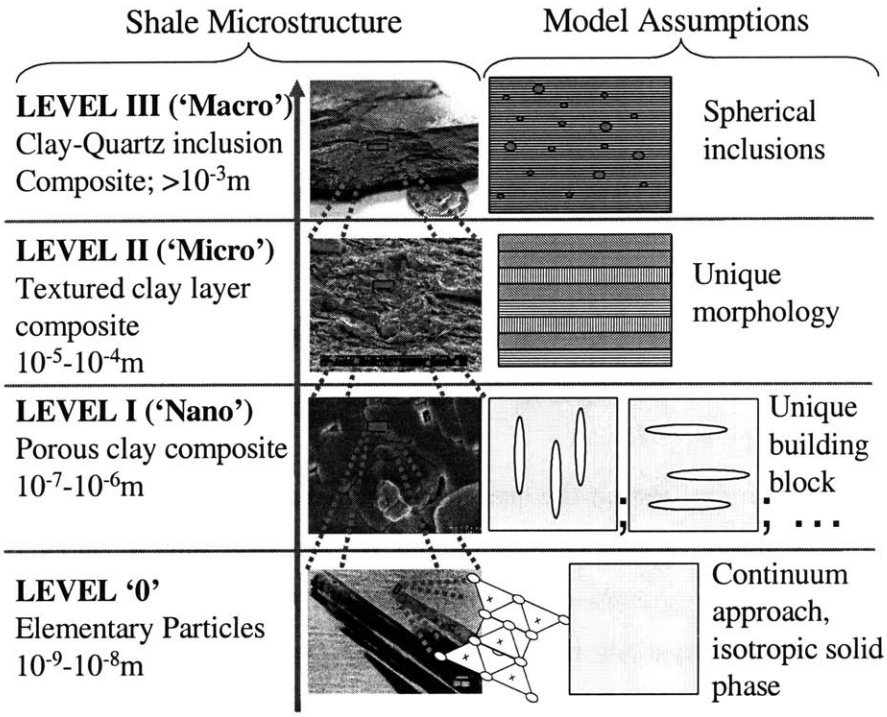

Figure 6-4: Summary of the assumptions of the proposed micromechanical model for shale materials.

6.2 Level 'I': Shale Building Block

The shale building block is composed of a solid phase and a saturated pore space. This morphology is captured by microporomechanics theory.

6.2.1 Micromechanics Approach of Porous Systems

The theory of micromechanics applied to porous systems, called microporomechanics, is now well established (Dormieux and coworkers [11], [29], [30]). It assumes that a porous medium, here the shale building bock, is composed of biconnected solid and pore spaces.

Constitutive Equations

From a macroscopic point of view, the classical relations of anisotropic poroelasticity apply [4], [24]:

$$\boldsymbol{\Sigma} = \mathbb{C}^I_{\text{hom}} : \mathbf{E} - \mathbf{b}^I p \tag{6.2a}$$

$$\phi - \phi_0 = \mathbf{b}^I : \mathbf{E} + \frac{p}{N^I} \tag{6.2b}$$

where superscript I indicates that the quantity is defined at level I: $\mathbb{C}^I_{\text{hom}}$ is the stiffness tensor, $\mathbf{b}^I$ the 2nd order tensor of Biot coefficients and N^I the solid Biot modulus. $\phi - \phi_0$ is the change of porosity where ϕ_0 is the clay porosity evaluated from (4.2), and p the fluid pressure. In the macroscopic poroelasticity theory, solids and fluids coexist at the same location. From a microscopic point of view, solid and fluid phases are dissociated. For a zero applied strain $\mathbf{E}$, $\mathbf{b}^I$ relates the fraction of pore pressure rise to a stress increase $\boldsymbol{\Delta\sigma} = -\mathbf{b}^I \Delta p$, while N^I translates it into a porosity change: $\phi - \phi_0 = p/N^I$. In this case, p and $\mathbf{E}$ are independent loading conditions to which the r.e.v. is subjected:

$$\underline{\boldsymbol{\xi}} = \mathbf{E} \cdot \underline{z} \quad (\partial\Omega) \tag{6.3}$$

$$\boldsymbol{\sigma} \cdot \underline{n} = -p\, \underline{n} \quad (\mathcal{I}^{sf}) \tag{6.4}$$

where $\partial\Omega$ is the external surface of the r.e.v., and $\mathcal{I}^{sf}$ the interface between solid and fluid phases.

Within the framework of microporomechanics theory, it is convenient to apply a continuous description of the microscopic stresses:

$$(\forall \underline{z} \in \Omega) \quad \boldsymbol{\sigma}(\underline{z}) = \mathbb{C}(\underline{z}) : \boldsymbol{\varepsilon}(\underline{z}) + \boldsymbol{\sigma}^p(\underline{z}) \tag{6.5}$$

where $\boldsymbol{\sigma}(\underline{z})$ and $\boldsymbol{\varepsilon}(\underline{z})$ stand for the local stress and strain tensors. $\mathbb{C}(\underline{z})$ and $\boldsymbol{\sigma}^p(\underline{z})$ are respectively the stiffness tensor and an eigenstress whose spatial distribution within the r.e.v. is given by:

$$\mathbb{C}(\underline{z}) = \begin{cases} 0 & (\Omega^p) \\ \mathbb{C}_s & (\Omega^s) \end{cases} \qquad \boldsymbol{\sigma}^p(\underline{z}) = \begin{cases} -p\mathbf{1} & (\Omega^p) \\ 0 & (\Omega^s) \end{cases} \tag{6.6}$$

where Ω^p and Ω^s stand for the domains occupied by pores and solids respectively, and $\mathbb{C}_s$ is the stiffness of the solid phase.

In order to make a link between $\mathbb{C}^I_{\text{hom}}, \mathbf{b}^I$ and N^I on the macroscopic side and quantities such as $\mathbb{C}_s$, ϕ_0 on the microscopic side, we consider two particular load cases. In the first one (denoted by $'$) the fluid pressure is zero, and the r.e.v. is loaded as a skeleton with empty pores. In the second load case (denoted by $''$) the fluid is pressurized under the strain boundary condition $\mathbf{E} = \mathbf{0}$.

First Load Case: $p = 0$

The first load case corresponds to a classical micromechanics problem in which a composite material composed of a solid and empty inclusions is subjected to a uniform boundary condition (6.3). In this case, following classical micromechanics (Zaoui [99]), the local strain $\boldsymbol{\varepsilon}'(\underline{z})$ is related to the macroscopic strain $\mathbf{E}$ by means of a forth order tensor $\mathbb{A}$, called strain concentration tensor:

$$\boldsymbol{\varepsilon}'(\underline{z}) = \mathbb{A}(\underline{z}) : \mathbf{E} \tag{6.7}$$

Since $\overline{\boldsymbol{\varepsilon}'(\underline{z})} = \mathbf{E}$ for compatibility between microscopic and macroscopic strain, this tensor satisfies the condition[1]:

[1] The average operators used in this sections are defined in Section 1.7.

$$\overline{\mathbb{A}(\underline{z})} = \mathbb{I} \tag{6.8}$$

Using (6.7) in (6.5) together with (6.6), the stress volume average $\boldsymbol{\Sigma}'$ in this load case reads:

$$\boldsymbol{\Sigma}' = \overline{\boldsymbol{\sigma}'(\underline{z})} = \overline{\mathbb{C}_s : \mathbb{A}(\underline{z})} : \mathbf{E} \tag{6.9}$$

and the change of porosity:

$$(\phi - \phi_0)' = \phi_0 \mathbf{1} : \langle \boldsymbol{\varepsilon}'(\underline{z}) \rangle_{\Omega^p} = \phi_0 \mathbf{1} : \langle \mathbb{A}(\underline{z}) \rangle_{\Omega^p} : \mathbf{E} \tag{6.10}$$

Finally, a comparison of (6.9) with (6.2a) and of (6.10) with (6.2b) allows to identify the homogenized stiffness tensor and the Biot coefficients:

$$\mathbb{C}^I_{\text{hom}} = \overline{\mathbb{C}_s : \mathbb{A}(\underline{z})} \tag{6.11}$$

$$\mathbf{b}^I = \phi_0 \, \mathbf{1} : \langle \mathbb{A} \rangle_{\Omega^p} \tag{6.12}$$

Second Load Case: $\mathbf{E} = \mathbf{0}$

In the second load case, the macroscopic state equations (6.2a) and (6.2b) read:

$$\boldsymbol{\Sigma}'' = \boldsymbol{\Sigma}^p = -\mathbf{b}^I \, p \tag{6.13}$$

$$\frac{p}{N^I} = (\phi - \phi_0)'' \tag{6.14}$$

From a micromechanics point of view, the second subproblem corresponds to a micro-to-macro eigenstress problem. This problem is conveniently solved using Levine's theorem:

$$\boldsymbol{\Sigma}^p = \overline{\boldsymbol{\sigma}^p(\underline{z}) : \mathbb{A}(\underline{z})} \tag{6.15}$$

Using (6.6) in (6.15), and combining this result with (6.13), we obtain:

$$\boldsymbol{\Sigma}'' = \boldsymbol{\Sigma}^p = -\mathbf{b}^I \, p \equiv -\phi_0 \, \mathbf{1} : \langle \mathbb{A} \rangle_{\Omega^p} \, p \tag{6.16}$$

A straightforward comparison of Eq. (6.16) with (6.12) shows that the Levine theorem provides a second means to determine the Biot coefficient tensor.

Furthermore, The porosity change in this subproblem is given by:

$$(\phi - \phi_0)'' = \phi_0 \mathbf{1} : \ \left\langle \boldsymbol{\varepsilon}''(\underline{z}) \right\rangle_{\Omega^p} \tag{6.17}$$

If we use in (6.17) the compatibility condition and Hooke's law, we obtain:

$$(\phi - \phi_0)'' = (1 - \phi_0)\mathbf{1} : \left(- \left\langle \boldsymbol{\varepsilon}''(\underline{z}) \right\rangle_{\Omega^s} \right) = -(1 - \phi_0)\mathbf{1} : \mathbb{C}_s^{-1} : \left\langle \boldsymbol{\sigma}''(\underline{z}) \right\rangle_{\Omega^s} \tag{6.18}$$

Moreover, the stress average reads (6.5):

$$\boldsymbol{\Sigma}'' = \overline{\boldsymbol{\sigma}''(\underline{z})} = (1 - \phi_0) \left\langle \boldsymbol{\sigma}''(\underline{z}) \right\rangle_{\Omega^s} - \phi_0 p \mathbf{1} \tag{6.19}$$

Finally, using (6.16) in (6.19), and substituting this result in (6.18), the porosity change in the subproblem reads:

$$(\phi - \phi_0)'' = -\mathbf{1} : \mathbb{C}_s^{-1} : (\phi_0 \mathbf{1} - \phi_0 \mathbf{1} : \langle \mathbb{A} \rangle_{\Omega^p}) \, p \tag{6.20}$$

Last, from a comparison of (6.20) with (6.2b), the solid Biot modulus is is obtained by:

$$\frac{1}{N^I} = \phi_0 \mathbf{1} : \mathbb{C}_s^{-1} : \mathbf{1} : (\langle \mathbb{A} \rangle_{\Omega^p} - \mathbb{I}) \tag{6.21}$$

$$= \mathbf{1} : \mathbb{C}_s^{-1} : \left(\mathbf{b}^I - \phi_0 \mathbf{1} \right) \tag{6.22}$$

Equations (6.11), (6.12) and (6.21) give the expression of the homogenized material poroelastic properties as a function of stiffness of the solid and the strain concentration tensor $\mathbb{A}(\underline{z})$. These coefficients describe the general poroelastic deformation at level 'I'. These are the two input parameters required to complete the homogenization at Level I.

6.2.2 Homogenization Schemes

In our case, $\mathbb{C}_s$ is the stiffness tensor of the (assumed) isotropic clay solid (bulk modulus k_s, shear modulus g_s):

$$\mathbb{C}_s = 3k_s \mathbb{J} + 2g_s \mathbb{K} \tag{6.23}$$

where J_{ijkl}=1/3 ($\delta_{ij}\delta_{kl}$) and $\mathbb{K} = \mathbb{I} - \mathbb{J}$ are the spherical and deviatoric projections of the forth order identity tensor $I_{ijkl} = \frac{1}{2}(\delta_{ik}\delta_{jl} + \delta_{il}\delta_{jk})$, and δ_{ij} is the Kronecker delta.

The forth-order strain localization tensor $\mathbb{A}(\underline{z})$ depends on the microstructure. In general, $\mathbb{A}(\underline{z})$ cannot be assessed analytically. However, a good estimate of $\mathbb{A}(\underline{z})$ can be obtained by exploiting the dominant features of the composite microstructure.

Eshelby's Inclusion Problem

An analytical expression of the strain concentration tensor $\mathbb{A}$ can be obtained in the particularly simple case of a composite consisting of one ellispsoidal inclusion perfectly bonded to an infinite isotropic matrix, subjected to uniform strains $\mathbf{E}^0$ at infinity. In this case, Eshelby (1957) [34] showed that the strains in the inclusion are uniform and read:

$$\boldsymbol{\varepsilon}_p = \left[\mathbb{I} + \mathbb{P}_p^0 : (\mathbb{C}_p - \mathbb{C}^0)\right]^{-1} : \mathbf{E}^0 \tag{6.24}$$

where $\mathbb{C}_p$ is the stiffness of the inclusion, and $\mathbb{C}^0$ the one of the matrix. The tensor $\mathbb{P}_p^0$ depends on the shape of the inclusion, and on the stiffness properties of the matrix, and can be obtained from the matrix Green's function G^0:

$$P^0_{p,ijkl} = -\left(\partial^2 \left(\int_V G^0_{ik}(\underline{z} - \underline{z}')dV\right)/\partial x_j \partial x_l\right)_{(ij)(kl)} \tag{6.25}$$

where $(ij)(kl)$ stands for the symmetrization with respect to (ij) and (kl). The Green's function $G^0_{ik}(\underline{z} - \underline{z}')$ expresses the displacement at point $\underline{z}$ in the direction i in a linear elastic solid of stiffness $\mathbb{C}^0$ subjected to a unit force $\delta(\underline{z} - \underline{z}')$ applied in direction k at point $\underline{z}'$. $\delta(\underline{z} - \underline{z}')$ is such that $\delta(0) = \infty$, $\delta(\underline{z} \neq \underline{z}') = 0$ and $\int_V \delta(\underline{z} - \underline{z}')dV(\underline{z}) = 1$. The analytical expressions of tensor $\mathbb{P}_p^0$ and the Eshelby tensor are defined by:

$$\mathbb{S}_p^0 = \mathbb{P}_p^0 : \mathbb{C}^{0,-1} \tag{6.26}$$

where $\mathbb{C}^{0,-1}$ is the inverse of the matrix stiffness tensor. The expressions of $\mathbb{P}_p^0$ and $\mathbb{S}_p^0$ for oblate spheroids ($h < D$) in an isotropic matrix are given in Appendix E (see Eshelby, 1957 [34], and Mura, 1987 [62]).

The case of an inclusion in an infinite matrix can be extended in several manners to real composites, first by playing with the shape of the ellipsoid. For instance, cylindrical or here penny-shaped inclusions can be used to model cylinders or cracks; second, by assigning an arbitrary stiffness $\mathbb{C}^0$ to the heterogeneous environment of an inclusion, different homogenization schemes are obtained. Finally, the strain $\mathbf{E}^0$ "seen" locally by the inclusion may be different from the overall boundary condition $\mathbf{E}$.

Dilute Scheme

For a composite containing very few non interacting inclusions denoted by $r > 1$ in a matrix of stiffness $\mathbb{C}^1$, the strains inside the inclusions are directly given by (6.24), where $\mathbf{E}^0$ coincides with the uniform strain $\mathbf{E}$ applied at the boundary of the r.e.v. (*ie.* relation (6.3)). This dilute estimate of the strain concentration tensor $\mathbb{A}_r^{dil}$ in the inclusions in obtained from (6.7) in the form:

$$\mathbb{A}_r^{dil} = \left[\mathbb{I} + \mathbb{P}_r^1 : (\mathbb{C}_r - \mathbb{C}^1)\right]^{-1} \tag{6.27}$$

In the matrix, $\mathbb{A}_1^{dil}$ is obtained from the compatibility relation (6.8) in the form:

$$\mathbb{A}_1^{dil} = \mathbb{I} - \sum_{r>1} f_r \left[\mathbb{I} + \mathbb{P}_r^1 : (\mathbb{C}_r - \mathbb{C}^1)\right]^{-1} \tag{6.28}$$

Finally, the corresponding dilute homogenized stiffness is obtained from (6.11), (6.27), and (6.28):

$$\mathbb{C}^{dil} = \sum_{r>1} f_r \mathbb{C}_r : \mathbb{A}_r^{dil} + (1 - \sum_{r>1} f_r)\mathbb{C}^1 : \mathbb{A}_1^{dil} \tag{6.29}$$

Interactions Between Phases

The analytical dilute case can be extended to a real multiphase composite: the strain in each phase r is assumed to be the one in an inclusion of stiffness $\mathbb{C}_r$ embedded in a fictitious matrix of stiffness $\mathbb{C}^0$, subjected to a uniform strain $\mathbf{E}^0$:

$$\boldsymbol{\varepsilon}_r = \left[\mathbb{I} + \mathbb{P}_r^0 : (\mathbb{C}_r - \mathbb{C}^0)\right]^{-1} : \mathbf{E}^0 \tag{6.30}$$

The strain average combined with equation (6.30) yields the following expression of $\mathbf{E}^0$

$$\mathbf{E}^0 = \left\{ \sum_r f_r \left[\mathbb{I} + \mathbb{P}_r^0 : (\mathbb{C}_r - \mathbb{C}^0) \right]^{-1} \right\}^{-1} : \mathbf{E} \tag{6.31}$$

where $\mathbf{E}$ is the strain applied to the r.e.v.. From (6.7), (6.24) and (6.31), the estimated expression of the strain concentration tensor becomes:

$$\mathbb{A}_r^{est} = \left[\mathbb{I} + \mathbb{P}_r^0 : (\mathbb{C}_r - \mathbb{C}^0) \right]^{-1} : \left\{ \sum_s f_s \left[\mathbb{I} + \mathbb{P}_s^0 : (\mathbb{C}_s - \mathbb{C}^0) \right]^{-1} \right\}^{-1} \tag{6.32}$$

Substitution of Eq. (6.32) in (6.11) gives an estimate of the homogenized stiffness tensor $\mathbb{C}^{est}$:

$$\mathbb{C}^{est} = \sum_r f_r \mathbb{C}_r : \left[\mathbb{I} + \mathbb{P}_r^0 : (\mathbb{C}_r - \mathbb{C}^0) \right]^{-1} : \left\{ \sum_s f_s \left[\mathbb{I} + \mathbb{P}_s^0 : (\mathbb{C}_s - \mathbb{C}^0) \right]^{-1} \right\}^{-1} \tag{6.33}$$

Mori-Tanaka Scheme

In a matrix/inclusion morphology let index 1 correspond to the matrix, and $r > 1$ to the inclusion phases. If we replace the reference stiffness $\mathbb{C}^0$ by the stiffness of the matrix $\mathbb{C}_1$, we obtain an explicit expression of the homogenized stiffness tensor, called the Mori-Tanaka estimate [61]:

$$\mathbb{C}^{MT} = \sum_{r>1} f_r \mathbb{C}_r : \left[\mathbb{I} + \mathbb{P}_r^0 : (\mathbb{C}_r - \mathbb{C}_1) \right]^{-1} : \left\{ \sum_{s>1} f_s \left[\mathbb{I} + \mathbb{P}_s^0 : (\mathbb{C}_s - \mathbb{C}_1) \right]^{-1} \right\}^{-1} \tag{6.34}$$

Self-Consistent Scheme

For polycrystals where all phases play similar roles in the microstructure, the self consistent estimate uses as a reference stiffness $\mathbb{C}^0$, the unknown homogenized stiffness $\mathbb{C}^{SC}$. This results in an implicit equation for the homogenized stiffness

$$\mathbb{C}^{SC} = (1 - \phi^I)\mathbb{C}_c : \left[\mathbb{I} + \mathbb{P}_c^{SC} : (\mathbb{C}_c - \mathbb{C}^{SC}) \right]^{-1} : \left\langle \left[\mathbb{I} + \mathbb{P}_c^{SC} : (\mathbb{C}_c - \mathbb{C}^{SC}) \right]^{-1} \right\rangle^{-1} \tag{6.35}$$

The validity of this scheme was confirmed for polycrystals for which the phases volume fractions do not differ much from each other [99]. This is less likely to be the case of porous

clays.

Differential Effective Medium Theory

Finally, another way to treat the problem of interaction between inclusions, is the differential effective medium theory, which consists in using a dilute homogenization (6.29) iteratively by adding very small increments of inclusions in an already homogenized medium, until the total inclusion volume fractions reaches its target value. This scheme has no real physical explanation, except that it would consider an infinite number of homogenization steps, and thus inclusion sizes. It seems appreciated in rock mechanics and acoustics but is implicit, iterative, and becomes more complex to handle in the case of anisotropic materials [63], [48].

Choice for the Shale Elementary Building Block

In our case, we consider the pores as inclusions in a matrix. This morphology appears to us well captured by the Mori-Tanaka estimate:

$$\langle \mathbb{A}(\underline{z}) \rangle_{\Omega^s} \simeq \mathbb{A}_s^{est} = \left[(1-\phi^I)\mathbb{I} + \phi^I \left(\mathbb{I} - \mathbb{S}_\rho^s \right)^{-1} \right]^{-1} \tag{6.36}$$

$$\langle \mathbb{A}(\underline{z}) \rangle_{\Omega^p} \simeq \mathbb{A}_\phi^{est} = \left(\mathbb{I} - \mathbb{S}_\rho^s \right)^{-1} : \left[(1-\phi^I)\mathbb{I} + \phi^I \left(\mathbb{I} - \mathbb{S}_\rho^s \right)^{-1} \right]^{-1} \tag{6.37}$$

where $\mathbb{S}_\rho^s$ is the Eshelby tensor [34] that depends on the aspect ratio $\rho = h/D$ of the pores and the Poisson's ratio of the matrix (see Appendix E). Using the estimate (6.36) in (6.11) yields the homogenized stiffness of a transversely isotropic material in the principle material axis, defined by the pore plane that extends in the $x1' \times x2'$ plane, and whose normal is oriented in direction $x3'$. The tensor of Biot coefficients is a diagonal tensor having as components:

$$b_{ij} = \begin{bmatrix} b_{11} & 0 & 0 \\ & b_{11} & 0 \\ & & b_{33} \end{bmatrix} \tag{6.38}$$

where b_{11} and b_{33} represent the Biot coefficients in the horizontal and vertical direction in the shale building block. Using (6.37) in (6.12), we obtain:

$$b_{11} = \phi_0^I \left[A^{est}_{\phi,1111} + A^{est}_{\phi,1122} + A^{est}_{\phi,1133}\right] \tag{6.39a}$$

$$b_{33} = \phi_0^I \left[2A^{est}_{\phi,1133} + A^{est}_{\phi,3333}\right] \tag{6.39b}$$

6.2.3 Poroelastic Properties in Rotated Configurations

For the forthcoming statistical analysis of the nanoindentation results, it is convenient to express the homogenized stiffness of the shale building block in a coordinate system $(x1, x2, x3)$, in which the pore plane's normal orientation is defined by the Euler angles θ and φ (see Figure 6-5):

$$\underline{n} = \sin\theta\cos\varphi\,\underline{e}_1 + \sin\theta\sin\varphi\,\underline{e}_2 + \cos\theta\,\underline{e}_3 \tag{6.40}$$

$\theta = \varphi = 0$ corresponds to a pore plane oriented by the normal pointing in direction $x3$; and $\theta = \pi/2, \varphi = 0$ and $\theta = 0, \varphi = 0$ corresponds to pore planes oriented by a unit normal in direction $x1$ and $x2$, respectively. The relations between the second order strain and stress tensors in the reference and rotated configurations are given by:

$$\mathbf{E}_{\theta,\varphi} = \mathbf{R}(\theta,\varphi)\cdot\mathbf{E}_0\cdot\mathbf{R}(\theta,\varphi)^T \tag{6.41a}$$

$$\mathbf{\Sigma}_{\theta,\varphi} = \mathbf{R}(\theta,\varphi)\cdot\mathbf{\Sigma}_0\cdot\mathbf{R}(\theta,\varphi)^T \tag{6.41b}$$

where $\mathbf{R}(\theta,\varphi)$ is the rotation matrix:

$$R_{ij}(\theta,\varphi) = \begin{bmatrix} 1 & 0 & 0 \\ 0 & \cos(\theta) & -\sin(\theta) \\ 0 & \sin(\theta) & \cos(\theta) \end{bmatrix} \begin{bmatrix} \cos(\varphi) & -\sin(\varphi) & 0 \\ \sin(\varphi) & \cos(\varphi) & 0 \\ 0 & 0 & 1 \end{bmatrix} \tag{6.42}$$

Using (6.41) in (6.2a), the poroelastic constants read in the rotated configuration:

$$\mathbb{C}^I_{\text{hom}}(\theta,\varphi) = \mathbf{R}(\theta,\varphi)\cdot\mathbb{C}^I_{\text{hom}}(0,0)\cdot\mathbf{R}(\theta,\varphi)^T \tag{6.43a}$$

$$\mathbf{b}^I(\theta,\varphi) = \mathbf{R}(\theta,\varphi)\cdot\mathbf{b}^I(0,0)\cdot\mathbf{R}(\theta,\varphi)^T \tag{6.43b}$$

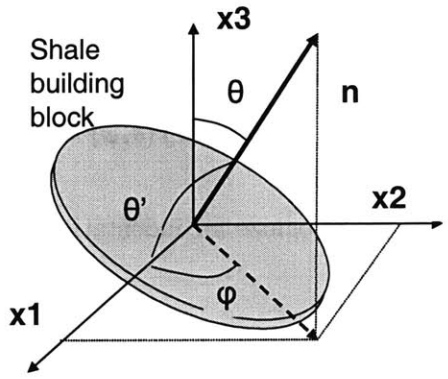

Figure 6-5: Orientation of a transverse isotropic shale elementary building block, defined by the direction of its axis of symmetry by means of the two Euler angles θ and φ in the cartesian system $Ox_1x_2x_3$.

6.3 Level 'I': Statistical Analysis

With the microporomechanics model in hand, we can now turn to analyzing the nanoindentation results. Following our discussion in Section 6.2.3, we consider that the mean nanoindentation results represent statistical averages of a representative sample of indentation tests on elementary building blocks present on a specific surface (Fig. 5-6). If all orientation are represented with equal probability, the statistical average of the indentation tests on this surface oriented in the $xJ-$direction tends to the limit:

$$\mu_{M_J} = \frac{1}{2\pi} \int_{\theta=0}^{\pi} \int_{\varphi=0}^{2\pi} M_J(\theta, \varphi) \sin\theta \, d\varphi \, d\theta \tag{6.44}$$

when the number of tests tends to infinity; where $M_J(\theta, \varphi)$ is the indentation modulus of a single indentation test on an elementary building block rotated by Euler angles θ and φ *w.r.t.* the indentation axis xJ. Assuming $M_J(\theta, \varphi)$ to be a continuous function, the indentation modulus has two extrema: a minimum for indentation normal to the pore plane, *ie.* $\underline{n} \cdot \underline{e}_J = 1$, and a

maximum for indentation in the pore plane, *ie.* $\underline{n} \cdot \underline{e}_J = 0$ (see also Fig. 6-2):

$$\forall \underline{n} \cdot \underline{e}_J = 1 \Rightarrow M_J(\theta, \varphi) = \min M \tag{6.45a}$$

$$\forall \underline{n} \cdot \underline{e}_J = 0 \Rightarrow M_J(\theta, \varphi) = \max M \tag{6.45b}$$

Combining (6.40) with (6.45), we recognize for indentation in bedding directions (axis $x1$ and $x2$) and normal to it (axis $x3$):

$$\begin{array}{lllll} \min M & = M_1(\pi/2, 0) & = M_2(\pi/2, \pi/2) & = M_3(0, \varphi) & \\ \max M & = M_1(0, \varphi) & = M_2(0, \varphi) & = M_3(\pi/2, \varphi) & \\ & = M_1(\theta, \pi/2) & = M_2(\theta, 0) & & \end{array} \tag{6.46}$$

The minimum value $\min M$ is strictly the indentation modulus for indentation in the symmetry axis of a transversely isotropic material, which is related to the elastic constants $\mathbb{C}_{\text{hom}}(0,0)$ through (3.35). Similarly, the maximum value $\max M$ is the indentation modulus for indentation in the plane of symmetry of a transversely isotropic material, which is related to $\mathbb{C}_{\text{hom}}(0,0)$ through (3.50). For any other orientation of the pore plane defined by $\cos\theta'(\theta, \varphi) = \underline{n} \cdot \underline{e}_J$ (Fig. 6-5), the link between the indentation modulus $M_J(\theta')$ and the elasticity of the building block $\mathbb{C}_{\text{hom}}(0,0)$ is estimated from a generalization of (3.50):

$$M_J(\theta') \simeq \frac{1}{\pi\sqrt{\mathcal{H}_K \mathcal{H}_L}} \tag{6.47}$$

satisfying:

$$M_J(\theta' = 0) = \min M \tag{6.48a}$$

$$M_J(\theta' = \pi/2) = \max M \tag{6.48b}$$

where $\mathcal{H}_K = \mathcal{H}(\theta' = 0)$ and $\mathcal{H}_L = (\theta' = \pi/2)$ are the extreme values of the Green's function angular part $\eta(\theta')$ given by (3.36)[2] and are represented schematically on Figure 6-6 by H_1

[2]This interpolation of the extreme values of the Green's function angular part $\eta(\theta')$ is justified by the fact that the half-space Green's function, π-periodic by definition, conserves its evenness, because of a material plane of symmetry.

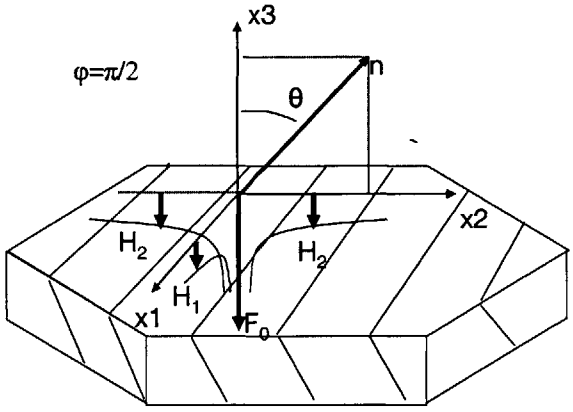

Figure 6-6: Schematic representation of the surface Green's function extreme profiles, when the axes of material symmetry and indentation (x_3) form any angle θ. Without loss of generality we consider that $\varphi = \pi/2$ to evaluate the extreme values of $\mathcal{H}$ in the $x_1$and x_2 directions, H_1 and H_2.

and H_2 respectively. However, in contrast to the explicit expressions (3.35) and (3.50), these extreme values need to be evaluated numerically for $\theta =]0, \pi/2[$.

Relation (6.47) gives the variation of indentation moduli as a function of the pore plane orientation $\cos\theta' = \underline{n} \cdot \underline{e}_J$ situated in between the two extrema, $\min M$ and $\max M$. Substitution of (6.47) in Eq. (6.44) comes to assume a uniform orientation distribution of building blocks (*ie.* pore orientations) on a specific surface. A refinement of the average (6.44) can be achieved by introducing a non-uniform orientation distribution function $W(\theta, \varphi)$:

$$\mu_{M_J} = \frac{1}{2\pi} \int_{\theta=0}^{\pi} \int_{\varphi=0}^{2\pi} M_J(\theta, \varphi)\, W(\theta, \varphi) \sin\theta \, d\varphi \, d\theta \tag{6.49}$$

This orientation distribution function needs to satisfy :

$$\frac{1}{2\pi} \int_{\theta=0}^{\pi} \int_{\varphi=0}^{2\pi} W(\theta, \varphi) \sin\theta \, d\varphi d\theta = 1 \tag{6.50}$$

For shale materials, orientation distribution functions were first introduced by Sayers [74], and have gained some popularity as an important tool to account for a non-uniform distribution of the orientation of clay particles, that can be determined experimentally (see e.g. [52]). We employ this concept here to account for a non-uniform orientation distribution of building

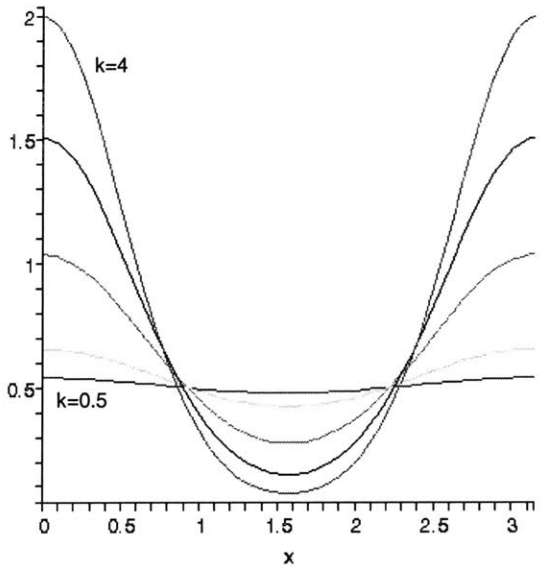

Figure 6-7: Gaussian-like orientation distribution function, for k=0.5, 1, 2, 3, 4.

blocks. We choose a π-periodic Gaussian like function:

$$W(\theta, k) = w_k \cosh(k \cos\theta)) \tag{6.51}$$

where $w_k = 2/k \cosh k$ is a normalization constant, and k a parameter referring to the degree of preferred alignment: $k = 0$ means an absence of any preferred alignment, and $k > 0$ induces a second source of anisotropy in the shale micromechanics model, as shown on Figure 6-7 plots.

The resulting statistical average (6.49) illustrated on Figure 6-8 depends on the elastic constants of the isotropic solid clay phase –bulk modulus k_s, shear modulus g_s (see (6.23))– the pore aspect ratio $\rho = h/D$ and the $k-$ factor; in addition to the clay porosity ϕ^I. It provides a direct link between the $4+1$ model parameters and the experimental mean nanoindentation stiffness values $M^I_{1,\text{exp}} \equiv \mu_{M_1}$ and $M^I_{3,\text{exp}} \equiv \mu_{M_3}$, respectively the anisotropy ratio $M^I_{1,\text{exp}}/M^I_{3,\text{exp}}$, given by (5.4).

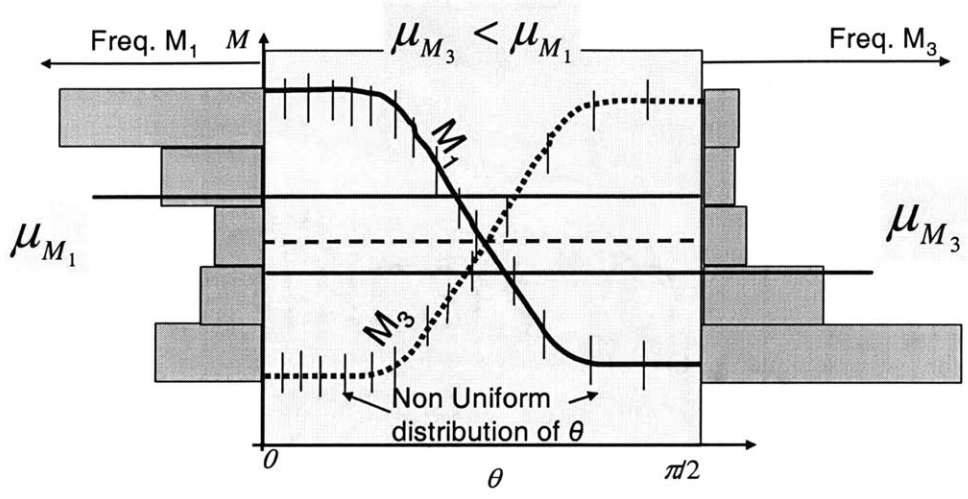

Figure 6-8: Mean value and distribution of indentation moduli in the two indented direction at the nano-scale (Level I). The anisotropy depends on the anisotropy of the shale building blocks (*ie.* on the pore aspect ratio), and on the orientation distribution function (*ie.* k-factor).

6.4 Level 'II': Layered Clay Porous Matrix

We consider that the textured clay layer composite has an infinite number of layers, each being characterized by the orientation of the pores (θ, φ) (Figure 6-3). The inherent assumption in layered composites mechanics is that the strain parameters ε_{11}, ε_{22}, ε_{12} are uniform, as well as the stress components σ_{13}, σ_{23}, σ_{33}. This is true for a laminates with homogeneous layers, which is a special case of the scale separability condition (2.54). There are many different formulations for stress-strain averages of laminates [98], [33]. The one we retain here is the method proposed by El Omri *et al.* [33], which provides an explicit formulation of the laminate stiffness tensor as a function of each layer stiffness, using stress-strain hybrid averages. We extend this method to the porous laminate, for which the layer behavior is defined by the poroelastic state equation:

$$\sigma_{ij} = C_{ijkl}\, \varepsilon_{kl} - b_{ij}\, p \tag{6.52}$$

The idea is to rewrite the poroelastic state equation in a plane-antiplane basis:

$$\begin{pmatrix} \sigma_P \\ \sigma_A \end{pmatrix} = \begin{bmatrix} c_{PP} & c_{PA} \\ c_{AP} & c_{AA} \end{bmatrix} \begin{pmatrix} \varepsilon_P \\ \varepsilon_A \end{pmatrix} - \begin{pmatrix} b_P \\ b_A \end{pmatrix} p \tag{6.53}$$

where subscript P refers to the plane components $11, 22, 12$, whereas subscript A refers to the anti-plane components $31, 23, 33$, and the subscript A, P to the permuted configuration. Adopting the matrix representation of second and forth order tensors proposed by Helnwein [46], which is different from the classical Voigt representation[3], the plane-antiplane components of any symmetric second order tensor a_{ij} are obtained from:

$$\mathbf{a} = \mathbb{P} : \begin{pmatrix} a_P & a_A \end{pmatrix}^T = \begin{pmatrix} a_{11} & a_{22} & a_{33} & \sqrt{2}\, a_{23} & \sqrt{2}\, a_{31} & \sqrt{2}\, a_{12} \end{pmatrix}^T \tag{6.54}$$

yielding:

$$\begin{pmatrix} a_P & a_A \end{pmatrix}^T = \mathbb{P}^T : \mathbf{a} = \begin{pmatrix} a_{11} & a_{22} & \sqrt{2}\, a_{12} & \sqrt{2}\, a_{31} & \sqrt{2}\, a_{23} & a_{33} \end{pmatrix}^T \tag{6.55}$$

where the matrix operator $\mathbb{P}$ reads:

$$\mathbb{P} = \begin{bmatrix} 1 & 0 & 0 & 0 & 0 & 0 \\ 0 & 1 & 0 & 0 & 0 & 0 \\ 0 & 0 & 0 & 1 & 0 & 0 \\ 0 & 0 & 0 & 0 & 0 & 1 \\ 0 & 0 & 0 & 0 & 1 & 0 \\ 0 & 0 & 1 & 0 & 0 & 0 \end{bmatrix} ; \mathbb{P}^{-1} = \mathbb{P}^T = \begin{bmatrix} 1 & 0 & 0 & 0 & 0 & 0 \\ 0 & 1 & 0 & 0 & 0 & 0 \\ 0 & 0 & 0 & 0 & 0 & 1 \\ 0 & 0 & 1 & 0 & 0 & 0 \\ 0 & 0 & 0 & 0 & 1 & 0 \\ 0 & 0 & 0 & 1 & 0 & 0 \end{bmatrix} \tag{6.56}$$

The plane-antiplane components in (6.53) thus read:

$$\begin{pmatrix} \sigma_P & \sigma_A \end{pmatrix}^T = \mathbb{P}^T : \boldsymbol{\sigma} \tag{6.57a}$$

$$\begin{pmatrix} \varepsilon_P & \varepsilon_A \end{pmatrix}^T = \mathbb{P}^T : \boldsymbol{\varepsilon} \tag{6.57b}$$

$$\begin{pmatrix} b_P & b_A \end{pmatrix}^T = \mathbb{P}^T : \mathbf{b} \tag{6.57c}$$

[3] See section 1.7 in which these notations are defined.

Similarly, the stiffness components are obtained from:

$$\mathbb{C}_{A,P} = \begin{bmatrix} c_{PP} & c_{PA} \\ c_{AP} & c_{AA} \end{bmatrix} = \mathbb{P}^T : \mathbb{C} : \mathbb{P} \tag{6.58}$$

where $\mathbb{C} = \mathbb{C}^I_{\text{hom}}(\theta, \varphi)$ is the stiffness tensor of each layer, given by (6.43a) in function of the elastic constants of the building block and the orientation of the pore plane (θ, φ). Implemented in matrix form, its components read [46]:

$$C_{ijkl} = \begin{bmatrix} C_{1111} & C_{1122} & C_{1133} & \sqrt{2}C_{1123} & \sqrt{2}C_{1131} & \sqrt{2}C_{1112} \\ & C_{2222} & C_{2233} & \sqrt{2}C_{2223} & \sqrt{2}C_{2231} & \sqrt{2}C_{2212} \\ & & C_{3333} & \sqrt{2}C_{3323} & \sqrt{2}C_{3331} & \sqrt{2}C_{3312} \\ & & & 2C_{2323} & 2C_{2331} & 2C_{2312} \\ & & & & 2C_{3131} & 2C_{3112} \\ sym & & & & & 2C_{1212} \end{bmatrix} \tag{6.59}$$

The plane-antiplane representation allows for the following remarkable averaging relations:

$$\varepsilon_P \equiv \overline{\varepsilon_P} = E_P = \begin{pmatrix} E_{11} & E_{22} & \sqrt{2}\,E_{12} \end{pmatrix}^T \tag{6.60a}$$

$$\sigma_A \equiv \overline{\sigma_A} = \Sigma_A = \begin{pmatrix} \sqrt{2}\,\Sigma_{31} & \sqrt{2}\,\Sigma_{23} & \Sigma_{33} \end{pmatrix}^T \tag{6.60b}$$

The remaining stress and strain components, not included in laminate averaging relations (6.60) are obtained from a partial inversion of (6.53):

$$\begin{pmatrix} \sigma_P \\ \varepsilon_A \end{pmatrix} = \begin{bmatrix} k_{PP} & k_{PA} \\ k_{AP} & k_{AA} \end{bmatrix} \begin{pmatrix} E_P \\ \Sigma_A \end{pmatrix} - p \begin{pmatrix} l_P \\ l_A \end{pmatrix} \tag{6.61}$$

where

$$\begin{aligned} &k_{PP} = c_{PP} - c_{PA}\, c_{AA}^{-1}\, c_{AP} \quad ; \quad l_P = b_P + c_{PA}\, c_{AA}^{-1}\, b_A \\ &k_{AA} = c_{AA}^{-1} \\ &k_{PA} = -k_{AP}^T = c_{PA}\, c_{AA}^{-1} \quad ; \quad l_A = -c_{AA}^{-1}\, b_A \end{aligned} \tag{6.62}$$

Averaging (6.61) yields:

$$\begin{pmatrix} \Sigma_P \\ E_A \end{pmatrix} = \begin{pmatrix} \overline{\sigma_P} \\ \overline{\varepsilon_A} \end{pmatrix} = \begin{bmatrix} \overline{k_{PP}} & \overline{k_{PA}} \\ \overline{k_{AP}} & \overline{k_{AA}} \end{bmatrix} \begin{pmatrix} E_P \\ \Sigma_A \end{pmatrix} - p \begin{pmatrix} \overline{l_P} \\ \overline{l_A} \end{pmatrix} \tag{6.63}$$

Finally, after partial inversion, we obtain:

$$\begin{pmatrix} \Sigma_P \\ \Sigma_A \end{pmatrix} = \begin{bmatrix} C^{\text{hom}}_{PP} & C^{\text{hom}}_{PA} \\ C^{\text{hom}}_{AP} & C^{\text{hom}}_{AA} \end{bmatrix} \begin{pmatrix} E_P \\ E_A \end{pmatrix} - p \begin{pmatrix} b^{\text{hom}}_P \\ b^{\text{hom}}_A \end{pmatrix} \tag{6.64}$$

where

$$\begin{aligned} C^{\text{hom}}_{PP} &= \overline{k_{PP}} - \overline{k_{PA}} \left(\overline{k_{AA}}\right)^{-1} \overline{k_{AP}} \quad ; \quad b^{\text{hom}}_P = \overline{l_P} + \overline{k_{PA}} \left(\overline{k_{AA}}\right)^{-1} \overline{l_A} \\ C^{\text{hom}}_{AA} &= \left(\overline{k_{AA}}\right)^{-1} \\ C^{\text{hom}}_{PA} &= \left(C^{\text{hom}}_{AP}\right)^T = \overline{k_{PA}} \left(\overline{k_{AA}}\right)^{-1} \quad ; \quad b^{\text{hom}}_A = -\left(\overline{k_{AA}}\right)^{-1} \overline{l_A} \end{aligned} \tag{6.65}$$

The homogenized stiffness of the porous laminate in the original configuration is obtained by inverse application of (6.58):

$$\mathbb{C}^{II}_{\text{hom}} = \mathbb{P} : \mathbb{C}^{\text{hom}}_{A,P} : \mathbb{P}^T \tag{6.66}$$

Similarly, application of (6.57c) yields the tensor of Biot coefficients in the original basis:

$$\mathbf{b}^{II} = \mathbb{P} : \mathbf{b}^{\text{hom}}_{A,P} \tag{6.67}$$

The last poroelastic constant, the Biot modulus N^{II}, is a scalar which is not affected by the rotation of the porosity. As a consequence, the Biot modulus is uniform throughout the layered system, and coincides with the solid Biot modulus of the layered composite given by (6.21) and (6.37):

$$N^{II} \equiv N^I \tag{6.68}$$

Last, the volume average operation in (6.63) of the stiffness matrices $\overline{k_{IJ}}$ reads for a uniform orientation distribution of the pore planes in the laminate:

$$\overline{k_{IJ}} = \frac{1}{2\pi} \int_{\theta=0}^{\pi} \int_{\varphi=0}^{2\pi} k_{IJ}(\theta, \varphi) \sin(\theta) d\varphi d\theta \tag{6.69}$$

Similarly to (6.49) it is appropriate to introduce a non-uniform orientation distribution to

account for some degree of preferred alignment:

$$\overline{k_{IJ}} = \frac{1}{2\pi}\int_{\theta=0}^{\pi}\int_{\varphi=0}^{2\pi} k_{IJ}(\theta,\varphi)W(\theta,k)\sin(\theta)d\varphi d\theta \tag{6.70}$$

where $W(\theta,k)$ is the orientation distribution function (6.51). The same non-uniform orientation average operation is applied to all averages in (6.65); including the one involved in the determination of the Biot coefficients.

The resulting homogenized stiffness (6.66) of the porous clay laminate, therefore, depends on the elastic constants of the isotropic solid clay phase –bulk modulus k_s, shear modulus g_s (see (6.23))–, the pore aspect ratio $\rho = h/D$ and the $k-$ factor; in addition to the clay porosity $\phi^I = \phi^{II}$. Using $\mathbb{C}^{II}_{\text{hom}}$ from (6.66) in (3.35) and (3.50) provides the link between these $4+1$ model parameters, and the microindentation stiffness values $M^{II}_{1,\text{exp}}$ and $M^{II}_{3,\text{exp}}$, respectively the anisotropy ratio $M^{II}_{1,\text{exp}}/M^{II}_{3,\text{exp}}$, given by (5.6).

6.5 Level 'III': Macroscopic Undrained Elasticity

6.5.1 Drained Poroelastic Properties

We consider shale materials at the macroscopic scale to be composed of a textured porous matrix and (mainly) quartz inclusions of approximately spherical shape that are randomly distributed throughout the anisotropic porous matrix Ω_M (Figure 6-9). The problem is conveniently treated in the framework of microporomechanics presented in Section 6.2.1 [85]. We adopt a continuous description of the stress field in the heterogeneous r.e.v.:

$$\text{in } V_{III} : \boldsymbol{\sigma}(\underline{z}) = \mathbb{C}(\underline{z}) : \boldsymbol{\varepsilon}(\underline{z}) + \boldsymbol{\sigma}^p(\underline{z}) \tag{6.71}$$

together with the following distributions of the elastic properties $\mathbb{C}(\underline{z})$ and the eigenstress $\boldsymbol{\sigma}^p(\underline{z})$:

$$\mathbb{C}(\underline{z}) = \begin{cases} \mathbb{C}_M \text{ in } \Omega^M \\ \mathbb{C}_i \text{ in } \Omega^i \end{cases} \qquad \boldsymbol{\sigma}^p(\underline{z}) = \begin{cases} -\mathbf{b}_M\, p \text{ in } \Omega^M \\ 0 \text{ in } \Omega^p \end{cases} \tag{6.72}$$

where $\mathbb{C}_M = \mathbb{C}^{II}_{\text{hom}}$ is the stiffness tensor of the porous clay laminate (6.66), $\mathbb{C}_i = 3k_i\mathbb{J} + 2g_i\mathbb{K}$ is the stiffness tensor of the (assumed isotropic) quartz inclusion phase; and $\mathbf{b}_M = \mathbf{b}^{II}$ is the

second order Biot coefficient tensor of the porous clay laminate (6.67). Following the linear microporomechanics approach, we decompose the problem in two sub-problems:

First Load Case: $p = 0$

The first sub-problem corresponds to drained conditions, for which $p = 0$. We assume that the r.e.v. is subjected to a uniform displacement boundary condition, so that the solid boundary conditions to which the solid phase is subjected read:

$$\text{on } \partial V_{III} \quad : \quad \underline{\xi}'(\underline{z}) = \mathbf{E} \cdot \underline{z} \tag{6.73a}$$

$$\text{on } \mathcal{I}_{sf} \quad : \quad \boldsymbol{\sigma} \cdot \underline{n} = 0 \tag{6.73b}$$

The macroscopic strain tensor $\mathbf{E}$ is related to the microscopic strain by the strain localization condition:

$$\boldsymbol{\epsilon}'(\underline{z}) = \mathbb{A}(\underline{z}) : \mathbf{E} \tag{6.74}$$

$\mathbb{A}(\underline{z})$ satisfies the compatibility condition:

$$\mathbf{E} = \overline{\boldsymbol{\epsilon}'(\underline{z})} \Leftrightarrow \mathbb{I} = (1 - f_i) \langle \mathbb{A} \rangle_{\Omega^M} + f_i \langle \mathbb{A} \rangle_{\Omega^i} \tag{6.75}$$

where $f_i = \left|\Omega^i\right| / \left|\Omega^{III}\right| = 1 - f_M$ is the inclusion volume fraction. Use of (6.74) in (6.71) together with the elastic distribution (6.72) yields after volume averaging, the macroscopic stress, and the homogenized stiffness of the composite:

$$\boldsymbol{\Sigma}' = \overline{\boldsymbol{\sigma}'(\underline{z})} = \mathbb{C}^{III}_{\text{hom}} : \mathbf{E} \; ; \; \mathbb{C}^{III}_{\text{hom}} = \mathbb{C}_M + f_I (\mathbb{C}_i - \mathbb{C}_M) : \langle \mathbb{A} \rangle_{\Omega^i} \tag{6.76}$$

The change of the porosity in the subproblem reads:

$$\left[\; (\phi - \phi_0)^{III} \right]' = \mathbf{b}^{III} : \mathbf{E} \tag{6.77}$$

where $\mathbf{b}^{III}$ is the second order tensor of homogenized Biot coefficients.

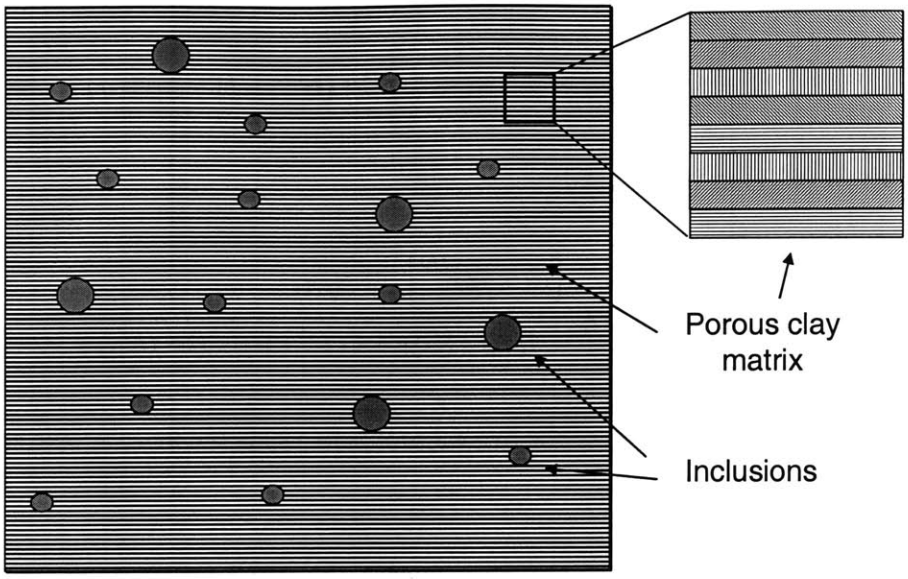

Figure 6-9: Modelisation of shales as an anisotropic porous matrix of clay containing randomly distributed spherical inclusions.

Second Load Case: $\mathbf{E} = \mathbf{0}$

The second sub-problem we consider is the zero-displacement boundary problem, whereas the porosity is pressurized. For the eigenstress distribution (6.72), we obtain the macroscopic stress and the homogenized Biot coefficients from Levine's theorem (6.15):

$$\boldsymbol{\Sigma}'' = \overline{\boldsymbol{\sigma}^p(\underline{z}) : \mathbb{A}(\underline{z})} = -\mathbf{b}^{III} p;\ \mathbf{b}^{III} = \mathbf{b}_M : (\mathbb{I} - f_i \langle \mathbb{A} \rangle_{\Omega^i}) \tag{6.78}$$

The change of the porosity in the subproblem reads:

$$\left[(\phi - \phi_0)^{III}\right]'' = (1 - f_i)\left(\mathbf{b}_M : \langle \boldsymbol{\varepsilon}'' \rangle_{\Omega^M} + \frac{p}{N_M}\right) \tag{6.79}$$

where $N_M = N^{II}$. We eliminate $\langle \boldsymbol{\varepsilon}'' \rangle_{\Omega^M}$ in (6.79) to the benefit of pressure p, by considering the stress average in this sub-problem, in which $\mathbf{E}'' = \overline{\boldsymbol{\varepsilon}''(\underline{z})} = 0$:

$$\begin{aligned} \boldsymbol{\Sigma}'' &= (1 - f_i) \langle \boldsymbol{\sigma}'' \rangle_{\Omega^M} + f_i \langle \boldsymbol{\sigma}'' \rangle_{\Omega^i} \\ &= (\mathbb{C}_M - \mathbb{C}_i) : (1 - f_i) \langle \boldsymbol{\varepsilon}'' \rangle_{\Omega^M} - (1 - f_i)\, \mathbf{b}_M p \end{aligned} \tag{6.80}$$

Thus, from the equality of (6.78) and (6.80):

$$(1-f_i)\left\langle \varepsilon'' \right\rangle_{\Omega^M} = -\left(\mathbb{C}_M - \mathbb{C}_i\right)^{-1} : \left(\mathbf{b}^{III} - (1-f_i)\,\mathbf{b}_M\right) p \tag{6.81}$$

Finally, use of (6.81) in (6.79) yields:

$$\begin{gathered} \left[(\phi-\phi_0)^{III}\right]'' = \frac{p}{N^{III}}; \\ \frac{1}{N^{III}} = \frac{1-f_i}{N_M} - f_i \mathbf{b}_M : \left(\mathbb{C}_M - \mathbb{C}_i\right)^{-1} : \mathbf{b}_M : \left(\mathbb{I} - \langle \mathbb{A} \rangle_{\Omega^i}\right) \end{gathered} \tag{6.82}$$

In summary, a superposition of the two subproblems yields the macroscopic state equations of the shale composite material:

$$\boldsymbol{\Sigma} = \mathbb{C}^{III}_{\text{hom}} : \mathbf{E} - \mathbf{b}^{III} p \tag{6.83a}$$

$$(\phi-\phi_0)^{III} = \mathbf{b}^{III} : \mathbf{E} + \frac{p}{N^{III}} \tag{6.83b}$$

together with the poroelastic properties:

$$\mathbb{C}^{III}_{\text{hom}} = \mathbb{C}_M + f_I \left(\mathbb{C}_i - \mathbb{C}_M\right) : \langle \mathbb{A} \rangle_{\Omega^i} \tag{6.84a}$$

$$\mathbf{b}^{III} = \mathbf{b}_M : \left(\mathbb{I} - f_i \langle \mathbb{A} \rangle_{\Omega^i}\right) \tag{6.84b}$$

$$\frac{1}{N^{III}} = \frac{1-f_i}{N_M} + f_i \mathbf{b}_M : \left(\mathbb{C}_i - \mathbb{C}_M\right)^{-1} : \mathbf{b}_M : \left(\mathbb{I} - \langle \mathbb{A} \rangle_{\Omega^i}\right) \tag{6.84c}$$

The input to this homogenization step are the poroelastic properties of the porous clay laminate, $\mathbb{C}_M = \mathbb{C}^{II}_{\text{hom}}$, $\mathbf{b}_M = \mathbf{b}^{II}$, $N_M = N^{II}$, the (quartz) inclusion volume fraction f_i, and an estimate of the volume average of the inclusion strain concentration tensor $\langle \mathbb{A} \rangle_{\Omega^i}$. Given the matrix–inclusion morphology, such an estimate is suitably provided by the Mori-Tanaka scheme (6.34):

$$\langle \mathbb{A} \rangle_{\Omega^M} \simeq \mathbb{A}^{est}_M = \left[(1-f_i)\mathbb{I} + f_i \left(\mathbb{I} + \mathbb{P}^M : \left(\mathbb{C}_i - \mathbb{C}_M\right)\right)^{-1}\right]^{-1} \tag{6.85}$$

where $\mathbb{P}^M$ is the P-tensor for isotropic spherical inclusions in a transverse isotropic matrix. It is given in Appendix E of this report.

6.5.2 Undrained Poroelastic Properties

In order to assess the undrained properties, one needs to find the relation between macroscopic stress and strain when the fluid mass $m = \rho_{fl}\phi$ stays constant in the r.e.v.. ρ_{fl} stands for the fluid density and varies with the pore pressure. In the linear case:

$$\rho_{fl} = \rho_{fl}^0 \left(1 + \frac{p}{K_{fl}}\right) \tag{6.86}$$

where K_{fl} is the fluid bulk modulus and ρ_{fl}^0 is the reference fluid density (for water $K_{fl} = 2.3$ GPa). Then the change of fluid mass contained in the r.e.v. is such that:

$$\frac{m - m_0}{\rho_{fl}^0} = \phi - \phi_0 + \phi_0 \frac{p}{K_{fl}} \tag{6.87}$$

With (6.87), the two poro-elastic state equations (6.83a) and (6.83b) are written in the form:

$$\mathbf{\Sigma} = \mathbb{C}_{u,\text{hom}}^{III} : \left(\mathbf{E} - \mathbf{B}^{III} \frac{m - m_0}{\rho_{fl}^0}\right) \tag{6.88}$$

$$\frac{m - m_0}{\rho_{fl}^0} = \mathbf{b}^{III} : \mathbf{E} + \frac{p}{M^{III}} \tag{6.89}$$

where:

- M^{III} is the Biot modulus for the porous solid and is defined by :

$$\frac{1}{M^{III}} = \frac{1}{N^{III}} + \frac{\phi_0}{K_{fl}} \tag{6.90}$$

- $\mathbb{C}_{u,\text{hom}}^{III}$ is the macroscopic undrained stiffness tensor

$$\mathbb{C}_{u,\text{hom}}^{III} = \mathbb{C}_{\text{hom}}^{III} + M^{III}\ \mathbf{b}^{III} \otimes \mathbf{b}^{III} \tag{6.91}$$

- $\mathbf{B}^{III}$ is the second order tensor of Skempton coefficients

$$\mathbf{B}^{III} = M^{III} (\mathbb{C}_{u,\text{hom}}^{III})^{-1} : \mathbf{b}^{III} \tag{6.92}$$

6.6 Discussion

The micromechanical model developed in this study is not the first of this kind for shale materials. Indeed, in order to go beyond empirical relations of shale acoustic anisotropy, several micro-mechanical models have been proposed (Hornby *et al.*, 1994, [48], Jakobsen *et al.*, 2003 [50]) to estimate the elastic properties of shales from parameters such as porosity, silt inclusion volume fractions, and parameters describing the clay particle orientation distribution functions (ODF). The shale morphology used by Hornby *et al.* [48] comes very close to our shale think-model (Fig. 4-10). It is based on the concept of a 'perfect shale' of parallel clay particles intermixed with porosity. However, in contrast to our approach, Hornby *et al.* consider a constant pore aspect ratio equal to 1/20. A second difference with our approach is that Hornby *et al.* consider the porous clay matrix of shales as a polycrystal of elementary building blocks with various orientations, thus omitting the pronounced laminate structure of shale materials. Finally, similarly to our approach, inclusions are added at Level 'III'. This representation was used also by Jakobsen *et al.* [50] who discussed the choice of elastic upscaling schemes for shales.

6.6.1 Level '0' to Level 'I'

There is an ongoing debate on the choice of a scheme for porous materials, especially for particulate microstructures [48], [50]. The debate originates from the observation that even for low porosities, pores are connected, and are not isolated inclusions in a solid matrix, as implied by the application of upscaling schemes based on Eshelby's inclusion problem. A second matter of concern relates to the high contrast between the elastic properties of solids and pores. The influence of microstructure on the overall stiffness is critical. Therefore, the choice of a particular upscaling scheme is a delicate one.

More precisely, when the inclusions are softer than the matrix (*eg.* pores), it has been shown [44], [96] that the Mori-Tanaka scheme yields an upper bound for the homogenized stiffness tensor. Unlike the dilute expression (6.29), the Mori-Tanaka scheme takes into account the interactions between pores by associating the Eshelby inclusion problem with average strain boundary condition (6.31), even though it applies to clear matrix/inclusion morphologies where

interactions between inclusions are minimal.

As a consequence, the Mori-Tanaka estimate does not predict a porosity threshold above which the pores isolate the clay particles, leading to a zero composite stiffness. Such a porosity threshold may exist in high porosity shales. In the case of our three shale materials, the clay porosity is moderate and is compatible with the Mori Tanaka scheme. However, we should keep in mind this limitation for high porosity shale materials: even if pores can overlap, unlike solid inclusions, there must be a porosity above which the porous clay stiffness vanishes.

Hornby *et al.* [48] used another scheme to mix porosity and clays, by considering a self-consistent scheme for a 50% porosity shale building block. Then using the differential effective medium theory, solid phase was added until the porosity value ϕ^I was reached. As pointed out by Jakobsen *et al.* [50], this method is sensitive to the starting point used for the self consistent scheme.

Finally, the Mori-Tanaka and self-consistent estimates used in our study can be generalized to more specific microstructures when spatial distributions of inclusions are known (Ponte-Castagneda and Willis, 1995 [70], Jakobsen *et al.* 2003 [50]). In our study we have not considered this possibility which demands quite complicated statistical analysis of the microstructure of shales, and requires additional unknown model parameters.

6.6.2 Level 'I' to Level 'II'

The choice of a laminate to model the spatial distribution of flakes as a function of their orientation is a rough approximation to add a maximum amount of anisotropy from the layered structure. On the expenses of a supplementary step in the model from the building block up to the clay phase, this representation provides a simple and explicit homogenization scheme. In terms of microstructure, the laminate scheme is of course reductionist compared to the actual shale morphology (Fig. 4-8). Like in a series system where the weakest layer takes most of the deformations, the anisotropic behavior of the laminate model is dominated by the compliance of the layer with horizontal (connected) pores.

In order to go a step further and capture more information about the morphology than the classical matrix/inclusion one, it is possible to capture with additional degrees of freedom, statistical properties of spatial distributions of flakes with particular orientations. The wavy

structure could even be determined in a unique homogenization step from Level '0' to Level 'II'. Jakobsen *et al.* [50] proposed other schemes derived from the work of Ponte Castagneda and Willis (1995) [70]. The new explicit and self consistent estimates rely on two point statistics to find the effective behavior of composites. For example, when the spatial distribution of inclusions is known through a probability density $p^{(r)}(\underline{z})$ for finding an inclusion of type r centered at $\underline{z}$, or a joint probability density $p^{(rs)}(\underline{z},\underline{z}')$ for finding an inclusion of type r centered at $\underline{z}$ and an inclusion of type s centered at $\underline{z}'$, new microstructural elements can be taken into account. In the case of parallel flat ellipsoids, knowledge about the spatial distribution of pores would refine the model. However, this may have less influence than the crucial pore shape, and is even harder to assess experimentally. The Mori-Tanaka estimate we used here has for spatial distribution a natural probability density: $p^{(rr)}(\underline{z},\underline{z}')$ has a natural ellipsoidal symmetry with the same aspect ratio as the inclusions. Pores are not proportionally closer in one or the other direction.

6.6.3 Level 'II' to Level 'III'

The relevance of the Mori-Tanaka scheme is limited when it comes to high inclusion volume fractions. The assumptions about the shape, perfectly spherical, and the isotropic spatial distribution could lead to underestimating the macroscopic anisotropy of shales in which inclusions are gathered on horizontal planes (see Fig. 4-9). However, since the contrast between clay and inclusion stiffness is not infinite, the choice of a scheme is less critical here than for the treatment of the porosity (see Section 6.6.1).

In terms of morphology, the model does not capture an eventual local morphology of flakes around the inclusions, forming a soft shell. Furthermore, the scales of the layering ($\sim 10\mu m$) and the size of the inclusions ($\sim 50\mu m$) are not much separated. The presence of inclusions may even be felt on-average in the measurement of the anisotropy at the microscale close to inclusions. This would require a statistical treatment similar to the one of Level 'I' nanoindentations.

Another potential limitation linked to high inclusion volume fraction comes from the observation that the porosity locally increases in the vicinity of inclusions [58] especially for inclusion-rich shales. This particular morphology is not considered here.

Finally, for the calculation of the undrained macroscopic stiffness tensor, the state of water

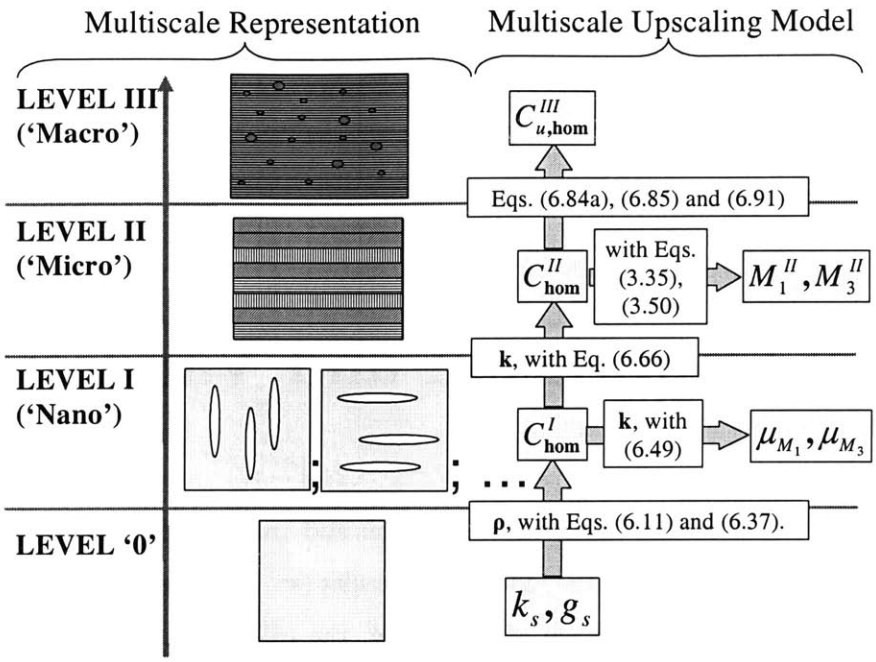

Figure 6-10: Flow chart of the forward application of the multiscale upscaling model.

in very thin pores (of a few nanometer size) raises the question whether water properties in such a configuration can be defined as bulk fluid phase as employed in Section 6.5.2.

6.7 Conclusion: A Four Parameters Micromechanical Model.

The articulation of our approach relies on the combination of continuum-based homogenization and indentation analysis. A four parameter (E_s, ν_s, ρ, k)[4], three-step homogenization model is designed to explain the observed shale anisotropic elasticity at each scale. It is based on the identification of individual phases, clay particles and pores and morphological features: orientation and spatial distribution of the flakes at Level 'I' and 'II'. A flow chart of a forward application of the model is given in Figure 6-10. This model is now ready for calibration and validation with the available indentation analysis, mineralogy of the three shales investigated this study.

[4] (E_s, ν_s) are derived from (k_s, g_s) using the relations (1.16) given in Section 1.7.

Chapter 7

Model Calibration and Validation

This chapter presents details about the calibration and validation of four-parameter model. The calibration is achieved using the indentation results (see Sections 5.5.1 and 5.6.1). In order to check the relevance and accuracy of the model, the calibration procedure itself can give an answer, since the existence of a solution (E_s *or* M_s, ν_s, ρ, k) to the inverse analysis of the expression of the indentation moduli ($M^I_{1,\text{exp}}, M^I_{3,\text{exp}}, M^{II}_{1,\text{exp}}, M^{II}_{3,\text{exp}}$) is not guaranteed.

Following the calibration, the model is validated by comparing predicted stiffness values of shales at Level 'III' with the experimental ultrasonic measurements (see Section 5.7.2). Two aspects of the prediction will be closely examined: the prediction of the overall stiffness values, and the prediction of the macroscopic anisotropy.

7.1 Calibration

Our model relies on two main assumptions: (1) The porous clay phase of shales is a continuous solid with pores; and (2) the pure clay stiffness is isotropic. By means of these two assumptions, we arrive at reducing the total numbers of model degrees of freedom to four: the elastic constants of the isotropic solid clay phase –bulk modulus k_s, shear modulus g_s (see (6.23)) or plane stress modulus M_s and Poisson's ratio ν_s–, the pore aspect ratio $\rho = h/D$ and the $k-$ factor.

7.1.1 Methodology: Choice of Experimental Values

To complete the model we need to calibrate and validate the model. This is achieved in two steps: validation with the 4 nanoindentation results, and validation with an independent set of experimental values.

For the calibration, we will only use the four results of the nano- and microindentation analysis from level I and II, and search for each shale material (porosity and inclusion volume fraction given) for the optimum set of model parameters (M_s, ν_s, ρ, k) that best fit the experimental constraints:

$$\begin{aligned}
\left|M^I_{1,\text{exp}} - \mu_{M_1}(M_s, \nu_s, \rho, k)\right| &\leq \epsilon^I_1 \\
\left|M^I_{3,\text{exp}} - \mu_{M_3}(M_s, \nu_s, \rho, k)\right| &\leq \epsilon^I_3 \\
\left|M^{II}_{1,\text{exp}} - M^{II}_1(M_s, \nu_s, \rho, k)\right| &\leq \epsilon^{II}_1 \\
\left|M^{II}_{3,\text{exp}} - M^{II}_3(M_s, \nu_s, \rho, k)\right| &\leq \epsilon^{II}_3
\end{aligned} \tag{7.1}$$

where μ_{M_J} is the statistical model average (6.49), $M^{II}_J\,(J = 1, 3)$ is the model indentation modulus given by an application of the model stiffness $\mathbb{C}^{II}_{\text{hom}}$ from (6.66) in (3.35) and (3.50), and ϵ^J_j are some prescribed (absolute) error values. Ideally, $\epsilon^J_j = 0$. For consistency with the model derivations, the experimental values of nanoindentation moduli $M^I_{1,\text{exp}}$ and $M^I_{3,\text{exp}}$ are average values of the test results, whereas the experimental microindentation moduli $M^{II}_{1,\text{exp}}$ and $M^{II}_{3,\text{exp}}$ refer to peak values. Indeed, $M^{II}_J\,(J = 1, 3)$ and $\mathbb{C}^{II}_{\text{hom}}$ are unique predicted values, and must match with the representative experimental material response, given by the microindentation results in Figure 5-8. Unlike nanoindentation results, the microindentation moduli distributions exhibit one-peak shapes, so that the determination of peak values $M^{II}_{1,\text{exp}}$ and $M^{II}_{3,\text{exp}}$ is not biased by the choice of this particular model[1].

[1] Practically, this was achieved by taking the peak value of a fitted smooth non symmetric distribution function. Figs. 5-7 and 5-8 show Gaussian distributions with fitted average and standard deviations on the experimental data. The optimal parameters were such that the errors on the cumulative distributions was minimal. The corresponding peak values do not differ much from the mean values or the values of the highest peaks. The choice of the bin size was made such that the divisions are small enough to highlight the main features, and large enough to contain a sufficient number of points to avoid unrepresentative secondary peaks (noise).

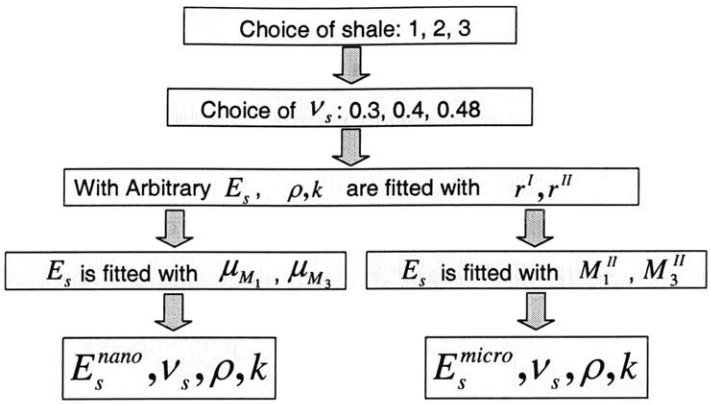

Figure 7-1: Calibration procedure of the four model parameters. The calibration error is given by fitting either the nano- or micro- indentation value after determining the anisotropic ratios for an arbitrary Poisson's ratio.

7.1.2 Calibration Procedure

The calibration procedure is iteratively performed for each shale. The homogenization steps are explicit, but cannot be inversed easily: the following step-by-step procedure is employed:

1. Choice of the solid phase Poisson's ratio: the values $\nu_s = 0.3$, 0.4 and 0.48 are considered.

2. The two anisotropic ratios r^I and r^{II}, defined by:

$$r^I = \frac{M^I_{3,\text{exp}}}{M^I_{1,\text{exp}}} \tag{7.2}$$

$$r^{II} = \frac{M^{II}_{3,\text{exp}}}{M^{II}_{1,\text{exp}}} \tag{7.3}$$

   are fitted using the two anisotropy parameters ρ and k, independently of the solid phase's Young's Modulus E_s and of the actual values of indentation moduli (which are linearly related).

3. Error estimation of the calibration: with the fixed degree of freedom ν_s, the last parameter M_s or E_s is independently calibrated to best match either the nanoindentation moduli or the microindentation moduli. The optimal ν_s is the one that minimizes the difference between these calibrated stiffness moduli E_s (or M_s).

7.1.3 Calibration Results

Calibration Errors

Table 7.1 provides a summary of the calibration procedure. The difference between the two independently calibrated solid phase stiffness moduli M_s was found smaller than the standard deviation resulting from the backward homogenization method (on the order of $\sim 7 - 10GPa$ based on the standard deviations of the experimental results; see Table 7.1). This shows that the model reproduces well the results with only 3 degrees of freedom. However it was not possible to find ν_s such that the calibration error was zero. The reason for this is that the model can explain an overall increase of the anisotropy but not an overall increase or decrease of the indentation moduli from Level 'I' to Level 'II'. The overall calibration error $\epsilon = E_s^{micro} - E_s^{nano}$, refers to the difference $(M^{II}_{3,1\,\mathrm{exp}} - M^{I}_{3,1\,\mathrm{exp}})$ that the model cannot capture. In general, ϵ is greater than the trend $(M^{II}_{3,1\,\mathrm{exp}} - M^{I}_{3,1\,\mathrm{exp}})$, which shows the limited accuracy of the determination of M_s as a results of a backward application of an uspcaling model. ϵ was found to be negative for shale 1, zero for shale 2 and positive for shale 3. For shale 1, the decrease of the overall moduli from Level 'I' to Level 'II' could be explained by the effect of porosity at a higher scale, due to a particular pore connectivity that is not sensed in nanoindentations. For shale 2, the evolution is captured by the model: the error is almost zero. Finally, for shale 3, the opposite trend is observed: the values at level 'II' are relatively stiffer than the ones at level 'I'; most probably as a consequence of the effect of inclusions, or an influence of the surface roughness which interacts here with the low indentation depths achieved in a stiffer shale. Given the small standard deviation of the indentation results at Level 'II', we will keep the E_s^{micro} values as a reference for further analyzes.

Clay Poisson's Ratios ν_s

The effect of the solid phase Poisson's ratio on the calibration error was found to be insignificant. In fact, the calibrated values of M_s and E_s do not depend much on the chosen value of ν_s. The choice of values of $\nu_s \geq 0.3$ was made because the adding of very flat pores leads to reducing the anisotropic Poisson's ratios ν_{12}, ν_{13} (see Section 1.7) to very small values that would barely make any physical sense. Given that the deformation occurs mainly in the pore space, the

incompressible solid assumption $\nu_s = 0.5$ may even seem reasonable.

Clay phase stiffness E_s or M_s

An interesting observation is that the plane-stress modulus of the pure clay phase, $M_s = E_s/\left(1-\nu_s^2\right)$, is almost the same for all three shale materials (and even more so for the Young's modulus E_s!), which are quite different in mineralogy, burial depth, porosity, etc. (see Table 4.1). The average value of $M_s \approx 35GPa$ is somewhat smaller than the indentation modulus of pure mineral crystals (compare with Table 5.1), and clearly greater than average indentation stiffness values obtained by nanoindentation at larger scales. For $\nu = 0.4$, the average value of E^{nano} and E^{micro} yields:

$$M_s = 34.4 - 37.2 - 34.4 \text{ GPa} \tag{7.4}$$

$$E_s = 28.9 - 31.2 - 28.5 \text{ GPa} \tag{7.5}$$

But if one only considers the calibrated values from Level 'II' for $\nu = 0.4$, we obtain:

$$M_s = 32 - 38 - 41.1 \text{ GPa} \tag{7.6}$$

$$E_s = 26.7 - 31.9 - 34.5 \text{ GPa} \tag{7.7}$$

We notice a slight increase of the solid phase stiffness from shale 1 to shale 3, *ie.* with decreasing porosity. However, given the limited precision of such a backward homogenization, it is delicate to link this trend with mineralogy.

Pore Aspect Ratio ρ

The main difference in between the different shale materials comes from the anisotropy parameters: the pore aspect ratio ρ, and the alignment factor k. ρ scales almost linearly with the clay porosity, as shown on Figure 7-2:

$$\rho = c\phi^I \tag{7.8}$$

where $c = 0.1745$. It is readily understood that a model with a unique pore aspect ratio (as the one of Hornby *et al.* [48]) cannot capture this trend, relying solely on the k factor to capture

From Level		'I'	'II'	'I'	'II'	'I'	'II'
Shale #		1					
ν_s	[1]	0.3	0.3	0.4	0.4	0.48	0.48
ρ	[1]	0.057		0.054		0.0515	
k	[1]	0.9					
M_s	[GPa]	34.5	30	36.7	32	38.9	34.2
E_s	[GPa]	31.4	27.3	30.8	26.7	29.9	26.3
error	[GPa]	$-4.5/-4.1$		$-4.7/-3.9$		$-4.7/-3.6$	
on M_s/E_s	[1]	.15		.147		.137	
Shale #		2					
ν_s	[1]	0.3	0.3	0.4	0.4	0.48	0.48
ρ	[1]	0.037		0.036		0.034	
k	[1]	3.4					
M_s	[GPa]	35.1	36	36.4	38	38.5	41
E_s	[GPa]	31.9	32.8	30.6	31.9	29.6	31.6
error	[GPa]	0.9/0.8		1.6/1.3		2.5/1.9	
on M_s/E_s	[1]	.025		.042		.061	
Shale #		3					
ν_s	[1]	0.3	0.3	0.4	0.4	0.48	0.48
ρ	[1]	0.0155		0.0148		0.014	
k	[1]	1.4					
M_s	[GPa]	30.7	38.5	32.5	41.1	34.5	44
E_s	[GPa]	28	35	27.3	34.5	26.6	33.9
error	[GPa]	7.8/7.1		8.6/7.2		9.5/7.3	
on M_s/E_s	[1]	.203		.209		.216	

Table 7.1: Summary of model calibration procedure.

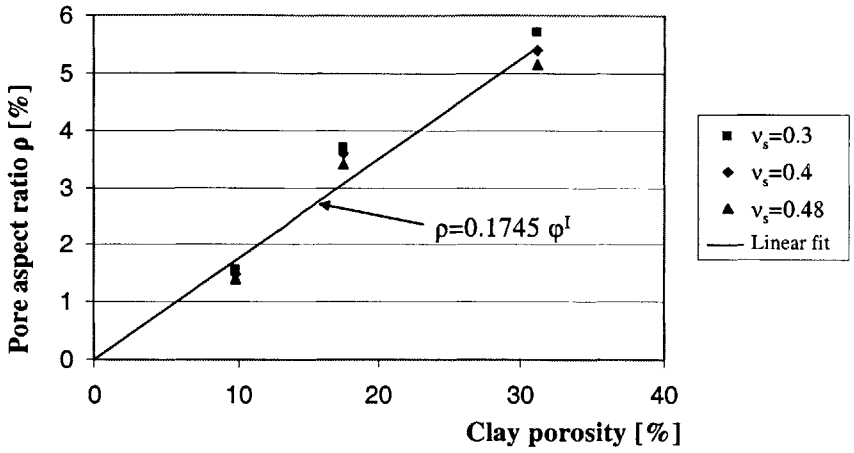

Figure 7-2: Calibrated pore aspect ratio ρ as a function of clay porosity ϕ_c (for $\nu = 0.3$).

an overall anisotropy.

$k-$Factor of the Clay Particles Alignment

As expected from the nanoindentation results, k is smaller for the (almost) isotropic shales 1 and 3 at level 'I' and higher for shale 2. k appears to be quite independent of the porosity and the pore aspect ratio. Motivated from nanoindentation results and SEM and ESEM images of shale materials, it is very likely that a preferred alignment of building blocks relates to silt-size inclusions that may disturb the deposition alignment of clay particles in the course of the deposition history. It should therefore be related to size and distribution of inclusions within the porous clay laminate. However, based on the multiscale investigation of three shale materials only, it is still to early to be conclusive.

7.1.4 Discussion of Calibration Results

It is tempting to interpret the calibrated parameters as physical quantities, and to analyze the full stiffness tensors at the scale of the shale building block (level I), or the layered porous clay phase (level II).

Pore Size and Morphology

The experimental values of the pore throat radius of shale 1,2 and 3 are 4, 6.7 and 13.3 nm (see Fig. 4-7). With these values, it is possible to calculate the diameter D and the volume V of the pores in each shale, if we assume that the pore throat radius gives the thickness of the pores:

$$D \simeq \frac{2r_p}{\rho} = 465 - 290 - 515\ nm \tag{7.9}$$

$$\begin{aligned} V &= \frac{\pi}{3} D^2 r_p \simeq \frac{4\pi r_p^3}{3\rho^2} \\ &= 3.0 - 0.5 - 1.1 \times 10^{-3} \mu m^3 \end{aligned} \tag{7.10}$$

Furthermore, the clay porosity of each shale gives access to the number of pores n per volume of shale porous clay phase:

$$n = \frac{\phi^I}{V} \simeq 100 - 390 - 80\ pores/\mu m^3 \tag{7.11}$$

Interestingly, the values of D, V, n for all shale materials are on the same order. This is the more remarkable, as any error on the pore throat radius is to the power 3 in Eq. (7.10). The pore density seems to be the consequence of the common morphology of the clay particles in the three indented shales; and possibly of all shales. This would mean that shales differ, apart from the amount of inclusions, just in thickness and orientation of the pores.

Finally, the $k-$factor is hard to correlate with the clay porosity or inclusion volume fractions of the three indented shales. The typical observed values of k are in the (wide) range of what has been measured experimentally in the literature [48], [26] in the form of different orientation distribution functions[2]. The analysis of the particle orientations was not available for the three indented shales, so we could not compare the values of k to experimental values.

Intuitively, it is difficult to know whether the calibrated value of k is smaller or higher than a physical one. First of all, one needs to understand how the fitting procedure of ρ and k operates. Fig. 7-3 gives the evolution of the anisotropy ratios r^I and r^{II} as a function of k for a typical

[2] Hornby *et al.* [48] chose a classical (non periodic) Gaussian distribution with an arbitrary standard deviation $\pi/9$.

shale: $\phi^I = 0.2$, $M_s = 35$GPa, $\nu_s = 0.3$, with various pore aspect ratios: $(0.077, 0.035, 0.007)$. k is linked to the difference between the anisotropic ratios r^I and r^{II}: for $k = 0$, $r^I = 1 > r^{II}$ whereas r^{II} and r^I merge for high $k-$values to the anisotropy of the elementary building block that depends on ρ. For two experimental values of r^{II} and r^I, there is one and only one set (ρ, k) that yields the desired anisotropy.

Given that the layered structure introduces the highest possible effect of spatial distribution, it is most likely that the curve giving r^{II} overestimates the experimental anisotropy with a less pronounced additional effect of layering (but still converging to the same asymptotic when $k \to \infty$). In other words, the choice of a layered structure leads to slightly overestimating in the calibration the pore aspect ratio and the k value.

Finally, given the size of clay particles compared to the depth of indentation, one cannot exclude the possibility that for the nanoindentations, particles may rotate during nanoindentation tests, converging towards similar configurations in both indentation directions relatively to the indenter position (*e.g.* become parallel to it). This would decrease the overall indentation modulus, and reduce the anisotropy. In this case, our calibration procedure would underestimate k and ρ.

Properties of the Shale Building Block

Among the other output information provided by the model calibration, the stiffness tensor of the shale building block is of outmost importance. The individual stiffness coefficients appear very contrasted, especially for C_{13}. For instance, we have for shale 1 ($M_s = 34.5, \nu_s = 0.3$, in GPa): $C_{11} = 24, C_{12} = 7.7, C_{13} = 1.7, C_{33} = 3.1, C_{11} = 2.1$, and for shale 3 ($M_s = 38.5, \nu_s = 0.3$, in GPa): $C_{11} = 36, C_{12} = 11.3, C_{13} = 1.9, C_{33} = 4.2, C_{11} = 3$. In terms of indentation moduli, the predicted peak values at level 'I' that correspond to the indentation moduli in the stiff and weak axes of the elementary block, $\max M$ and $\min M$, are for the three shales (on average from different calibrated values of M_s, ν_s):

$$(\max M, \min M) = (15; 4) - (19.5; 5.5) - (23.5; 6)\ GPa \tag{7.12}$$

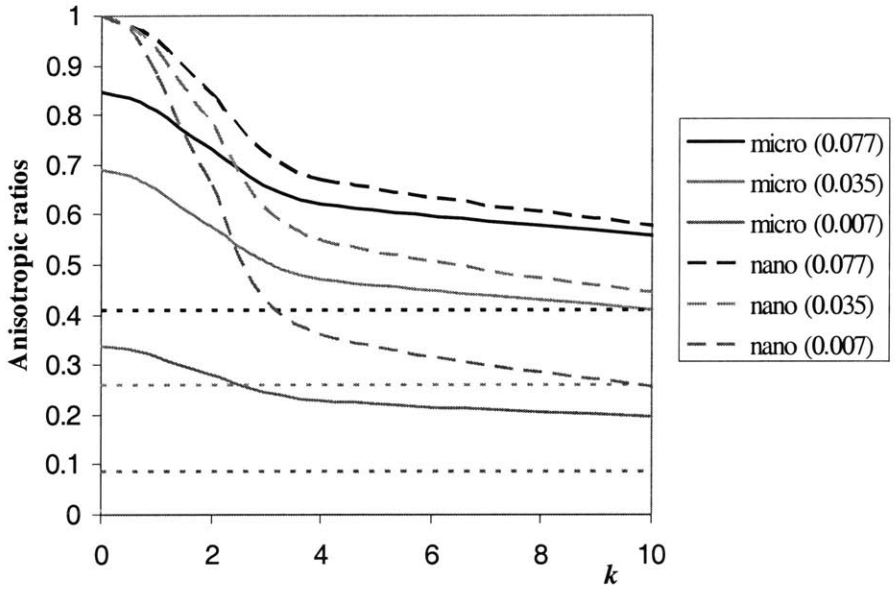

Figure 7-3: Anisotropic ratios r^I (nano), r^{II} (micro) as a function of k for various pore aspect ratios $(0.077; 0.035; 0.007)$ for a shale with $M_s = 35GPa$, $\nu_s = 0.3$ and $\phi_c = 0.2$. The horizontal asymptotes give the anisotropic ratios of the shale building block.

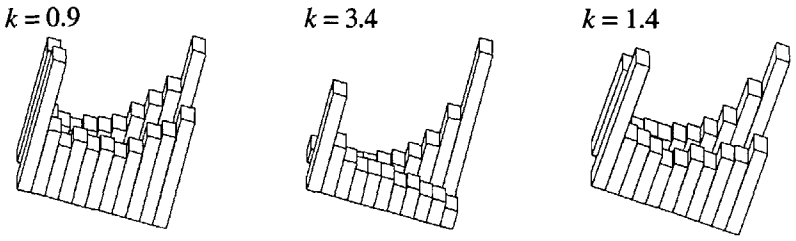

Figure 7-4: Predicted distributions of nanoindentation moduli for shales 1 (left), 2 (middle) and 3 (right), normal to bedding (front) and in bedding (back) directions. The histogram is obtained from 200 simulated tests.

These values are in good agreement with the range of nano-indentation moduli found in the frequency plots of Fig. 5-5.

An additional, qualitative argument for the relevance of the model can be made using the predicted model distributions of indentation moduli at Level 'I'. Fig. 7-4 shows the clear bimodal predicted distribution predicted from 200-tests samples, in in-bedding direction and normal-to-bedding direction. As the anisotropy increases through the $k-$parameter, the distributions become non symmetric, which is in good agreement with the experimental observation (Fig. 5-5). The presence of other peaks in the experimental frequency plots could be an effect of experimental noise such as surface roughness. It can also come from the fact that with force driven tests, the depths differ roughly by a factor of 2 from one extreme of the range to the other. The material is not the same over the whole range of indentation moduli. Finally, an eventual rotation of flakes during the loading phase could lead to an additional intermediary peak.

But the overall picture that emerges from the calibration procedure at Levels '0', 'I' and 'II', testifies to the relevance of our model.

7.2 Validation by Means of Prediction of the Macroscopic Stiffness

7.2.1 Procedure

For validation purposes, we use a second independent experimental data set for each shale material: the dynamic elastic stiffness values determined by UPV measurements, $\mathbb{C}_{\text{exp}}^{III,dyn}$(provided by ChevronTexaco, see Section 5.7.2). We compare these dynamic values to the undrained model stiffness values, which are obtained from the poroelastic model properties $\mathbb{C}_{\text{hom}}^{III}, \mathbf{b}^{III}, M^{III}$ (relations (6.91), (6.84b) and (6.90)).

This validation reads formally:

$$\left|\left|\mathbb{C}_{\text{exp}}^{III,dyn} - \mathbb{C}_{\text{hom}}^{III,un}\right|\right| \leq \epsilon^{III} \tag{7.13}$$

where a small error ϵ^{III} corresponds to a perfect prediction.

The inclusions contain mostly quartz, but also very stiff component in fewer quantities. Appendix F provides a generalization of the relations (6.84) for several types of inclusions. For the sake of simplicity, we use a single family of inclusion with average inclusion stiffness properties. The difference on the undrained homogenized stiffness $\mathbb{C}_{\text{hom}}^{III,un}$ was found to be almost insignificant. The undrained properties were derived using a bulk water modulus $K_{fl} =$ 2.3 GPa.

7.2.2 Predicted Macroscopic Undrained Stiffness

The comparison of experimental *vs.* predicted undrained stiffness properties is displayed in Figures 7-5, 7-6 and 7-7. Since this data set has not been used in the calibration of the model parameters, the good agreement (except for shale 3, which will be examined later) is a good indication of the model's capability to capture the essential poroelastic behavior of shale materials. We can see that the influence of the choice of ν_s for calibration has a very small effect on the macroscopic stiffness. It seems that the calibration made with the microindentations gives better predictions. All coefficients are reasonably well predicted, except C_{13}, which is generally underestimated, while C_{44} tends to be overestimated.

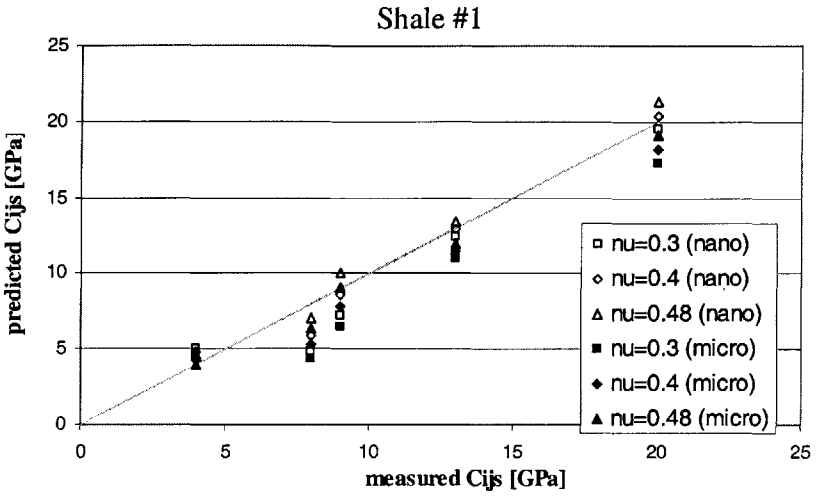

Figure 7-5: Predicted vs. measured C_{ij}s, for shale #1 using the calibrated input parameters.

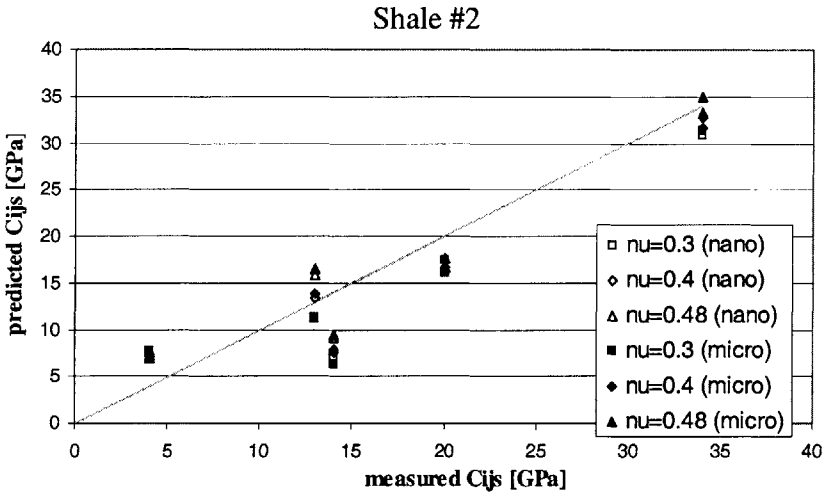

Figure 7-6: Predicted vs. measured C_{ij}s, for shale #2 using the calibrated input parameters.

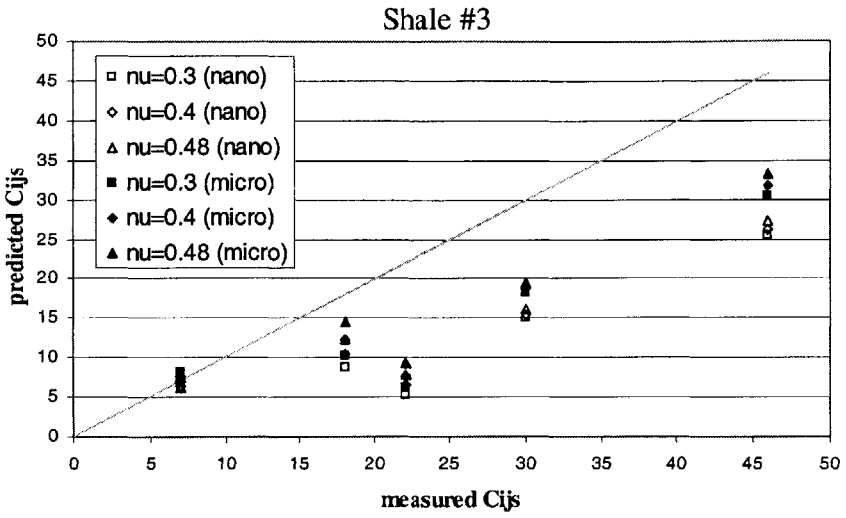

Figure 7-7: Predicted vs. measured C_{ij}s, for shale #3 using the calibrated input parameters.

7.2.3 Anisotropy

The anisotropy induced by the pore aspect ratio can be considered as the base source of anisotropy of shales. Figure 7-8 summarizes the experimental and predicted ratios of anisotropy in terms of indentation moduli, at levels 'I', 'II and 'III' and for the three shales investigated in our study. A distinction is made at level 'I', between the anisotropy of the building block (solid lines), and the anisotropic ratio obtained from indentations (dotted lines). The shale building block anisotropy is very similar for the three shales: $r^0 \simeq 0.27$. A second source of anisotropy of shales stems from some preferential orientation of building blocks at level 'I' in the statistical measure r^I, and at Level 'II' in r^{II}, which is captured in our model through the $k-$factor. On Fig. 7-8, we can clearly see that for all shales, r^{II} is smaller than r^I, but higher (closer to 1) than the one of the elementary building block of Level 'I'. At Level 'III', the model predicts less anisotropy than what is obtained from UPV measurements, but conserves the relative degree of anisotropy between shale 1, 2, and 3. This could be explained by some anisotropy induced by the inclusion distribution in the microstructure, which is not captured by a model with spherical, randomly distributed inclusions. The predicted anisotropic ratios are closer to 1 than the experimental ones, especially for shales 2 and 3 that contain more inclusions than shale 1.

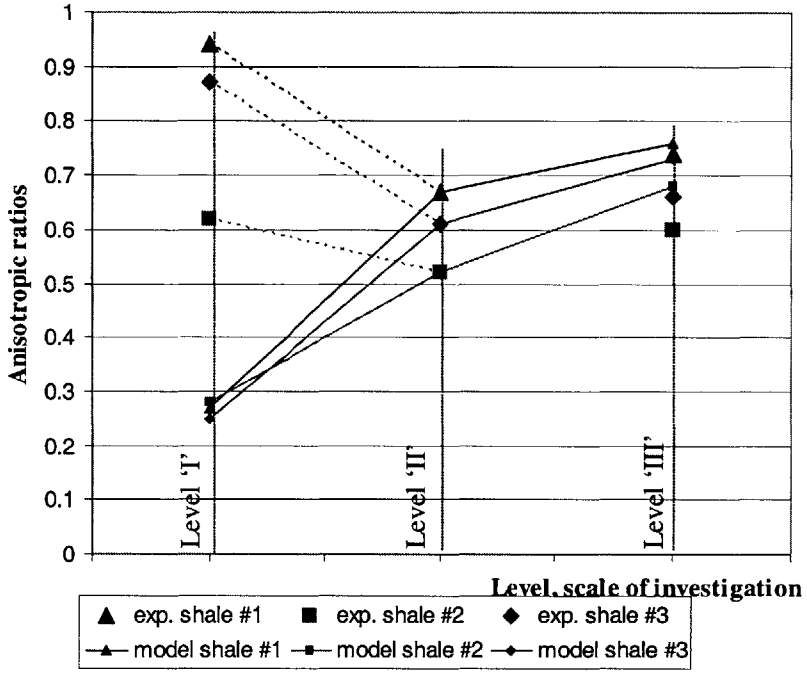

Figure 7-8: Experimental (from nano-, micro- indentations, and macro- UPV measurements) and predicted anisotropic ratios at levels 'I', 'II' and 'III'. The dotted lines refer to the statistical measure of anisotropy at Level 'I'.

7.2.4 Poroelastic Properties

Table 7.2 provides a summary of the predicted poroelastic properties at different scales for the three shale materials considered in this study. The input parameters are the values from Table 7.1, where we use for the solid phase stiffness the calibration results from the microindentation tests: $M_s = M_s^{micro}$. It is worth noting that the difference in between the Biot coefficients strongly reflects the anisotropy induced by the pore aspect ratio. The anisotropy of the Biot coefficients decreases from the shale elementary block to Level 'II' and to Level 'III' as the homogenized stiffness. On the other hand, unlike the stiffness constants, the Biot coefficients are sensitive to the choice of ν_s in the calibration. Indeed, both vertical and horizontal Biot coefficients tend to 1, for increasing Poisson's ratios. In the limit of the incompressible solid phase, $\nu_s = 1/2$, all Biot coefficients are equal to 1: The volumetric strain is entirely transmitted through the pore space deformation.

7.2.5 The Case of Shale #3

How can we explain that the model underestimates the stiffness of shale #3 by almost 30%? There is little difference in the indentation moduli between Shale #2 and shale #3 at levels 'I' and 'II' (see Tables 5.3 and 5.4) whereas their macroscopic stiffness differ by 20-30%. There are slightly more inclusions in shale #3, but this difference is too small to quantitatively explain the stiffness increase of shale #3 relative to shale #2 between micro and macro scale. Therefore, from an experimental point of view, there must be another phase at work in shale #3, that is not sensed in indentation tests, but strongly in UPV-measurements.

This phase is most probably a hematite phase present in shale #3. Such a hematite phase coats clay particles, acting as a cementing agent. During the high-stress indentation loading phase, this coating is broken, while it remains intact in the low stress-amplitude ultrasonic experiments. If we assume that clay particles are entirely coated, the strain would be strongly non uniform along one particle, especially at level 'I' where the depth of indentation is smaller than the size of one clay flake. Thus, the elastic response at the beginning of the unloading would reflect a smaller damaged stiffness. This may also explain why indentation moduli at Level 'I' are somewhat smaller than the ones at Level 'II'.

We want to consider the role of hematite in our micromechanics model. Figure 7-9 displays

	Shale #		1			2			3		
Level 0	ν_s	[1]	0.3	0.4	0.48	0.3	0.4	0.48	0.3	0.4	0.48
(M_s^{micro})	M_s	[GPa]	30	32	34.2	36	38.0	41	36.3	38.7	41
Level I	C_{11}	[GPa]	20.8	22.8	25.3	30.1	32.9	37.2	35.8	39.3	43.9
$\theta = 0$	C_{12}	[GPa]	6.7	9.9	13.3	9.7	14.4	19.9	11.3	17	23.1
$\varphi = 0$	C_{13}	[GPa]	1.4	2	2.8	2.1	3.1	4.4	1.9	3.0	4.4
(Drained)	C_{33}	[GPa]	2.7	2.8	3.0	4.2	4.5	4.8	4.2	4.4	4.7
	C_{44}	[GPa]	1.9	1.8	1.7	2.9	2.7	2.6	3.0	2.8	2.7
	b_{11}	[1]	0.58	0.87	0.94	0.49	0.68	0.92	0.44	0.66	0.91
	b_{33}	[1]	0.92	0.95	0.99	0.9	0.93	0.98	0.91	0.94	0.99
	N	[GPa]	4.54	4.47	4.46	5.9	5.99	6	4.9	5.96	5
Level II	C_{11}	[GPa]	11.2	11.5	11.9	18.5	19.2	20.3	19.0	19.7	20.5
(Drained)	C_{12}	[GPa]	3.1	3.9	4.6	5	6.6	8.2	5.1	6.4	7.8
	C_{13}	[GPa]	1.6	2.1	2.7	2	2.8	3.7	2.1	3.1	4
	C_{33}	[GPa]	5.8	5.9	6.2	6.3	6.6	6.9	8.4	8.7	9
	C_{44}	[GPa]	3.1	2.9	2.8	4.4	4.2	4.1	5.0	4.8	4.6
	b_{11}	[1]	0.77	0.87	0.94	0.7	0.82	0.95	0.71	0.84	0.96
	b_{33}	[1]	0.87	0.92	0.99	0.88	0.92	0.98	0.86	0.92	0.98
	N	[GPa]	4.54	4.47	4.46	5.9	5.99	6	4.9	5.96	5
Level III	C_{11}	[GPa]	17.3	18.1	16.5	31.3	32.7	34.8	30.4	31.7	33.2
(Undrained)	C_{12}	[GPa]	N.A.	N.A.	N.A.	N.A.	N.A.	N.A.	N.A.	N.A.	N.A.
	C_{13}	[GPa]	N.A.	N.A.	N.A.	N.A.	N.A.	N.A.	N.A.	N.A.	N.A.
	C_{33}	[GPa]	11.1	11.5	9.3	16	16.7	17.5	18.2	18.8	19.6
	C_{44}	[GPa]	N.A.	N.A.	N.A.	N.A.	N.A.	N.A.	N.A.	N.A.	N.A.
	b_{11}	[1]	0.73	0.83	0.92	0.62	0.73	0.84	0.61	0.72	0.83
	b_{22}	[1]	0.84	0.89	0.95	0.83	0.87	0.92	0.79	0.84	0.98
	N	[GPa]	5.37	5.28	5.3	7.63	7.7	7.69	6.4	6.45	6.47

Table 7.2: Predicted poroelastic properties at different scales.

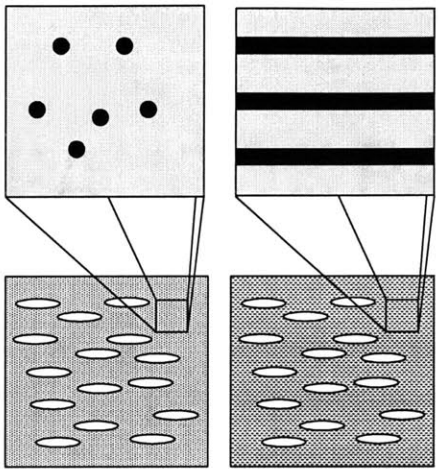

Figure 7-9: Schematic micromechanical model of the hematite coating. In the damage configuration (left), hematite is considered as dispersed inclusions in a clay matrix. In the intact state (right), hematite coating is represented as a laminate with layers of clay minerals.

a very schematic micromechanical model for both damaged and intact situations, that can be used for a quantitative assessment. We use the damage model (Fig, 7-9, left) to refine the calibration model, and use the intact one (Fig, 7-9, right) to predict macroscopic undrained stiffness $\mathbb{C}^{III}_{u,\text{hom}}$. This model adds one homogenization step to the previous presented one. For the calibration model, a Mori-Tanaka estimate (6.34) is used in which hematite is represented in form of inclusions in a clay matrix. In the prediction model, the laminate scheme (6.66), also used between Levels 'I' and 'II', is employed. These refined models do not require any additional unknown parameter: the stiffness of hematite, and its volume fraction in the clay phase f_h, are known; here, $f_h = 0.058$ from Table 4.1. The separation of scales condition (2.55) may not be verified in this additional homogenization step, but our intention is to obtain an order of magnitude of the influence of hematite microstructure in the clay phase. Fig. 7-10 displays the predicted undrained stiffness with the hematite reinforced model of the solid phase at level 'I'. The predicted stiffness coefficients are now in excellent agreement with the experimental values. The anisotropy is slightly underestimated, maybe due to the choice of a transversely isotropic solid phase. These results show that a single phase can be very important, even when other parameters like volume fractions and individual constituents stiffness are kept equal.

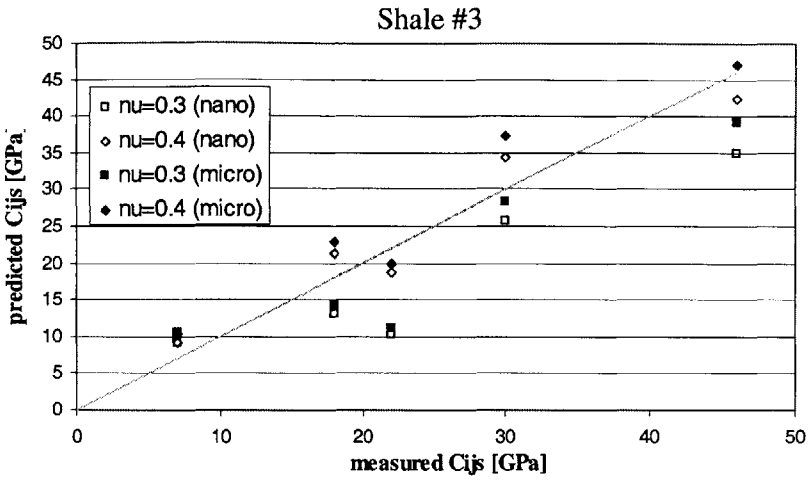

Figure 7-10: Predicted vs. measured C_{ij}s, for shale 3 using a hematite reinforced micromechanical model. The model calibration was made with the damaged hematite model .

The results are summarized in Table 7.3. From the calibrated solid phase stiffness E_s and Poisson's ratio ν_s, the clay stiffness was back analyzed knowing the stiffness of hematite and its volume fraction. We obtained a slightly modified clay solid phase stiffness which is closer to the calibrated E_s for the other shale materials.

7.3 Conclusion

Is it possible to capture the observed macroscopic variability of shales elastic properties through a handful of easily identifiable varying parameters? The question raised at the beginning of our study can now be answered: By means of four model parameters, the multiscale elastic properties of shales have been modeled quite successfully. In particular, the observed evolution of the anisotropy was explained, as a consequence of common morphological features.

Two of the model parameters, the elastic constants of the pure clay phase, seem to be (almost) independent of the specific shale material, and in particular of the mineralogy. A third model parameter, the pore aspect ratio, appears to be related to the porosity; most probably as a result of the burial diagenesis: the greater the burial depth, the higher the packing density of

		Level 'III' Undrained	
ν_{clay}	[1]	0.315	0.415
M_{clay}	[GPa]	36.3	38.7
E_{clay}	[GPa]	32.7	32
ν_s	[1]	0.3	0.4
M_s	[GPa]	38.5	41.1
E_s	[GPa]	35	34.5
C_{11}	[GPa]	39.4	47.2
C_{12}	[GPa]	N.A.	N.A.
C_{13}	[GPa]	N.A.	N.A.
C_{33}	[GPa]	28.5	37.5
C_{44}	[GPa]	N.A.	N.A.
b_{11}	[1]	0.5	0.56
b_{33}	[1]	0.62	0.58
N	[GPa]	20.33	32.28

Table 7.3: Predicted poroelastic properties of shale 3 at different scales, using a hematite reinforced model.

the clay particles. Such high packing densities are indicative of an ordered structure of the shale building blocks (clay particle packages) at level 0. The $k-$factor which is the only remaining (true) degree of freedom of the model, provides another source of anisotropy.

What we retain from the calibration-validation procedure is the following:

1. The little difference in clay stiffness between different shale materials gives a strong argument to support our assumption that the elasticity of shales materials is determined primarily by the porosity and the inclusion volume fractions, which are taken into account in our model. The influence of the clay mineralogy seems more difficult to assess.

2. The little difference in the anisotropic ratio of the elementary building block between different shales suggests that by their particulate nature, porous clay composites share a common instrinsic anisotropy, due probably to common particle shapes.

3. From the calibration procedure, the orientation distribution of the clay particles in form of the $k-$parameter, does not exhibit significant invariant properties. In turn, the accuracy of the calibration and the good predictive capabilities of the model confirm the relevance of the laminate model of the particles spatial distribution at Level 'II'.

Chapter 8

Towards an Engineering Model for Shale Materials

The three investigated shale materials have different mineralogy, porosity and inclusion volume fractions, but they do not represent all possible shales. One needs another sample of shale materials to test the model in more extreme situations and to confirm our interpretation of the model parameters. In this chapter, six other shales of known mineralogy and porosity will be used to test our model. We start out by assessing the model parameters from the available experimental data. Then we compare the predicted homogenized stiffness with available experimental values. Finally, the model is refined to improve its predictive capability a larger range of shale materials. In particular, low porosity and high porosity shales will be discussed.

8.1 Test of the Model on Other Shales

To test the predictive capabilities of the model, we use three other shales tested by Chevron-Texaco and three shales of known mineralogy and porosity found in the literature.

8.1.1 Choice of Model Parameters

Table 8.1 displays the volume fractions and porosities of the six shales used as a base to test the model predictive capabilities. The mineralogy of shales 4, 5 and 6 was provided by ChevronTexaco. The mineralogy of the Cretaceous, Jurrassic and Kimmeridge shales were

shale		4	5	6	C [48]	J [49]	K [49]
Inclusions	Total	29	27.4	14	65	35	39
	Quartz	20	18	9	50	29	30
	KFedspar	6	3	1	11	2	2
	Plagioclase	2	4	1	0	0	5
	Calcite	0	1	0	0	1	0
	Mg-Calcite	0	0	0	0	0	0
	Dolomite	0	1	0	0	1	0
	Pyrite	0	0	0	4	2	2
	Siderite	2	1	3	0	0	0
	Ankerite	0	0	0	0	0	0
	Hematite	0	0	1	0	0	0
Porosity (PMI)		19.6	26.2	11.8	11	9.2	2.5
Clay	Total	51	46.4	74	24	56	58
	Kaolinite	-	-	-	4	-	22
	Illite	-	-	-	9	-	30
	Smectite	-	-	-	8	-	5
	Other (Chl.)	-	-	-	3	-	2
Clay Porosity		27.9	36.1	13.7	31.3	14	4.1

Table 8.1: Mineralogy (volume percent) of the six shale materials considered for testing the predictive capabilities of the model (C= Cretaceous shale, J=Jurassic shale, K=Kimmeridge shale).

found in the literature [53], [48], [49], [50].

Table 8.2 summarizes the chosen model parameters for the 6 shales used. The input elements for the predictions are:

1. A single set of elastic constants of the pure clay phase ($M_s = 35$ GPa, $\nu_s = 0.3$).

2. The pore aspect ratio determined from the clay matrix porosity with relation (7.8).

3. The $k-$factor was interpolated from the values of our three shale materials: A high value of k was chosen for low porosity, low inclusion content shales. Inversely, for high porosity, high inclusion content shales, a lower value of k was chosen. In all other cases, more importance was given to the porosity in the choice of the k-factor. Figure 8-1 reports the values of k for all shales in a clay porosity *vs.* inclusion volume fraction plot. For shales 1, 2, and 3, the k-values were calibrated from the indentation tests. For the other shales, the values were chosen by considering similarity with shales 1, 2 and 3, leading to a satisfactory prediction of the macroscopic shale anisotropy. Therefore, we can try

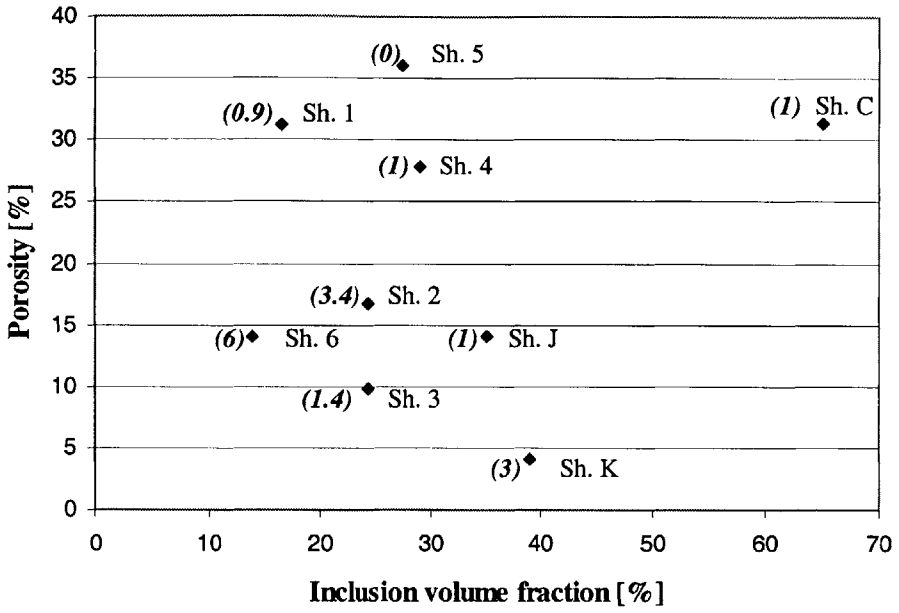

Figure 8-1: Empirical relations between the calibrated k parameter, inclusion volume fractions, and clay porosity ϕ_c. The values of k are indicated in italic on the graph.

to be more precise about the choice of k knowing a priori porosity and inclusion volume fraction only. A trend appears on Figure 8-1, that k decreases for increasing clay porosity and inclusion content. It is difficult to conclude which of the two parameters dominates the evolution of k in the present set of data. Shale #3 seems to be particular among the other shales, since its k-value is surprisingly low. This may be a consequence of its high hematite content, while it is premature to extract interpolation formula from Figure 8-1. The trend on this figure gives some hints that more research on shale elasticity could lead to an assessment of k, from the mineralogy and porosity data.

8.1.2 Prediction of Undrained Macroscopic Stiffness.

Figure 8-2 displays a comparison of predicted *vs.* experimental values for the new set of shale materials. What is given for these shale materials is the porosity, the inclusion volume fraction and the clay mineralogy (Table 8.1). The input for the predictions are given in Table 8.2.

Shale	4	5	6	C [48]	J [49]	K [49]
Inclusions	31	29	14.4	65	35	39
Clay Porosity	31	44	14.1	31.3	14	4.1
M_s [GPa]	35	35	35	35	35	35
ν_s [1]	0.3	0.3	0.3	0.3	0.3	0.3
ρ [1]	0.057	0.077	0.026	0.072	0.028	0.0077
k [1]	1	0	6	1	1	3

Table 8.2: Clay porosities, inclusion volume fractions, and chosen model parameters for shale materials.

The comparison of predicted *vs.* experimental dynamic measurements shows generally a good agreement for all shale materials, in which the clay phase is the load bearing phase. This is the case of shale materials having neither an excessive clay porosity, nor an excessive inclusion volume fraction. In this case, the overall anisotropy, through C_{33}/C_{11} is well predicted. However, a trend appears that is general for all shales: the model tends to underestimate the macroscopic stiffness of very low porosity shales, and to overestimate the stiffness of high porosity shale materials.

8.2 Limitations

Some limitations of the predictive capabilities of our model relate to: either high silt inclusion materials or extremely low or high porosity shale materials. Both limitations are probably due to limitations of the homogenization scheme we employ. Indeed, the schemes employed assume that the load bearing phase is the clay phase (and not the inclusion phase), so that predictions will certainly be inaccurate for high quartz inclusion shale materials (for example cretaceous shale having $f_i = 65\%$). Furthermore, it is quite unlikely that the schemes can capture extremely low packing density (*ie.* ultra-high porosity materials), which are much below the random close-packed limit (RCP) [28]. In fact:

- Inclusion rich shales may no longer have a clay load bearing phase. Moreover, the Mori-Tanaka scheme is limited to inclusion volume fractions smaller than 20-30%: it cannot predict the contacts between inclusions, which may certainly affect the mechanical response of inclusion rich shales.

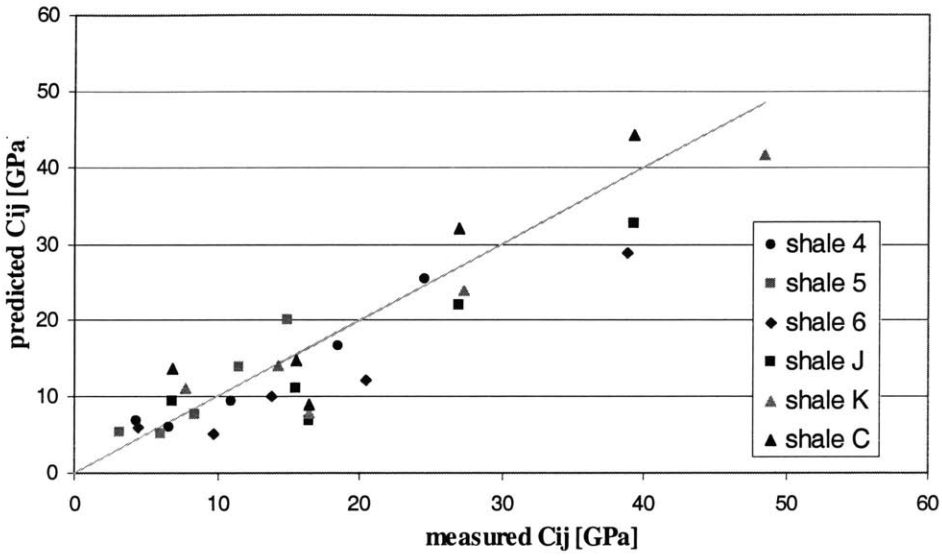

Figure 8-2: Predicted *vs.* measured C_{ij}s, for the 6 additional shales using the calibrated input parameters.

- The stiffness of shales with very high porosity seems to be overestimated by the model. This is not surprising: the range of validity of the Mori-Tanaka scheme is limited, and does not predict a critical porosity beyond which the homogenized stiffness goes to zero. From packing theory, it is known that such particulate systems cannot achieve porosity higher than some threshold [51], [28].

- The model underpredicts the overall stiffness of very low porosity shale materials by up to 30% (*e.g.* shale #6). This may be due to a stiffening effect induced by a lower particle-to-particle contact compliance and a higher coordination number[1]. Such a trend was observed in the calibrated solid phase stiffness of shales 1, 2 and 3 in (7.6) and (7.7). This suggests that, as the porosity decreases, the deformation activates the intrinsic stiffness of clay minerals rather than their interface properties.

- Shale #3 in particular is a low porosity, very compacted shale, for which the calibrated

[1] In granular material systems, the coordination number refers to the average number of contacts per particle [51].

model predictions underestimate the macroscopic values. But shale #3 also has a different morphology at level '0': it is a mixture of clay particles and hematite. An explanation for the discrepancy between microindentations and macroscopic values may come from the different levels of strain achieved in theses experiments: During the indentation loading phase, the thin hematite coatings and cementing precipitates break and contribute in the unloading phase as unconnected inclusions in a clay matrix as discussed previously. By contrast, for UPV measurements, levels of strain are so small that the hematite is intact, and its microstructure plays a stiffening role. That is why a refined version of the micromechanical model was designed for shale #3, which gives a good estimate of the macroscopic stiffness.

- It may be possible that the effect of clay mineralogy plays a role on the elastic properties. For instance smectite rich shales may be softer in general than other, all other parameters being equal. From the present investigation however, the clay porosity appears as the dominant factor, that must be predicted accurately. Figure 8-3 displays C_{11} and C_{33} at Level 'II' as a function of porosity. The model predictions employ a unique solid phase stiffness ($M_s = 35$ GPa,$\nu_s = 0.3$), the linear relation (7.8) between porosity and pore aspect ratio, and $k = 1.5$. The figure also displays experimental values obtained from the calibration of the indented shales. For the other shales, a backward homogenization scheme (level 'III' to level 'II') was applied to extract from the macroscopic stiffness the pure clay phase behavior. It is interesting to note that the model predicts an almost linear increase of the stiffness with the clay content. The experimental points are well captured by the model in the range of porosities of shales 1,2 and 3. However, the experimental trend seems to give to porosity a more important effect on the stiffness than the model does, hinting towards the existence of a clay content threshold (resp. clay porosity threshold) below which the stiffness goes to zero (around $(1 - \phi_c) \sim 40\%$). Such a threshold is not included in our mode, which may explain why our model underpredicts (resp. overpredicts) low (resp. high) porosity shales.

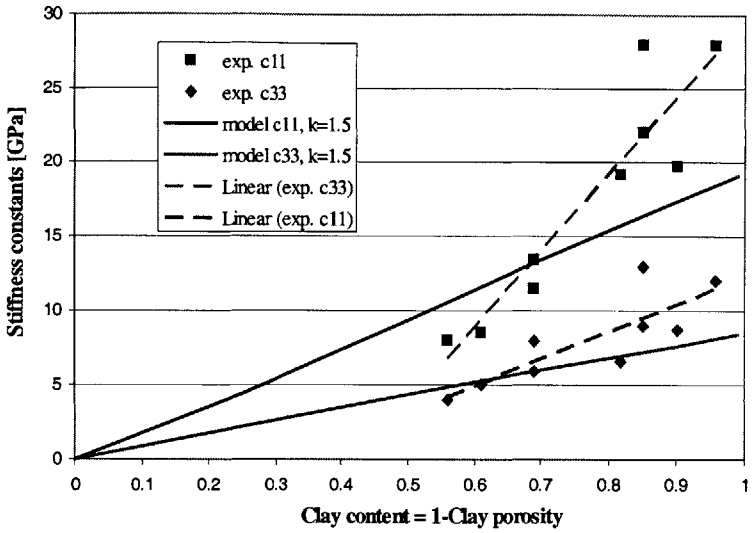

Figure 8-3: Effect of porosity on C_{11} and C_{33} coefficients of shale porous clay phase (Level 'II'). The model predictions with unique solid phase stiffness and porosity/aspect ratio relation for k=1.5 are are compared with experimental points.

8.3 Refinements

One way to refine the model in order to follow the experimental trend found on Figure 8-3, is to use different values for the solid phase stiffness depending on the clay porosity. This solid phase stiffness should range at least from 25 to 50 GPa, in order to give good predictions for all shales studied here. This method is no doubt useful, and may have a physical meaning for low porosity shales: in a high compaction state, the particle to particle contact activates the clay stiffness (rather than the interfaces). As a consequence, the solid phase stiffness, which includes contact properties, is stiffer. On the other hand, this method hides the limitations of the Mori-Tanaka scheme which is incapable of predicting percolation thresholds for high porosity shales.

8.3.1 Refinement For High Porosity Shales

The mercury porosimetry data (Fig. 4-7) show that all pores have the same size. We assume that this is the case with the ellipsoidal representation of pores. In this case, there is a threshold ϕ^{crit} at which all pores will percolate and isolate solid elements. In order to model this

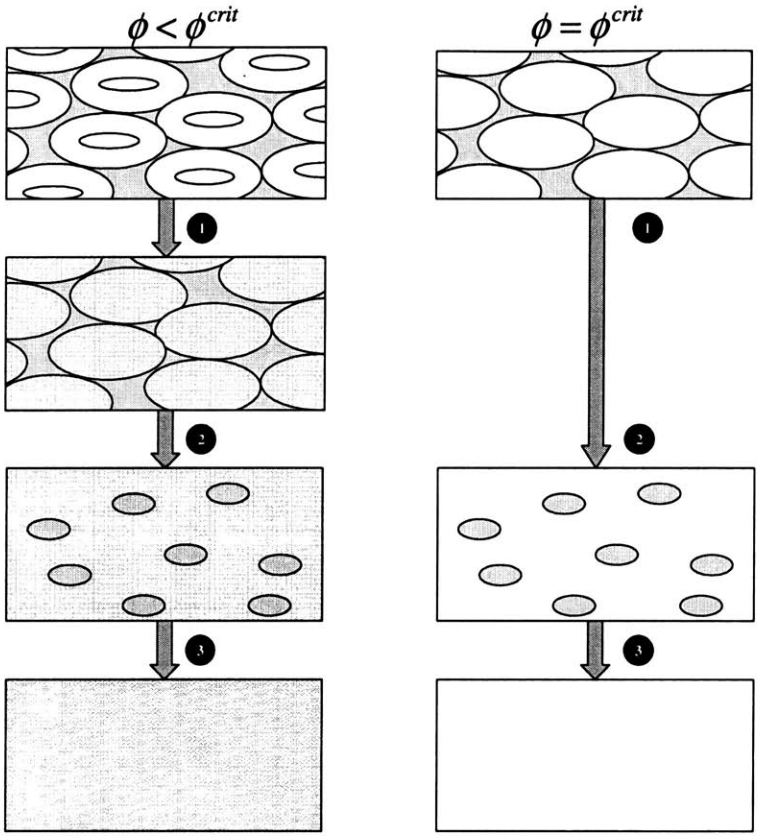

Figure 8-4: Modified micromechanical model of the shale elementary building block. Two homogenization steps are used, and the solid is divided artificially in two phases. The first solid phase is mixed with the enclosed porosity (1), and then reinforced by the second one (2 and 3).

phenomenon, it is convenient to separate the homogenization into two steps. In a first step, we consider the material at its porosity threshold ϕ^{crit}, and the remaining solid phase will be seen as an inclusion in the pore space (Fig. 8-4, right). For smaller porosities (Fig. 8-4, left), pores fill a fraction of the space they occupy at critical porosity, the other fraction being occupied by the solid phase.

First, the porosity is mixed with this surrounding solid. Then, the remaining solid phase is added as inclusions in this homogenized medium. For low porosities, this scheme merges with the Mori-Tanaka estimate, but yields a zero homogenized stiffness once the porosity reaches a threshold value. Indeed, in this case, the first homogenization gives a zero stiffness which will

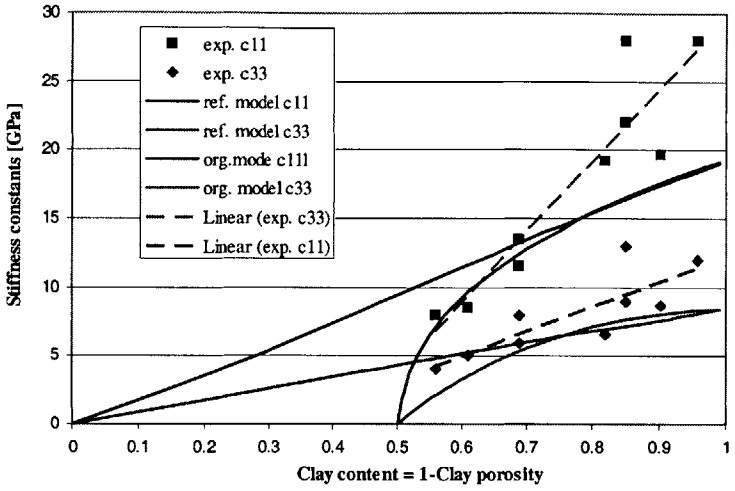

Figure 8-5: Effect of porosity on C_{11} and C_{33} coefficients of shale porous clay phase (Level 'II'). The model predictions are reported with a unique solid phase stiffness and k=1.5. Two different relations ϕ *vs.* ρ are considered: a linear one, and a quadratic one with a minimal value of ρ_0.

not be modified by adding solid inclusions (Fig. 8-4, right).

This model adds another unknown parameter to the problem, ϕ^{crit}. Figure 8-5 shows the difference between the original model and the modified one, at the scale of the shale building block Level 'II'. The stiffness coefficients C_{11} and C_{33} backanalyzed from macroscopic data are also displayed on the graph for comparison. In a first approximation, it seems reasonable to say that this threshold common to all shales. From all the shales presented in our study and from Fig. 8-5, it is likely that $\phi^{crit} \approx 50\%$. The modified model presented on Figure 8-5 uses a threshold of porosity of 50%, and reproduces well the experimental trend of C_{11} for high porosity shales. It underestimates the values of C_{33}, but for high porosity shales, the choice of $k = 1.5$ may not be representative. Indeed, k affects more more C_{33} than C_{11}.

8.3.2 Refinement For Low Porosity Shales

A possible refinement for low porosity shales consists in modeling the respective influence of contact and bulk forces in the solid phase elasticity at level '0'. This could give a quantitative

explanation of an eventual solid phase stiffening occurring in low porosity shales. A stiffer solid phase then gives stiffer homogenized stiffness predictions. The difficulty comes from modeling contact properties in a linear continuum framework.

A possibility would be to model the clay particles as inclusions in a solid possessing low shear modulus. This fluid-like medium would account for the low contact compliance between clay particles. By changing the proportion of clay in this mixture representing our current solid phase stiffness, one could easily model stiffer or softer solid phases. It would also explain give better predictions of the coefficients C_{13} than C_{44} at the macroscale, but it is premature to consider this method for a practical use. In fact, this approach requires the allocation of a volume to a fictitious phase that is supposed to model surface properties.

Another way to allow the model to predict a higher stiffness for low porosity shales consists in postulating a non linear relation between porosity and aspect ratio. Indeed, for very low porosities, pore aspect ratios in the order of 1/80 do not make much physical sense. If one assumes that the pore aspect ratio reaches a strictly positive value ρ_0 for a zero porosity, then the model predicted macroscopic stiffness are higher. However, the anisotropy is severely reduced. In this case, the intrinsic anisotropy of clay minerals might play a role.

8.4 Conclusion

The proposed multiscale shale model has generally good predictive capabilities, particularly for shales in which the porous clay phase in the load bearing phase. In this case, it is possible to predict the stiffness of shale materials with high accuracy. For more extreme morphologies and compositions, the predictions come close to the experimental ones by $\pm 30\%$. The two limitations of the proposed model relate to very high or very low clay porosity materials. Two possible micromechanical approaches are presented. One proposes a model for high porosity shales that predicts a critical porosity at which the stiffness of porous clays vanishes. The other gives a micromechanical model for the solid phase stiffening for low porosity shales. These approaches are compatible; and the model for high porosity shales does not differ much from the model used for the indentation calibration.

Part V

Conclusion and Perspectives

Chapter 9

Conclusions

9.1 Summary of the Main Findings

We raised the question whether it were possible to break shale materials down to a scale where materials no longer change from one material to another, and to upscale the behavior from the nanoscale to the macroscale of engineering applications. Based on a combination of indentation analysis and microporomechanics analysis of shale materials, the tentatively answer is yes!

1. Level '0': At a nanoscale, most geomaterials are colloidal material systems, in which repulsive contact forces are in equilibrium with cohesive bonds. The material response in shales at very fine scales is dominated by these surface properties, rather than by mineral properties. It is most likely that the scale of material invariant properties of natural composites is related to the predominant effect of such surface properties, which no-doubt depend on the type of mineral bonding. We come to this conclusion from the backanalysis of measured nano and micro indentation results of shales, which seem to converge towards a single set of material properties for each class of materials: a conceptual pure clay solid phase stiffness.

2. Level 'I': At a scale of hundreds of nanometers, shales possess characteristic packing densities, as a consequence of the material genesis, *ie.* deposition and burial diagenesis. This packing density defines a particular solid-pore space microstructure, the shale building block, *ie.* the packages of clay particles. Shale invariant properties (from level '0') and

the packing mode (from level 'I') translate into a base mechanics behavior. The porosity ('one minus packing density') which manifests itself at this scale, defines much of the poromechanics behavior of shales at larger scales.

3. Level 'II': At a micrometer scale, the behavior of shale materials is a consequence of morphology; *ie.* of the particular orientation and spatial distribution of building blocks. The preferred alignment of building blocks increases the elastic anisotropy, as well as their privileged deposition along planes of separation.

4. Level 'III': This is the scale where this approach catches up with other experimental techniques, by bringing new insight into the mechanical sources of elastic properties and some quantitative means to assess elastic properties.

9.2 Contributions of this Study

In this study, several new contributions were made. They include:

1. The explicit determination of the indentation modulus of transverse isotropic solids, as a function of stiffness constants, when the indented surface belongs to a plane of material symmetry (Chapter 3, Section 3.1.2).

2. The multiscale micromechanical modeling of shale elastic properties (Chapter 6).

3. The interpretation of indentation tests on shale materials in a statistical sense (Chapter 6, Section 6.3 with Section 5.5.2 of Chapter 5).

4. The identification of some material invariant properties of shales, and in particular of some key parameters controlling the anisotropy of shales: the pore aspect ratio and the orientation distribution of clay particles (Chapter 7, Section 7.1).

5. An engineering approach to predict shale elastic properties with accuracy from accessible field quantities, such as mineralogy and porosity (Chapter 7, Section 7.2 and Chapter 8).

6. A refined micromechanical model that predicts the elastic properties of shales with high porosity (Chapter 8, Section 8.3.1).

9.3 Current Limitations and Perspectives

Our approach has pushed the limits of nanoindentation and microporoelastic analysis further. It appears that the elastic analysis of nanoindentation load *vs.* depth curves is limited by the accuracy of the determination of the contact area. Indeed, indentation analysis relies on approximate interpretations, since the solutions of elastoplastic contact problems do not exist.

Continuum microporomechanics is a powerful technique, but its tools do not apply, by definition, to particulate materials such as compacted clay minerals, which form the load bearing phase of shales. In particular, the capability of micromechanics to model interface properties, which most probably govern elastic and strength properties of shale materials, is still very limited.

It appears that our multiscale micromechanical model had some difficulties in predicting the stiffness properties of shales with very low and very high porosities. The proposed model refinements can provide an answer, but need more experimental testing. The model also failed to determine C_{44}, C_{13} stiffness constants with accuracy. This limitation may originate from the assumption about the isotropy of the clay solid phase stiffness.

Finally, by modeling the anisotropy of shale materials with two simple parameters, it appears that the determination of the k-parameter is difficult from mineralogy and porosity only. This determination could be improved if indentation tests were performed on other shale materials and used for model calibration.

Therefore, a investigation of shale mechanical properties should combine:

1. An analysis of the indentation of materials with elastoplastic and time-dependent properties,
2. The development of upscaling schemes for particulate and colloidal systems,
3. A better determination of shale microstructure and mechanical properties at all scales,
4. A better understanding of the physics of clay particles;

Then it should ultimately be possible to 'break the code' of shale materials; relate elasticity, strength and permeability of shales at the macroscopic scale, to morphological parameters,

mineralogy, and constitutive properties. Things will still take some time regarding strength properties, requiring advances in the interpretation of strength properties from indentation tests and in non-linear microporomechanics, to ultimately arrive at identifying material invariant nanostrength properties. This is a formidable challenge!

9.4 Industrial Benefits

The initial objective of this study of shale elasticity was to identify the stiffness of different types of clay minerals and their relative impact on the macroscopic elasticity. By means of nanoindentation and microporomechanics, we showed that it is the porosity and the associated anisotropy that determines shale elastic properties, especially C_{11} and C_{33}. This identification of the key parameters of shale elasticity is of great benefit for the industry: the most accessible data are the shale bulk density, that gives access to the shale cutting porosity, assuming that the mineral densities are about the same (on the order of 2.65). The other accessible information is the coefficient C_{33} that one can obtain from a simple seismic vertical compressive wave velocity measurement. Using these two information in addition to the invariant shale properties, it is possible -with the developed model- to determine the in-bedding stiffness C_{11}, which is more difficult to obtain in the field. In practice, this method will need an iterative process, but will eventually provide an estimate of the full stiffness tensor of the considered shale layer, and thus potentially some information about the wave propagation properties, that have become more and more critical in recent years, as the need for high quality reservoir imaging has been growing.

Appendix A

Model of the Indentation Unloading Load *vs.* Depth Unloading Curves

This Appendix develops a new method to calculate the area of contact in an indentation test, from the shape of the unloading load *vs.* depth curve. It complements the developments presented in Chapter 2 (Section 2.2.5), and aims at improving the Oliver and Pharr method (2.52) [64] of the determination of the contact area.

Several authors have studied the indentation unloading phase [69], [73]. Since the self-similarity is not valid anymore, since the unloading phase is equivalent to the reloading phase of a sharp indenter in an imprint. The conventional analysis of indentation cannot be applied. In order to circumvent this obstacle, Pharr *et al.* [69] have introduced the concept of an equivalent indenter. The problem of the indentation in an imprint is modeled by the indentation in a half-space with an indenter with a particular shape. This shape reflects the distance between the original indenter and the deformed surface. Pharr *et al.* used indenter shapes described by $f(\rho) \propto \rho^n$ which are not compatible with the dimensional analysis. Our objective is to provide a different equivalent indenter shape which depends on the imprint geometry and is constructed from self-similar parameters.

A.1 Equivalent Indenter Concept

For a general elasto-plastic solid, the unloading phase of the indentation is assumed purely elastic. For a conical indenter, the permanent deformation can be characterized by:

- The depth h_f that is measured at the deepest point, relatively to the origin O, the first indented point on the half-space surface;
- the projected radius a_f of the imprint left on the surface, measured from the center of the imprint to the furthest observable edge of contact;
- the semi angle of the imprint around its origin α_f;
- The height η_f of the imprint sides relative to the half-space surface, *ie.* the final pile-up.

Fig. A-1 illustrates different types of imprints together with the related parameters. If we were able to construct the unloading phase by analyzing the indentation on an imprint, the reloading phase, then we would be able to:

- Obtain a better accuracy for determining the contact area in the estimation of the hardness and stiffness properties, by an inverse analysis of the unloading curve,
- Make a link between the strength properties and the observable characteristics of the imprint.

On Fig. A-1 we can see that in some particular cases (a), and (b), these parameters are not independent: $a_f = h_f \tan\alpha_f$ and $a_f = (h_f + \eta_f)\tan\alpha_f$, respectively. Even if we neglect the self equilibrated stress field remaining around the imprint, it is quite difficult to analyze quantitatively the indentation of such a modified half-space. However, it is possible to find an indenter shape depending on the imprint characteristics that gives a similar load vs depth curve when indenting a perfect elastic half space. In particular, Pharr and Bolshakov [69] have proposed the notion of an "equivalent indenter" defined by the conical profile $f(\rho,\theta) = B\rho^d$ in order to reproduce unloading curves whose monomial fits $P = a(h - h_f)^r$, and for which yield values of r around 1.2 to 1.6.for Berkovich indenter. For a perfectly elastic half-space and for such indenter shapes we have:

$$r = \frac{d+1}{d}$$

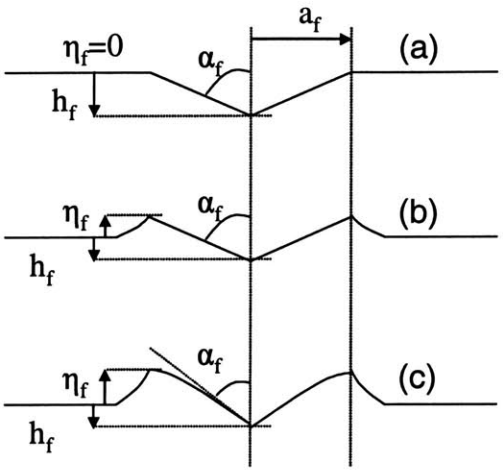

Figure A-1: Different imprint types, with the related parameters h_f, a_f, α_f, η_f.

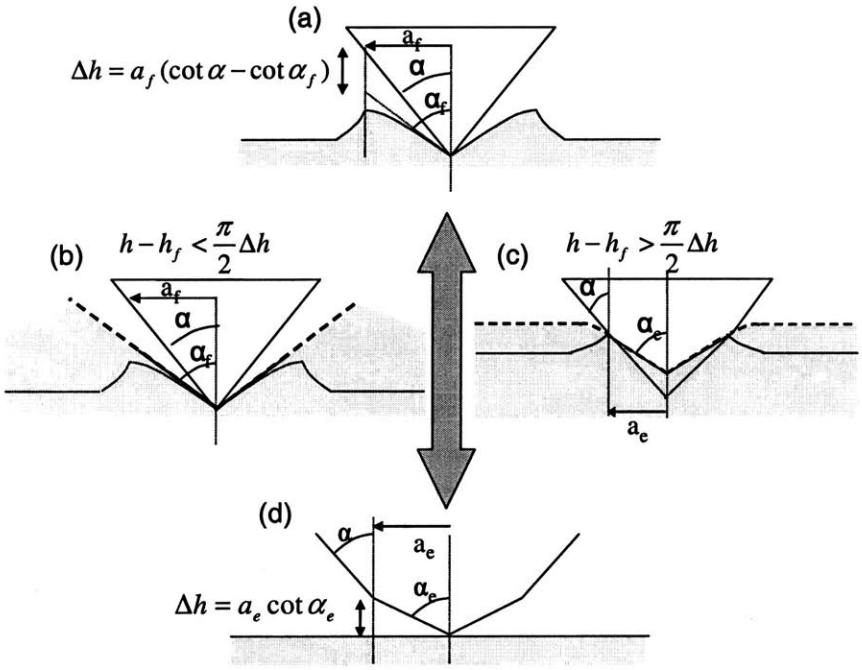

Figure A-2: The reloading phase (a) and the corresponding equivalent indenter (d). In the beginning (resp. end) of the reloading (resp. unloading), the imprint is considered infinitely large (b) and the indentation load vs. depth relation is approximated from the self similar one of a cone with angle α_e (d). For higher depth (c), the same relation for a special equivalent indenter (d) is used.

For instance, a parabolic indenter for which $d = 2$ will produce a load *vs.* depth exponent $r = 1.5$. This concept can be applied over for a large range of unloading curves [69], however physically speaking, the indenter shape parameters B and d offer limited interpretation.

Another way to model such equivalent indenters comes from the geometry of the imprint, and of the related reloading phase which we can separate into two steps. In order to simplify the analysis of the reloading phase we consider

$$h_e = h - h_f$$

- First, for h_e small compared to $f = h_f$, the indentation in the imprint is assumed to be equivalent to the indentation in an infinite conical half-space (Fig. A-2), which we model as an indentation of an infinite half-space with an equivalent indenter of semi-angle α_e defined by (Fig. A-2):

$$\cot \alpha_e = \cot \alpha - \cot \alpha_f \tag{A.1}$$

  Another possible definition of α_e was given by Sakai [73],

$$\alpha_e = \alpha_f - \alpha \tag{A.2}$$

  equating the angles left between the cone and the solid in the two cases, whereas we equate here the vertical distances between solid and cone:

$$\Delta h = a_f(\cot \alpha - \cot \alpha_f) = a_e \cot \alpha_e \tag{A.3}$$

  where we make the approximation that $a_f = a_e$. (A.2) and (A.3) give the same expression at the first order approximation for $\alpha_f \sim \pi/2$, but (A.3) is more convenient for writing the expressions of the indentation depths.

- Then in the second (resp. first) part of the reloading (resp. unloading) phase, the indenter is in contact with the whole imprint surface. The previous assumptions are made and the pile-up is neglected.

A.2 Equivalent Indenter Solution

For isotropic elastic half-spaces, and axi-symmetric convex indenter geometries, Sneddon's solution [78] gives indentation depth h_e and total load P as a function of the projected contact radius a (see equations (3.2) and (3.3)). For an equivalent indenter defined by the axi-symmetric shape (Figure A-2, bottom):

$$f(\rho) = \begin{cases} \rho \cot \alpha_e \ ; \ \rho < a_e \\ (\rho - a_e) \cot \alpha + a_e \cot \alpha_e \\ = \rho \cot \alpha - a_e \cot \alpha_f \ ; \ \rho > a_e \end{cases} \tag{A.4}$$

The load *vs.* depth can be parametrized by a. In a normalized form, we have

$$\overline{a} = \frac{a}{a_e}; \ \overline{h_e} = \frac{h_e}{a_e}; \ \overline{P} = \frac{P}{M a_e^2} \tag{A.5}$$

$$\overline{h_e}(\overline{a}) = \begin{cases} \frac{\pi}{2} \overline{a} \cot \alpha_e \ ; \ \overline{a} < 1 \\ \frac{\pi}{2} \overline{a} \cot \alpha - \overline{a} \arctan\left(\frac{1}{\sqrt{\overline{a}^2 - 1}}\right) \cot \alpha_f \ ; \ \overline{a} > 1 \end{cases} \tag{A.6}$$

$$\overline{P}(\overline{a}) = \begin{cases} \frac{\pi}{2} \overline{a}^2 \cot \alpha_e \ ; \ \overline{a} < 1 \\ \frac{\pi}{2} \overline{a}^2 \cot \alpha - \overline{a}^2 \left[\arctan\left(\frac{1}{\sqrt{\overline{a}^2 - 1}}\right) - \sqrt{\overline{a}^2 - 1}\right] \cot \alpha_f \ ; \ \overline{a} > 1 \end{cases} \tag{A.7}$$

The normalized slope $\overline{S}(\overline{a}) = d\overline{P}(\overline{a})/d\overline{h_e}(\overline{a}) = S(\overline{a})/(M a_e)$ verifies the BASh formula (2.20):

$$\overline{S}(\overline{a}) = 2\overline{a} \ ; \ \forall \overline{a} \tag{A.8}$$

Note from this linear formula, that the unloading load *vs.* depth of this model shows no angular point, since $\overline{h_e}(\overline{a})$ does not have a zero derivative for $\overline{a} = 1$, or equivalently, the derivative of $\overline{a}(\overline{h_e})$ *w.r.t.* $\overline{h_e}$ is always finite. We can extract the explicit classical $\overline{P}(\overline{a})$ *vs.* $\overline{h_e}(\overline{a})$ relation for $\overline{a} < 1$ only:

$$\overline{P}(\overline{a}) = \frac{2}{\pi} \overline{h_e}(\overline{a})^2 \ \tan \alpha_e; \ \overline{a} < 1$$

A.3 Inverse Analysis of Unloading Curves

There are four parameters in the model presented above: h_f, a_f, α_f, η_f plus the indentation Modulus M that do not determine the maximum contact radius $a_{\max}$ at which the reloading (resp. unloading) phase stops (resp. starts). There are then 6 independent parameters that we need to assess from the unloading curve plots. From experimental curves, some values are classically obtained: $h_{\max} = h(a_{\max}), P_{\max} = P(a_{\max}), S_{\max} = S(a_{\max})$ and sometimes h_f. Less classical ones include the energy ratio $W_{elastic}/W_{total}$ but we cannot not explore here *a priori* any shape of loading curve. Using an appropriate fitting procedure of the unloading load *vs.* depth curve, it is possible to isolate the point $(\overline{h_e}(1), \overline{P}(1))$, from the $log(P)$ *vs.* $log(h)$ or from the plots of dP/dh or d^2P/dh^2 as a function of h. This point gives access to $h_e(a_e), P(a_e), S(a_e)$:

$$h_e(a_e) = \frac{\pi}{2} a_e \cot\alpha_e \ ; \ P(a_e) = \frac{\pi}{2} M a_e^2 \cot\alpha_e \ ; \ S(a_e) = 2Ma_e \tag{A.9}$$

Then it is possible to find the value of h_f, a_f, α_f, η_f, $a_{\max}, M$ by proceeding as follows:

1. From

$$S(a_{\max})/S(a_e) = a_{\max}/a_e \tag{A.10}$$

$$\overline{a}_{\max} = \frac{S(a_{\max})}{S(a_e)} \tag{A.11}$$

it is possible to determine $\overline{a}_{\max} = a_{\max}/a_e$

2. From (A.10) and

$$\frac{P(a_{\max})}{P(a_e)} = \overline{a}_{\max}^2 - \overline{a}_{\max}^2 \frac{2}{\pi}\left[\arctan\left(\frac{1}{\sqrt{\overline{a}_{\max}^2 - 1}}\right) - \sqrt{\overline{a}_{\max}^2 - 1} - \frac{\pi}{2}\right] \frac{\tan\alpha}{\tan\alpha_f - \tan\alpha} \tag{A.12}$$

$$\tan\alpha_f = \tan\alpha \frac{\frac{P(a_{\max})}{P(a_e)} - \overline{a}_{\max}^2 \frac{2}{\pi}\left[\arctan\left(\frac{1}{\sqrt{\overline{a}_{\max}^2 - 1}}\right) - \sqrt{\overline{a}_{\max}^2 - 1}\right]}{\frac{P(a_{\max})}{P(a_e)} - \overline{a}_{\max}^2}$$

we can assess α_f, the angle of the imprint, and the equivalent indenter angle α_e using (A.1).

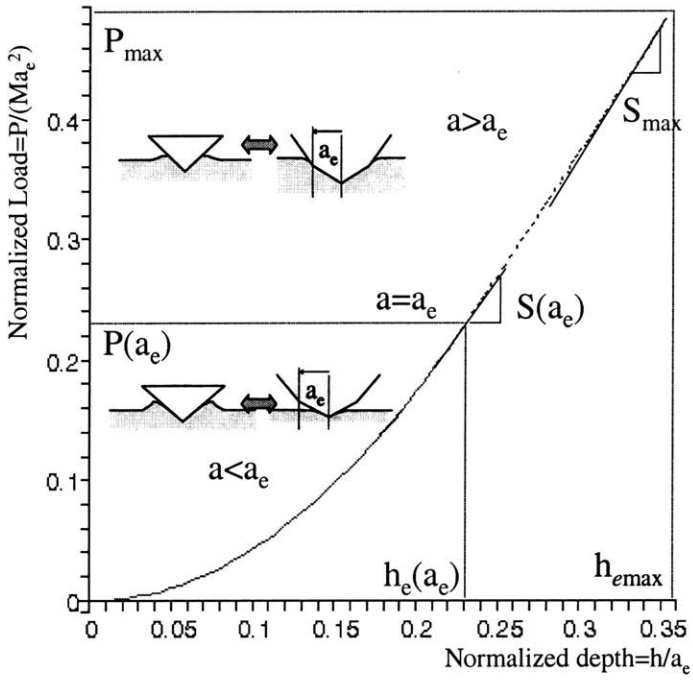

Figure A-3: The dimensionless load vs. depth curve predicted for a Berkovich equivalent conical indenter ($\alpha = 70.3°$), in an imprint defined by $\alpha_f = 78°$. $a_{\max}$ is chosen to be equal to $a_{\max} = 1.1a_e$.

3. From (A.10), (A.12) and

$$\frac{h(a_{\max}) - hf}{h(a_e) - h_f} = \frac{h_e(a_{\max})}{h_e(a_e)}$$

$$= \overline{a}_{\max} + \overline{a}_{\max}\left[1 - \frac{2}{\pi}\arctan\left(\frac{1}{\sqrt{\overline{a}^2_{\max} - 1}}\right)\right]\frac{\tan\alpha}{\tan\alpha_f - \tan\alpha} \tag{A.13}$$

We determine the permanent indentation depth h_f by:

$$h_f = \frac{h(a_{\max}) - \left\{\overline{a}_{\max} + \overline{a}_{\max}\left[1 - \frac{2}{\pi}\arctan\left(\frac{1}{\sqrt{\overline{a}^2_{\max}-1}}\right)\right]\frac{\tan\alpha}{\tan\alpha_f - \tan\alpha}\right\}h(a_e)}{1 - \left\{\overline{a}_{\max} + \overline{a}_{\max}\left[1 - \frac{2}{\pi}\arctan\left(\frac{1}{\sqrt{\overline{a}^2_{\max}-1}}\right)\right]\frac{\tan\alpha}{\tan\alpha_f - \tan\alpha}\right\}} \tag{A.14}$$

4. From (A.10), (A.12), (A.13) and

$$h(a_e) - h_f = h_e(a_e) = \frac{\pi}{2}a_e\cot\alpha_e \tag{A.15}$$

$$a_e = \frac{2}{\pi}\tan\alpha_e(h(a_e) - h_f) \tag{A.16}$$

we deduce the value of a_e (and a_f), as well as $a_{\max}$. (It is also possible to use $h(a_{\max}) - h_f$).

5. From (A.10), (A.12), (A.13), (A.15) and

$$S(a_{\max}) = 2Ma_{\max} \tag{A.17}$$

$$M = \frac{S(a_{\max})}{2a_{\max}} \tag{A.18}$$

the value of M can be found. (It is also possible to use $S(a_e)$, $P(a_{\max})$, or $P(a_e)$).

6. Finally, by comparing h_f with $a_e\cot\alpha_f$ we obtain an upper bound of the permanent pile up height η_f (see Fig. A-1(c)):

$$\eta_f < a_e\cot\alpha_f - h_f \tag{A.19}$$

By comparing $h(a_e) = h_e(a_e) + h_f$ with $a_e\cot\alpha_f$ we obtain a lower bound for η_f (see Fig. A-1(c)):

$$\eta_f > a_e\cot\alpha - h(a_e) \tag{A.20}$$

In order to compare the present derivation to the relatively simple method of Oliver and Pharr [64] we use

$$h_{c\max} = a_{\max} \cot \alpha \tag{A.21}$$

The previously assumed expression $h_{c\max}^{OP}$of the maximal contact depth reads for a conical indenter:

$$h_{c\max}^{OP} = h_{\max} - 2\left(1 - \frac{2}{\pi}\right)\frac{P_{\max}}{S_{\max}} \tag{A.22}$$

where:

$$h_{\max} = h_f + \frac{\pi}{2} a_{\max} \cot \alpha - a_{\max} \arctan\left(\frac{a_{\max}^2}{a_e^2} - 1\right)^{-1/2} \cot \alpha_f \tag{A.23}$$

Finally:

$$h_{c\max}^{OP} = h_f + a_{\max} \cot \alpha - \frac{2}{\pi} a_{\max} \arctan\left(\frac{a_{\max}^2}{a_e^2} - 1\right)^{-1/2} \cot \alpha_f - a_{\max}\left(1 - \frac{2}{\pi}\right)\sqrt{\frac{a_{\max}^2}{a_e^2} - 1}\cot \alpha_f \tag{A.24}$$

and:

$$h_{c\max} - h_{c\max}^{OP} = a_{\max}\left\{\frac{2}{\pi}\arctan\left(\frac{a_{\max}^2}{a_e^2} - 1\right)^{-1/2} + \left(1 - \frac{2}{\pi}\right)\sqrt{\frac{a_{\max}^2}{a_e^2} - 1}\right\}\cot \alpha_f - h_f \tag{A.25}$$

$h_{c\max} - h_{c\max}^{OP} = 0$ for a perfectly flat reindented half-space ($\alpha_f = \pi/2,\ h_f = 0$). In general, $-h_f < h_{c\max} - h_{c\max}^{OP} < a_{\max}\cot \alpha_f - h_f$ which means that the area of contact can be either under- or overestimated. For most indentations $a_e < a_{\max} < 2a_e$, and

$$0.86 a_{\max} \cot \alpha_f - h_f < h_{c\max} - h_{c\max}^{OP} < a_{\max} \cot \alpha_f - h_f \tag{A.26}$$

(the minimum of r.h.s. of (A.25) is obtained for $a_{\max}/a_e = \sqrt{2/(\pi - 2)} \simeq 1.32$). This difference then depends on η_f. From (A.21) and (A.26) we get:

$$a_{\max}(\cot \alpha - \cot \alpha_f) + h_f < h_{c\max}^{OP} < a_{\max}(\cot \alpha - 0.86 \cot \alpha_f) + h_f \tag{A.27}$$

So $h_{c\max}^{OP}$ is indeed very close to the left term $a_{\max} \cot \alpha_e + h_f$ referring to the first self-similar phase of the indentation ($a < a_e$).

A.4 Energy and Other Considerations

The elastically stored energy W_{el} reads:

$$W_{el} = \int_0^h P(h)dh = \int_0^{h(a)} P(a)\frac{dh}{da}(a)da$$

$$W_{el}(a < a_e) = M\frac{2}{3\pi}h_e^3 \tan\alpha_e = M\frac{\pi^2}{12}a^3 \cot^2\alpha_e$$

$$W_{el}(a_e) = M\frac{2}{3\pi}h_e^3 \tan\alpha_e = M\frac{\pi^2}{12}a_e^3 \cot^2\alpha_e$$

It seems that $W_{el}(a > a_e)$ cannot be evaluated analytically.

The hardness at the end of the loading phase is expressed as:

$$H_{\max} = \frac{P}{\pi a_{\max}^2} = \frac{M}{2}\cot\alpha - \frac{M}{\pi}\left[\arctan\left(\frac{1}{\sqrt{a_{\max}^2/a_e^2 - 1}}\right) - \sqrt{a_{\max}^2/a_e^2 - 1}\right]\cot\alpha_f \quad \text{(A.28)}$$

In general:

$$H = \frac{P}{\pi a^2} = \begin{cases} \frac{M}{2}\cot\alpha_e \ ; \ \overline{a} < 1 \\ \frac{M}{2}\cot\alpha - \frac{M}{\pi}\left[\arctan\left(\frac{1}{\sqrt{a^2/a_e^2 - 1}}\right) - \sqrt{a^2/a_e^2 - 1}\right]\cot\alpha_f \ ; \ \overline{a} > 1 \end{cases} \quad \text{(A.29)}$$

This method has the advantage to rely on self similar parameters describing the geometry of the indent: a_f, η_f, h_f, a_e are linearly related to $h_{\max}$. The scheme has not been verified on real data since it is quite difficult to isolate the point where the second loading phase begins. The drawback of the approach is that a non smooth equivalent indenter is unlikely to be the best representation. As pointed out in [65], the equivalent indenter should have a blunt tip, since the stress singularity during the reloading phase is completely removed. A refinement of this model could consist in taking a parabola of revolution in the first phase, then to consider a normal cone in the second phase.

Appendix B

Indentation of Materials with Time-Dependent Deformation

This Appendix extends the tools of indentation analysis by developing a new solution for the indentation of linear viscoelastic solids. As shown in the dimensional analysis in Section 2.2.3, including time dependent properties in the formulation of the contact problem renders the analysis intricate. However, it is possible to maintain the self-similarity of the problem as long as a simple viscoelastic model, or a poroelastic study with specific boundary conditions is applied. The main outcome from the theoretical derivations is an extension of the inverse analysis of experimental load *vs.* depth curves to more complex and real material behaviors.

B.1 Viscoelastic Behavior

B.1.1 Viscoelastic Material Properties

Viscoelasticity may be an issue when the indented material shows a creep behavior during the constant load phase. But it also affects the measurement of the elastic modulus during the unloading phase. We assume that, the stress strain relation shows some hereditary behavior of the form:

$$\sigma(t) + A\frac{d\sigma(t)}{dt} = B\varepsilon(t) + C\frac{d\varepsilon(t)}{dt} \tag{B.1}$$

In the case of isotropic materials, volumetric and deviatoric creep can be separated. Following Cheng *et al.* (2004) [13], such separation is achieved using

$$P^d s_{ij} = Q^d e_{ij} \ ; \ P^v \sigma_{kk} = Q^v \varepsilon_{kk} \tag{B.2}$$

where s_{ij} and e_{ij} are respectively the deviatoric stress and strain components $s_{ij} = \sigma_{ij} - \sigma_{kk}\delta_{ij}/3$, and $e_{ij} = \varepsilon_{ij} - \varepsilon_{kk}\delta_{ij}/3$. P^d, Q^d, P^v and Q^v are the linear operators:

$$P^d = \sum_{n=0}^{n=I_1} p_n^d \frac{\partial^n}{\partial t^n}, \ Q^d = \sum_{n=0}^{n=I_2} q_n^d \frac{\partial^n}{\partial t^n} \tag{B.3}$$

$$P^v = \sum_{n=0}^{n=J_1} p_n^v \frac{\partial^n}{\partial t^n}, \ Q^v = \sum_{n=0}^{n=J_2} q_n^v \frac{\partial^n}{\partial t^n} \tag{B.4}$$

where p_n^d, q_n^d, p_n^v and q_n^v are related to material constants. In the case of pure elasticity, the number of terms in (B.3) and (B.4) are such that I_1, I_2, J_1 and J_2 are zero, and

$$q_0^d/p_0^d = 2G \ ; \ q_0^v/p_0^v = 3K \tag{B.5}$$

where K and G are the bulk and shear moduli respectively. The volumetric stress strain law is assumed purely elastic whereas the deviatoric one contains a delayed behavior (Fig. B-1(a)) or a predominant viscous one (Fig. B-1(b)).

A 1-D analogy for the shear component can be captured by a spring-dashpot model in which spring elements correspond to the recoverable elastic strains. Depending on how these elements are assembled, one can distinguish two types of viscoelastic models from the load *vs.* depth curve (here in 1-D on Fig. B-1):

In the first case, after a cycle of loading and unloading, the total displacements do not come back to a zero value; whereas in the second case, a spring closes the end points of the dashpot so that if a zero force is prescribed, the total displacement will go back to zero after some period (creep recovery).

For the recoverable model, the equations (B.2) simplify:

$$\sigma_{kk} = 3K_1 \varepsilon_{kk} \ ; \ s_{ij} + p_1 \dot{s}_{ij} = q_0 e_{ij} + q_1 \dot{e}_{ij} \tag{B.6}$$

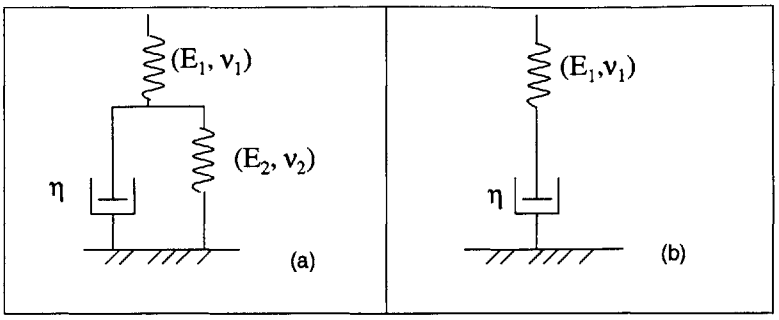

Figure B-1: 2D Standard viscoelastic model (a), and the particular case of Maxwell viscoelastic model (b).

where

$$p_1 = \frac{\eta}{G_1 + G_2} \; ; q_0 = \frac{2G_1G_2}{G_1 + G_2} \; ; \; q_1 = \frac{2G_1\eta}{G_1 + G_2} \tag{B.7}$$

The shear moduli G_1, G_2 and the elastic bulk modulus are derived from E_1, E_2, ν_1, ν_2 :

$$G_1 = \frac{E_1}{2(1+\nu_1)} \; ; \; G_2 = \frac{E_2}{2(1+\nu_2)} \; ; \; K_1 = \frac{E_1}{3(1-2\nu_1)} \tag{B.8}$$

The main difficulty coming from the time dependence, is the presence of the time variable. It is possible to get rid of the time using Laplace integral transforms, and solve the problem in the transform domain. The Laplace transform L_f of any function $f(t)$ is given by:

$$\hat{f}(s) = \hat{L}_f(s) = \int_{t=0}^{\infty} f(t)e^{-ts}dt \tag{B.9}$$

In the Laplace transform domain, all time derivatives are linear operators of s : $L_{f'}(s) = sL_f(s)$. All equations (boundary conditions, stress strain relation, etc.) can thus be written in the transform domain. The principle of superposition can then be applied: the solutions of the equations written with the variable s have the same solutions as the equations written with physical variables. Unfortunately, this principle is only valid when the surface S_u where displacements and the surface S_σ where force boundary conditions apply, do not depend on time. This is not the case for a general contact problem. For a flat punch, the principle holds, since the contact radius a is a constant. But for conical indentation one needs to restrict the

analysis first to a case where the area of contact is kept constant.

As discussed in Section 2.2.3, this is achieved by applying a Heaviside depth function:

$$h_0(t) = \begin{cases} 0, \ t < 0 \\ h_0, \ t \geq 0 \end{cases} \tag{B.10}$$

B.1.2 Step Depth: Relaxation

Since the area of contact is circular by symmetry and depends linearly on the maximum depth h_0 (see the dimensional analysis in Section 2.2.3), the actual area of contact follows a Heaviside function, too. In order to avoid the change of area of contact at time $t = 0$, the area of contact will still be defined as the final one for all times supposing that for $t < 0$, the displacements prescribed inside it, are zero.

The stress strain relation is written in the Laplace transform domain simply by transforming the differential equations linking stress and strain. The resulting expression is similar to a standard elastic Hooke's law in the variable s:

$$\hat{P}^d \hat{s}_{ij} = \hat{Q}^d \hat{e}_{ij} \ ; \ \hat{P}^v \hat{\sigma}_{kk} = \hat{Q}^v \hat{\varepsilon}_{kk} \tag{B.11}$$

The boundary conditions are also transformed:

$$h(\rho < a, z = 0, s) = \frac{h_0}{s} - \frac{\rho}{s \tan \alpha} \tag{B.12}$$

$$\sigma_{zz}(\rho > a, z = 0, s) = 0 \tag{B.13}$$

$$\sigma_{zr}(\rho > a, z = 0, s) = 0 \tag{B.14}$$

$$u(\rho \rightarrow \infty, z \rightarrow \infty, s) = 0 \tag{B.15}$$

The set of equations (B.11), (B.12) to (B.15) is coherent with a classical frictionless conical elastic indentation with a cone of half angle $s \tan \alpha$.

$$\sigma_{ij}, \varepsilon_{ij}, s_{ij}, e_{ij} \overset{replacing}{\longrightarrow} \hat{\sigma}_{ij}, \hat{\varepsilon}_{ij}, \hat{s}_{ij}, \hat{e}_{ij} \tag{B.16}$$

$$\bar{t}_i, \bar{u}_i \overset{replacing}{\longrightarrow} \hat{t}_i, \hat{u}_i \tag{B.17}$$

$$2G, 3K \overset{replacing}{\longrightarrow} \hat{Q}^d/\hat{P}^d, \hat{Q}^v/\hat{P}^v \tag{B.18}$$

Equivalently to the last replacement

$$E, \nu \overset{replacing}{\longrightarrow} \hat{E} = \frac{3\hat{Q}^d\hat{Q}^v}{2\hat{P}^d\hat{Q}^v + \hat{P}^v\hat{Q}^d}, \hat{\nu} = \frac{\hat{P}^d\hat{Q}^v - \hat{P}^v\hat{Q}^d}{2\hat{P}^d\hat{Q}^v + \hat{P}^v\hat{Q}^d} \tag{B.19}$$

The problem is solved using the classical result (3.12):

$$\begin{aligned} P(s) &= \frac{2}{\pi}\frac{E(s)}{1-\nu(s)^2}h^2 s\tan\alpha \\ &= \frac{2}{\pi}\frac{E(s)}{1-\nu(s)^2}\frac{h_0^2}{s}\tan\alpha \end{aligned} \tag{B.20}$$

where

$$\frac{E(s)}{1-\nu(s)^2} = \frac{\hat{Q}^d\left(2\hat{P}^d\hat{Q}^v + \hat{P}^v\hat{Q}^d\right)}{\hat{P}^d\left(2\hat{P}^v\hat{Q}^d + \hat{P}^d\hat{Q}^v\right)} \tag{B.21}$$

For the standard viscoelastic model (B.6),

$$\begin{aligned} \hat{P}^d(s) &= 1 + p_1 s\ ,\ \hat{Q}^d(s) = q_0 + q_1 s \\ \hat{P}^v(s) &= 1\ ,\ \hat{Q}^v(s) = 3K_1 \end{aligned} \tag{B.22}$$

$$\frac{E(s)}{1-\nu(s)^2} = \frac{4(3K_1G_1 + 3K_1G_2 + 3K_1\eta s + G_1G_2 + G_1\eta s)G_1(G_2+\eta s)}{(4G_1G_2 + 4G_1\eta s + 3K_1G_1 + 3K_1G_2 + 3K_1\eta s)(G_1+G_2+\eta s)} \tag{B.23}$$

The application of the inverse Laplace transform to (B.20) yields

$$P(t) = \frac{2}{\pi}\tan\alpha h_0^2\left[A + Be^{-\frac{t}{\tau_1}} + Ce^{-\frac{t}{\tau_2}}\right] \tag{B.24}$$

where

$$\begin{aligned} A &= \frac{4G_1G_2(3K_1G_1 + 3K_1G_2 + G_1G_2)}{(G_1+G_2)(3K_1G_1 + 3K_1G_2 + 4G_1G_2)} \\ B &= \frac{G_1^2}{G_1+G_2} \\ C &= \frac{27G_1^2K_1^2}{(4G_1+3K_1)(3K_1G_1 + 3K_1G_2 + 4G_1G_2)} \\ \tau_1 &= \frac{\eta}{G_1+G_2} \\ \tau_2 &= \eta\frac{3K_1+4G_1}{3K_1G_1 + 3K_1G_2 + 4G_1G_2} \end{aligned} \tag{B.25}$$

In the case of incompressible solid elements $\nu_1 = \nu_2 = 1/2$,

$$\frac{E(s)}{1-\nu(s)^2} = \frac{4E_1(E_2+3\eta s)}{3(E_1+E_2+3\eta s)} \tag{B.26}$$

Application of the inverse Laplace transform yields

$$P(t) = \frac{2}{\pi}\tan\alpha h_0^2\left[A + Be^{-\frac{t}{\tau_1}}\right] \tag{B.27}$$

where

$$\begin{aligned} A &= \frac{4E_1E_2}{3(E_1+E_2)} \\ B &= \frac{4E_1^2}{3(E_1+E_2)} \\ \tau_1 &= \frac{3\eta}{E_1+E_2} \end{aligned} \tag{B.28}$$

With this model, the limit $G_2 = 0$ corresponds to a Maxwell model (Fig. B-1(b))where the displacements are not infinite in a creep experiment.

$$P(t) = \frac{2}{\pi}\tan\alpha h_0^2\left[Be^{-\frac{t}{\tau_1}} + Ce^{-\frac{t}{\tau_2}}\right] \tag{B.29}$$

where

$$\begin{aligned} B &= G_1 \\ C &= \frac{9G_1K_1}{4G_1+3K_1} \\ \tau_1 &= \frac{\eta}{G_1} \\ \tau_2 &= \eta\frac{3K_1+4G_1}{3K_1G_1} \end{aligned} \tag{B.30}$$

Note that the total force is zero at the end of the relaxation phase ($t \to \infty$).

In the particular case of incompressible solid elements $\nu_1 = \nu_2 = 1/2$,

$$B = \frac{4E_1}{3}\ ;\ \tau_1 = \frac{3\eta}{E_1} \tag{B.31}$$

B.1.3 Load Step: Creep

It is possible to construct the displacement history necessary to obtain a step load profile. It is obtained directly from (B.24) by the theorem of superposition, without using the equivalence principle so that it does not violate the prior condition on the contact surface. In an incremental form, we note

$$dP(t) = \frac{2}{\pi} \tan \alpha R(t) d(h^2) \tag{B.32}$$

More generally, for any history of prescribed indentation depth $h(t)$,

$$P(t) = \frac{2}{\pi} \tan \alpha \int_0^t R(t-\tau) d(h^2(\tau)) \tag{B.33}$$

where $R(t)$ is the time dependent part of the relaxation function:

$$R(t) = \begin{cases} A + Be^{-\frac{t}{\tau_1}} + Ce^{-\frac{t}{\tau_2}}, \ t > 0 \\ 0, \ t < 0 \end{cases} \tag{B.34}$$

A creep function $h(t)$ depending on a step load $P(t) = P_0 H(t)$ is therefore characterized by

$$P_0 H(t) = \frac{2}{\pi} \tan \alpha \int_0^t R(t-\tau) d(h^2(\tau)) \tag{B.35}$$

This differential equation can be solved in the Laplace transform domain: $t \longrightarrow s$. The transformation gives

$$\frac{P_0}{s} = \frac{2}{\pi} \tan \alpha s \ \hat{R}(s) \widehat{h^2}(s) \tag{B.36}$$

and

$$\widehat{h^2}(s) = \frac{\pi P_0}{2 \tan \alpha s^2 \hat{R}(s)} = \frac{\pi P_0}{2 \tan \alpha} \frac{1 - \hat{\nu}^2}{s \hat{E}(s)} \tag{B.37}$$

from (B.20).

For the standard viscoelastic model considered, we obtain:

$$\widehat{h^2}(s) = \frac{\pi P_0}{2 \tan \alpha} \frac{(G_1(4G_2 + 4\eta s + 3K_1) + 3K_1(G_2 + \eta s))(G_1 + G_2 + \eta s)}{4s(K_1(3G_1 + 3G_2 + 3\eta s) + G_1(G_2 + \eta s))G_1(G_2 + \eta s)} \tag{B.38}$$

and

$$h(t)^2 = \frac{\pi P_0}{2\tan\alpha}[A + Be^{-t/\tau_1} + Ce^{-t/\tau_2}] \tag{B.39}$$

with

$$\begin{aligned} A &= \frac{(G_1+G_2)(4G_1G_2+3K_1G_1+3K_1G_2)}{4G_1G_2(3K_1G_1+3K_1G_2+G_1G_2)} \\ B &= -\frac{1}{4G_2} \\ C &= -\frac{3G_1^2}{4(3K_1+G_1)(3K_1G_1+3K_1G_2+G_1G_2)} \\ \tau_1 &= \frac{\eta}{G_2} \\ \tau_2 &= \eta\frac{3K_1+G_1}{3K_1G_1+3K_1G_2+G_1G_2} \end{aligned} \tag{B.40}$$

In a reverse analysis, in order to asses the coefficients of the model, one can perform a step load experiment and measure:

- The initial depth $h(0)$ to obtain the instantaneous response $A+B+C$
- The final depth $h(\infty)$ to obtain A
- The characteristic times τ_1 and τ_2

In general, unicity and existence of the solution are not guaranteed.

For incompressible solid the solution reads:

$$h(t)^2 = \frac{\pi P_0}{2\tan\alpha}\left[\frac{3}{4E_1} + \frac{3}{4E_2}\left(1 - e^{-\frac{E_2 t}{3\eta}}\right)\right] \tag{B.41}$$

and for a Maxwell viscoelastic model,

$$h(t)^2 = \frac{\pi P_0}{2\tan\alpha}\left[\frac{G_1+K_1}{4K_1G_1} + \frac{t}{4\eta} - \frac{G_1}{4K_1(3K_1+G_1)}e^{-\frac{t}{\eta}\frac{3K_1G_1}{3K_1+G_1}}\right] \tag{B.42}$$

B.1.4 Response to a Trapezoidal Loading

Now we can study the response to the classical loading conditions: a constant loading rate $\dot{P}$, dwelling phase ($\dot{P}=0$), and an unloading phase at $-\dot{P}$. The creep function is defined from (B.39) by

$$C(t) = \begin{cases} A + Be^{-\frac{t}{\tau_1}} + Ce^{-\frac{t}{\tau_2}},\ t > 0 \\ 0,\ t < 0 \end{cases} \tag{B.43}$$

Similarly to (B.35), the displacement response to a general loading history is given by:

$$h(t)^2 = \frac{\pi}{2\tan\alpha}\int_0^t C(t-\tau)dP(\tau) \tag{B.44}$$

$$h(t)^2 = \begin{cases} \frac{\pi}{2\tan\alpha}\dot{P}\int_0^t C(\tau)d\tau, t < t_1 \\ \frac{\pi}{2\tan\alpha}\dot{P}\int_{t-t_1}^t C(\tau)d\tau, t_1 < t < t_2 \\ \frac{\pi}{2\tan\alpha}\dot{P}\left[\int_{t-t_1}^t C(\tau)d\tau - \int_0^{t-t_2} C(\tau)d\tau\right], t > t_2 \end{cases} \tag{B.45}$$

In order to keep short expressions, the case of an incompressible solid gives:

$$h(t)^2 = \begin{cases} \frac{\pi}{2\tan\alpha}\dot{P}\frac{3}{4E_2^2E_1}\left[t(E_1+E_2)E_2 + 3E_1\eta\left(e^{\frac{-E_2t}{3\eta}} - 1\right)\right], t < t_1 \\ \frac{\pi}{2\tan\alpha}\dot{P}\frac{3}{4E_2^2E_1}\left[t_1(E_1+E_2)E_2 + 3E_1\eta e^{\frac{-E_2t}{3\eta}}\left(1 - e^{\frac{E_2t_1}{3\eta}}\right)\right], t_1 < t < t_2 \\ \frac{\pi}{2\tan\alpha}\dot{P}\frac{3}{4E_2^2E_1}\left[(t_1+t_2-t)(E_1+E_2)E_2 + 3E_1\eta\left(e^{\frac{-E_2t}{3\eta}}(1 - e^{\frac{E_2t_1}{3\eta}} + e^{\frac{E_2t_2}{3\eta}}) - 1\right)\right], t > t_2 \end{cases} \tag{B.46}$$

For $G_2 = 0$,

$$h(t)^2 = \begin{cases} \frac{\pi}{2\tan\alpha}\dot{P}\frac{1}{24\eta K_1^2G_1}\left[3t^2K_1^2G_1 + 6tK_1\eta(G_1+K_1) + 2G_1\eta^2\left(e^{\frac{-3K_1G_1t}{\eta(3K_1+G_1)}} - 1\right)\right], t < t_1 \\ \frac{\pi}{2\tan\alpha}\dot{P}\frac{1}{24\eta K_1^2G_1}\left[\begin{array}{c} -3t_1^2K_1^2G_1 + 6K_1^2G_1t_1t + 6K_1G_1\eta t_1 + 6K_1^2t_1\eta + \\ 2G_1\eta^2e^{\frac{-3K_1G_1t}{\eta(3K_1+G_1)}}\left(-e^{\frac{3K_1G_1t_1}{\eta(3K_1+G_1)}} + 1\right) \end{array}\right], t_1 < t < t_2 \\ \frac{\pi}{2\tan\alpha}\dot{P}\frac{1}{24\eta K_1^2G_1}\left[\begin{array}{c} -3K_1^2G_1(t^2+t_1^2+t_2^2) + 6(t_1+t_2-t)K_1\eta(G_1+K_1) \\ +2G_1\eta^2e^{\frac{-3K_1G_1t}{\eta(3K_1+G_1)}}\left(-e^{\frac{3K_1G_1t_1}{\eta(3K_1+G_1)}} - e^{\frac{3K_1G_1t_2}{\eta(3K_1+G_1)}} + 1\right) + 2G_1\eta^2 \end{array}\right], t > t_2 \end{cases} \tag{B.47}$$

This analysis shows that the hardness is no more independent of depth. The displacement response during the loading phase in Eq. (B.46) predicts a decrease of hardness during the loading phase, which has been the case for shales .Such pronounced viscoelastic effects could explain the (almost) linearity of the indentation curves on Fig. (5-1).

Appendix C

Scaling Relations and Approximated Expressions for Elasto-plastic Conical Indentations

When it comes to the indentation of composite materials, it is crucial to know more than just $h_{\max}$ about the scale investigated. Indentation tests are clearly surface tests, but access bulk properties. One needs to understand how the indented material is strained, and where the energies of elastic and plastic deformation are stored. This is important because the morphology of the material can change locally in the plastified region, and damage can occur as well. One must know from where the elasticity is recovered in order to check whether damage and plastic deformations influence the measured elastic properties. For instance, dealing with anisotropic heterogeneities, grains rotations can occur and lead to unrepresentative local properties interpretation.

One must distinguish the region where plastic deformations occur from the zone where elastic energy is activated. While the former is finite, the latter occupies, in theory, the whole half-space. As shown on Fig. (2-3), a finite element simulation performed in perfect linear elasticity of the stress field under the indenter shows that the zone where most of the elasticity is activated is nearly spherical with a diameter that is classically on the order of 3 to 5 times the indentation depth for a Berkovich indenter, and that can be associated with the diameter

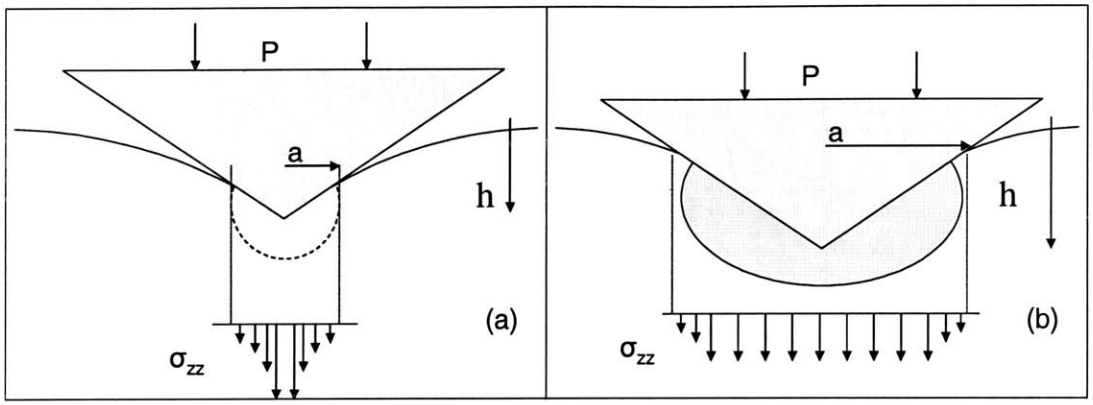

Figure C-1: Schematic pressure fields under the indenter, in perfect elasticity (a), elastoplastic (b) indentation when there is no pile-up.

of the contact zone.

The density of elastic energy decreases as function of the distance from the indenter: a rough estimate of its profile can be obtained by looking at the displacement response to a point indentation in an elastic half-space, the surface Green's function (see Section 3.0.4). The surface displacements are proportional to r^{-1}, strains and stresses to r^{-2} and energy density to r^{-4}. The decrease is the same for a real (not concentrated) indentation far from the indent. If we also assume from the finite element simulation that the energy density profile on the surface is also conserved at any point inside the half-space at a distance r from the origin, then the amount of energy stored on a sphere of radius r, centered at the origin decreases with r^{-2}. This asymptotic tail is well suited for integration so that finally the elastic energy stored outside a sphere of radius r decreases with r^{-1}. Finite element simulations and analytical studies [5] have shown that this is not much different whether a cone or a pyramid is considered. In the case of anisotropic materials, the activated zone shape will slightly change.

In real indentations, the zone where plastic deformation occurs is typically smaller, up to 1 to 3 times the indentation depth for a Berkovich indenter. Far from that region, the profile of elastic energy density is the same as for perfect elasticity. But inside, the stress singularity will no longer exist and smaller levels of stress and strain are encountered. In order to be more quantitative about the relative amount of elastic energy stored in the plastic zone, let

us compare the indentation on an elastoplastic material with the perfect elastic one where the elastic modulus is conserved (Fig. C-1). In both cases the overall load applied on the indenter is P. A greater area of contact $A_{ep} > A_e$ is achieved in the elastoplastic case so that:

$$P = \iint_{A_{ep}} \sigma_{zz}^{ep} = \iint_{A_e} \sigma_{zz}^{e} \tag{C.1}$$

In turn, the stresses in the plastic zone are assumed more or less constant in the case of a Von Mises material and smaller than the stresses in the perfect elastic contact zone (3.9):

$$p_{ep} = \sigma_{zz}^{ep}(\rho) < \sigma_{zz}^{e}(\rho) = p_e \cosh^{-1}\left(\frac{a_e}{\rho}\right) \tag{C.2}$$

where p_{ep} and p_e are the average pressures under the indenter, and a_{ep} and a_e are contact radii. From (C.1) and (C.2), it follows:

$$P = A_{ep}p_{ep} = A_e p_e \; ; \; \frac{p_e}{p_{ep}} = \left(\frac{a_{ep}}{a_e}\right)^2 \tag{C.3}$$

The elastic energy stored in a zone assumed to be of the size of the contact zone is:

$$E_e = \iiint_{V(A_e)} \boldsymbol{\sigma}^e : \mathbb{S} : \boldsymbol{\sigma}^e \; ; \; E_{ep} = \iiint_{V(A_{ep})} \boldsymbol{\sigma}^{ep} : \mathbb{S} : \boldsymbol{\sigma}^{ep} \tag{C.4}$$

By neglecting other components than σ_{zz} in the stress tensor, and taking the same profile of stress as in (C.2) where r is the distance to the origin, we obtain (by numerical integration for the pure elastic case):

$$E_e \simeq C^{-1}(.28)\; 2\pi p_e^2 a_e^3 \; ; \; E_{ep} \simeq C^{-1}\frac{2\pi}{3} p_{ep}^2 a_{ep}^3 \tag{C.5}$$

where C is a constant of elasticity, so that finally

$$\frac{E_e}{E_{ep}} \simeq \frac{a_{ep}}{a_e} \tag{C.6}$$

The elastic energies stored outside the "core" E'_e and E'_{ep} are roughly self-similar if one assumes that the stress fields are the same when expressed as a function of the dimensionless length

$r/a_e > 1$ and $r/a_{ep} > 1$. Then,

$$\frac{E'_e}{E'_{ep}} \simeq \left(\frac{a_e}{a_{ep}}\right)^3 \tag{C.7}$$

We can now calculate from the load *vs.* depth indentation curve in the perfect elastic case, the total energy stored in the contact zone,

$$P = \frac{2}{\pi} M h^2 \tan\alpha \; ; \; E_t = \int_{h=0}^{h_{\max}} P dh = \frac{2}{3\pi} M h^3 \tan\alpha \tag{C.8}$$

Expressed as a function of $a_e = \frac{2}{\pi} h \tan\alpha$ (C.8) yields:

$$E_e^t = \frac{\pi^2}{12 \tan^2\alpha} M a_{e\max}^3 \tag{C.9}$$

Doing the same for a flat punch, whose associated stress field [78],

$$\sigma_{zz}(\rho < a_{ep}, z = 0) = -\frac{Mh}{\pi a_{ep}^2} \sqrt{a_{ep}^2 - \rho^2} \tag{C.10}$$

is assumed to be close to the one of the elasto-plastic conical indentation, we have:

$$P = 2M a_{ep} h_{fp} = \pi a_{ep}^2 p_{ep} = \frac{\pi}{2\tan\alpha} M a_e^2 \tag{C.11}$$

where h_{fp} is the depth of the equivalent flat punch. Integration of P gives:

$$E_{ep}^t = \int_{a=0}^{a_{ep\max}} P dh = \frac{\pi^2}{3} p_{ep} a_{ep}^3 \tag{C.12}$$

and from (C.9) and (C.12)

$$\frac{E_e^t}{E_{ep}^t} = \frac{M}{4 p_{ep} \tan^2\alpha} \left(\frac{a_{e\max}}{a_{ep\max}}\right)^3 \tag{C.13}$$

In the limit case between pile-up and sink-in, $a_{ep} = \tan\alpha h$, and $h_{fp} = \frac{a_{ep}}{3\tan\alpha}$ if one considers that the volume of the penetrated cone $\frac{1}{3}\pi a_{ep}^2 (\frac{a_{ep}}{\tan\alpha})$ is equal to the one $\pi a_{ep}^2 h_{fp}$ of the equivalent flat punch. Then (C.11) and (C.12) lead to

$$P = 2M \frac{a_{ep}^2}{3\tan\alpha} \; ; \; E_{ep}^t = 2M \frac{a_{ep\max}^3}{9\tan\alpha} \tag{C.14}$$

Also, $\frac{a_{ep}}{a_e} \approx 1.13$. Finally, (C.13) is evaluated explicitly for a Berkovich indenter

$$\frac{E_e^t}{E_{ep}^t} = \frac{3\pi^2}{8\tan\alpha}\left(\frac{a_{e\max}}{a_{ep\max}}\right)^3 \approx 1.33\left(\frac{a_{e\max}}{a_{ep\max}}\right)^3 \approx 1.9 \tag{C.15}$$

Finally, (C.15) together with (C.6) and (C.7) yield:

$$\frac{E_{ep}}{E'_{ep}} \approx 1.1 \; ; \; \frac{E_e}{E'_e} \approx 1.8 \tag{C.16}$$

This rough estimate is not as accurate as results of finite element simulations, but it gives an order of magnitude of the proportion of elastic energy which is stored in the contact zone. This proportion tends to decrease as the indentation becomes more and more plastic. It also gives an order of magnitude of the ratio of the hardness over the indentation modulus M for which pile-up begins:

$$\frac{H}{M} = \frac{1}{3\pi\tan\alpha} \approx 0.038 \tag{C.17}$$

This value is very consistent with the ratio $Y/E \simeq 0.01$ that corresponds to pile up on Figure 2-6, if we assume that $H \simeq 3Y$, and $M \simeq E/0.9$. In this case (C.17) gives $Y/E \simeq 0.007$. Unfortunately, we could not test (C.17) with other indenter angles.

Appendix D

Shale Mass Fractions

Table D.1 gives the mineralogy of the six shales provided by ChevronTexaco. The mineral stiffness properties in Table D.2 were found in [59].

		Shale 1	Shale 2	Shale 3	Shale 4	Shale 5	Shale 6
Inclusions	Total	22	28	28.3	40	36	17
	Quartz	17	18	21	26	23	10
	KFedspar	22	3	1	3	6	1
	Plagioclase	11	2	2	6	4	0.6
	Calcite	0	1	0	0.6	1	0
	Mg-Calcite	0	0	0	0.5	0	1
	Dolomite	0	0	0	2	1	1
	Pyrite	.2	3	0.4	0	0	0.4
	Siderite	2	1	0.3	2	3	4
	Ankerite	1	0	0	0	0	0
	Hematite	0	0	5	0	0	1
Clay	Total	76	72	70	60	64	83
	1:1 kaolinite	36	21	9	8	22	42
	2:1	39	49	60	49	39	39
	Other	1	2	0.2	3	4	1.5

Table D.1: Mineralogy (mass fraction) of the investigated shale materials, provided by Chevron-Texaco.

		K [GPa]	G [GPa]
Inclusions	Quartz	37.9	44.3
	KFedspar	75.6	25.6
	Plagioclase	75.6	25.6
	Calcite	76.8	32
	Mg-Calcite	76.8	32
	Dolomite	94.9	45
	Pyrite	147.4	132.5
	Siderite	-	-
	Ankerite	-	-
	Hematite	98	93
clay	1:1 kaolinite	-	-
	2:1	-	-
	Other	-	-

Table D.2: Bulk and shear modulus of the principal minerals present in the investigated shales, from Mavko et al.

Appendix E

Eshelby and $\mathbb{P}$-tensors

E.0.5 Oblate Spheroidal Inclusion in an Isotropic Matrix

The non-zero components of the Eshelby tensor $\mathbb{S}$ for oblate spheroidal inclusions of aspect ratio $\rho = h/D < 1$ in a matrix of Poisson's ratio ν read:

$$S_{ijkl} = S_{jikl} = S_{ijlk} \tag{E.1}$$

$$\begin{aligned}
S_{1111} &= \frac{3}{8\pi(1-\nu)} I_{11} + \frac{1-2\nu}{8\pi(1-\nu)} I_1 = S_{2222} && \text{(E.2)}\\
S_{1122} &= \frac{1}{8\pi(1-\nu)} I_{12} + \frac{1-2\nu}{8\pi(1-\nu)} I_1 = S_{2211} && \text{(E.3)}\\
S_{1133} &= \frac{1}{8\pi(1-\nu)} \rho^2 I_{13} + \frac{1-2\nu}{8\pi(1-\nu)} I_1 && \text{(E.4)}\\
S_{3311} &= \frac{1}{8\pi(1-\nu)} I_{13} + \frac{1-2\nu}{8\pi(1-\nu)} I_3 = S_{3322} && \text{(E.5)}\\
S_{1212} &= \frac{1}{8\pi(1-\nu)} I_{12} + \frac{1-2\nu}{16\pi(1-\nu)} (I_1 + I_2) && \text{(E.6)}\\
S_{2323} &= \frac{1}{16\pi(1-\nu)} (1+\rho^2) I_{13} + \frac{1-2\nu}{16\pi(1-\nu)} (I_1 + I_3) && \text{(E.7)}
\end{aligned}$$

where:

$$I_1 = I_2 = \frac{2\pi\rho}{(1-\rho)^{3/2}} \left\{ \cos^{-1}\rho - \rho \left(1-\rho^2\right)^{1/2} \right\}, \; I_3 = 4\pi - 2I_1 \tag{E.8}$$

and:

$$I_{13} = I_{23} = \frac{(I_1 - I_3)}{(\rho^2 - 1)},\ 3I_{33} = 4\pi/\rho^2 - 2I_{13} \tag{E.9}$$

$$I_{11} = I_{22} = I_{12} = \pi - I_{13}/4 = \pi - \frac{(I_1 - I_3)}{4(\rho^2 - 1)} \tag{E.10}$$

Note that the Eshelby tensor in matrix notation is is not symmetric ($S_{iijj} \neq S_{jjii}$).

E.0.6 Spherical Inclusion in a Transversely Isotropic Matrix

The $\mathbb{P}$ tensor has the form of the stiffness tensor of a transverse isotropic material [55]:

$$P_{2222} = P_{1111},\ P_{2211} = P_{1122},\ P_{3311} = P_{1133},\ P_{2323} = P_{1313},\ P_{1212} = 1/2(P_{1111} - P_{1122}) \tag{E.11}$$

where:

$$P_{1111} = \frac{3}{16} I_1(C_{44}, C_{33} - 2C_{44}, C_{44} - C_{33}) + \frac{1}{16} I_2(1, -1) \tag{E.12}$$

$$P_{1122} = \frac{1}{16} I_1(C_{44}, C_{33} - 2C_{44}, C_{44} - C_{33}) - \frac{1}{16} I_2(1, -1) \tag{E.13}$$

$$P_{1133} = \frac{1}{4} I_1(0, -C_{13} - C_{44}, C_{13} + C_{44}) \tag{E.14}$$

$$P_{3333} = \frac{1}{2} I_1(0, C_{11}, C_{44} - C_{11}) \tag{E.15}$$

$$P_{1313} = \frac{1}{16} I_1(C_{11}, -2(C_{11} + C_{13}), C_{11} + C_{33} + 2C_{13}) - \frac{1}{16} I_2(0, -1) \tag{E.16}$$

and

$$I_1(l, m, n) = \frac{1}{C_{33}C_{44}} \int_{-1}^{1} \frac{\rho}{\left\{1 - (1 - \rho^2)\xi^2\right\}^{3/2}} \cdot \frac{l + m\xi^2 + n\xi^4}{\left\{\gamma_1^2 + (1 - \gamma_1^2)\xi^2\right\}\left\{\gamma_2^2 + (1 - \gamma_2^2)\xi^2\right\}} d\xi \tag{E.17}$$

$$I_2(l, m) = \int_{-1}^{1} \frac{\rho}{\left\{1 - (1 - \rho^2)\xi^2\right\}^{3/2}} \cdot \frac{l + m\xi^2}{\left\{\frac{1}{2}(C_{11} - C_{12}) + (C_{44} - \frac{1}{2}(C_{11} - C_{12}))\xi^2\right\}} d\xi \tag{E.18}$$

where γ_1^2, γ_2^2 are the roots of:

$$C_{33}C_{44}x^2 - (C_{11}C_{33} - 2C_{13}C_{44} - C_{13}^2)x + C_{11}C_{44} = 0 \tag{E.19}$$

Appendix F

Addition of r Inclusions Into an Anisotropic Porous Matrix

We consider shale materials at the macroscopic scale to be composed of a textured porous matrix and r types of inclusions of approximately spherical shape that are randomly distributed throughout the anisotropic porous matrix Ω_M. (see Section 6.5). Proceeding as in the case of one type of inclusion, we adopt a continuous description of the stress field in the heterogeneous r.e.v.(6.71)

$$\text{in}\,\Omega_{III} : \boldsymbol{\sigma}(\underline{z}) = \mathbb{C}(\underline{z}) : \boldsymbol{\varepsilon}(\underline{z}) + \boldsymbol{\sigma}^p(\underline{z}) \tag{F.1}$$

together with the following distributions of the elastic properties $\mathbb{C}(\underline{z})$ and the eigenstress $\boldsymbol{\sigma}^p(\underline{z})$ (6.72):

$$\mathbb{C}(\underline{z}) = \begin{cases} \mathbb{C}_M \text{ in } \Omega_M \\ \mathbb{C}_i \text{ in } \Omega_i \end{cases} \quad \boldsymbol{\sigma}^p(\underline{z}) = \begin{cases} -\mathbf{b}_M\, p \text{ in } \Omega_M \\ 0 \text{ in } \Omega_\phi \end{cases} \tag{F.2}$$

where $\mathbb{C}_M = \mathbb{C}^{\text{hom},II}$ is the stiffness tensor of the porous clay laminate defined by (6.66), $\mathbb{C}_i = 3k_i\mathbb{K}+2g_i\mathbb{J}$, $i \in \{1,n\}$ denoting the inclusion type among n different ones, is the stiffness tensor of the (assumed isotropic) inclusion phase i; and $\mathbf{b}_M = \mathbf{b}^{II}$ is the second order Biot coefficient tensor of the porous clay laminate given by (6.67). Following the linear microporomechanics approach, we decompose the problem in two sub-problems:

1. $p = 0$. In this case the compatibility condition (6.75) reads

$$\mathbf{E} = \overline{\varepsilon'(\underline{z})} \Leftrightarrow \mathbb{I} = \left(1 - \sum_{i=1}^{n} f_i\right) \langle \mathbb{A} \rangle_{\Omega_M} + \sum_{i=1}^{n} f_i \langle \mathbb{A} \rangle_{\Omega_i} \tag{F.3}$$

where $f_i = \Omega_i / \Omega_{III} = 1 - f_M$ for $i \in \{1, n\}$ are the inclusions volume fractions. The homogenized stiffness tensor of the material is given by

$$\mathbb{C}_{\text{hom}}^{III} = \mathbb{C}_M + \sum_{i=1}^{n} f_i \left(\mathbb{C}_i - \mathbb{C}_M\right) : \langle \mathbb{A} \rangle_{\Omega_i} \tag{F.4}$$

similarly to (6.76).

2. $\mathbf{E} = \mathbf{0}$. In this case the homogenized tensor of Biot coefficients is given from Levine's theorem (6.15) and the strain compatibility condition (F.3) by

$$\mathbf{b}^{III} = \mathbf{b}_M : \left(\mathbb{I} - \sum_{i=1}^{n} f_i \langle \mathbb{A} \rangle_{\Omega_i}\right) \tag{F.5}$$

similarly to relation (6.78) .The change of the porosity in the subproblem reads:

$$\left[(\phi - \phi_0)^{III}\right]'' = \left(1 - \sum_{i=1}^{n} f_i\right) \left(\mathbf{b}_M : \langle \varepsilon'' \rangle_{\Omega_M} + \frac{p}{N_M}\right) \tag{F.6}$$

where $N_M = N^{II}$. We eliminate $\left(1 - \sum_{i=1}^{n} f_i\right) \langle \varepsilon'' \rangle_{\Omega_M} = -\sum_{i=1}^{n} f_i \langle \varepsilon'' \rangle_{\Omega_i}$ in (F.6) to the benefit of pressure p, by considering the stress average in this sub-problem, in which $\mathbf{E}'' = \overline{\varepsilon''(\underline{z})} = 0$:

$$\boldsymbol{\Sigma}'' = \left(1 - \sum_{i=1}^{n} f_i\right) \langle \boldsymbol{\sigma}'' \rangle_{\Omega_M} + \sum_{i=1}^{n} f_i \langle \boldsymbol{\sigma}'' \rangle_{\Omega_I} = \sum_{i=1}^{n} f_i \left(\mathbb{C}_i - \mathbb{C}_M\right) : \langle \varepsilon'' \rangle_{\Omega_i} - \left(1 - \sum_{i=1}^{n} f_i\right) \mathbf{b}_M p \tag{F.7}$$

Thus, from the equality of (F.5) and (F.7):

$$\sum_{i=1}^{n} f_i \left(\mathbb{C}_i - \mathbb{C}_M\right) \quad : \quad \langle \varepsilon'' \rangle_{\Omega_i} = \mathbf{b}_M : \left[\left(1 - \sum_{i=1}^{n} f_i\right) \mathbb{I} - \left(\mathbb{I} - \sum_{i=1}^{n} f_i \langle \mathbb{A} \rangle_{\Omega_i}\right)\right] p \tag{F.8}$$

$$\mathbf{0} = \sum_{i=1}^{n} f_i \left[\left(\mathbb{C}_i - \mathbb{C}_M\right) : \langle \varepsilon'' \rangle_{\Omega_i} + \mathbf{b}_M : \left(\mathbb{I} - \langle \mathbb{A} \rangle_{\Omega_i}\right) p\right] \tag{F.9}$$

Finally, use of (F.8) and (F.9) in (F.6) yields:

$$\left[(\phi-\phi_0)^{III}\right]'' = \frac{p}{N^{III}};$$
$$\frac{1}{N^{III}} = \frac{1-\sum_{i=1}^{n} f_i}{N_M} - \sum_{i=1}^{n} f_i \mathbf{b}_M : (\mathbb{C}_M - \mathbb{C}_i)^{-1} : \mathbf{b}_M : \left(\mathbb{I} - \langle \mathbb{A} \rangle_{\Omega_i}\right) \tag{F.10}$$

where the following approximation was made: all terms in the sum (F.9) are assumed to be close to zero. Then, for inclusions with similar stiffness properties, representing a reasonably small total volume fraction of the shale, the errors made on the terms $\langle \varepsilon'' \rangle_{\Omega_i}$ compensate in the expression of N^{III} in relation (F.10).

In summary, a superposition of the two subproblems yields the macroscopic state equations of the shale composite material:

$$\boldsymbol{\Sigma} = \mathbb{C}_{\text{hom}}^{III} : \mathbf{E} - \mathbf{b}^{III} p \tag{F.11a}$$
$$(\phi-\phi_0)^{III} = \mathbf{b}^{III} : \mathbf{E} + \frac{p}{N^{III}} \tag{F.11b}$$

together with the poroelastic properties:

$$\mathbb{C}_{\text{hom}}^{III} = \mathbb{C}_M + \sum_{i=1}^{n} f_i \left(\mathbb{C}_i - \mathbb{C}_M\right) : \langle \mathbb{A} \rangle_{\Omega_i} \tag{F.12a}$$
$$\mathbf{b}^{III} = \mathbf{b}_M : \left(\mathbb{I} - \sum_{i=1}^{n} f_i \langle \mathbb{A} \rangle_{\Omega_i}\right) \tag{F.12b}$$
$$\frac{1}{N^{III}} = \frac{1-\sum_{i=1}^{n} f_i}{N_M} + \sum_{i=1}^{n} f_i \mathbf{b}_M : (\mathbb{C}_i - \mathbb{C}_M)^{-1} : \mathbf{b}_M : \left(\mathbb{I} - \langle \mathbb{A} \rangle_{\Omega_i}\right) \tag{F.12c}$$

The input to this homogenization step are the poroelastic properties of the porous clay laminate, $\mathbb{C}_M = \mathbb{C}_{\text{hom}}^{II}$, $\mathbf{b}_M = \mathbf{b}^{II}$, $N_M = N^{II}$, the inclusion volume fractions f_i, and an estimate of the volume average of the inclusion strain concentration tensors $\langle \mathbb{A} \rangle_{\Omega_i}$. Given the matrix–inclusion morphology, such an estimate is suitably provided by the Mori-Tanaka scheme:

$$\langle \mathbb{A} \rangle_{\Omega_M} \simeq \mathbb{A}_M^{est} = \left[(1 - \sum_{i=1}^{n} f_i)\mathbb{I} + \sum_{i=1}^{n} f_i \left(\mathbb{I} + \mathbb{P}^m : (\mathbb{C}_i - \mathbb{C}_m)\right)^{-1}\right]^{-1} \tag{F.13}$$

where $\mathbb{P}^m$ is the so-called P-tensor.

Bibliography

[1] Barenblatt, G. I. (1996). 'Scaling, Self-Similarity and Intermediate Asymptotics', Cambridge, Cambridge University Press.

[2] Barnett, D.M. and Lothe, J., (1975). 'Line force loadings on anisotropic half-spaces and wedges', *J. Appl. Phys.* 23, 470-474.

[3] Bennett, R.H., O'Brien, N.R. and Hulbert, M.H. (1991). 'Determinants of clay and shale microfabric signatures: Processes and mechanisms.' In R. Bennett, W. Bryant and M. Hulbert, ed, 'Microstructure of fine grained sediments: from mud to shale, Springer-Verlag, New York, Chapter 2, 5–32.

[4] Biot, M.A. (1941). 'General theory of three dimensional consolidation.' *J. Appl. Phys.*, 12, 155–164.

[5] Borodich F. M., Keer L. M. and Korach C.S. (2003). 'Analytical Study of Fundamental Nanoindentation Test Relations for Indenters of Non-Ideal Shapes'. *Nanotechnology* 14, 803-808.

[6] Borodich F. M. and Keer L. M. (2004). 'Evaluation of elastic modulus of materials by adhesive (no-slip) nano-indentation'. *Proc. R. Soc. Lond. A*, 460, 507-514.

[7] Boussinesq, J. (1885). 'Applications des potentiels a l etude de l equilibre et du mouvement des solides elastiques'. Gauthier-Villars.

[8] Brinell, J. A. (1901). 'Memoire sur les epreuves a bille en acier'. In *Congres International des Methodes d Essai des Materiaux de Construction*, Paris, Tome 2, 83-94.

[9] Brittan, J., Warner, M. and Pratt, G. (1995). 'Short Note: Anisotropic parameters of layered media in terms of composite elastic properties'. *Geophysics,* 60(4), 1243–1248.

[10] Bulychev, S.I., Alekhin, V. P., Shorshorov, M. Kh., Ternovskii, A. P. and Shnyrev, G. D., Ind. Lab. (1975, Transl: Zavodskaya Laboratoria) 41, 1137.

[11] Chateau, X. and Dormieux, L. (2002). 'Micromechanics of saturated and unsaturated porous media', *Int. J. Numer. Anal. Meth. Geomech.*, 26, 830–844.

[12] Cheng, L., Xia, X., Yu, W., Scriven, L. E. and Gerberich, W. W. (2000). 'Flat-Punch Indentation of Viscoelastic Material.' *J. of Polymer Science Part B: Polymer Physics* 38, 10-22.

[13] Cheng, L., Xia, X., Scriven, L. E. and Gerberich, W. W. (2004). 'Spherical-tip indentation of viscoelastic material.' *Mechanics of Materials.* In press.

[14] Cheng, Y. T. and Cheng, C. M. (1999). 'Scaling relationships in conical indentation of elastic perfectly plastic solids', *Int. J. Sol. Struc.* 36, 1231-1243.

[15] Cheng, Y. T. and Cheng, C. M. (2000). 'What is indentation hardness?', *Surface and Coatings Technology* 133-134, 417-424.

[16] Cheng, Y. T. and Cheng, C. M. (2004).'Scaling, dimensional analysis, and indentation measurements.' *Mat. Sc. and Eng.* R44, 91-149.

[17] Chollacoup, N., Dao, M. and Suresh, S. (2003). 'Depth sensing instrumented indentation with dual sharp indenters', *Acta Materialia,* 51, 3713-3729.

[18] Constantinides, G., Ulm, F.-J., and van Vliet, K.J. (2003). 'On the use of nanoindentation for cementitious materials', *Materials and Structures* 205 (Special issue of Concrete Science and Engineering) RILEM, 191–196.

[19] Constantinides, G., and Ulm, F.-J. (2004). 'The effect of two types of C–S–H on the elasticity of cement-based materials: Results from nanoindentation and micromechanical modeling.' *Cem. Concr. Res.*, Vol. 34 (1), 67–80.

[20] Constantinides, G. and Ulm, F.-J. (2004). 'Stiffness, strength and creep behavior of heat-cured cement pastes: a multiscale indentation investigation.' MIT Res. Rep. to Lafarge, Cambridge, MA, June 2004.

[21] Constantinides, G. (2004). Personal communication.

[22] Cosse, R. (1993). 'Basics of Reservoir Engineering'. Technip.

[23] Coussy, O. (1995). 'Mechanics of porous continua', J. Wiley & Sons, Chichester, UK.

[24] Coussy, O. (2004). 'Poromechanics', J. Wiley & Sons, Chichester, UK.

[25] Delafargue, A. and Ulm, F.-J. (2004). 'Explicit approximations of the indentation modulus of elastically orthotropic solids for conical indenters.' *Int. J. Solids Struct.* (in press).

[26] Djeran-Maigre, J., Tessier, D., Grunberger, D., Velde, B. and Vasseur, G. (1998). 'Evolution of microstructures and of macroscopic properties of some clays during experimental compaction. *Marine and Petroleum Geology*, 15, 109-128.

[27] Doerner M. F. and Nix W. D. (1986). 'A Method for Interpreting the Data from Depth-Sensing Indentation Instruments. *J. Mater. Res.* 1, 601-609.

[28] Donev, A., Cisse, I. Sachs, D., Variano, E.A., Stillinger, F.H., Connely, R., Torquato, S. and Chaikin, P.M. (2004). 'Improving the density of jammed disordered packings using ellipsoids', *Science* 303, 990–993.

[29] Dormieux, L., Molinari, A. and Kondo, D. (2002). 'Micromechanical approach to the behaviour of poroelastic materials', *J. Mech. Phys. Solids,* 50, 2203–2231.

[30] Dormieux, L. and Bourgeois, E.(2003). 'Introduction à la micromécanique des milieux poreux', *Presses de l'Ecole nationale des ponts et chaussées*, Paris, France.

[31] Dussaeault, M. B. (1994). 'Analysis of borehole stability'. In: Siriwardane H. J., Zaman M. M., editors. *Proceedings of the Eight International Conference on Computer Methods and Advances in Geomechanics*, 3, Rotterdam: Balkema, 125-137.

[32] Elliot H.A., 1949, 'Axial symmetric stress distributions in Aelotropic Hexagonal crystals: The Problem of the Plane and Related Problems'. *Proc. Camb. Phil. Soc.*, 45, 621-630.

[33] El Omri, A., Fennan, A., Sidoroff, F. and Hihi A. (2000). 'Elastic-Plastic homogenization for layered composites.' *European Journal of Mechanics A/Solids* 19, 585–601.

[34] Eshelby, J. (1957). 'The determination of the elastic field of an ellipsoidal inclusion, and related problems.' *Proceedings of the Royal Society London, Series A*, 241, 376–396.

[35] Fabrikant, V. I. (1988). 'Elastic field around a circular punch'. *J. Appl. Mech.* 55, 604-610.

[36] Fabrikant, V. I. (1989). 'Applications of potential theory in mechanics', Kluwer, The Nederlands.

[37] Feodorov, F. (1968). 'Theory of elastic waves in crystals'. Plenum Press, New York.

[38] Fischer-Cripps, A. C. (2002). 'Nanoindentation'. Springer Verlag, New-York.

[39] Galin, L. A. (1951). 'Contact Problems in Theory of Elasticity', translated by H. Moss. In: Sneddon, I. N. (Ed.), North Carolina State College.

[40] Ganneau, F.P. and Ulm, F.-J. (2004). 'From nanohardness to strength properties of cohesive-frictional Materials — Application to shale materials', MIT-CEE Res. Rep. (SM-Thesis), in preparation.

[41] Gmira, A., Zabat, M., Pellenq, R. J.- M. and Van Damme, H. (2004). 'Microscopic physical basis of the poromechanical behavior of cement-based materials'. Special issue of *Concrete Science and Engineering*, Vol. 37 (265), 3–14.

[42] Hanson, M. T. (1992). 'The Elastic Field for Conical Indentation Including Sliding Friction for Transverse Isotropy'. *J. Appl. Mech.,* 59, S123-S130.

[43] Harding, J. W. and Sneddon, I. N. (1945). 'The elastic stress field produced by the indentation of the plane surface of a semi-infinite elastic solid by a rigid punch'. *Proc. Cambridge Phil. Soc.* 41, 16-26.

[44] Hashin, Z. and Strikman, S. (1963). 'A variational approach to the theory of elastic behaviour of multiphase materials'. *J. Mech. Phys. Solids,* 11, 127-140.

[45] Hellmich, C. and Ulm, F.-J. (2002). 'A micromechanical model for the ultrastructural stiffness of mineralized tissues'. J. *Eng. Mech., (ASCE)*, 128(9),898-908.

[46] Helnwein, P. (2001). 'Some remarks on the compressed matrix representation of symmetric second-order and fourth-order tensors.' *Comput. Meth. Appl. Mech. Eng.* 190, 2753–2770.

[47] Hertz, H. (1881). 'On the contact of elastic solids (in German), Zeitschrift fur die reine und angewandte Mathematik'. English translation in miscellaneous papers (Translated by D. E. Jones and G. A. Schott): 99, 146-62, Macmillan, London (1896), 92:156-71.

[48] Hornby, B., Schwartz, L. and Hudson, J. (1994). 'Anisotropic effective medium modeling of the elastic properties of shales'. *Geophysics,* 59-10, 1570–1583.

[49] Hornby, B. (1998). 'Experimental laboratory determination of the dynamic elastic properties of wet, drained shales.' *J. Geophys. Res.*, 103(B12), 29,945-29,964.

[50] Jakobsen M., Hudson, J.A. and Johansen, T.A. (2003). 'T-matrix approach to shale acoustics'. *Geophys. J. Int.,* 154, 533–558.

[51] Jaeger, H.M., and Nagel, S. R. (1992). 'Physics of granular state', *Science*, Vol. 255, No. 5051, 1523–1531.

[52] Johansen, T.A., Ruud, B.O. and Jakobsen, M. (2004). 'Effect of grain scale alignment on seismic anisotropy and reflectivity of shales.' *Geophysical Prospecting*, 52, 133–149.

[53] Jones, L.E.A. and Wang, H.F. (1994). 'Ultrasonic velocities in Cretaceous shales from the Williston basin.' *Geophysics,* 46, 288–297.

[54] Katti, D., Schmidt, S., Gosh, D. and Katti, K. (2003). 'Modeling response of pyrophyllite clay interlayer to applied stress using steered moelcular dynamics'. personal communication.

[55] Laws, N. (1985). 'A note on penny-shaped cracks in transversely isotropic materials'. *Mechanics of Materials*, 4, 209-212.

[56] Love, A.E.H. (1939). 'Boussinesq's problem for a rigid cone'. *Quart. J. Math.,* 10, 161-175.

[57] Lu, J., Suresh, S. and Ravichandran, G. (2003). 'Dynamic indentation for determinating the strain rate sensivity of metals'. *J. Mech. Phys. Solids,* 51, 1923-1938.

[58] Marion, D., Nur, A., Yin, H., and Han, D. (1992). 'Compressional velocity and porosity in sand-clay mixtures.' *Geophysics*, 57(4), 554–563.

[59] Mavko, G., Mukerji, T. and Dvorkin, J. (1998). 'The Rock Physics Handbook'. Cambridge University Press, UK.

[60] Mitchell, J. (1993). 'Fundamentals of soil behavior'. J. Wiley & Sons, New York.

[61] Mori, T. and Tanaka, K. (1973). 'Average stress in the matrix and average elastic energy of materials with misfitting inclusions'. *Acta. Metall.*, 21, 571-574.

[62] Mura, T. (1987). 'Micromechanics of defects in solids'. Kluwer Academic, Dordrecht, 1987.

[63] Norris, A.N. (1985). 'A differential scheme for the effective moduli of composites'. *Mechanics of Materials*, 4, 1-16.

[64] Oliver, W.C. and Pharr, G.M. (1992). 'An improved technique for determining hardness and elastic modulus using load and displacement sensing indentation experiments.' *J. Mater. Res.*, 7(6), 1564–1583.

[65] Oliver, W.C. and Pharr, G.M. (2004). 'Measurement of hardness and elastic modulus by instrumented indentation: Advances in understanding and refinements to methodology.' *J. Mater. Res.*, 19(1), 3–20.

[66] Ovaert, T. C. (1993). 'On the Indentation of a Transversely Isotropic Half-Space With Application to Thin Solid Lubricant Films'. *ASME J. Tribol.*, 115, 650-657.

[67] Pharr, G. M., Oliver, W. C. and Brotzen, F. R. (1992). 'On the generality of the relationship among contact stiffness, contact area, and elastic modulus during indentation'. *J. Mat. Res.*, 7(3), 613-617.

[68] Swadener J. G., Rho J. Y. and Pharr, G. M. (2001). 'Effects of Anisotropy on Elastic Moduli Measured by Nanoindentation in Human Tibial Cortical Bone.' *J. Biomed. Mat. Res.*, 57, 108-112.

[69] Pharr, G. M. (2002). 'Understanding nanoindentation unloading curves.' *J. Mater. Res.*, 17 (10), 2660-2671.

[70] Ponte Castagneda, P. and Willis, J.R. (1995). 'The effect of spatial distribution on the effective behavior of composite materials and cracked media.' *J. Mech. Phys. Solids*, 43 (12). 1995, p 1919-1951.

[71] Prasad, M., Kopycinska, M., Rabe, U. and Arnold, W. (2002). 'Measurement of Young's modulus of clay minerals using atomic force acoustic microscopy.' *Geophys. Res. Let.*, 29(8) 1172, 13-1 – 13-4.

[72] Pratson, L.F., Stroujkova, A., Herrick, D., Boadu, F. and Malin, P. (2003). 'Predicting seismic velocity and other rock properties from clay content only.' *Geophysics*, 68(6), 1847–1856.

[73] Sakai, M. (2003). 'Elastic recovery in the unloading process of pyramidal microindentation' *J. Mater. Res.*, 18 (7), 1631-1640.

[74] Sayers, C.M. (1994). 'The elastic anisotrophy of shales', *J. Geoph. Res.*, 99(B1), 767–774.

[75] Sayers, C. (1999). 'Stress-dependent seismic anisotropy of shales.' *Geophysics*, 64(1), 93–98.

[76] Shi, D., Lin, Y. and Ovaert, T. C. (2003). 'Indentation of an Orthotropic Half-Space by a Rigid Ellipsoidal Indenter.' *ASME J. Tribol.*, 125, 223-331.

[77] Sneddon, I. (1965). 'The relation between load and penetration in the axi-symmetric Boussinesq problem for a punch of arbitrary profile.' *In. J. Eng. Sc.*, 3, 47-57.

[78] Sneddon, I. editor (1977). 'Application of Integral Transforms in the Theory of Elasticity.' Springer Verlag, Wien-New York.

[79] Suquet, P. editor (1997). 'Continuum micromechanics' Springer Verlag, Wien-New York.

[80] Swadener, J. G. and Pharr, G. M., (2001). 'Indentation Modulus of Elastically Anisotropic Half-Spaces by Cones and Parabolae of Revolution.' *Philos. Mag. A*, 81, 447-466.

[81] Tabor, D. (1951). 'Hardness of metals', Clarendon press, Oxford.

[82] Ternovskii, A. P., Alekhin, V. P., Shorshorov, M. Kh. and Khrushchov, M. M., Ind. Lab. (1973, Transl: Zavodskaya Laboratoria) 39, 1242.

[83] Thomsen, L. (1986). 'Weak elastic anisotropy.' *Geophysics,* 52(10), 1954–1966.

[84] Thomsen, L. (2001). 'Seismic anisotropy.' *Geophysics,* 66(1), 40–41.

[85] Ulm, F.-J., Constantinides, G. and Heukamp, F.H. (2004). 'Is concrete a poromechanics material? – A multiscale investigation of poroelastic properties', *Materials and Structures*, Special issue of *Concrete Science and Engineering*, Vol. 37 (265), 43–58.

[86] Ulm, F.-J., Constantinides, G., Delafargue A., Abousleiman, Y., Ewy, R., Duranti, L., McCarty, D.K. (2004). 'The sources of anisotropy of shale materials – I. Nanoindentation Investigation of Shale Materials; II. Microporoelastic Modeling.' MIT Res. Rep. to Chevron-Texaco, Cambridge, MA, July, 2004.

[87] Vanorio, T., Prasad, M. and Nur, A. (2003). 'Elastic properties of dry clay mineral aggregates, suspensions and sandstones.' *Geophys. J. Int.*, 155, 319–326.

[88] Velde B. (1995). 'Origin and mineralogy of clays.' Springer-Verlag, New York.

[89] Vlassak J.J. and Nix W.D. (1993). 'Indentation modulus of elastically anisotropic half spaces.' *Phil. Mag. A,* 67 (5), 1045–1056.

[90] Vlassak J.J. and Nix, W.D. (1994). 'Measuring the elastic properties of anisotropic materials by means of indentation experiments.' *J. Mech. Phys. Solids,* 42 (8), 1223–1245.

[91] Vlassak J. J., Ciavarella M, Barber J. R. and Wang X., 2003, 'The Indentation Modulus of Elastically Anisotropic Materials for Indenters of Arbitrary Shape.' *J. Mech. Phys. Solids,* 51, 1701-1721.

[92] Wang, Z., Wang, H. and Cates, M.E. (2001). 'Effective elastic properties of solid clays'. *Geophysics,* 66(2), 428–440.

[93] Wang, Z. (2002). 'Seismic anisotropy in sedimentary rocks. Part 1: A single plug laboratory method; Part 2: Laboratory data.' *Geophysics,* 67(5), 1415–1422 (part I) and 1423–1440 (part II).

[94] Weaver, (1989). 'Clay, muds and shale. Development in Sedimentology', 44, Elsevier.

[95] Willis, J.R., (1966). 'Herztian Contact of Anisotropic Bodies'. *J. Mech. Phys. Solids,* 14, 163-176.

[96] Willis, J.R. (1977). 'Bounds and self-consistent estimates for the overall moduli of anisotropic composites.' *J. Mech. Phys. Solids*, 25, 185-202.

[97] Willis, J. R. (1981). 'Variational and related methods for the overall properties of composites', *Adv. Appl. Mech.* 21, 1-78.

[98] Willis, J. R. (2002). 'Mechanics of composites'. Lecture notes from the Ecole Polytechnique, Palaiseau, France.

[99] Zaoui, A. (1997). 'Materiauz heterogenes et composites.' Lecture notes from the Ecole Polytechnique, Palaiseau, France, in french.

[100] Zaoui, A. (2002). 'Continuum micromechanics: Survey.' *J. Eng. Mech. (ASCE),* 128(8). 808–816.